



HAL
open science

Characterization of the dystrophic muscle by ^{23}Na NMR and ^1H NMR T spectrum

Teresa Gerhalter

► **To cite this version:**

Teresa Gerhalter. Characterization of the dystrophic muscle by ^{23}Na NMR and ^1H NMR T spectrum. Medical Physics [physics.med-ph]. Université Paris Saclay (COMUE); Freie Universität (Berlin), 2018. English. NNT : 2018SACLS219 . tel-01842257

HAL Id: tel-01842257

<https://theses.hal.science/tel-01842257>

Submitted on 18 Jul 2018

HAL is a multi-disciplinary open access archive for the deposit and dissemination of scientific research documents, whether they are published or not. The documents may come from teaching and research institutions in France or abroad, or from public or private research centers.

L'archive ouverte pluridisciplinaire **HAL**, est destinée au dépôt et à la diffusion de documents scientifiques de niveau recherche, publiés ou non, émanant des établissements d'enseignement et de recherche français ou étrangers, des laboratoires publics ou privés.

Characterization of the dystrophic muscle by ^{23}Na NMR and ^1H NMR T_2 spectrum

Thèse de doctorat de Freie Universität Berlin et l'Université Paris-Saclay, préparée à l'Université Paris Sud

École doctorale n°575 electrical, optical, bio-physics and engineering (EOBE)

DEPARTMENT OF BIOLOGY | CHEMISTRY | PHARMACY
Spécialité de doctorat: Imagerie et physique médicale

Thèse présentée à Paris et à Berlin, et soutenue à Paris, le 12/07/2018, par

Teresa Gerhalter

Composition du Jury :

Andrew BLAMIRE Professeur, Newcastle University	Rapporteur
Fritz SCHICK Professeur, Universitätsklinikum Tübingen	Rapporteur
Sigmar STRICKER Professeur, Freie Universität Berlin	Rapporteur
Maria REICHENBACH Chargée de recherche, Freie Universität Berlin	Examineur
Emmanuel DURAND Professeur, Université Paris Sud	Examineur, Président
Pierre CARLIER Directeur de recherche, CEA	Directeur de thèse
Simone SPULER Professeur, Freie Universität Berlin	Co-Directrice de thèse/ Rapporteur
Benjamin MARTY Chargé de recherche, Institut de Myologie	Invité

Acknowledgement

The first acknowledgement is to the patients and their families who were willing to participate in my study. Repeated visits to the hospital are not always easy to manage especially with children who are already touched by a muscle disorder. I am sincerely grateful for the efforts the children and their parents made toward our clinical research. I am also very thankful for the numerous healthy volunteers that gave time to participate in the studies.

This co-tutelle thesis was part of the binational MyoGrad PhD program, which allowed me to get to know numerous researchers of the international muscle science research community and also provided me with a broaden knowledge about different aspects of muscle dystrophy. I would like to thank both my supervisors, Pierre Carlier and Simone Spuler. Pierre has always been available to provide advice and support during my doctoral studies. He has taught me much about being a researcher in muscle sciences and has provided an enriching environment to cultivate my critical thinking and NMR expertise. I wish to thank him for his persistence in making sure that I learn my physics properly. Also the support and confidence of Simone contributed to my professional development. Assisted by Verena Schöwel, who lend always a sympathetic ear to me, I was able to obtain some experience in preclinical research profiting from their expertise. This French-German collaboration was very enriching not only professionally but also personally and I have to thank Susanne Wissler and Julie Vandenheede, who helped me a lot with all the administration issues related to my binational supervised thesis.

During my time as PhD student, I was supported by my tutor Benjamin Marty. I truly appreciate all the time and effort he put to back my thesis. He was always very encouraging and helped me throughout my thesis work. Being patient and assisting me with technical and theoretical pitfalls in the daily life of a NMR researcher, he greatly took care of me whenever needed. I would also like to thank Aurea Bach, who taught me a lot about animal NMR and assisted me during my preclinical test. A big thank you to Pierre-Yves Baudin for providing informatics tools and support to treat data, to Ericky Caldas for fruitful discussion about T_2 , and to

Harmen Reyngoudt for shearing his knowledge about NMR spectroscopy and statistics. I also would like to thank all my colleagues of the NMR laboratory for their encouragement, troubleshooting, and the nice time I had with them in Paris. Merci à tous pour ces moments inoubliables qui ont passé tellement vite.

The clinical study would not have been possible without the collaboration with Armin Nagel and his “MR Physik” group in Erlangen. A huge thank you to Armin for enabling this collaboration on a short notice. It was a pleasure to work in such a young and dynamic group and I wouldn't like to miss the good times in Erlangen. I especially enjoyed working with Lena Gast on multiple quantum filtered sequences and I also appreciated her support during the clinical study. Ich freue mich schon auf den nächsten Berg und auf viele weitere Aktivitäten mit euch!

I would like to thank Andrew Blamire, Fritz Schick, and Sigmar Stricker for accepting to review this manuscript and Maria Reichenbach and Emmanuel Durand for being part of the jury.

Several organizations financed this work. At the beginning, the Institute of Myology was funding my work for six months. Siemens Healthcare S.A.S. financed it then for another three years, for which I am very grateful. Furthermore, the German-French University provided a grant toward the project to support my travels between Germany and France. Moreover, the clinical study in Erlangen was supported by the Johannes and Frieda Marohn Foundation (to Armin Nagel and Regina Trollmann, 2016). My thanks also go to the Imaging Science Institute (Erlangen, Germany) for providing us with measurement time at the 3T scanner.

Zum Schluss möchte ich auch noch gerne meiner Familie und Freunden daheim danken. Ihr habt mir meine leider immer sehr kurzen Aufenthalte sehr angenehm gestaltet und euch auch sehr spontan für mich Zeit genommen. Ich weiß das sehr zu schätzen! Das hat mir viel Energie und Motivation zum Arbeiten gegeben.

Table of contents

Abstract.....	v
Zusammenfassung.....	vii
Résumé	ix
Résumé extensif : Caractérisation du muscle dystrophique par RMN du ²³ Na et spectres RMN du T ₂ du ¹ H	xi
Introduction générale.....	xi
Etat de l'art	xii
Objectif.....	xiv
Démarche expérimentale	xv
General introduction	1
1.1 The role of nuclear magnetic resonance in establishing biomarkers for diseased muscles....	1
1.2 Thesis objectives	4
1.3 Structure of the thesis	6
A brief reminder on skeletal muscle.....	9
2.1 Anatomy and architecture of skeletal muscle.....	9
2.2 Energy metabolism.....	12
2.3 Role of sodium in biological tissue	12
2.3.1 Transmembrane electrochemical gradient	12
2.3.2 Homeostasis of organism	15
2.4 Skeletal muscle damage and regeneration	15
2.5 The diverse group of muscular dystrophies	17
2.5.1 Dysferlinopathies and the role of dysferlin in the membrane repair mechanism.....	18
2.5.2 The pathological disease progression of Duchenne muscular dystrophy and concurrent ion alterations	19

Nuclear magnetic resonance	23
3.1 Basic principles of nuclear magnetic resonance	23
3.1.1 Magnetic polarization and Larmor frequency.....	23
3.1.2 Magnetization excitation.....	26
3.1.3 Longitudinal and transverse relaxation.....	28
3.1.4 Chemical shift	31
3.2 From nuclear magnetic resonance spectroscopy to imaging.....	32
3.2.1 Nuclear magnetic resonance spectroscopy.....	32
3.2.2 Nuclear magnetic resonance imaging	33
3.3 A special nucleus: sodium	34
3.3.1 NMR properties of ^{23}Na	34
3.3.2 Quantification of the total sodium content	37
3.3.3 NMR techniques to probe sodium in different compartments.....	38
3.4 Applications of NMR in the dystrophic skeletal muscle	46
3.4.1 NMR-based outcome measures in the dystrophic skeletal muscle	46
3.4.2 ^{23}Na NMR research in muscle dystrophies.....	50
Methods for quantitative NMR acquisitions in the skeletal muscle.....	55
4.1 Hardware.....	55
4.1.1 NMR scanners.....	55
4.1.2 Coils	55
4.2 Fat quantification	56
4.2.1 ^1H spectroscopy	56
4.2.2 Dixon.....	57
4.3 Fast T_1 measurement.....	58
4.3.1 Fast spin-echo sequence	58
4.4 Water T_2 measurement	59
4.4.1 Advanced models for water T_2 mapping	59
4.4.2 Multi-component water T_2 relaxation evaluation using ISIS-CPMG.....	61
4.5 pH measurement.....	63
4.5.1 ^{31}P spectroscopy	63
4.5.2 ^1H spectroscopy	64
4.6 ^{23}Na NMR methods for sodium quantification	65
4.6.1 Development of a non-localized ^{23}Na NMR protocol.....	65
4.6.2 Double quantum filter with magic angle sequence	69
4.6.3 Fast ^{23}Na NMR imaging sequences.....	70
4.7 Post-processing tools and statistical analysis.....	76
Characterization of healthy skeletal muscle tissue by ^{23}Na NMR.....	77
5.1 Monitoring the variations of ^{23}Na NMR signals during different vascular filling conditions in comparison to ^1H T_2 alterations	77
5.1.1 Materials and methods	77

5.1.2	Results	80
5.1.3	Discussion	86
5.2	Signal quantification for non-localized ²³Na NMR spectroscopy	90
5.2.1	Materials and methods	90
5.2.2	Results	92
5.2.3	Discussion	94
5.3	Impact of prolonged ischemia in murine skeletal muscle monitored by ²³Na and ¹H NMR..	96
5.3.1	Materials and methods	96
5.3.2	Results	97
5.3.3	Discussion	99
5.4	Double- and triple-quantum filtered ²³Na NMR in human resting skeletal muscle tissue...	101
5.4.1	Materials and methods	102
5.4.2	Results	103
5.4.3	Discussion	104
5.5	Conclusion	105
 Preclinical studies of the murine dystrophic muscle.....		 107
6.1	Murine models for muscular dystrophies	107
6.2	Materials and methods.....	109
6.3	Characterisation of a novel dysferlin-deficient murine model by NMR	113
6.4	Results of standard NMR protocol for <i>mdx</i> model	119
6.5	Validation of new NMR outcome measures on dystrophic murine models	123
6.6	Discussion	126
6.6.1	NMR characterization of the dysferlin-deficient murine models.....	126
6.6.2	NMR characterization of the dystrophin-deficient murine models.....	128
6.6.3	Sensitivity of ²³ Na NMR and ISIS-CPMG sequences to the dystrophic muscle	130
6.6.4	Limitations.....	132
6.7	Conclusion	132
 Characterization of the dystrophic muscle by quantitative ²³ Na NMR and ¹ H NMR in a clinical setting		 135
7.1	Characterization of skeletal muscle of Duchenne muscular dystrophy patients by ²³Na NMR and ¹H NMR	135
7.2	Materials and methods.....	136
7.3	Results	140
7.3.1	Visit 1: DMD in comparison with control group.....	140
7.3.2	Baseline and six-month follow up of DMD patients.....	148
7.4	Discussion	151
7.5	Conclusion	154

General discussion, conclusion & perspectives	155
8.1 Methodological contributions of the thesis	155
8.2 ²³Na NMR in the future: is it worth it?	158
List of abbreviations and symbols.....	I
List of figures	IV
List of tables	XVI
Bibliography	XIX

Abstract

As for other organs, nuclear magnetic resonance (NMR) of skeletal muscle can be repeated as many times as needed, making it perfectly suited for a non-invasive longitudinal monitoring of neuromuscular patients during clinical trials. The aim of the thesis is to investigate the sensitivity of novel NMR outcome measures (OM) aiming to quantify pathological changes in the dystrophic muscle. Muscular dystrophy (MD) refers to a heterogeneous group of diseases with progressive muscle wasting and associated weakness characterized by variable degrees of necrosis, regeneration, ionic homeostasis disturbances, chronic inflammation, and, ultimately, resulting in the replacement of muscles by fibro-fatty tissue. My focus was on the evaluation of ^{23}Na NMR and advanced ^1H transverse relaxation time (T_2) techniques as early, sensitive OM. ^{23}Na NMR measures the tightly controlled sodium concentrations and distribution in skeletal muscle tissue. This biophysical information can be used to assess ion homeostasis and cell integrity. However, ^{23}Na NMR suffers from a low sensitivity and *in vivo* concentration compared to ^1H . Alterations in the muscle ^1H T_2 , commonly interpreted as an indicator of disease activity, are linked to a variety of non-specific events like oedema, inflammation, or necrosis that precede the actual muscle replacement by fat.

Protocols including different ^{23}Na NMR and ^1H T_2 methods were implemented to evaluate healthy and dystrophic skeletal muscle tissues of animal models and patients. First, a non-localized ^{23}Na NMR protocol was developed in order to reduce the usually long acquisition times of ^{23}Na NMR and it was validated on healthy subjects under different vascular filling conditions. The ^{23}Na NMR approach was more sensitive than standard global ^1H T_2 to monitor acute changes in extracellular volume fractions of the leg. Our ^{23}Na NMR protocol permits the monitoring of total and intracellular weighted ^{23}Na signal in less than 15 minutes. In the context of MD, these OM offer novel options to investigate ion channel/transporter impairments, membrane integrity, or even, indirectly, fibrosis formation.

Murine models represent a valuable tool to study the pathological progress of MD and to test possible therapeutic interventions. Additionally, the specificity of NMR techniques to monitor certain pathologies can be validated on well-described murine models. Here, a new murine model for dysferlinopathy named *MMex38* was characterized by standard NMR techniques. Severity of disease activity and progression was reflected by the significant fatty replacement, showing for the first time in mice some similarity with the phenotype observed in humans. A comprehensive protocol including

the ^{23}Na and ^1H T_2 OM demonstrated hydro-ionic homeostasis disturbances in different murine MD models.

In a natural history study on Duchenne muscular dystrophy (DMD) patients in Erlangen, different NMR imaging and spectroscopy methods were combined to evaluate their sensitivity to monitor the pathological processes of MD at an early stage of the disease. We demonstrated that DMD patients exhibit elevated total sodium concentrations and ^{23}Na intracellular weighted signal as well as water T_2 at the early disease stage preceding the fibro-fatty infiltration. Intracellular sodium accumulations did not systematically parallel water T_2 increases. This work provides evidence that ^{23}Na NMR could offer a sensitive outcome measure able to monitor specific alteration of the dystrophic muscle at a very early stage.

Zusammenfassung

Wie bei anderen Organen kann die Magnetresonanztomographie (MRT) der Skelettmuskulatur so oft wie nötig wiederholt werden, da keine ionisierende Strahlung eingesetzt wird. Aufgrund dieser Eigenschaft ist sie perfekt für eine nicht-invasive longitudinale Überwachung neuromuskulärer Patienten im Rahmen von klinischen Studien geeignet. Ziel meiner Dissertation war es, die Sensitivität neuer MRT-basierter Biomarker zur Quantifizierung pathologischer Veränderungen im dystrophischen Muskel zu untersuchen. Muskeldystrophie (MD) beschreibt eine heterogene Gruppe von Krankheiten mit progressivem Muskelschwund und Muskelschwäche, die durch unterschiedlichen Grad an Nekrose, Regeneration, Ionenhaushaltstörungen, chronischer Entzündung und schließlich Fett- und Bindegewebs-einlagerungen im Muskel charakterisiert wird. Mein Schwerpunkt lag auf der Evaluierung von ^{23}Na MRT Messungen und Messungen der transversalen ^1H Relaxationszeit (T_2) als sensitive und frühe Biomarker. Mittels ^{23}Na MRT kann die streng regulierte Natriumkonzentration und ihre Verteilung im Muskelgewebe untersucht werden. Diese biophysikalischen Informationen können verwendet werden, um den Ionenhaushalt und die Zellintegrität zu bewerten. Allerdings wird ^{23}Na MRT durch eine geringere Sensitivität und *in-vivo*-Konzentration der Natriumionen im Vergleich zu ^1H MRT beeinträchtigt. Veränderungen der ^1H T_2 -Zeit im Muskel, die gemeinhin als Indikator für die Krankheitsaktivität der Muskeldystrophie interpretiert werden, sind mit einer Vielzahl von unspezifischen Ereignissen wie Ödemen, Entzündungen oder Nekrose verbunden, die dem tatsächlichen Ersatz von Muskel- durch Fettgewebe vorausgehen.

In dieser Arbeit wurden Protokolle mit verschiedenen ^{23}Na -MRT- und ^1H - T_2 -Methoden implementiert, um gesundes und dystrophisches Skelettmuskelgewebe von Tiermodellen und Patienten zu bewerten. Zunächst wurde ein nicht-lokalisiertes ^{23}Na MRT-Protokoll entwickelt, um die meist langen Aufnahmezeiten der ^{23}Na MRT zu reduzieren. Dieses Protokoll wurde bei gesunden Probanden unter verschiedenen Gefäßfüllbedingungen validiert. Der ^{23}Na MRT-Ansatz erwies sich als sensibler und somit als geeigneter zur Überwachung akuter Veränderungen des extrazellulären Volumenanteils des Beins als die Standard ^1H T_2 -Messungen. Unser ^{23}Na MRT-Protokoll erlaubt die Überwachung des gesamten und intrazellulär gewichteten ^{23}Na -Signals in weniger als 15 Minuten. Im Zusammenhang mit MD bieten diese Biomarker neuartige Möglichkeiten, Beeinträchtigungen der Ionenkanäle/Transporter, die Membranintegrität, oder sogar indirekt die Bindegewebsbildung zu untersuchen.

Mausmodelle stellen einen wertvollen Modellorganismus dar, um den pathologischen Fortschritt von MD zu untersuchen und mögliche therapeutische Interventionen zu prüfen. Darüber hinaus kann die Spezifität von MRT-Techniken zur Überwachung bestimmter Pathologien mittels gut beschriebener Mausmodelle validiert werden. Hier wurde ein neues Mausmodell für Dysferlinopathie namens *MMex38* durch Standard-MRT-Techniken charakterisiert. Der Schweregrad der Erkrankungsaktivität und des -fortschrittes wurde durch die signifikante Fettinfiltration reflektiert. Dies zeigte zum ersten Mal in Mäusen Ähnlichkeiten mit dem Phänotyp, der bei Menschen beschrieben wird. Ein umfassendes Protokoll mit ^{23}Na MRT und ^1H T₂-basierenden Biomarkern zeigte zusätzlich hydroionische Haushaltsstörungen in verschiedenen Mausmodellen für MD.

Für eine Verlaufsstudie bei Patienten mit Duchenne Muskeldystrophie (DMD) in Erlangen wurden verschiedene MRT-Bildgebungs- und Spektroskopiemethoden kombiniert, um deren Empfindlichkeit zur Überwachung der pathologischen Prozesse von MD in einem frühen Stadium der Erkrankung zu bewerten. Wir haben gezeigt, dass DMD Patienten erhöhte Gesamtnatriumkonzentrationen und intrazellulär gewichtetes ^{23}Na Signal, sowie Wasser T₂ in der frühen Krankheitsstufe vor der Fett- und Bindegewebsinfiltration aufweisen. Das intrazellulär gewichtete Natriumsignal war systematisch erhöht, auch bei normalen Wasser T₂-Werten. Diese Arbeit lieferte Beweise dafür, dass ^{23}Na MRT sensible Biomarker bieten könnte, die eine spezifische Veränderung des dystrophischen Muskels in einem sehr frühen Stadium überwachen können.

Résumé

La résonance magnétique nucléaire (RMN) du muscle squelettique est parfaitement adaptée à une surveillance longitudinale des patients atteints de maladies neuromusculaires. Le but de la thèse était d'étudier la sensibilité de nouveaux biomarqueurs RMN visant à quantifier les changements pathologiques dans le muscle dystrophique. La dystrophie musculaire (DM) désigne un groupe hétérogène de maladies avec une atrophie musculaire progressive associée à un état de faiblesse. Elle est caractérisée par des degrés variables de nécrose, de régénération, de troubles de l'homéostasie ionique, d'inflammation chronique et finalement par le remplacement des muscles par du tissu fibro-graisseux. Mon objectif était d'évaluer la RMN du ^{23}Na et les techniques avancées de mesure du temps de relaxation transversal ^1H (T_2) en tant que des biomarqueurs sensibles et précoces. La RMN du ^{23}Na mesure les concentrations de sodium étroitement contrôlées et donne sa distribution dans le tissu. Cette information peut être utilisée pour évaluer l'homéostasie ionique et l'intégrité cellulaire. Cependant, la concentration *in vivo* en ^{23}Na est faible, la RMN du ^{23}Na souffre donc d'une faible sensibilité par rapport à ^1H . L'altération du T_2 ^1H du muscle, communément interprétée comme un indicateur de l'activité de la maladie, est liée à une variété d'événements non-spécifiques tels que l'œdème, l'inflammation ou la nécrose, qui précèdent le remplacement musculaire par la graisse.

Des protocoles comprenant diverses méthodes de RMN du ^{23}Na et de ^1H T_2 ont été mis en œuvre pour évaluer les tissus musculaires squelettiques sains et dystrophiques sur des modèles animaux et sur patients. Tout d'abord, un protocole de RMN du ^{23}Na non localisé a été développé afin de réduire les temps d'acquisition habituellement longs de la RMN du ^{23}Na . Ce protocole a été validé sur des sujets sains sous différentes conditions de remplissage vasculaire. L'approche de la RMN du ^{23}Na était plus sensible que celle du ^1H T_2 standard pour surveiller les changements aigus importants dans les fractions de volume extracellulaire de la jambe. Notre protocole de RMN du ^{23}Na permet la surveillance du signal de ^{23}Na total et intracellulaire pondéré en moins de 15 minutes. Ces biomarqueurs offrent de nouvelles options pour étudier les altérations des canaux ioniques/transporteurs, l'intégrité de la membrane ou même, indirectement, la formation de fibrose.

Les modèles murins représentent un outil précieux pour étudier l'avancée pathologique de la maladie. De plus, la spécificité des techniques de RMN pour le suivi de certaines pathologies peut être validée sur des modèles murins bien décrits. Ici, un nouveau modèle murin de dysferlinopathie nommé *MMex38* a été caractérisé par des techniques de RMN standard. La sévérité de l'activité de la

maladie et sa progression ont été reflétées par un remplacement graisseux significatif, montrant pour la première fois chez la souris une certaine similitude avec le phénotype observé chez l'homme. Un protocole complet comprenant les biomarqueurs de ^{23}Na et $^1\text{H T}_2$ a démontré des perturbations de l'homéostasie hydro-ionique pour différents modèles murins de MD.

Dans une étude d'histoire naturelle sur des patients atteints de dystrophie musculaire de Duchenne (DMD) réalisée à Erlangen, différentes méthodes d'imagerie et de spectroscopie ont été combinées pour évaluer leur sensibilité dans la surveillance de processus pathologiques à un stade précoce de la maladie. Ces patients présentaient des concentrations élevées de sodium total et un signal pondéré intracellulaire de ^{23}Na élevé ainsi que de $^1\text{H T}_2$ élevé au stade précoce de la maladie précédant l'infiltration fibro-grasseuse. Les accumulations de sodium intracellulaire ne sont pas systématiquement parallèles aux augmentations du $^1\text{H T}_2$. Ce travail fournit des preuves que la RMN du ^{23}Na pourrait offrir un biomarqueur sensible capable de surveiller l'altération spécifique du muscle dystrophique à un stade très précoce.

Résumé extensif : Caractérisation du muscle dystrophique par RMN du ^{23}Na et spectres RMN du T_2 du ^1H

Introduction générale

La dystrophie musculaire (DM) désigne un groupe hétérogène de maladies neuromusculaires qui se caractérisent par une dégénérescence du tissu musculaire se traduisant par une atrophie du muscle et une perte de force. Cela peut provoquer dès l'enfance des difficultés pour marcher ou se servir de ses bras ou de ses mains. La Dystrophie Musculaire de Duchenne (DMD) est un exemple connu de myopathie causée par une mutation du gène codant la protéine dystrophine. Les fibres musculaires détruites sont progressivement remplacées par de la graisse et du tissu conjonctif, provoquant une perte totale de l'ambulation au cours de l'adolescence. Ces patients meurent avant d'atteindre l'âge adulte, généralement à cause d'insuffisance respiratoire ou cardiaque. Bien que cette maladie soit rare, elle touche tout de même un garçon sur 3500.

L'imagerie par Résonance Magnétique Nucléaire (RMN) est généralement utilisée pour le suivi longitudinal de la pathologie et dans l'évaluation de traitement car elle permet de réaliser des examens atraumatiques et non ionisants. Les progrès méthodologiques et instrumentaux réalisés en RMN au cours des trois dernières décennies ont été considérables. Ce passage d'une imagerie contemplative (localisation et détermination de la taille apparente d'une lésion) à une imagerie quantitative (extraction de paramètres caractérisant le degré physiopathologique de la lésion) a permis d'améliorer considérablement le suivi clinique, mais nécessite de définir des biomarqueurs quantitatifs. Trois indicateurs de RMN sont couramment intégrés dans les protocoles de recherche clinique : le volume musculaire contractile, le pourcentage de graisse intramusculaire et le temps de relaxation transversal (T_2) de l'eau musculaire. Ils permettent de quantifier respectivement la trophicité du muscle, les dégénérescences graisseuses chroniques et l'œdème tissulaire. Le pourcentage de graisse est un biomarqueur important chez les patients, mais il caractérise un processus chronique tardif et irréversible. Le T_2 de l'eau est un marqueur plus précoce de l'activité de la maladie, mais il est non spécifique et peut refléter de l'inflammation, de la nécrose, une dénervation...

De nombreux efforts sont réalisés pour développer des biomarqueurs de processus spécifiques et plus précoces. Les infiltrations graisseuses sont généralement précédées par une altération métabolique incluant des redistributions ioniques et un cycle de nécroses et de réparations. Pour cela, la RMN du sodium (^{23}Na) et les spectres RMN du proton (^1H) représentent des outils d'évaluation prometteurs car ils permettent de quantifier des paramètres dont les valeurs sont modifiées dès le début de la pathologie. Des dizaines d'études cliniques ont pour objectif de développer des médicaments pour guérir les maladies neuromusculaires ou du moins ralentir leur progression. Le développement de ces outils d'évaluation permettrait non seulement la quantification des effets des traitements, mais aussi de mener des études plus fondamentales visant à comprendre les mécanismes sous-jacents des myopathies. Dans ce contexte, les spectres du ^{23}Na et du ^1H , représentant des biomarqueurs plus spécifiques, méritent d'être davantage explorés.

Etat de l'art

L'ion sodium (Na^+) joue un rôle fondamental dans la physiologie du corps humain, est impliqué dans un grand nombre de fonctions au niveau cellulaire, et produit, après le ^1H , le signal RMN le plus important parmi les atomes biologiques d'intérêt. La RMN du ^{23}Na est donc considérée depuis de nombreuses années comme un complément attrayant à la RMN du ^1H pour la détection et l'évaluation de plusieurs anomalies physiologiques. Depuis les années 1970, des équipes ont développé des séquences de spectroscopie et d'imagerie, et des développements sont actuellement réalisés afin de les appliquer dans des protocoles cliniques.

L'ion Na^+ est important dans le maintien de l'osmolalité plasmatique, il influe sur les phénomènes de contraction-dilatation du volume cellulaire. À l'extérieur de la cellule, la concentration en Na^+ est 10 fois plus importante qu'à l'intérieur de la cellule, ce qui contribue à la différence de potentiel électrique entre l'intérieur et l'extérieur. Il y a un influx entrant d'ions Na^+ passif d'un point de vue énergétique. Par contre, il existe aussi un autre flux inverse, qui compense le flux passif des ions Na^+ . Ce flux inverse est entretenu par la pompe sodium-potassium consommatrice d'énergie. La pompe à sodium permet donc de rejeter les ions Na^+ en dehors de la cellule pour maintenir constant le gradient de concentration. Les modifications de la concentration en sodium intracellulaire sont généralement causées par des pathologies altérant la fonction/intégrité des cellules, ou alors responsables d'altérations métaboliques, ce qui est le cas de nombreuses DM. Chez les patients atteints de Dystrophie Musculaire de Duchenne par exemple, la concentration en sodium intracellulaire peut être multipliée par trois ou quatre par rapport à un niveau normal. Tous ces changements métaboliques ont lieu avant le remplacement graisseux du muscle squelettique. A la ligne pour la RMN du ^{23}Na , la séparation des signaux intracellulaires et

extracellulaires est alors cruciale afin d'établir des biomarqueurs sensibles aux altérations métaboliques. Plusieurs techniques de RMN permettent de discriminer le signal du ^{23}Na provenant des compartiments intracellulaires et extracellulaires.

Les études les plus anciennes ont proposé de séparer le signal extracellulaire du signal intracellulaire grâce à des agents de contraste permettant de décaler la fréquence de résonance du sodium extracellulaire. Néanmoins, ces réactifs sont toxiques pour l'homme et ne peuvent être utilisés que sur des modèles animaux pour de la recherche fondamentale. Une autre méthode, applicable chez l'homme, consiste à profiter de la différence de temps de relaxation longitudinale entre les deux compartiments et à utiliser une séquence d'inversion-récupération avec un temps d'inversion permettant d'éliminer le signal provenant de l'un ou l'autre des compartiments. Le signal des ions Na^+ peu mobiles peut être également recueilli grâce à des séquences de filtrage quantique. Ce signal provient de l'ensemble des ions proches ou liés à des macromolécules, et dans le contexte des DM, il pourrait représenter un paramètre intéressant pour caractériser l'intégrité des membranes cellulaires, mais aussi la formation de fibrose interstitielle.

Récemment, grâce à l'augmentation des champs magnétiques des scanners de RMN cliniques, des séquences d'imagerie du sodium avec des résolutions spatiales de l'ordre de quelques millimètres cube ont été développées. Néanmoins, les temps d'acquisitions correspondants et les rapports signal-sur-bruit obtenus sur les images restent encore loin de ce qui peut être réalisé en proton. Pour les séquences les plus évoluées, il faut environ 10 minutes pour obtenir une image reflétant la concentration totale en sodium. Cette image correspond de plus à un mélange des signaux provenant de tous les compartiments. Afin d'obtenir une information relative à la bio-distribution du sodium il faut également acquérir une deuxième séquence qui sera pondérée en signal intracellulaire et dont le temps d'acquisition est généralement supérieur. Pour cela, nous proposons dans cette thèse un protocole spectroscopique, permettant de mesurer plusieurs paramètres relatifs à la bio-distribution du sodium et aux interactions avec les macromolécules avec un temps d'acquisition égal à celui nécessaire pour obtenir une seule image en sodium.

D'autre part, la relaxation transversale T_2 des protons de l'eau dans le muscle est déterminée majoritairement par la structure et la concentration en macromolécules, qui sont altérées par les processus d'inflammation et de nécrose, communément observés dans les DM. Les techniques de cartographies T_2 permettent de détecter et de quantifier ces sites d'inflammation et de nécrose et sont caractérisés par une élévation du T_2 global (mono-exponentiel) des protons de l'eau. Néanmoins, il est connu depuis de nombreuses années que la relaxation T_2 du signal RMN du ^1H est multi-exponentielle. Ce comportement est interprété comme une conséquence de la

compartimentation anatomique de l'eau tissulaire et les échanges dans les espaces intracellulaire, interstitiel et vasculaire. La séquence de spectroscopie CPMG permet d'acquérir des courbes de relaxation T_2 avec une résolution temporelle et un rapport signal-sur-bruit suffisant pour une analyse multi-exponentielle robuste. Chez les sujets sains, l'extraction des spectres de T_2 à partir des données CPMG permet de caractériser les différents compartiments par la valeur intrinsèque de leur T_2 et leurs fractions relatives. Des études préliminaires menées chez des patients souffrant de maladies neuromusculaires ont montré que ces spectres T_2 pouvaient être largement modifiés.

Pour mieux comprendre les changements pathologiques, il serait donc très utile de combiner l'information de comportement obtenue par les spectres de T_2 du ^1H avec l'information sur la bio-distribution du sodium mesurée par la RMN du ^{23}Na . Bien que quelques études suggèrent déjà que certains paramètres métaboliques du ^{23}Na peuvent être altérés dans les maladies neuromusculaires, aucun essai clinique multicentrique n'a pour l'instant été entrepris. Seules quelques études de faisabilité ont été rapportées au niveau du muscle squelettique concernant les maladies musculaires et l'exercice.

Objectif

L'objectif de ce travail de thèse est la caractérisation du muscle squelettique par RMN dans le contexte des DM. Il s'agit de développer, d'optimiser des séquences de spectroscopie du ^{23}Na et de les évaluer en combinaison avec des spectres RMN du T_2 du ^1H et des séquences standards tout en tenant compte des restrictions associées à la pratique clinique. Il faudra également démontrer l'utilité et la valeur ajoutée du sodium par rapport la RMN conventionnelle du ^1H .

Des protocoles comprenant différentes méthodes de RMN du ^{23}Na et de ^1H T_2 ont été mis en œuvre pour évaluer les tissus musculaires squelettiques sains et dystrophiques de modèles animaux et de patients. Tout d'abord, un protocole de RMN du ^{23}Na non localisé a été développé afin de réduire les temps d'acquisition habituellement longs pour la RMN du ^{23}Na . Ce protocole a été validé sur des sujets sains sous différentes conditions de remplissage vasculaire. Au cours de cette étude, la valeur ajoutée de la RMN du ^{23}Na a été démontrée par rapport aux séquences standards mesurant le T_2 de l'eau.

Par la suite, des protocoles de RMN du ^{23}Na et du ^1H ont été développés sur des modèles animaux afin de les caractériser. Les modèles murins représentent un outil précieux pour étudier l'avancée pathologique de la maladie et pour tester d'éventuelles interventions thérapeutiques. De plus, la spécificité des techniques de RMN pour le suivi de certaines pathologies peut être validée sur des modèles murins bien décrits. Ici, un nouveau modèle murin de dysferlinopathie nommé MMex38

a été caractérisé par des techniques de RMN standard. De plus, un protocole complet comprenant les biomarqueurs de ^{23}Na et ^1H T₂ a investigué des perturbations de l'homéostasie hydro-ionique de différents modèles murins de MD.

Dans une étude d'histoire naturelle, réalisée à Erlangen chez des patients atteints de DMD, différentes méthodes d'imagerie et de spectroscopie ont été combinées pour évaluer leur sensibilité afin de surveiller les processus pathologiques de cette maladie à un stade précoce.

Démarche expérimentale

Le protocole de RMN du ^{23}Na non localisé a été développé sur un scanner 3T corps entier avec une antenne linéaire ^{23}Na optimisée pour la jambe. Le protocole (Figure R.1) consistait en une séquence de décroissance d'induction libre (FID), de triple filtrage quantique (TQF) et d'inversion-récupération (IR-LL) pour un temps d'acquisition total de 14 minutes.

Le signal FID correspond à la somme du sodium extra- et intracellulaire, il représente alors la concentration totale en sodium. La séquence de filtrage quantique a été utilisée pour mesurer la concentration des noyaux en mouvement restreint dans le tissu musculaire. Le rapport TQF/FID calculé comme un index reflétant les fractions relatives et les concentrations en ^{23}Na des compartiments intracellulaire et proche des membranes, et extracellulaire.

Nous avons aussi évalué les temps de relaxation longitudinale et transversale du ^{23}Na . Des spectres T₂* ont été obtenus à partir de la décroissance temporelle du signal de FID par une méthode de déconvolution. Ceci a permis de déterminer une fraction à T₂* court du sodium ainsi que les valeurs des T₂* courts et longs. Un temps de relaxation T₁ global a été estimé à partir de la séquence IR-LL par un ajustement mono-exponentiel de la repousse du signal à différents moments après inversion de l'aimantation.

Toutes ces séquences ont tout d'abord été appliquées sur fantômes (de l'eau avec des concentrations différentes de NaCl et d'agarose). Ensuite, des premières expériences in vivo ont été réalisées sur des volontaires sains. Ces tests ont validé les séquences développées pour des études plus sophistiquées. Le but de cette première étude était d'acquérir des spectres du sodium sur la jambe droite de volontaires dont le volume extracellulaire était modifié par compression avec une bande élastique (Figure R.2). Les séquences optimisées de RMN du ^{23}Na (FID, TQF, IR-LL) ont été utilisées pour caractériser les fractions relatives et les concentrations en ^{23}Na des compartiments intracellulaire, extracellulaire et proche des membranes au cours de ce paradigme de drainage vasculaire, remplissage vasculaire et retour à des conditions basales.

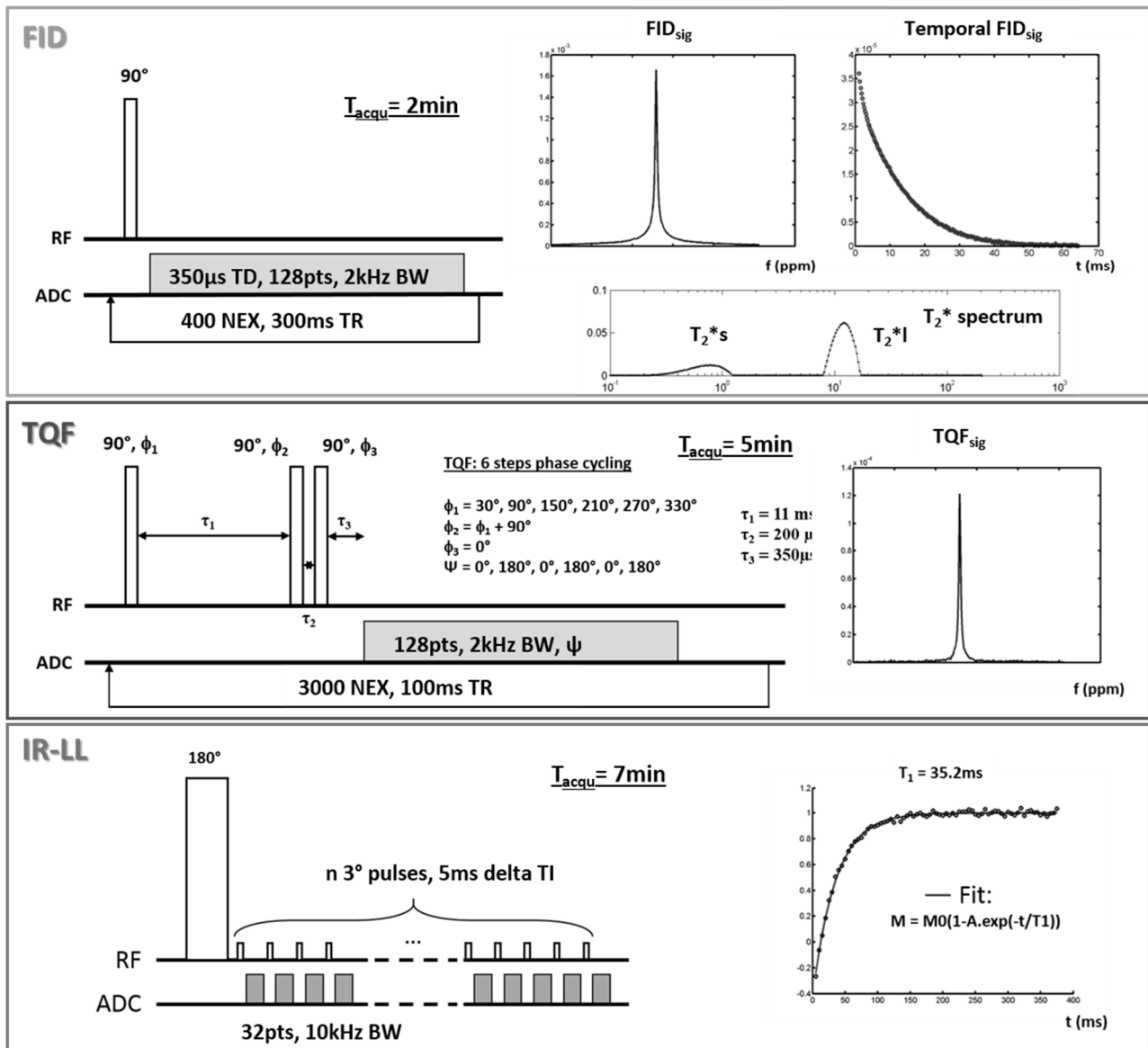


Figure R.1: Chronogrammes des trois séquences ^{23}Na utilisées (FID, TQF et IR-LL) avec un exemple de spectres obtenus ou d'évolution des signaux temporels.

Des variations significatives de signaux FID, de signaux TQF, de rapports TQF/FID, de valeurs de T_1 et de la fraction en T_2^* court ont été observées entre les trois conditions. Les signaux FID et les valeurs de T_1 étaient augmentés au cours du remplissage vasculaire et diminués au cours du drainage par rapport aux conditions de contrôle, alors que la tendance inverse a été observée pour le T_2^* court, le rapport TQF/FID ainsi que le signal TQF. Le rapport TQF/FID a été l'indice le plus robuste et le plus sensible pour discriminer les trois conditions. Des corrélations significatives ont été mesurées entre T_1 et le rapport TQF/FID et entre la fraction en T_2^* court et le rapport TQF/FID. Cette première étude a démontré que la spectroscopie RMN du ^{23}Na , des indices sensibles aux changements de la bio-distribution du sodium et de l'interaction avec les macromolécules peuvent être acquis dans les

muscles squelettiques humains avec des temps d'acquisition compatibles avec l'investigation des patients dans un cadre de recherche clinique.

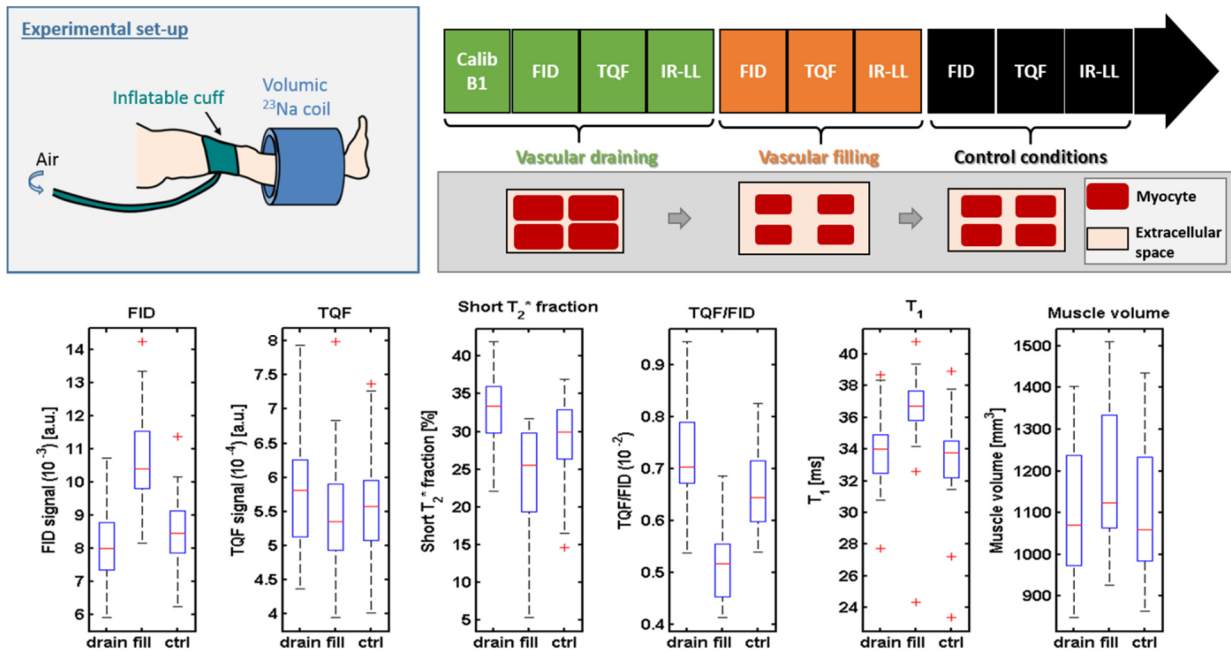


Figure R.2: Graphe représentant le déroulement de l'étude dans laquelle le volume extracellulaire était modifié par compression avec une bande élastique (en haut à gauche); le protocole était: drainage vasculaire, puis remplissage vasculaire et finalement une condition de contrôle (en haut à droite); les changements de paramètres du ^{23}Na entre des volumes extracellulaire différents sont également représentés.

La sensibilité de ce protocole de RMN du ^{23}Na a été comparée aux séquences plus standards de RMN du proton. L'approche de RMN du ^{23}Na était plus sensible que celle du ^1H T_2 standard pour détecter les changements importants dans les fractions de volume extracellulaire de la jambe. Notre protocole de RMN du ^{23}Na permet donc un suivi quantitatif du signal de ^{23}Na total et pondéré intracellulaire en moins de 15 minutes. Dans le cadre de la MD, ces biomarqueurs offrent de nouvelles options pour étudier les altérations des canaux ioniques/transporteurs, l'intégrité de la membrane ou même, indirectement, la formation de fibrose.

Au cours de ce travail de thèse, j'ai également géré un projet d'imagerie RMN en collaboration avec l'ECRC à Berlin où a été développé un nouveau modèle murin de dysferlinopathie. Les dysferlinopathies sont des dystrophies musculaires récessives dues à des mutations dans le gène de la dysferline, une protéine transmembranaire impliquée dans la réparation des membranes. Ce nouveau modèle murin de dysferlinopathie, nommé MMex38, a été étudié par RMN du ^1H sur un scanner préclinique 7T. Pour faire cela, j'ai paramétré des séquences comprenant de l'imagerie anatomique, des cartographies T_2 et T_1 ainsi que de la spectroscopie localisée du ^1H (PRESS). Le muscle malade du modèle murin de dysferlinopathie a été étudié et comparé avec des muscles de

souris saines et avec un deuxième modèle de Dysferlinopathie plus établi nommé BLAJ. À ma connaissance, cette étude a été la première description complète d'un modèle murin de dysferlinopathie par différentes modalités de RMN. La coloration au Oil Red O et la microscopie électronique ont déjà révélé des accumulations lipidiques significatives au sein des myofibres de souris déficientes en dysferline. Cette importante infiltration grasseuse, plus prononcée dans les muscles proximaux que dans les muscles distaux, a été confirmée par l'augmentation des taux de graisse mesuré par RMN. La sévérité de l'activité de la maladie et sa progression ont été reflétées par un remplacement grasseux significatif, montrant pour la première fois chez la souris une certaine similitude avec le phénotype observé chez l'homme (Figure R.3). Notre description du modèle confirme ainsi la pertinence du modèle MMex38 pour imiter l'activité de la maladie et la progression de LGMD 2B humaine (Myopathie des ceintures avec déficit en dysferline). Ceci est en contraste avec d'autres modèles dystrophiques murins comme le *mdx*, un modèle de la myopathie de Duchenne, qui ne parviennent pas à reproduire l'importante altération de la trophicité musculaire présente chez les patients humains.

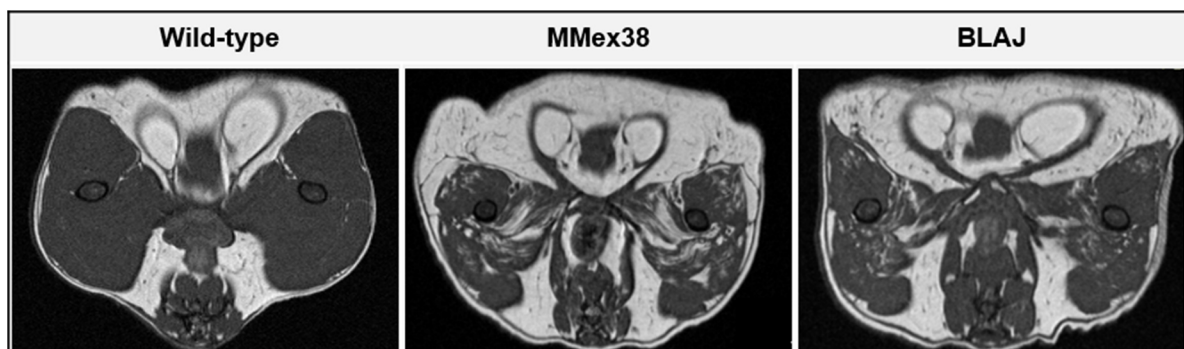


Figure R.3: Images ^1H représentant les cuisses d'une souris saine (wild-type), du nouveau modèle murin de dysferlinopathie, MMex38, et du modèle de Dysferlinopathie plus établis, BLAJ.

En complément, des souris *MMex38* saines et des souris *mdx* ont été étudiées avec un protocole complet comprenant les biomarqueurs de ^{23}Na et ^1H T_2 . Nous avons observé des perturbations de l'homéostasie hydro-ionique chez les différents modèles murins de MD. Les indices RMN du ^{23}Na étaient sensibles pour distinguer le muscle dystrophique du tissu musculaire squelettique sain. Alors que les souris *MMex38* ont montré une augmentation du T_1 du sodium et une diminution de TQF/FID, les souris *mdx* ont montré une augmentation du rapport TQF/FID avec un T_1 du sodium inchangé. Ceci pourrait refléter différents processus physiopathologiques tels qu'une augmentation de la concentration de sodium intracellulaire et une redistribution de l'eau dans les différents compartiments tissulaires. Ce fut la première étude RMN du ^{23}Na sur le muscle dystrophique murin. Le deuxième paramètre de validation était d'obtenir/de mesurer les spectres de T_2 à partir de la séquence ISIS-CPMG. Une augmentation du T_2 court a été observée chez les souris

mdx par rapport aux souris saines, ce qui pourrait être expliqué par une augmentation de l'eau dans le compartiment extravasculaire avec des fractions relatives constantes. La même tendance a été observée par la suite chez les patients dystrophiques (voir ci-dessous). Ces résultats encourageants nous incitent à une corrélation systématique des images RMN avec des coupes histologiques afin de comprendre les processus physiopathologiques responsables de ces variations. Ainsi, les spectres ^1H T_2 et les indices RMN du ^{23}Na se sont avérés sensibles pour détecter les changements dans le muscle dystrophique dans une petite cohorte.

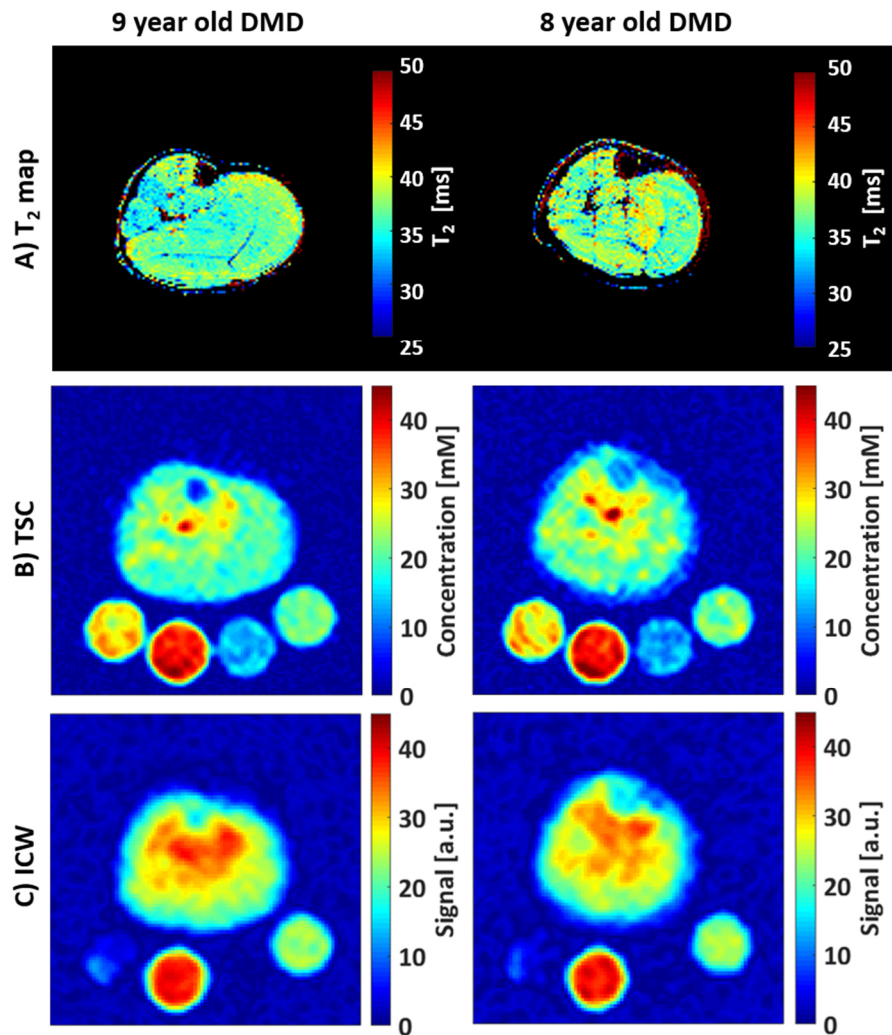


Figure R.4: Cartographies **A)** du T_2 du ^1H , **B)** de la concentration totale en sodium, et **C)** du signal de sodium pondéré intracellulaire au niveau de la jambe de deux garçons atteints de DMD. Alors que les cartes de T_2 du ^1H et la concentration totale en sodium présentent les muscles avec des valeurs normales, les signaux de sodium pondérés intracellulaire sont élevés.

Enfin, j'ai démontré l'utilité de la RMN du ^{23}Na dans un contexte clinique. Weber *et al.* ont déjà démontré que la concentration de Na^+ musculaire, détectée par RMN chez les garçons atteints de DMD, était augmentée et restait élevée lors d'un réexamen par rapport à des témoins sains. Sur la

base de ces expériences préliminaires, nous avons en outre voulu étudier le potentiel de la RMN du ^{23}Na pour servir de biomarqueur précoce et sensible dans les DM. Dans une étude d'histoire naturelle sur les patients atteints de DMD réalisée à Erlangen, différentes séquences d'imagerie et de spectroscopie ont été acquises pour évaluer leur sensibilité afin de suivre les processus pathologiques de la MD à un stade précoce de la maladie. Nous avons démontré que les patients atteints de DMD présentaient des concentrations élevées en sodium total mais aussi que le signal pondéré intracellulaire de ^{23}Na ainsi que du T_2 d'eau au stade précoce de la maladie précédant l'infiltration fibro-grasseuse. Les accumulations de sodium intracellulaire ne sont cependant pas systématiquement parallèles aux augmentations du T_2 d'eau. Certains muscles relativement épargnés, comme le tibial antérieur, présentaient tout de même une augmentation de la concentration totale en sodium et un signal sodium pondéré intracellulaire chez les patients atteints de DMD. Alors que nous avons trouvé une bonne corrélation entre le T_2 de l'eau et la concentration totale en sodium, ce qui pourrait refléter des changements œdémateux, le signal de sodium pondéré intracellulaire s'est également révélé élevé en présence du T_2 d'eau normale (Figure R.4). Ainsi, le signal de sodium pondéré intracellulaire est très probablement un biomarqueur plus sensible que la concentration totale en sodium ou le T_2 de l'eau pour détecter les déséquilibres en Na^+ .

Aujourd'hui, l'utilisation de la RMN du ^{23}Na lors d'examens cliniques reste limitée en raison des coûts élevés, des longs temps d'acquisition ainsi que de sa complexité de mise en place. Ainsi, la question est de savoir si cela vaut la peine de d'étendre la RMN du ^{23}Na au-delà du champ de recherche pour répondre au besoin d'un biomarqueur précoce et sensible. Ce serait le cas si la RMN du ^{23}Na s'avère plus sensible à certains changements pathologiques que la RMN du ^1H , fournissant des informations supplémentaires, qui ne peuvent être récupérées par d'autres méthodes. Mon travail fournit des preuves que le RMN du ^{23}Na pourrait offrir un biomarqueur sensible capable de suivre de façon quantitative les altérations spécifiques du muscle dystrophique à un stade très précoce.



General introduction

The general introduction addresses the need for non-invasive biomarkers that monitor disease progression and the response to the treatment. For that, I will introduce NMR as a non-invasive tool for skeletal muscle characterization and its role to offer outcome measures in the field of muscular dystrophies. Finally, I will highlight the objective of the work and the structure of this manuscript.

1.1 The role of nuclear magnetic resonance in establishing biomarkers for diseased muscles

Muscular dystrophy (MD) refers to a group of hereditary diseases with progressive muscle weakness involvement and loss of muscle mass. Different genetic mutations lead to distinct forms of muscular dystrophy with a broad spectra of symptom's severity. The most common type of MD in children is Duchenne muscular dystrophy (DMD) which alone affects about 1 in every 3,500 to 5,000 born boys. The mutation in DMD patients leads to an increased permeability of the cell membrane, to chronic inflammation and ultimately to progressive muscle degeneration, where the muscle tissue is replaced by fatty and fibrotic tissue [1].

Yet, there is no cure for any form of muscular dystrophy. Current medication and therapy manage the symptoms and at the most decelerate the disease progression. However, MDs have been recently receiving increasing attention and several programs have been launched at a (multi-) national level (see for example: <https://www.afm-telethon.fr/guerir/traitements-638>, <http://treatnmd.ncl.ac.uk/>, <http://www.aktionbenniundco.de>, <http://www.parentprojectmd.org>, <https://www.jain-foundation.org/scientific-resources/therapeutic-strategies>). Moreover, the progress of gene therapy and pharmacogenetics is on the edge to change the course of MD [2], [3]. In September 2016, the U.S. Food and Drug Administration conditionally approved the first exon-skipping based drug, named eteplirsen, to treat DMD after a hot debate over its therapeutic effect. A response of the European Medicines Agency for conditional approval in the European Union is anticipated in the coming weeks. Because of these developments in the therapeutic field, new needs have emerged over the past years with the necessity to monitor muscle response to interventions. To date, the clinical investigation of muscular dystrophies commonly involves genetic, biochemical, and histopathological methods along with physical examinations. The gold standard for muscle evaluation is a muscle biopsy combined with molecular staining. This method is invasive and strongly site dependent as the sampled volume is small. In addition, strength and functional tests are regularly used as clinical tools to monitor the disease progression and response to therapy. Examples

for functional tests are the six-minute walk test, ten-meter walk/run, rise from floor, or grip test. A main drawback of these assessments is the dependency of patient's motivation and ability, which can represent a challenge for children and patients at a later stage of disease. Further, these methods are also in parts biased by the investigator/physician/physiotherapist. Thus, there is a need for non-invasive biomarkers that can provide reliable and sequential information about the disease progression monitoring natural disease progression and response to treatment.

Muscle-imaging techniques are non-invasive tools that can complement the physical examinations as well as expand our understanding of the pathophysiological evolution. Imaging tools in medicine have been developed for more than one century, which led to the application of many advanced imaging techniques. At the beginning, they have been exploited to anatomically investigate the structure of the human body (X-ray, ultrasound and NMR imaging). Nowadays, they can be additionally used to analyse the function and metabolism of organs *in vivo* in a non-invasive manner (NMR spectroscopy, functional NMR imaging, Ultrasound Doppler, and nuclear imaging e.g. positron emission tomography and single photon emission computed tomography). In the 1980s, ultrasound has been for example reported to detect the pathological changes in dystrophic muscle and also to guide muscle biopsies [4]. Although this technique is easily accessible and inexpensive compared to other imaging tools, US is highly operator-dependent and the visualization of deeper muscles embodies another limitation. In addition, X-ray computed tomography (CT) was used to study the dystrophic muscle and the disease related intramuscular fat infiltration [5]. This technique is not operator dependent and enables an improved view of deeper muscles, but the applied radiation potentially damages body cells.

Over the last two decades, NMR has become an important non-invasive tool for studying the muscle structure and composition. Radiologists successfully and frequently use NMR for clinical investigation of soft tissue. In the field of muscle research, NMR has replaced CT for several reasons. First, NMR has a higher sensitivity than CT for early fat infiltration in muscles and offers an improved view of anatomical details in soft tissue. Another benefit of nuclear magnetic resonance is the absence of ionizing radiation. Additionally, it enables multi-planar scanning, which is of importance for patients who are not able to stay in the desired position during the scan. The on-going research in the NMR field has accelerated the clinical use and the development of biomarkers to investigate disease progression and response to treatment. These days, NMR is applied for several purposes in muscle related areas e.g. measurement of diffusion, skeletal-muscle perfusion, blood flow, and tumour metabolism [6]–[8].

Recently, various NMR techniques have been developed and applied to examine muscular dystrophies [9]. Imaging tools allow the quantification of muscle wasting and its processes of muscle degradation including inflammation and fat infiltration. A variety of NMR methods can be employed to identify affected muscle groups, to quantify the severity of muscle wasting, and to visualize the microstructure of the tissue by assessing the diffusion properties [10].

To date, some quantitative NMR techniques made it already into clinical trials fulfilling the prerequisites to be used as quantitative reliable outcome measures [9]. The three established outcome measures, which have been used to provide information about disease progression and to monitor the treatment response, are:

- Muscle trophicity by measuring either muscle surface or volume
- Fat infiltration (chronic degeneration) by quantifying the percentage of fat signal in the affected muscles
- Disease activity by measuring the transverse relaxation time (T_2) of the affected muscles

Several clinical studies on muscular dystrophies employed these outcome measures (3.4.1). The NMR outcome measures correlate well with the functional tests and can provide complementary information about the cause of decreased muscle strength. The imaging approach also has been proven to better detect and monitor the effect of therapy when compared to motor function measure [11]. Nevertheless, the assessment of the fat infiltration might not be a predictive marker of the disease evolution. The disease progression can be highly heterogeneous between patients as well as in an individual patient, which hinders the establishment of a biomarker based solely on the fat quantification. Another NMR contrast is the tissue T_2 reflecting the motility of the water protons in the tissue. Changes in the tissue T_2 occur during pathological processes including inflammation, necrosis, or oedema. Thus, water T_2 can serve as a sensitive biomarker for pathological alterations that precede the actual muscle replacement by fat. In DMD, the muscle water T_2 is very sensitive to the steroid treatment. Yet, water T_2 values almost normalize with steroid treatment, which is the standard treatment against the chronic inflammation in DMD [12]. Therefore, any beneficial effects of other treatments like exon-skipping could occur unnoticed in steroid-treated patients.

Thus, the research focus lies on the identification of NMR outcome measures that are more specific to physiological or biochemical changes. Ideally, they can serve as predictive and sensitive biomarkers at early disease evolution, possibly preceding any macroscopic degenerative changes in muscle tissue. In this manner, other potential biomarkers of disease activity in MD patients have been under investigation such as phosphorus (^{31}P) NMR spectroscopy (NMRS). ^{31}P NMRS can depict

pathophysiological relevant cellular changes in patients such as energy metabolism and tissue pH alterations. Since biochemical changes commonly precede morphological and functional alterations, ^{31}P NMRS presents itself as a promising tool for an early evaluation of muscle dystrophies. The muscles of DMD patients possess a leaky membrane leading to an altered ion distribution. Other neuromuscular diseases are related to mutations in genes of ion channel proteins. Advanced nuclear magnetic resonance sequences such as sodium (^{23}Na) NMR could track these alterations in the ion distribution [13].

To conclude, NMR is becoming more important in the field of muscular dystrophies. It has the potential to assess muscle wasting and to measure changes in the muscle properties even in early stages of muscular dystrophies. It thus holds a promise to clarify functional and metabolic alterations in healthy and diseased state. However, further investigations still need to establish NMR applications as indispensable biomarkers in clinic that complement current outcome measures to track disease progression and therapy efficacy.

1.2 Thesis objectives

The aim of the thesis is to investigate the dystrophic muscle using different NMR techniques. I evaluated the potential of these NMR techniques in providing predictive and sensitive biomarkers for the evaluation of disease progression in MD. The thesis focuses on the evaluation of two different methods, ^{23}Na NMR and advanced proton (^1H) T_2 techniques, which were applied to investigate healthy and dystrophic skeletal muscle tissue. Both, sodium concentration and T_2 of water are sensitive to (patho-) physiological changes in skeletal muscle tissue. On one hand, ^{23}Na NMR quantifies the sodium content and distribution in skeletal muscle tissue. On the other hand, methods measuring the ^1H T_2 are commonly used to highlight and quantify sites of inflammation, oedema, and necrosis – or more generally the disease activity.

Sodium (Na^+) is an essential component in the maintenance of the body homeostasis and in the transmembrane electrochemical gradient. Changes in the Na^+ gradient across the cell membrane indicate a pathological process such as an increased intracellular sodium concentration resulting in cell swelling and eventually cell death. Thus, ^{23}Na NMR helps to assess directly and quantitatively new metabolic information about the cell viability and provides important information complementary to the standard ^1H NMR imaging (NMRI). The first developments of ^{23}Na NMR already dates back to the late 70s with a recent increased attention in the past years. In DMD among other diseases, ^{23}Na NMRI detected increased muscular Na^+ concentration compared to healthy age-matched controls [14]. Nevertheless, ^{23}Na NMR is not a clinical tool due to several limitations that

lead to a low signal to noise ratio (SNR) and thus long acquisition times. Additionally, the extracellular sodium signal cannot be separated unambiguously from the intracellular sodium signal without the help of toxic shift reagents. In order to add ^{23}Na NMR to clinical examination protocols, short acquisition times are crucial. Thus, we tested the feasibility and sensitivity of the spectroscopy approach leading to much shorter acquisition times than with imaging sequences.

In contrast to ^{23}Na NMR, proton T_2 is much more frequently employed for the non-invasive muscle tissue characterization. As aforementioned, ^1H T_2 is used to investigate the progressive destruction of muscle tissues in DMD since it is a sensitive biomarker of the inflammatory, necrotic, and oedematous processes. The oedema-like muscular changes increase ^1H T_2 values. This process can be osmotically and mainly intracellular driven. As the sodium ion is a main player in the water balance, it is of great interest to compare alterations in the ^1H T_2 with the ^{23}Na NMR signal. Although ^1H T_2 represents an intensively investigated NMR biomarker, one important consideration of the ^1H T_2 measurement remains the origin of the signal. It is a non-specific marker affected by different underlying (patho-) physiological events. Furthermore, global T_2 measurements are biased by the presence of fat infiltration in the muscle. This bias can be very important in the dystrophic muscle tissue. Thus, a significant presence of fat can completely mask such events as inflammation or oedema in case of global T_2 measurement. Different methods exist to extract the muscle water T_2 , including more sophisticated fitting approaches like bi-component extended phase graph (EPG) [15] or tri-exponential models [16]. Besides, a localized spectroscopy approach, namely ISIS-CPMG (image selected in vivo spectroscopy Carr-Purcell-Meiboom-Gill method) [17], provides T_2 spectra allowing to investigate the multi-component ^1H T_2 relaxation behaviour in skeletal muscle.

Given that the focus of the thesis is on identification and evaluation of new NMR outcome measures, ^{23}Na NMR methods to investigate cellular function were combined with advanced ^1H T_2 techniques to examine the muscle composition. During this work, protocols including different ^{23}Na NMR methods and ^1H T_2 quantification approaches were applied to study first the healthy skeletal muscle and then the dystrophic muscle of animal models and patients. Ultimately, this work also aimed to establish reference data for MDs and to provide a basis for the development of ^{23}Na -based NMR outcome measures of disease progression and response to treatment.

1.3 Structure of the thesis

The manuscript consists of three parts: The first part provides a deeper theoretical background to understand the pathological processes in the dystrophic muscle and the applied NMR methods (Chapter 2 and 3). The second part presents the results of the investigations I performed in humans and mice (Chapter 4-7). Finally, I summarize and discuss the main contributions to the scientific field (Chapter 8).

Chapter 2 comprises of a theoretical part about skeletal muscle tissue and introduces the architecture of muscle as well as MD and their underlying pathophysiology. It highlights the important role of the sodium ion in human's metabolism as well as associated alterations in MD.

Chapter 3 is a theoretical chapter on NMR imaging and spectroscopy including the basic concepts of nuclear magnetic resonance. It also illustrates some important approaches for sodium assessment including inversion recovery and multiple quantum filters. Finally, the focus lies on the application of NMR as outcome measure to study the pathological processes in dystrophic muscles and on initial ^{23}Na NMR studies to monitor changes in the homeostasis in MD patients.

The second part describes the different experiments, which I performed on the clinical and on the preclinical NMR scanners at Institute of Myology in Paris. Additionally, I worked on a clinical NMR scanner at the University Hospital Erlangen in collaboration with its Radiology Department.

Chapter 4 illustrates the NMR sequences that have been implemented in different protocols during the thesis work. In particular, it explains two different methods for fast ^{23}Na NMR acquisition in skeletal muscle tissue. First, we combined three different non-localized ^{23}Na NMR sequences to establish a short protocol for lower leg tissue characterization. Additionally, a fast sodium imaging method, developed by Armin Nagel [18], is introduced that was later used in the DMD clinical study.

Chapter 5 comprises four different studies using non-localized ^{23}Na NMR sequences to characterize the skeletal muscle tissue at rest and during different vascular filling conditions. This chapter describes also an approach to quantify the non-localized ^{23}Na NMR signals. These studies can be seen as feasibility and evaluation tests towards the development of sensitive ^{23}Na -based NMR outcome measures of disease progression. The first study presented in this chapter was published in the *Physiological Reports Journal* (Gerhalter *et al.* 2017 Acute changes in extracellular volume fraction in skeletal muscle monitored by ^{23}Na NMR spectroscopy) [19]. Other results are the object of five proceedings contributions (Marty *et al.* 2015 ISMRM, Gerhalter *et al.* 2015 ESMRMB, Gerhalter *et al.* 2016 Myology, Gerhalter *et al.* 2016 ESMRMB, Gerhalter *et al.* 2017 ESMRMB).

In chapter 6, the murine dystrophic muscles of different MD models were characterized by ^{23}Na , ^{31}P , and ^1H NMR methods. On one hand, a new murine model for dysferlinopathy named *MMex38* was characterized for the first time by standard ^1H and ^{31}P NMR techniques. The results were compared to an established and well-characterized murine model for dysferlinopathy (*BLAJ*). The preliminary results are the object of two proceedings contributions (Gerhalter *et al.* 2016 WMS, Gerhalter *et al.* 2016 SFM). Part of this NMR characterization study is in redaction to be submitted to the *Metabolism - Experimental and Clinical Journal* complemented by metabolomics data. Then, the proposed ^{23}Na and ^1H based NMR outcome measures were tested on *MMex38* and *mdx* mice, which are the most common used animal model for DMD.

Chapter 7 presents a natural history study on DMD patients in Erlangen. A dozen of young DMD patients and age-matched healthy controls underwent a quantitative characterization of their lower leg by ^{23}Na and ^1H NMR. The origin of NMR signal changes present in dystrophic muscle tissues was analysed by combining the different parameters. This study also evaluated the specificity of ^{23}Na NMR biomarkers and their applicability in clinical studies. This study is still ongoing as we invite the patients to come back every six months for a longitudinal NMR examination. Nine DMD patients came so far for a second time, which allows a longitudinal examination of the disease progression. Hence, I evaluated with the second visit the short-term sensitivity of the ^{23}Na -based outcome measure to the disease progression. This chapter comprises one paper in redaction and international proceedings contributions. A methodological paper is under preparation to be submitted to the *Radiology Journal*. Other results are the object of three accepted proceeding contributions (Gerhalter *et al.* 2018 ISMRM, Gerhalter *et al.* 2018 ISMRM workshop: MR Imaging of $^{\text{X}}$ -Nuclei, and Gerhalter *et al.* 2018 ICNMD).

Finally, chapter 8 briefly summarizes the work and methodological contributions of the thesis. After a general conclusion, a personal perspective tries to elucidate the possible future of ^{23}Na NMR.

A brief reminder on skeletal muscle

This chapter deals first with the anatomy and architecture (2.1) and energy metabolism (2.2) of the skeletal muscle tissue followed by a description of the essential role of the sodium ion in muscle function and homeostasis (2.3). Then, the regeneration process upon muscle damage is explained (2.4). The final subchapter introduces the broad family of muscular dystrophies with a special focus on DMD and limb-girdle muscular dystrophy of type 2B (LGMD 2B) (2.5).

2.1 Anatomy and architecture of skeletal muscle

Skeletal muscle, smooth muscle, and cardiac muscle are the three main types of muscle tissues found in mammals. Skeletal muscle has a striated pattern and tendons attach the tissue to the skeleton. The somatic nervous system controls voluntarily the contraction of the skeletal muscle fibres. They make up 40 to 50 % of the body mass in humans and more than 400 different sizes of skeletal muscle exist [20]. Skeletal muscles are indispensable for several physiological processes such as locomotion, maintenance of posture, and metabolic activity.

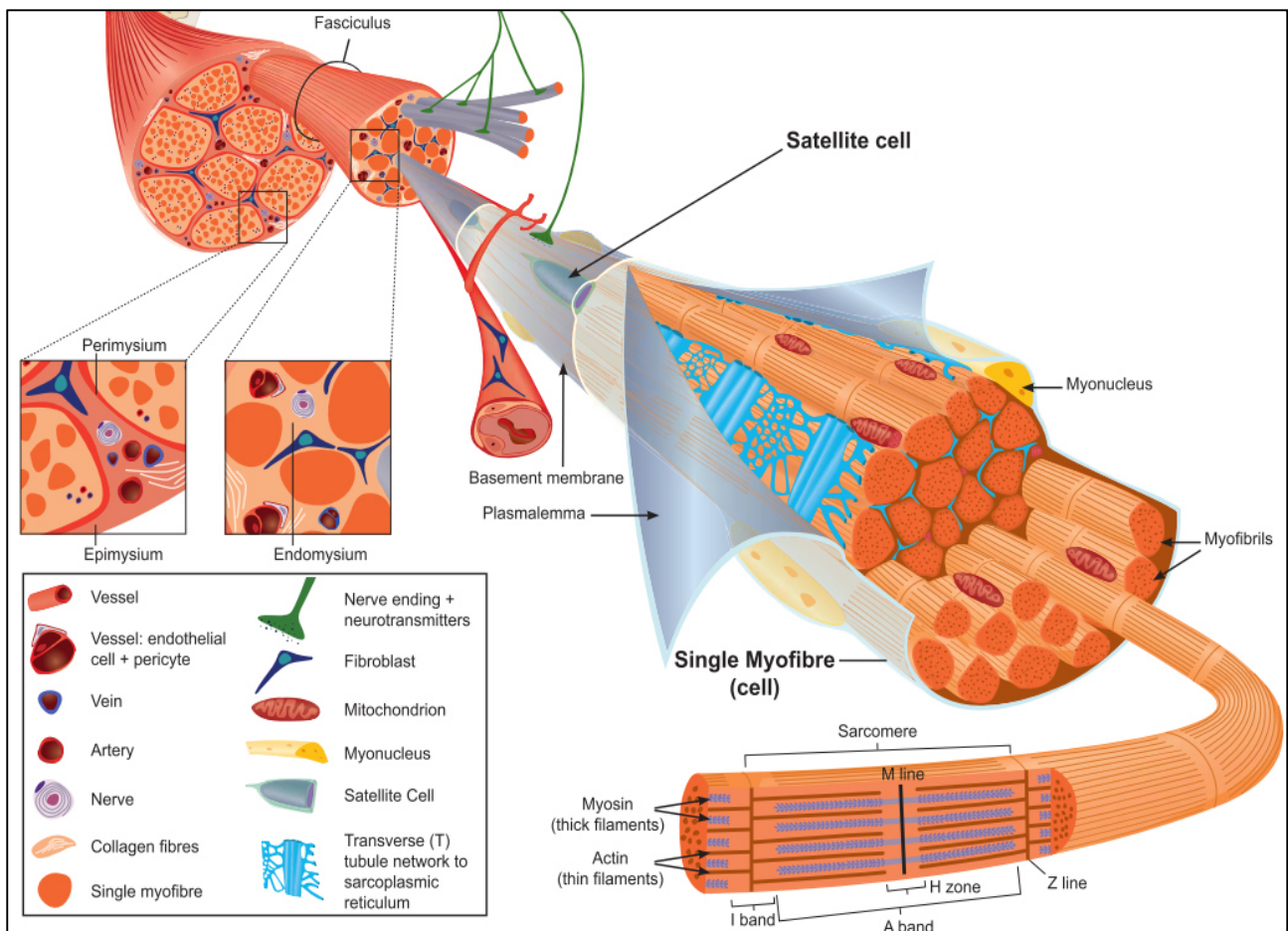


Figure 1: Scheme of skeletal muscle and associated structures [21].

The skeletal muscle has a highly organized architecture; bundles of longitudinal fibres are arranged within a bundle structure (Figure 1). A dense network of blood vessels provides the muscle with nutrients and oxygen, whereas connective tissue layers provide support and protection to withstand external forces of contraction to the myofibres. Tens to hundreds muscle fibres, called fasciculus, form one muscle covered by a connective tissue layer known as epimysium. The fascicles are made up of many smaller bundles consisting of muscle cells (myofibres) and are held together by the connective tissue called perimysium. The perimysium provides a pathway to the veins and arteries and nerves through the muscle. The third connective tissue layer in the skeletal muscle called endomysium is located between the fibres. It ensheathes individual myofibres and provides a pathway for capillaries and motor neurons endings.

Myofibres represent the cellular units of the skeletal muscle and they are organized in a linear and repetitive fashion for muscle contraction. The myofibres exhibit a distinctive banding pattern under the microscope originating from the arrangement of cytoskeletal elements (Figure 2). The main elements are myosin and actin, also known as thick and thin filaments, organized in a repetitive fashion parallel to each other and to the axis of the cell in the so-called sarcomere. Six actin filaments surround one myosin filament. Those two elements are crucial for the sarcomere shortening and muscle contraction. The sarcomere's cytoskeleton is composed of transversal structures including the Z and M lines and longitudinal filaments that are parallel with the thick and thin filament. During muscle contraction, the myosin (thick filament) slides past the actin (thin filament) forming a sort of cross-bridge between the myosin head on the actin filament.

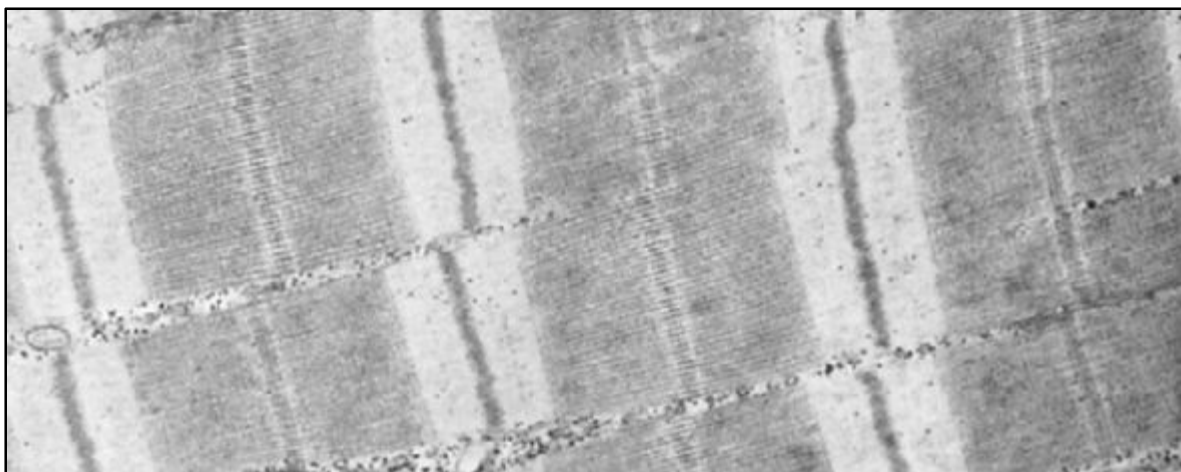








Figure 2: Distinctive banding pattern of muscle myofibrils originating from the arrangement of actin and myosin filaments. Zoom-in from [20].

Myofibres are multinucleated cells surrounded by the sarcolemma (plasma membrane) and the basement membrane (layer of extracellular matrix). The basement membrane provides a scaffold for the myofibres and some components of this membrane play an active role in regenerative

process after injury. The sarcolemma represents a barrier limiting the myocytes intracellular environment to the extracellular space. The permeability of the sarcolemma to ions and other compounds plays an important role in the origin of electrical potential and in the metabolic activity (2.3). The rest of the cytoplasm of a single myofibre is densely packed with organelles of different cellular functions e.g. mitochondria for the energy production, sarcoplasmic reticulum for calcium storage and release, and Golgi apparatus for protein sorting among other structures. The myonuclei are usually located in the space between myofibres and the sarcolemma at the periphery of each myofibre. They are flattened post-mitotic nuclei, thus cannot divide. In addition, satellite cells (SC) are located between the basement membrane and the sarcolemma. The muscle SC possess the capacity to self-renew and are responsible for skeletal muscle growth and repair after injuries or in conditions of muscle wasting [22].

Table 1: The four major classes of fibre and their phenotypes identified in mammalian muscle based on the MyHC composition. Note that IIb fibres are usually not found in human. MyHC, myosin heavy chain. Data extracted from [23].

MyHC type	I fibres	IIa fibres	IIx fibres	IIb fibres
Twitch duration	Slow			Fast
Shortening velocity	Slow			Fast
Cross-sectional area	Small			Large
Metabolism	Oxidative			Glycolytic
Endurance	High			Low
Energy efficiency	High			Low

Muscle fibres can adapt their size as well as internal structure such as the number of mitochondria and extracellular surroundings (e.g. capillary density) to the metabolic activity [24]. Muscle fibres are classified by myosin ATPase activity at differing pH and different isoforms of the myosin heavy chain (MyHC), a part of the myosin protein that is involved in cross-bridge cycling and sarcomere shortening. In human muscles, three major isoforms of MyHC are expressed: fibre type I, IIa, and IIx (Table 1). Type I fibres are slow twitching oxidative fibres with a slow shortening velocity and are highly resistant to fatigue with a great energy efficiency. Type II fibres are fast twitching fibres with a strong ATPase activity at alkaline pH that are divided into several subtypes based on the MyHC isoform. IIx fibres display a glycolytic metabolism and can contract fast and generate short bursts of strength, hence have a low endurance and low energy efficiency. Fibre type IIa have oxidative and glycolytic enzymes making them more resistant to fatigue than IIx fibres and faster regarding twitch duration and shortening velocity than fibre I. In rodents a fourth major form called IIb was identified expressing a very fast form of myosin. The fibre type distribution in the body

depends on the action and task of the muscle. Hybrid muscle fibres exist expressing more than one MyHC isoform. This heterogeneity might be important in the muscle plasticity [23], [25].

2.2 Energy metabolism

Muscle function highly depends on optimal energy supply and efficient source utilization. The energy is supplied in form of adenosine triphosphate (ATP), which is hydrolysed into adenosine diphosphate (ADP) and one phosphate (Figure 3). This hydrolysis releases more than 7300 calories of energy. Removal of the second phosphate converts the ADP further into adenosine monophosphate (AMP) releasing again energy for the muscle contraction. To maintain a constant ATP amount of around 4 mM, the muscle continuously forms ATP to sustain the muscle metabolic system. The three main metabolic systems provide ATP supply: 1) phosphocreatine - creatine system, 2) glycogen - lactic acid system, and 3) aerobic system. For further details the reader is referred to [20].

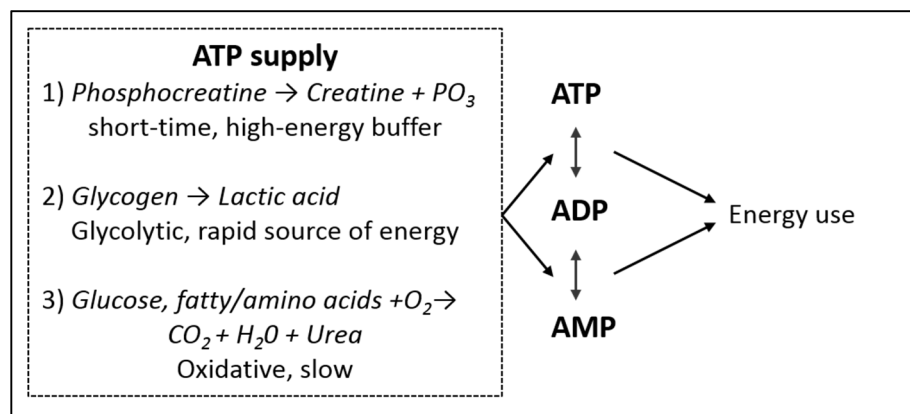


Figure 3: Muscle metabolism systems supplying energy for muscle contraction. Adapted from [20].

2.3 Role of sodium in biological tissue

Numerous ions play a crucial role in the function of the human body. Sodium is an essential component that is responsible for the transmembrane electrochemical gradient and the maintenance of the body homeostasis.

2.3.1 Transmembrane electrochemical gradient

Various physiological processes in the human body are electrochemical controlled and are based on the maintenance of ion gradients between different fluid compartments. Even small disturbances in the electrolyte balance can lead to severe functional changes. The lipid bilayer of cell membranes functions as a barrier for most polar molecules (having an electric di- or multi-pole moment) and thus maintains different concentrations of solutes in the intra- and extracellular compartment. The combination of selective passive permeability and active transport leads to large differences of ion concentrations inside and outside the cell (Table 2). In the muscle, the extracellular

compartment contains for example a ten-fold higher sodium ion concentration than the intracellular space ($[\text{Na}]_i = 5 \text{ to } 15 \text{ mM}$ compared to $[\text{Na}]_e = 145 \text{ mM}$). This concentration differences allow the cell to store potential energy as an electrochemical gradient for various purposes (e.g. to drive transport processes across the membrane, to convey electrical signals in electrically excitable cells, to generate ATP...).

Table 2: Ion concentrations of intracellular and extracellular compartment of a mammalian cell. Values taken from [26].

Component	Intracellular concentration in mM	Extracellular concentration in mM
Na⁺	5 to15	145
K⁺	140	5
Mg²⁺	0.5	1 - 2
Ca²⁺	10 ⁻⁴	1 - 2
Cl⁻	5 to 15	110

Various ion channels and transporters regulate the concentration of Na⁺ (Figure 4). Sodium channels allow Na⁺ ions to diffuse faster down their electrochemical gradients across the lipid bilayer and are responsible for the initial rise and the propagation of action potentials in muscles. They are voltage driven, which means that they are not continuously open like pores but are instead gated by a voltage stimuli. The number of Na⁺ channels and their activated fraction controls the excitability of myofibres. In skeletal muscles two isoforms of the Na⁺ channel are expressed, namely Nav1.4 and Nav1.5. While Nav1.5 is only expressed in immaturred and denervated muscles, Nav1.4 is found in slow and fast fibres of adults [24], [27]–[29].

Two important protein pumps that play a key role in the regulation of sodium are the sodium/calcium exchanger (NCX) and the sodium/hydrogen exchanger (NHE). The NCX uses the Na⁺ gradient to pump Ca²⁺ out of the cell. Its transportation rate depends on the concentration of both ions as well as the membrane potential. An increase of ATP can activate the NCX, which plays a crucial role in the calcium extrusion after contraction. Another vital factor for muscles is the pH of the intracellular compartment in order to ensure for example the best functionality of enzymes. NHE directly transports H⁺ out of the cell coupled to an influx of Na⁺ maintaining the intracellular pH. Almost all tissues express the Na-H antiporters, but yet only the isoform NHE1 was found in skeletal muscle. Intracellular acidosis activates the NHE via proton binding to the transporter and is thus one of the main transporters for pH regulation [24], [26], [30].

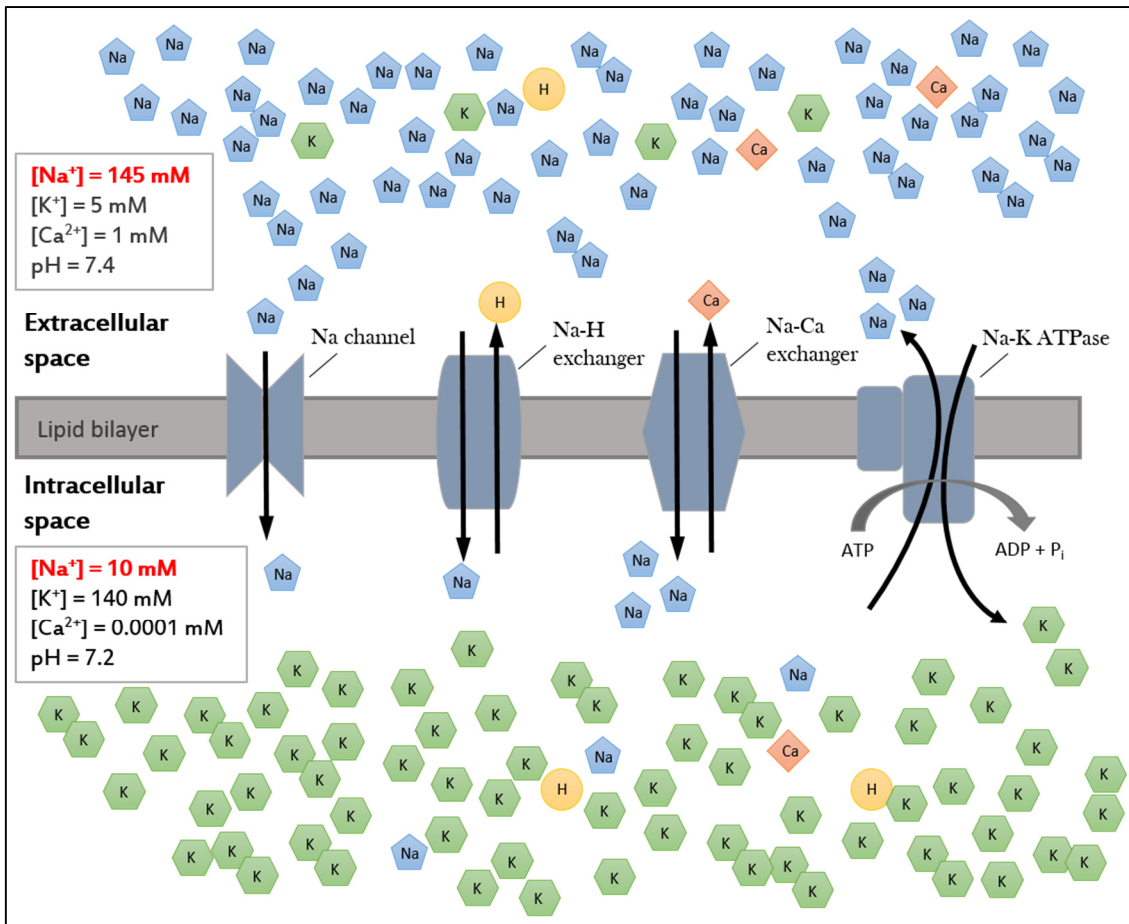


Figure 4: Schematic diagram of main Na^+ fluxes across the membrane. The following transmembrane proteins are involved: Na channel, Na-H exchanger, Na-Ca exchanger, and the Na-K ATPase.

On the contrary, only one significant mechanism pumps Na^+ out of the cell in order to maintain the concentration differences between inside and outside of cells. The Na-K ATPase uses the energy of ATP hydrolysis to exchange three intracellular Na^+ ions for two extracellular K^+ ions. This results in a net current across the membrane making the cell's inside more negative. During excitation of the muscle cells, Na-K pumps have a crucial function in the clearance of extracellular K^+ , which is a main contributor to muscle fatigue. They also aid to reverse depolarization resulting from exercise and muscle disease. Inhibiting the Na-K pump activity or reduction of their content reduces the muscle contractility and vice versa. Consequently, activity and capacity of the Na-K pump are regulated to fulfil the needs of skeletal muscle cells. In the short term, quick activation of the Na-K ATPase is possible by an increase in transport activity. Different hormones and conditions can stimulate this acute activation. The most widespread stimulus is a higher intracellular Na^+ concentration due to an excitation-induced Na^+ influx. Additionally, other stimuli can regulate the content of Na-K ATPase in a long-lasting and slower term. Such stimuli increasing Na-K ATPase performance include training, insulin, K^+ overload among others. Negative stimuli are e.g. immobilization, K^+ deficiency, diabetes, and some muscle diseases [31].

2.3.2 Homeostasis of organism

Besides being part of the electrochemical gradient, sodium holds also a central position in the homeostasis of the organism including the fluid and electrolyte balance. Cellular life depends on the ability to control tightly the solute/water balance. Most tissues including the muscle consist of 70 - 80 % water by weight, which is divided into the extracellular fluid and the intracellular fluid compartments [32]. The water flux between the compartments is directed by osmotic and hydraulic gradients. Extracellular fluid surrounds a cell with a relatively constant concentration of electrolytes in order to function properly. There is a variety of osmotically active ions and molecules that are involved in the volume control mechanisms [20]. Since Na⁺ makes up about 94 % of the extracellular osmoles, it is the only cation exerting significant osmotic pressure. Normally, Na⁺ levels are tightly controlled around 140 mM in the extracellular volume and remain somewhat stable with seldom changes more than 2 - 3 % [20]. If they do, the blood pressure and intracellular/interstitial fluid volumes alter consequently. Several mechanisms are responsible for the regulation of osmolarity, with two main actors: (i) the osmoreceptor-ADH system and (ii) the aldosterone mechanism (see [20] for details). The Na⁺ balance is thus crucial for the osmoregulation and its disturbance leads to pathological states such as hypertension or oedema [30], [32], [33]. Disruptions in the tightly controlled sodium gradient are also linked with some MDs (2.5).

2.4 Skeletal muscle damage and regeneration

As previously described, the skeletal muscle is a highly organized tissue needed for many physiological processes. Muscle tissue withstands chronic mechanical and physiological stress provoking degenerative processes on a daily basis. Regeneration mechanisms try to maintain a proper contractile function. Depending on the size of the membrane injury, different membrane repair mechanisms are triggered to reseal the membrane disruption. Tiny membrane injuries are spontaneously resealed without the help of an active membrane repair mechanism. Injuries bigger than one-nanometre trigger an active resealing mechanism. Smaller injuries activate a Ca²⁺ (calcium)-dependent active repair process that involves the formation of a lipid patch built by fusion of intracellular vesicles (local membrane repair). This active repair process is described in 2.5.1 due to the involvement of the dysferlin protein in the membrane-repair mechanism (Mutations in the dysferlin-encoding gene are linked to certain MD). After a larger injury, SC take responsibility of the muscle regeneration and mediate the restoration of functional muscle fibres (Figure 5) [34].

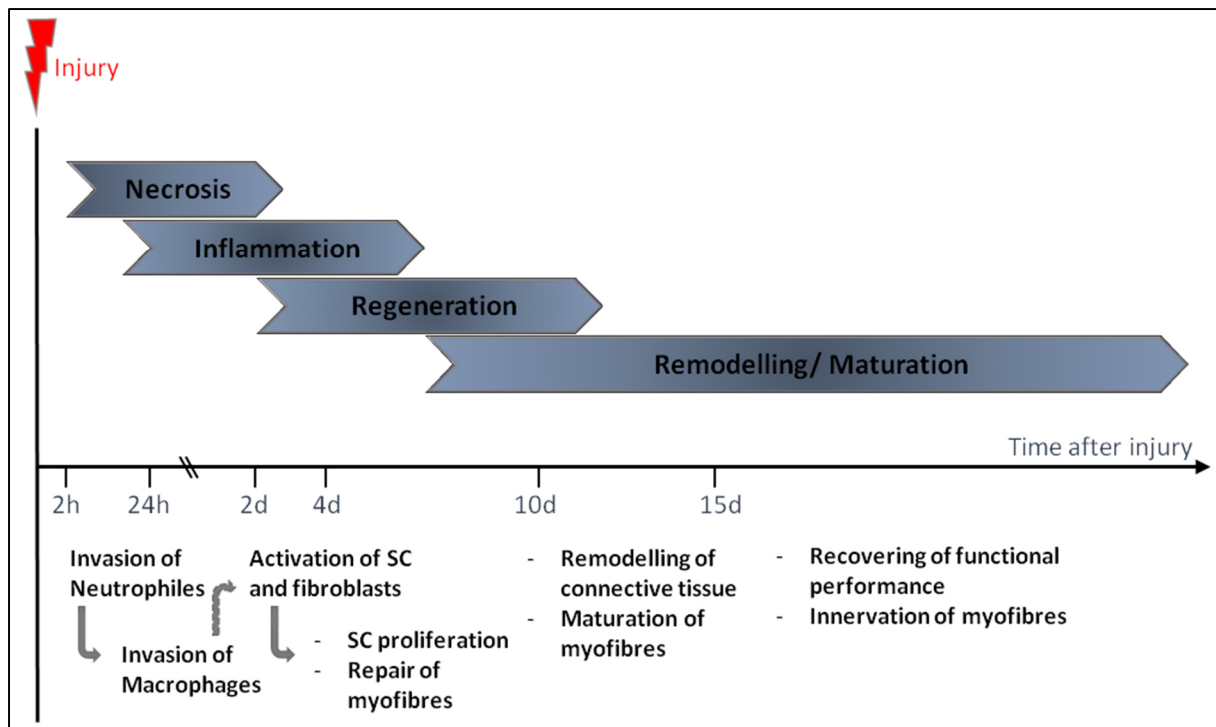


Figure 5: Scheme of skeletal muscle regeneration represented by the four interrelated and time-dependent phases: necrosis, inflammation, regeneration, and remodelling and maturation of the injured myofibre. Time line based on murine experiments. Adapted from [34]. h hours, d days, SC satellite cells.

The SC-involved regeneration activates several cell types sequentially in four interrelated and time-dependent phases after injury: (i) necrosis, (ii) inflammation, (iii) regeneration, and (iv) remodelling/maturation. Upon sarcolemma rupture, Ca^{2+} ions move into the cell inducing proteolysis of the fibres. This rapid necrosis activates a controlled inflammation where specific inflammatory cell populations (e.g. neutrophils, macrophages) invade the muscle to clean the area and activate SC. During the regeneration phase, activated SC and fibroblasts initiate the remodelling and maturation of myofibres and remodelling of connective tissue, respectively. The new formed myofibres align and either form new fibres or fuse to the remaining myofibres [35].

This cycle represents the common injury/regeneration process with transient collagen deposition and inflammatory infiltration. In the case of chronic disease/injury, the regeneration process is exhausted and remodelling of the connective tissue occurs with permanent deposition of fibrotic tissue (Figure 6). During the chronic inflammation, an increased number of macrophages rises pro-fibrotic factors leading to excessive extracellular matrix (ECM) accumulation in muscle tissue and altering the satellite cell function and regeneration [36]. As a result, SC are exhausted over time or lose the ability of self-renewal, thus the muscle tissue becomes replaced by adipose and fibrotic tissue [37]. The accumulation of ECM leads finally to muscle tissue dysfunction.

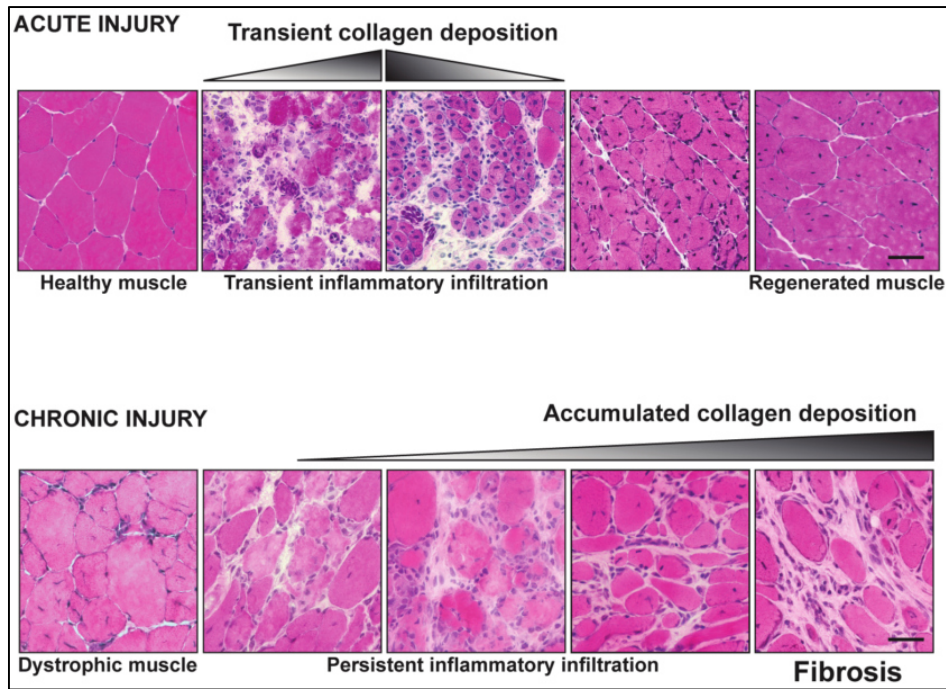


Figure 6: Inflammatory infiltration in acute and chronic muscle repair. Acute injury of skeletal muscle leads to a rapid and controlled inflammation. Transient inflammatory infiltration occurs to remove damaged myofibres and promote regeneration and remodelling of the muscle. During chronic injury on the contrary, a persistent inflammatory infiltration leads to an excessive accumulation of extracellular matrix components. This deposition inhibits the myofibres repair and muscle replacement by fibrotic tissue occurs [37]. Bars = 50 μ m.

2.5 The diverse group of muscular dystrophies

MD are inherited disorders characterized by variable degrees and distribution of skeletal muscle wasting and weakness. Although, they have their primary defect within the skeletal muscles, the heart can be also seriously affected in some types [1]. So far, more than 30 types of MD have been identified that involve mutations encoding different proteins [22]. In many MD, proteins that should stabilize the sarcolemma are affected impairing their initial role. The mutations lead to a fragile or leaky membrane with an increase in Ca^{2+} influx and cycles of inflammation and regeneration. Thus, the genetic defects cause persistent fibre degeneration with chronic inflammation and excessive deposition of collagen. The fibro-fatty infiltration reduces patient's mobility progressively so that they become eventually restricted to a wheelchair. The symptoms vary highly in age of onset, severity of symptoms, and rate of progression. Table 3 lists a selection of dystrophies that are relevant to this manuscript [1], [38], [39].

As MD differ in gene mutations, also the affected muscle groups, the age of onset, as the rate of muscle degeneration are not the same. In addition, different mutations in the same gene can lead to several different forms of dystrophy and even the same mutation has been shown to give rise to

different forms of dystrophy [40]. This diversity turns the diagnostic as well as management and treatment of the patients to an important but difficult task. So far, treatment can only decelerate disease progression. For example, DMD patients are commonly under anti-fibrotic treatment to counteract the increase in fibrotic tissue, which represents a predictive marker of a poor motor outcome [41], [36].

Table 3: Selection of muscular dystrophies that are relevant to the current work. Note that all these diseases are inherited.

Muscular dystrophy	Progressive muscle wasting affecting	Onset age
Becker muscular dystrophy (BMD)	Lower limb, hips, shoulders, heart	Child- or adulthood (mild form of DMD)
Duchenne muscular dystrophy (DMD)	Lower limb, hips, shoulders, heart	Childhood
Facioscapulohumeral dystrophy (FSHD)	Facial, upper arm shoulder	Childhood, early adolescence
Limb-girdle muscular dystrophy (LGMD)	Proximal muscle of pelvis and shoulders, sometimes heart, 32 different types	Childhood, late adolescence to adulthood
Myotonic dystrophy (MD1 and MD2)	Distal, neck or face, later heart	At birth (MD1) or adulthood (MD2)

2.5.1 Dysferlinopathies and the role of dysferlin in the membrane repair mechanism

Among the many mutations leading to MD are those that are found in the large-sized dysferlin gene (DYSF), which encodes for the transmembrane protein of the same name [42], [43]. The mutations in *DYSF* cause the most frequent adult-onset limb girdle muscular dystrophy, LGMD 2B, the Miyoshi myopathy, and other more rare forms of dysferlinopathies [44]. Dysferlinopathy patients show muscle weakness starting mainly in the lower limbs. Later, the disease progresses involving paravertebral and proximal upper girdle muscles. Patients lose their ambulation within ten to fifteen years after onset. These symptoms are paralleled commonly with high levels of creatine kinase, which indicates an increase of sarcolemma permeability and its gradually degeneration [45].

Dysferlin is a large transmembrane protein that is highly expressed in skeletal muscle and heart. In the skeletal muscle, it is located to the plasma membrane and t-tubule network. The exact role of dysferlin in the membrane is no yet fully understood, but it is involved in protein vesicle trafficking and fusion linked to the membrane repair [46].

Since membrane damage occurs physiologically and frequently in skeletal muscle, active membrane-repair mechanisms are conserved across eukaryotic cells. As aforementioned, the repair of large injuries involves the activation of SC as described in 2.4. For smaller injuries, a Ca^{2+} -dependent membrane repair mechanism is triggered without SC involvement. Dysferlin plays a key role in this Ca^{2+} -dependent process [47]; it comprises of multiple Ca^{2+} sensitive domains and

regulates Ca^{2+} homeostasis. It was found to be enriched in t-tubule membrane, where it is implicated in maintaining Ca^{2+} homeostasis following cellular stress [48]. A membrane disruption provokes Ca^{2+} influx into the cell leading to an area of high Ca^{2+} concentration around the damaged zone (Figure 7). The altered Ca^{2+} concentration triggers among other mechanisms the aggregation of dysferlin-carrying vesicles in this area, which then fuse with the plasma membrane in order to reseal it [49]. Alternatively, dysferlin-deficient muscle fibres undergo disruption of Ca^{2+} homeostasis following acute mechanical stress that leads to damage, inflammation, and necrosis. In the following, intermyofibrillar lipids and progressive adipocyte replacement causes the progressive decrease of muscle function [50].

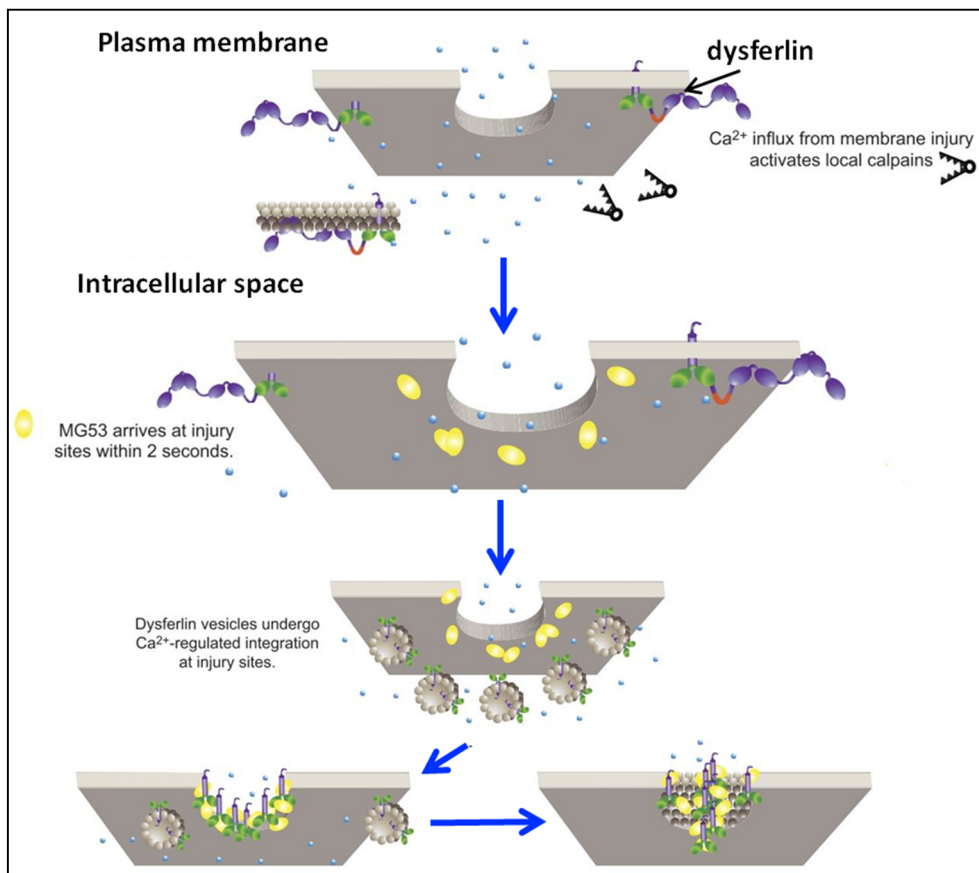


Figure 7: Dysferlin plays a key role in the Ca^{2+} -dependent membrane repair. The dysferlin protein is located in the cell membrane and cytoplasmic vesicles. After a local injury, the Ca^{2+} influx activates local calpains that cleave dysferlin protein. Dysferlin-containing cytoplasmic vesicles are recruited to the site of membrane injury. These vesicles fuse with one another and with the sarcolemma thus resealing the disrupted area. Adapted from [35].

2.5.2 The pathological disease progression of Duchenne muscular dystrophy and concurrent ion alterations

DMD is an X-linked genetic disease caused by mutations in the dystrophin gene. Dystrophin is a cytoskeletal protein that maintains the mechanical stability of myofibres during contractions and its loss causes aberrant mechanotransduction [51]. Furthermore, this protein shows complex

interactions with other structural and signalling molecules, thus playing a central role in muscle differentiation and organization of myofibres as contractile units [52] as well as in membrane repair in skeletal muscle [47]. The onset of DMD occurs in early childhood with difficulties in running and later on to stand up. The progressive muscle loss and fibrosis causes an early death through cardiac and respiratory failure in the early adulthood [1], [41]. Mutations in the dystrophin gene cause compared with DMD the milder Becker muscular dystrophy (BMD). The age of onset of BMD is around twelve years, while some patients show symptoms much later. The course of the disease is more benign and death occurs usually in the fourth or fifth decade of life. In contrast with DMD, the dystrophin protein is not completely absent in BMD, however, it is not fully functional; the amount is either reduced or its size is abnormal [53].

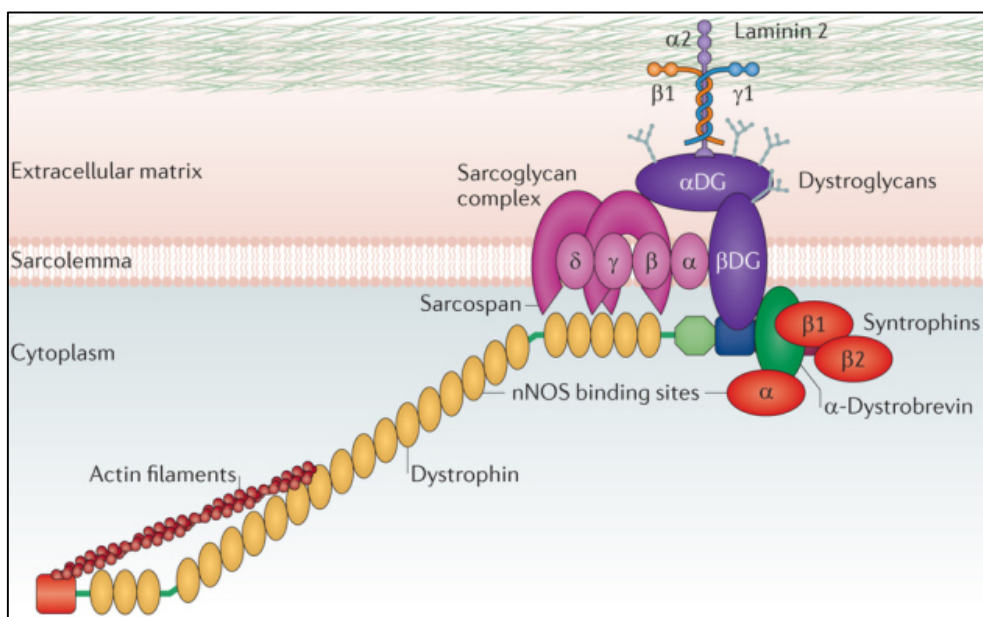


Figure 8: The dystrophin-glycoprotein complex (DGC) connects actin filaments through the cell membrane to the surrounding ECM [54].

Dystrophin is part of the dystrophin-glycoprotein complex (DGC) that connects the cytoskeleton through the cell membrane to the surrounding ECM, the fibrous endomysium (Figure 8). The dystrophin-mediated link stabilizes the sarcolemmal structure and transmits force laterally. Thus, an absence or impairment reduces muscle stiffness; the sarcolemmal integrity and stability is lost. The loss of sarcolemmal integrity in patients suffering from DMD or BMD leads eventually to the aforementioned symptoms of muscle degeneration, necrosis, and fibrosis [55], [56]. Although, dysferlin is not a part of the DGC, altered expression levels have been also demonstrated in DMD patients [57].

The high concentration of plasma creatine kinase implies an increased membrane permeability that allows muscle specific enzymes to leak out of the cell and extracellular ions such as Ca^{2+} to enter the cell. Dystrophic cells show indeed an increase of intracellular Ca^{2+} , which in return

activates proteases leading to cell necrosis [56]. The exact function of dystrophin and the role of the observed abnormal intracellular calcium concentration ($[Ca_i]$) remain unclear despite years of research. Turner *et al.* [58] showed already in the late 1980s that the absence of dystrophin results in the inability to maintain a low $[Ca_i]$ and leads to a prolonged elevation of the $[Ca_i]$ during stimulation. The higher $[Ca_i]$ thus resulted in a greater myofibre degradation. However, besides the Ca^{2+} entry pathways across the sarcolemma, modifications of ion transport proteins could play a crucial role in the generation of abnormal high Ca^{2+} concentrations in MD. Moreover, cells lacking dystrophin not only demonstrated altered Ca^{2+} concentrations, but also increased $[Na_i]$. However, the underlying cellular mechanisms are still unclear with several possibilities including deregulation of the Na-K ATPase, sodium channels, and exchangers.

Dunn *et al.* [59] reported an increase of the Na-K ATPase content in *mdx* mice suggesting that the elevated activity is caused by increased Na-K pump concentration. Furthermore, the absence of dystrophin modifies the expression level, distribution, and gating properties of the Nav1.4 channel leading to an abnormally high sodium concentration [60]. Hirn *et al.* [61] showed that deregulation of Nav1.4 significantly alters the Na^+ influx into the dystrophic cell leading to increased $[Na_i]$. They further reported that in the absence of dystrophin the Nav1.4 channel protein is not anchored properly in the membrane. Besides, the NCX has a high capacity to transport Ca^{2+} from the cell; this transport works also in the reversed mode following the transmembrane ion gradients. Deval *et al.* [62] demonstrated that an increase of $[Ca_i]$ can be triggered by a decrease of external Na^+ thus stimulating the reverse mode of the exchange mechanism of the NCX. This produced elevated $[Ca_i]$ in DMD myotubes, which they related to an enhanced mechanism of Ca^{2+} -induced Ca^{2+} -released process. Additionally, the isoform NHE-1 can elevate the $[Na_i]$ and produce elevated $[Ca_i]$ via coupling to the NCX. Iwata *et al.* [63] demonstrated in dystrophic hamsters and mice that NHE inhibition has a protective effect against muscle degeneration by reducing muscle damage and improving the muscle performance.

Regardless the underlying cause of increased Na_i levels in DMD, the Na^+ alterations motivated researchers to monitor sodium concentrations by ^{23}Na NMR. 3.4.2 presents later in more detail the feasibility studies to quantify *in vivo* the increased sodium concentrations.

Nuclear magnetic resonance

This chapter describes selected aspects of the NMR theory that are relevant to this work. Every technique that relies on the NMR phenomenon in order to analyse liquids, solids, or tissues involves three basic steps:

- Magnetic polarization: an alignment of the magnetic nuclear spins due to the application of an external magnetic field
- Excitation: a perturbation of the aligned system by absorption of specific radio frequency pulse
- Relaxation: a return from the excited state caused by the excitation to the minimum potential energy state (thermal equilibrium) while the emitted electromagnetic signal is detected

The appropriate combination of those basic steps enables one to analyse physical properties of the system of interest. The first part, which was inspired by textbooks of de Graaf [64] and Levitt [65], explains the basic concepts of the NMR phenomenon (3.1) to understand spectroscopic and imaging acquisitions (3.2). 3.3 talks about the NMR properties of the sodium nucleus and the different approach to separate the intracellular from the extracellular ^{23}Na signal. Finally, 3.4 highlights the role of NMR as an outcome measure of MD.

3.1 Basic principles of nuclear magnetic resonance

The phenomenon of NMR can be explained using two different approaches: with classical and quantum mechanics. Here, I first use quantum mechanics to describe the concept of nuclear spin, which is a form of angular momentum. Then, the weak interactions of nuclei with a magnetic field (polarization, excitation, and relaxation) are introduced based on the classical description with Bloch equations.

3.1.1 Magnetic polarization and Larmor frequency

In quantum mechanics, the angular momentum, I , is quantized taking only discrete values (half-integral ($1/2, 3/2, 5/2 \dots$) and integral numbers ($0, 1, 2, 3 \dots$)). Non-zero nuclear spins are a prerequisite for NMR. In general, the angular momenta are distributed on $2I + 1$ cones. Nuclei with a spin of $1/2$, e.g. ^1H , have thus two possible spin states $m = 1/2$ and $m = -1/2$ according to $m = -I, -I + 1, \dots, +I$. In the absence of an external field, each of the $2I + 1$ cones with the same I but different m have the same energy; they are degenerated. In the presence of an external magnetic field, the degeneracy is broken causing each of the $2I + 1$ sublevels to have a slight different energy

level (Figure 9). This splitting of the energy levels in an external magnetic field is called Zeeman splitting.

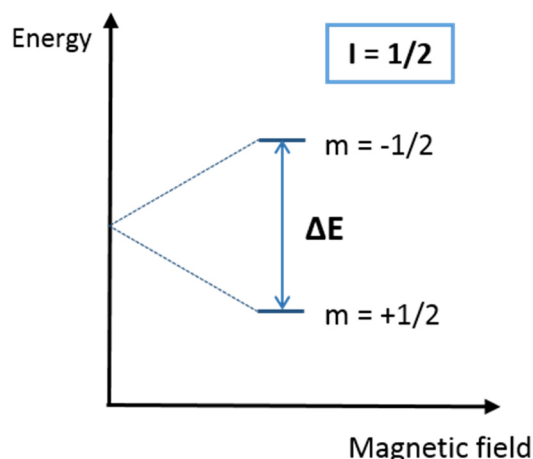


Figure 9: Zeeman splitting of energy levels of a nucleus with spin $I = 1/2$. The degeneracy of the m sublevels is broken in the presence of an external magnetic field causing an energy separation between the m sublevels.

For a spin of $1/2$, the state $m = 1/2$, which has magnetic moment parallel with the magnetic field \vec{B}_0 , has a lower energy and is more stable than $m = -1/2$ (magnetic moment anti-parallel to \vec{B}_0). The energy difference between the two different states ΔE is given by:

$$\Delta E = \gamma \left(\frac{h}{2\pi} \right) B_0$$

Where h is the Planck's constant and γ the gyromagnetic ratio, which is dependent on the nuclei under investigation.

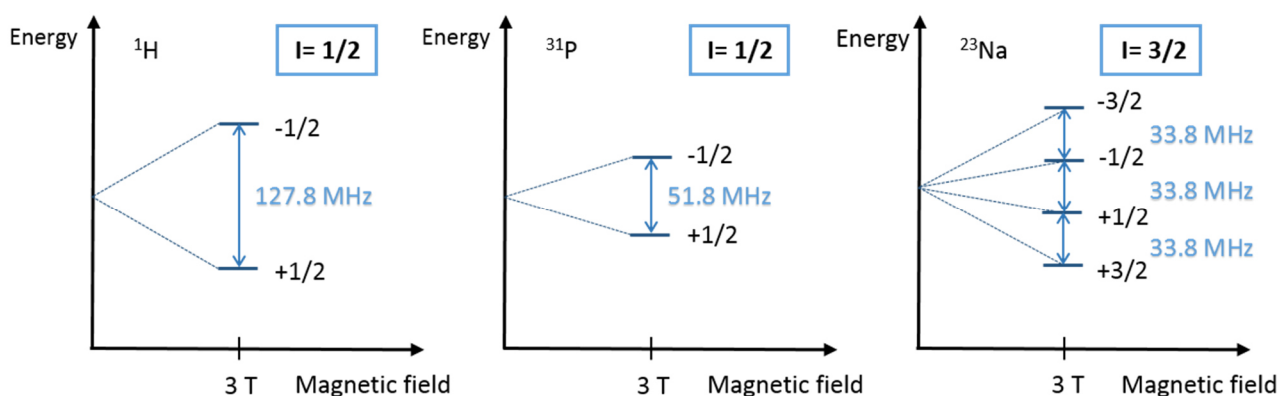


Figure 10: Zeeman diagrams from spin $I = 1/2$ (^1H and ^{31}P) and spin $I = 3/2$ (^{23}Na) in an external magnetic field $B_0 = 3\text{T}$.

Figure 10 shows sketches of the Zeeman diagrams for ^1H , ^{31}P , and ^{23}Na nuclei as a function of applied magnetic field. The ^1H and the ^{31}P nuclei are both spin $1/2$, thus the nuclear ground state (no external magnetic field applied) splits in two sublevels when exposed to a magnetic field. The ^{23}Na nucleus has a spin of $3/2$; so the nuclear ground state splits into four levels according to the $2I + 1$ degeneracy rule. The energy difference between the levels differs between the nuclei in the same

magnetic field, because of the different gyromagnetic ratios of the nuclei. The gyromagnetic ratio of ^1H is about two and a half times higher than the one of ^{31}P and four times higher than γ of ^{23}Na , making the ^1H nucleus more sensitive than the other nuclei and thus the Zeeman splitting of ^1H larger at the same magnetic field.

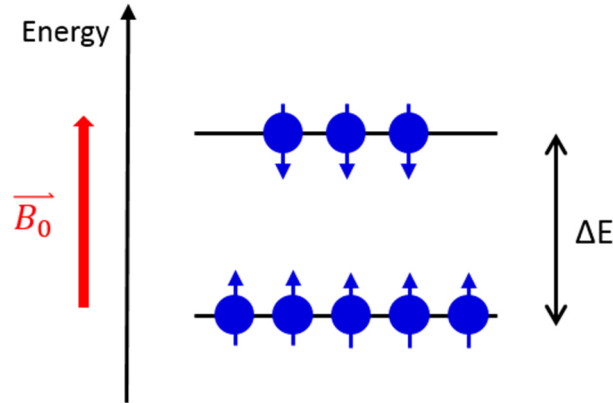


Figure 11: Population of spins in the presence of an external magnetic field \vec{B}_0 . While the lower energy level corresponds to the magnetic moments parallel with \vec{B}_0 , the spins in the higher energy level are aligned anti-parallel with \vec{B}_0 .

A macroscopic sample contains many spins that are randomly distributed on the $2I + 1$ cones. The presence of an external magnetic field causes a small energy difference between the spin states and thus a small difference in the population of these spin states with a bias towards the lower energy state (Figure 11). This difference in population gives rise to a net magnetization M_0 of the macroscopic sample that is proportional to B_0 :

$$M_0 = \left(\frac{\gamma h}{2\pi}\right)^2 \left(\frac{n B_0}{4kT}\right)$$

Where k is the Boltzmann constant, T the absolute temperature, and n the total number of nuclear spins in the macroscopic sample. Thus, the magnetization and therefore the final received NMR signal are proportional to the population difference of the spin states.

In the following, the classical description is used to explain the interaction of the resulting magnetic moment $\vec{\mu}$ with external magnetic fields. The rotating nuclei feel a torque in the presence of an external magnetic field \vec{B}_0 . The interaction between $\vec{\mu}$ and \vec{B}_0 is described by:

$$\frac{d\vec{\mu}}{dt} = \gamma \vec{\mu} \times \vec{B}_0$$

The amplitude of the magnetic moment is constant and changes only its orientation relative to the magnetic field. Thus, the magnetic moment precesses about \vec{B}_0 in an angle Θ and with a quantized amplitude μ_z (Figure 12).

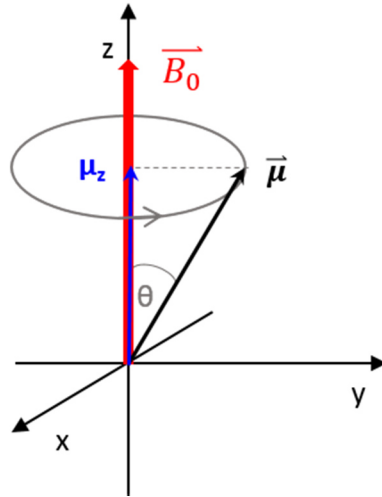


Figure 12: Magnetic moment $\vec{\mu}$ precessing in an external magnetic field \vec{B}_0 .

The precession frequency, the so-called Larmor frequency, ω_L is directly proportional to the applied magnetic field \vec{B}_0 and the gyromagnetic ratio γ , which depends on the nucleus of interest. This is described by the Larmor equation:

$$\omega_L = \gamma B_0$$

A resonant absorption by nuclear spins only occurs when the correct frequency equalling the Larmor precession frequency is applied to match the discrete energy differences ΔE between the levels in a constant magnetic field \vec{B}_0 . The magnetic moment emerged in an external magnetic field possess the magnetic energy defined as follows:

$$E = -\vec{\mu} \cdot \vec{B}_0 = -\mu B_0 \cos\theta$$

Where θ describes the angle between the external magnetic field \vec{B}_0 and the magnetic moment $\vec{\mu}$. At $\theta = 180^\circ$, the magnetic energy is maximized, while it is minimized when $\vec{\mu}$ is parallel with \vec{B}_0 ($\theta = 0^\circ$).

3.1.2 Magnetization excitation

At thermal equilibrium, the net magnetization has only a longitudinal component in the z-axis. In order to study the nuclear magnetization, the net longitudinal magnetization vector needs to be rotated towards the xy-plane (transverse plane). The deflection of the longitudinal magnetization can be realised by a second magnetic field \vec{B}_1 applied perpendicular to \vec{B}_0 as an RF pulse applied at the Larmor frequency (switched on for a finite time and turned off again). The net magnetization \vec{M}_0 initially aligned with the +z-axis precesses about the static magnetic field \vec{B}_0 and the RF field \vec{B}_1 in the transverse plane during the RF pulse. Because of the experienced torque from the applied \vec{B}_1 field, \vec{M}_0 rotates towards the transverse plane. If the applied RF pulse is long enough, \vec{M}_0 can completely rotate onto the transverse plane or flip to the -z-axis (Figure 13).

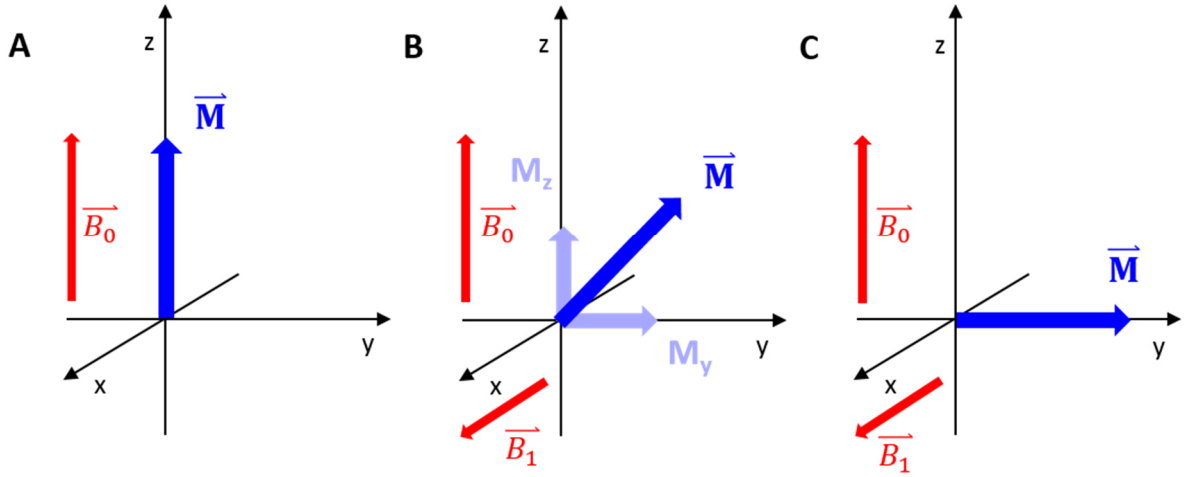


Figure 13: Excitation of magnetization in the rotating frequency frame. **A)** At thermal equilibrium, a net magnetization vector along $+z$ without a net magnetization in the transverse plane. **B)** The net magnetization rotates towards the $+y$ -axis during the application of \vec{B}_1 . **C)** If the RF pulse is calibrated for a complete excitation, a net magnetization vector along $+y$ -axis is created and no magnetization remains along z -axis.

Since the two magnetic fields \vec{B}_0 and \vec{B}_1 act simultaneously on the net magnetization, the rotation of \vec{M}_0 is rather complex. At thermal equilibrium, the z -component of \vec{M}_0 is constant:

$$\frac{d\vec{M}_z(t)}{dt} = 0$$

While the x - and y -components are randomly organized on the cone and precess about \vec{B}_0 at the Larmor frequency:

$$\frac{d\vec{M}_x(t)}{dt} = -\gamma \vec{M}_y \vec{B}_0 \quad \text{and} \quad \frac{d\vec{M}_y(t)}{dt} = -\gamma \vec{M}_x \vec{B}_0$$

During excitation, a RF pulse is applied in the form of:

$$\vec{B}_1(t) = B_1 \cos(\omega t)[\vec{x}] - B_1 \sin(\omega t)[\vec{y}]$$

Where \vec{x} and \vec{y} are the unit vectors along the x and y axes. The combined effect of \vec{B}_0 and \vec{B}_1 on the magnetization are then described by the so-called Bloch equations in the laboratory frame:

$$\begin{aligned} \frac{d\vec{M}_x(t)}{dt} &= \gamma [\vec{M}_y(t)B_0 - \vec{M}_z(t)B_1 \sin(\omega t)] \\ \frac{d\vec{M}_y(t)}{dt} &= \gamma [\vec{M}_z(t)B_1 \cos(\omega t) - \vec{M}_x(t)B_0] \\ \frac{d\vec{M}_z(t)}{dt} &= \gamma [\vec{M}_x(t)B_1 \sin(\omega t) - \vec{M}_y(t)B_1 \cos(\omega t)] \end{aligned}$$

To simplify the analysis of NMR phenomena, the complex motion of precessing can be described in the rotating frame of reference. Thus, the precessional motion around \vec{B}_0 is frozen by transforming the coordinate system so the observer rotates with spins at Larmor frequency. In this rotating frame of reference concept, the Cartesian axes (x' , y' , z') rotate about \vec{B}_0 with frequency ω . Thus, the three components of the magnetization in the rotating frame are given by:

$$M'_x = M_x \cos(\omega t) - M_y \sin(\omega t), \quad M'_y = M_x \sin(\omega t) + M_y \cos(\omega t), \quad \text{and} \quad M'_z = M_z$$

3.1.3 Longitudinal and transverse relaxation

After an RF pulse, some part of the magnetization is placed in the transverse plane resulting in a transverse magnetization. Afterwards, the transverse magnetization experiences only the magnetic field \vec{B}_0 and starts to precess coherently about \vec{B}_0 at the Larmor frequency. This induces an electromotive force (EMF) in the receiver coil located in the transverse plane during NMR experiments. The induced EMF directly creates the NMR signal, and its time dependency is called free induction decay (FID).

The components of the net magnetization \vec{M}_0 return to the thermal equilibrium in an exponential manner, but with different time constants T_1 and T_2 . The relaxation processes for the three components of the magnetization vector \vec{M} in the rotating frame can be written as:

$$\frac{d\vec{M}_{x'y'}(t)}{dt} = -\frac{\vec{M}_{x'y'}(t)}{T_2}, \quad \text{and} \quad \frac{d\vec{M}_{z'}(t)}{dt} = -\frac{\vec{M}_{z'}(t) - \vec{M}_0}{T_1}$$

The longitudinal relaxation time T_1 or also called spin-lattice relaxation time refers to the return of longitudinal magnetization M_z after the excitation RF pulse. It involves energy transfer from the spins to the surrounding lattice. T_2 is the transverse relaxation time or spin-spin relaxation time. It involves the energy transfer between spins and represents the disappearance of transverse magnetizations M_x and M_y , which is an entropy process. The energy exchange between the spins causes a reduction in phase coherence and an increase in entropy. T_2 is always less than or equal to T_1 .

Thus, the signal intensity M_z recovers following a 90° RF pulse through T_1 relaxation during the recovery time t according to (Figure 14):

$$M_z(t) = M_0 (1 - e^{-\frac{t}{T_1}})$$

The T_1 is the time constant for regrowth of longitudinal magnetization that is specific for each tissue. It is the time required for the z-component of the magnetization to reach about 63 % of its maximal value. The T_1 relaxation time can be calculated by obtaining NMR spectra at different recovery times. The saturation recovery or inversion recovery methods are very wide used techniques to measure the T_1 relaxation (4.3).

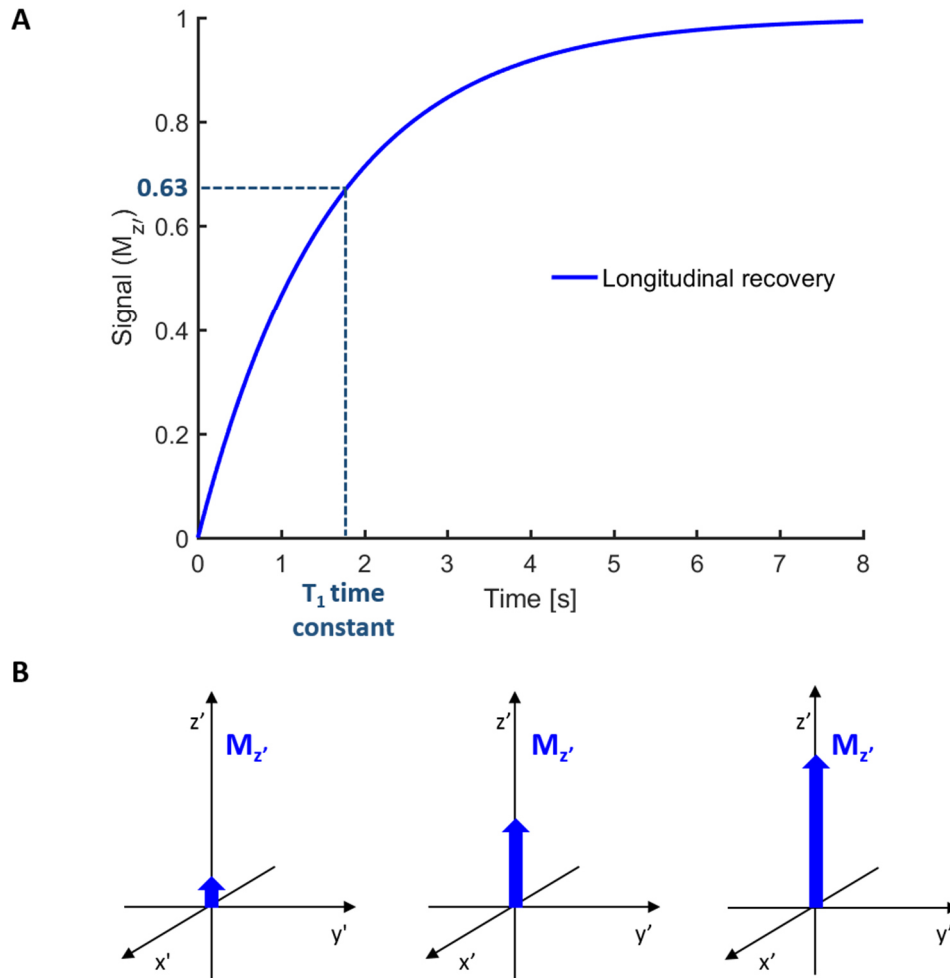


Figure 14: Spin-lattice (T_1) relaxation. **A)** The longitudinal magnetization relaxes back to thermal equilibrium value with a T_1 relaxation time constant. **B)** After a 90° RF pulse no net macroscopic magnetization $M_{z'}$ remains. Given time, the longitudinal magnetization returns in an exponential manner.

Following a 90° RF pulse rotating \vec{M}_0 in the transverse plane, the induced transverse magnetization M_{xy} decreases as a function of time due to T_2 relaxation (Figure 15). The corresponding spectrum is fitted to an exponential curve derived from the Bloch equations according to:

$$M_{xy}(t) = M_{xy}(0) \times e^{-t/T_2}$$

The T_2 is the time constant for decay of transverse magnetization. It is the time required for the transverse magnetization to fall to about 37 % of its initial value. However, macroscopic and microscopic inhomogeneities, which lead to locally different \vec{B}_0 magnetic fields across the object resulting in a distribution of Larmor frequencies in the magnetic field \vec{B}_0 , accelerate this T_2 relaxation. Therefore, the resulting signal of a macroscopic object in the presence of inhomogeneity is described by T_2^* relaxation referring to the more rapid loss of transverse magnetization than caused by pure T_2 relaxation (see 4.4 for methods to measure the T_2).

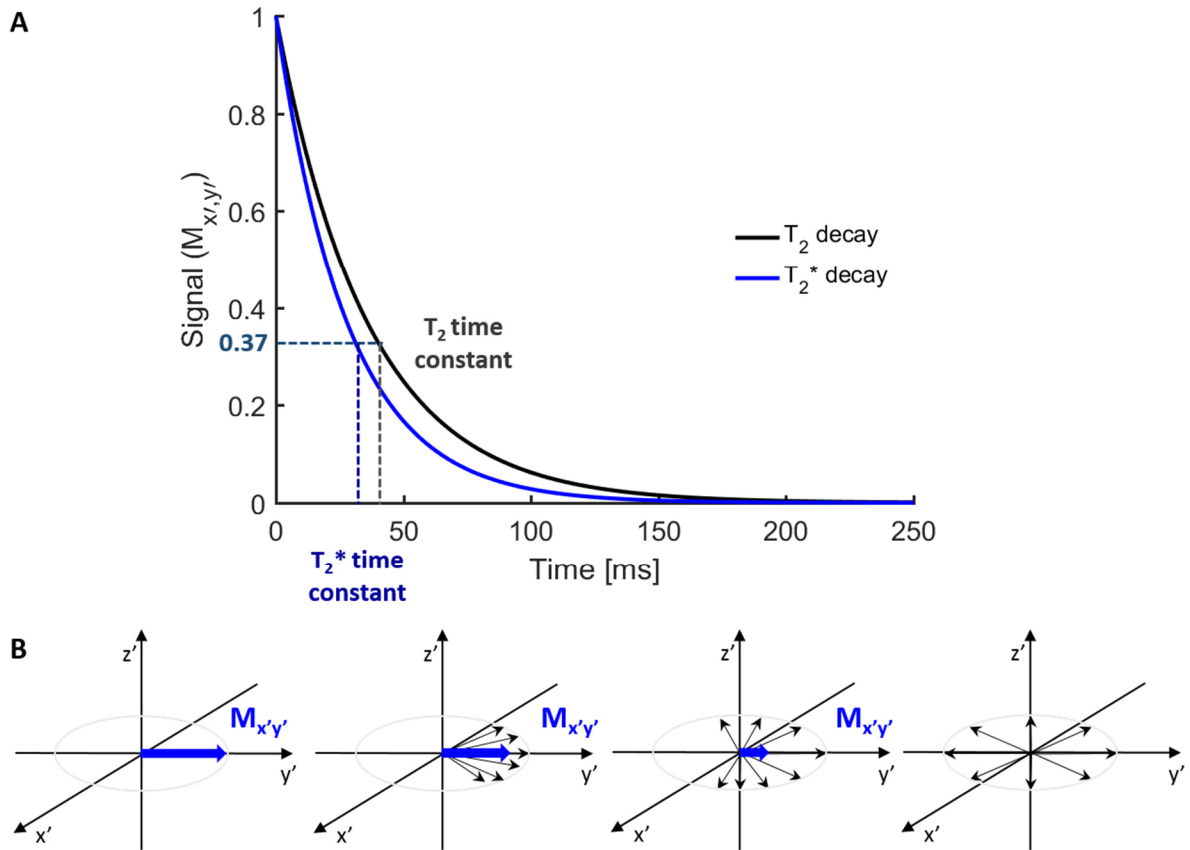


Figure 15: Spin-spin (T_2) relaxation. **A)** The transverse magnetization decays with a T_2 relaxation time constant in a perfect homogeneous magnetic field and with a T_2^* relaxation time constant at presence of magnetic field inhomogeneity. **B)** After a 90° RF pulse excitation, the net magnetization is rotated towards $+y'$ -axis and phase coherence is generated (transverse magnetization along the $+y'$ -axis). During the relaxation, the phase coherence decreases in the transverse plane and the resulting transverse magnetization disappears with time.

The mechanism by which the longitudinal relaxation occurs is the dipolar coupling between nuclear magnetic dipoles. On the other hand, the transverse relaxation occurs due to exchange of energy between excited nuclei and low energy state nuclei that leads to the randomization of spins in xy -plane. Both mechanisms are related to the correlation time τ_c of the nuclei:

$$\tau_c = \frac{4 \pi r^3 \eta}{3 k T}$$

Where k is the Boltzmann constant, T the absolute temperature, η the viscosity coefficient, and r the radius. τ_c is by definition the time it takes a molecule to rotate one radian ($360^\circ/2\pi$). The formula demonstrates that the larger the molecule the slower it moves. Small molecules (like free water) can rapidly rotate having long T_1 and T_2 times. As the motion gets slower, like in proteins or solids, T_2 shortens and T_1 increases again (Figure 16).

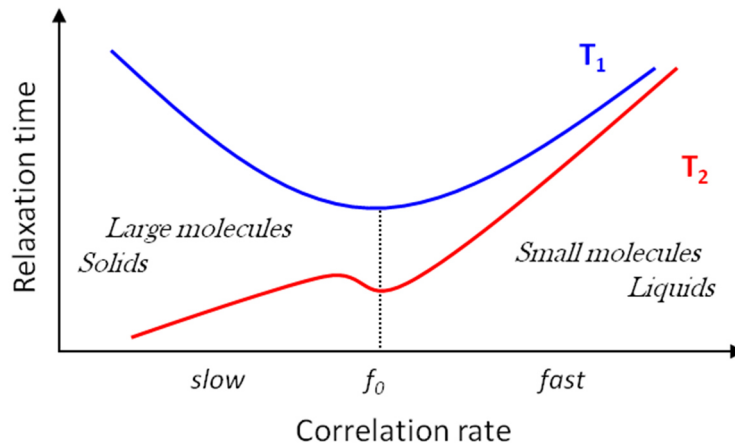


Figure 16: T_1 and T_2 relaxation times as a function of the correlation rate. The minimum of T_1 and the “dip” of the T_2 are at Larmor frequency f_0 .

Since the T_1 relaxation is dominated by the exchange of energy between spins and environment, the relaxation time of T_1 has its optimum at the Larmor frequency. On the contrary, the T_2 relaxation is based on the energy exchange between spins. So the slower the spins move (the greater their contact), the more efficient can be this energy transfer and the shorter is T_2 .

3.1.4 Chemical shift

Chemical shift refers to changes in the resonance frequency of a nucleus due to alterations in molecular environment. This relative shift in Larmor frequency is caused by shielding of the nuclei from \vec{B}_0 by surrounding electrons (and other nuclei). These electrons rotate in an opposite sense to the spin precession in \vec{B}_0 , which in return involves motion of charge and therefore induces an additional magnetic moment μ_e . The electrons decrease therefore the magnetic field sensed by the atomic nuclei and the real resonance condition is as follows:

$$\omega = \gamma B_0(1 - \sigma)$$

Where σ is the shielding constant depending on the chemical environment. One example of this effect is the fat-water shift in ^1H NMR. The shift caused by non-uniformity in the local magnetic field is linearly dependent on the magnetic field strength. For practical reasons, the chemical shift δ is expressed in parts per million (ppm), which makes it independent of magnetic field strength:

$$\delta = \frac{\omega_{metab} - \omega_{ref}}{\omega_{ref}} \times 10^6$$

Where ω_{metab} and ω_{ref} correspond to the frequencies of the metabolite of interest and a reference resonance, respectively. The investigated metabolite is commonly referred to a reference compound whose chemical shift should be independent of external variables such as temperature and ionic strength, and produce a strong resonance signal.

3.2 From nuclear magnetic resonance spectroscopy to imaging

3.2.1 Nuclear magnetic resonance spectroscopy

NMRS is a powerful tool to analyse the chemical structure of molecules that consist of nuclei with a magnetic moment. Examples of commonly used nuclei for *in vivo* NMRS applications are ^1H , ^{31}P , and ^{23}Na (Table 4).

Table 4: NMR properties of commonly used nuclei. Values extracted from [64].

Element	Spin	Gyromagnetic ratio ($10^7 \text{ rad T}^{-1}\text{s}^{-1}$)	Gyromagnetic ratio relative to ^1H	Natural abundance (%)
^1H	$1/2$	26.75	-	99.99
^{31}P	$1/2$	10.84	0.4	100
^{23}Na	$3/2$	7.08	0.26	100

The ^1H nucleus is the most sensitive nucleus to NMR due to its high gyromagnetic ratio and high natural abundance. ^1H NMRS enables the detection of a large number of biologically relevant metabolites such as different neurotransmitters and related compounds in the brain. In skeletal muscles, it is possible among others to observe intra- and extramyocellular lipids on ^1H NMRS (4.5.2). The second most used NMRS technique relies on the ^{31}P nucleus to study the energy metabolism, pH, and magnesium concentration (4.5.1). ^{23}Na NMR is a subject of increased interest in medical research as it can inform about the tissue viability and can therefore provide complementary information to the common used ^1H and ^{31}P NMRS (3.4.2).

In NMRS, the collected signal of the object of interest represents a sum of chemical compounds. The obtained time signal is visualised in the frequency domain by the Fourier transformation, which allows the quantification of the individual contribution of each chemical compound (Figure 17). The spectra can be evaluated through calculation of the area under the peak or more advanced fitting approaches. The spectra can be further analysed by the ratios of the different peaks and by quantification using internal or external references. Thus, depending on the experimental design, relative or absolute quantification can be achieved. Different metabolites are detected and quantified *in vivo* enabling to study a variety of metabolites present in biological tissues. To date, a variety of metabolic markers has been explored to detect and quantify disease progression.

Concentrations and composition of metabolites change *in vivo* throughout the object. The use of a surface coil is one simple way of signal localization. This approach is nevertheless restricted to areas close to the body surface. NMRS is often combined with localization methods (e.g. point resolved spectroscopy (PRESS) [66], image selected *in vivo* spectroscopy (ISIS) [67],...). A combination

of excitation pulse sequences and gradient sequences selects the volume of interest. The PRESS method for example consists of a slice-selective 90° excitation pulse, followed by two slice-selective 180° refocusing pulses. The slice selections are orthogonal, which preserves only the signal from the volume of interest at the intersection of the three selected slices.

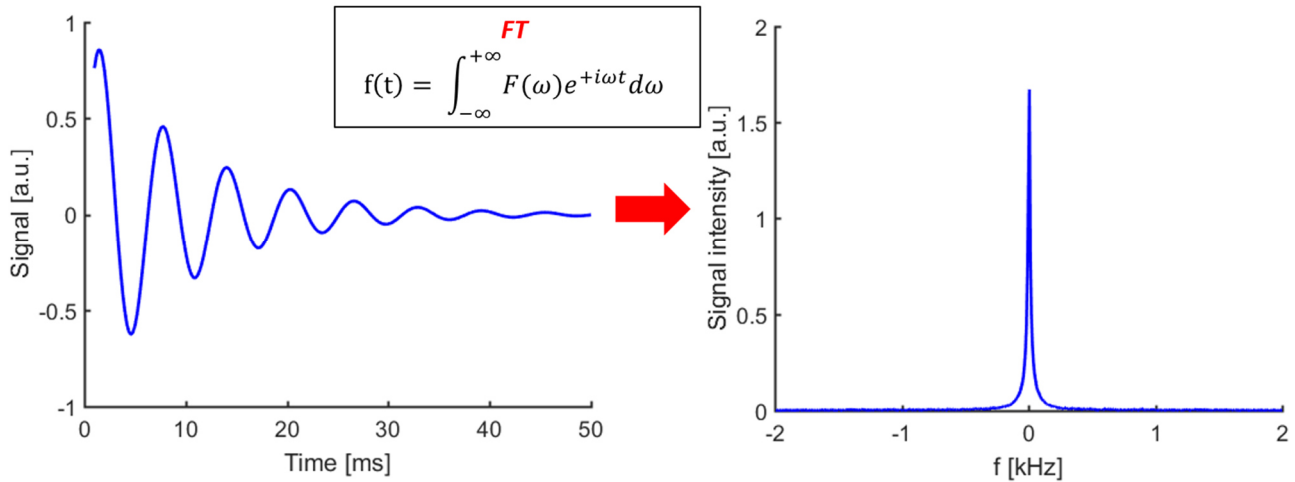


Figure 17: The free induction decay following an excitation pulse in the time-domain. The corresponding frequency-domain spectrum is obtained by computing the Fourier transform of the FID.

3.2.2 Nuclear magnetic resonance imaging

While NMRS provides quantitative identification of metabolites in tissues and fluids, NMRI takes images of the body represented as the sum of all metabolites in one voxel (dominated by the water resonance due to high abundance). By adjusting different experimental parameters, great soft tissue contrast can be generated (T_1 weighted, T_2 weighted, proton density weighted...). To acquire an image of an object, magnetic field gradients make the resonance frequency and phase dependent on its spatial position. Usually, a NMRI magnet comprises three gradient coils to encode independently all three dimensions (see [64] for more details). The signal acquisition in NMR imaging requires sampling of the so-called k-space in the spatial frequency domain. The complex values acquired during the NMRI measurement are further Fourier transformed to obtain the images.

3.3 A special nucleus: sodium

^{23}Na NMR has the potential to assess directly and quantitatively metabolic information about the cell viability and to add important information to the standard ^1H NMR. Still challenges related to the properties of the sodium nucleus hinder its broad utilization. Nevertheless, ^{23}Na NMR represents a subject of increasing interest in biomedical research due to recent availability of high field scanners. The following section provides an understanding of the quadrupolar nature of the sodium nucleus (3.3.1). Then, I will discuss the quantification of total sodium content (3.3.2) and different methods to achieve an intracellular weighting of the ^{23}Na signal (3.3.3).

3.3.1 NMR properties of ^{23}Na

The sodium nucleus has a relatively high gyromagnetic ratio and yields the second strongest NMR signal after ^1H . The NMR sensitivity for sodium is 9.3 % of the proton sensitivity, but the concentration in biological tissues is a few thousand times smaller than that of water (Table 5) causing a much lower SNR.

Table 5: List of main biological and physical differences between ^1H and ^{23}Na NMR.

	^1H NMR	^{23}Na NMR
Spin	$1/2$	$3/2$
Gyromagnetic ratio ($10^6 \text{ rad s}^{-1}\text{T}^{-1}$)	267.5	70.8
Concentration in skeletal tissue	$\sim 80 \text{ M}$	10 - 140 mM
T_2 relaxation in skeletal muscle	Multi-exponential (short T_2 of 32 ms, long T_2 of 120-180 ms...)	Bi-exponential (short T_2 of 0.5- 1 ms and long T_2 of 10-20 ms)

Spin $1/2$ nuclei such as ^1H exhibit only a magnetic dipole moment. In contrast, the sodium nucleus possesses a $3/2$ spin. The nuclear ground state splits into four levels according to the $2I + 1$ degeneration rule (3.1.1). Additionally, the electric charge distribution of the nucleus is not spherically symmetrical (Figure 18). In that case, the relaxation process is not dominated by dipole-dipole interactions but rather by the quadrupolar moment of the nucleus that interacts with the electric field gradient (EFG) produced by the molecular environment. The electric field gradient is a tensor with three principal values associated with three principal axes. The parameter eq is the largest principal value of the EFG. The EFG fluctuates in time because of thermal motion. Depending on its frequency, this fluctuation modulates the relative energies of the nuclear spin states.

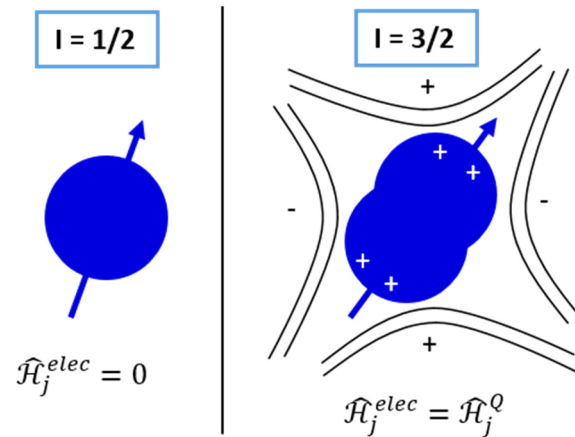


Figure 18: Electric charge distribution of 1/2 and 3/2 nuclei. A spin 1/2 is spherical exhibiting no electric interaction between the nucleus and the electric field. On the other hand, a spin of 3/2 has a quadrupolar electric charge distribution that interacts with the electric field gradient.

The averaged quadrupolar interaction frequency $\overline{\omega_Q}$ that is sensed by the nucleus is defined by the simplified equation [68]:

$$\overline{\omega_Q} = \frac{eQ eq}{4 \hbar} (3 \cos^2 \theta - 1)$$

Where \hbar is the Dirac's constant, eQ the electric quadrupole moment of the nucleus, eq the major element of the diagonalized EFG tensor, and θ the angle between the element's direction and the direction of the magnetic field B_0 . Thus, the quadrupolar coupling depends on the nuclear quadrupole moment (for ^{23}Na nucleus $10.4 \times 10^{-28} \text{ m}^2$) and the molecular property represented by the EFG that are created by the surrounding electrons [65].

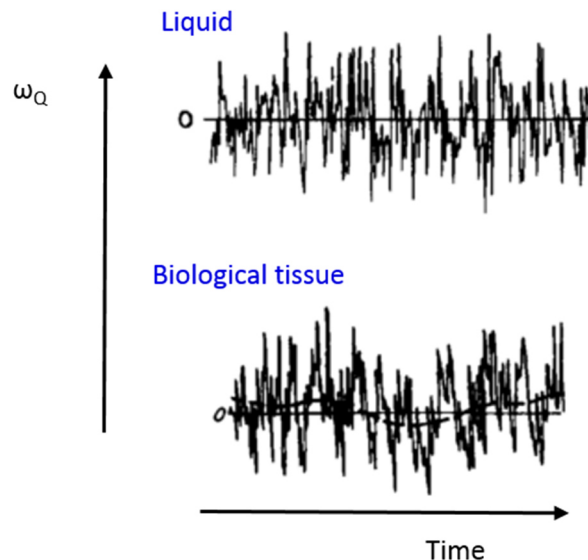


Figure 19: Time dependence of quadrupolar interactions in the laboratory frame. The quadrupolar interaction frequency ω_Q is modulated in time due to thermal motion within the lattice. In liquid, the quadrupolar interactions are averaged to zero in a relatively short time. In biological tissue, the quadrupolar interaction frequency is slower resulting in non-zero averaged ω_Q . Adapted from [69].

Figure 19 depicts the time dependence of quadrupolar interactions in different environments. In liquids, the static quadrupolar interactions are averaged to zero since the ω_Q fluctuations are so fast that the correlation time is small compared with the reciprocal of the Larmor frequency, ω_L^{-1} (case $\omega_L \times \tau_c \ll 1$ with the rotational correlation time τ_c). In contrast, sodium nuclei experience in solids nonzero averaged quadrupolar interactions ($\overline{\omega_Q} \neq 0$). In biological tissues, the sodium ions are in close contact with negatively charged macromolecules, which results in slower modulation of the ω_Q . This slower modulation is superimposed on the fast zero-averaged fluctuations, which are produced by the on-going modulations of the hydration shells of the sodium ions. Thus, the overall $\overline{\omega_Q}$ is not zero. In biological samples such a muscle tissue, the half-period of the slower fluctuation is similar to ω_L^{-1} , but still less than the $\overline{\omega_Q}^{-1}$, which leads to a spectrum with three isochronous resonances (case $\omega_L \times \tau_c \approx 1$).

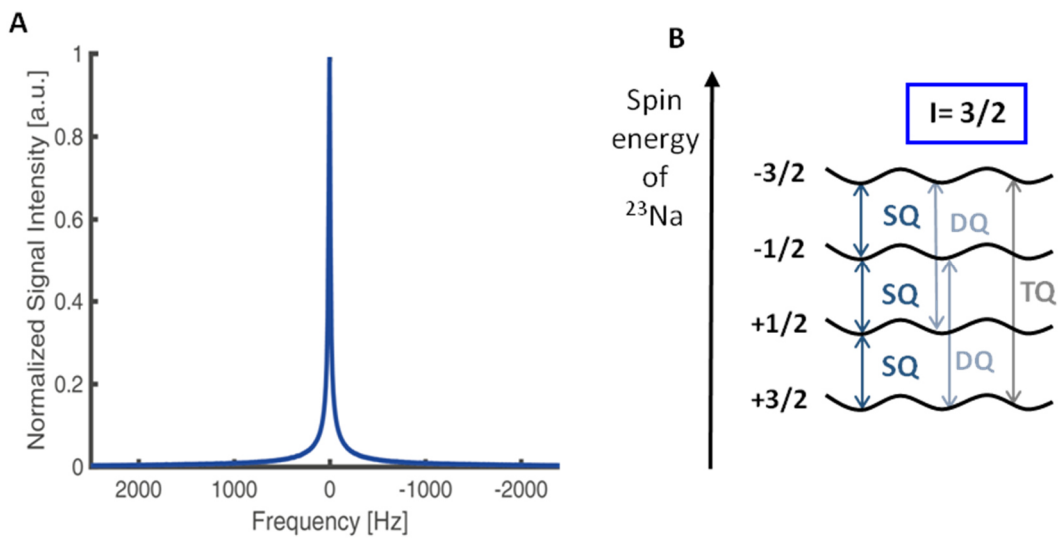


Figure 20: **A)** *In vivo* ^{23}Na spectrum from human calf: the three single quantum coherences give rise to one broad peak. **B)** Energy levels of sodium nucleus in an external magnetic field. The spin $3/2$ nuclei can undergo single ($-3/2 \leftrightarrow -1/2$, $-1/2 \leftrightarrow +1/2$, $+1/2 \leftrightarrow +3/2$), double ($-3/2 \leftrightarrow +1/2$, $-1/2 \leftrightarrow +3/2$), and triple ($-3/2 \leftrightarrow +3/2$) quantum coherences/transitions.

The central resonance is superimposed on the broader satellite resonances giving one single broad peak in the ^{23}Na *in vivo* spectrum (Figure 20A). In biological tissues, the quadrupolar interaction usually causes bi-exponential relaxation behaviour. As a result of these quadrupolar interactions, the relaxation times of ^{23}Na are extremely sensitive to the surrounding environment and are much shorter than those of ^1H [68]–[70]. As a nucleus with a spin higher than $1/2$, sodium exhibits more than one allowed transition between Zeeman split energy levels. It can undergo single, double, and triple quantum transitions/coherences as shown in Figure 20B. A single quantum coherence (SQC) corresponds to a change of quantum state of $\Delta m = \pm 1$. Double quantum coherence (DQC) and triple quantum coherence (TQC) refer to the quantum spin state that changes

by $\Delta m = \pm 2$ or $\Delta m = \pm 3$, respectively. While only SQCs are observable relating to the transverse magnetization, the DQC and TQC are generally not observable.

As ^{23}Na has four nuclear spin states (energy levels), three single quantum transitions are possible with the relative contributions of 3:4:3. The corresponding energy levels and relaxation rates depend on the motional regime of the system and therefore on the nature of the molecular environment. If the quadrupolar nucleus is in a spatially homogeneous system such as in a fluid, it can tumble very fast and the three transitions have the same resonance frequency, which results in a single mono-exponential T_2 and T_1 relaxation. However, if the sodium nucleus is in biological tissue, static and dynamic quadrupolar effects slow down the tumbling motion. Thus, the two outer transitions ($-3/2 \leftrightarrow -1/2$ and $+1/2 \leftrightarrow +3/2$) relax faster than the inner transition ($-1/2 \leftrightarrow +1/2$) leading to bi-exponential relaxation. In this case ($\omega_L \times \tau_c \approx 1$), the bi-exponential relaxation behaviour is described with short and long relaxation times [69], [71]:

$$M_z(t) = M_0 \left(1 - 0.2 e^{-\frac{t}{T_{1s}}} - 0.8 e^{-\frac{t}{T_{1l}}} \right)$$

$$M_{xy}(t) = M_{xy}(0) \left(0.6 e^{-\frac{t}{T_{2s}}} + 0.4 e^{-\frac{t}{T_{2l}}} \right)$$

Where T_{1s} and T_{1l} are the short and long longitudinal relaxation times, and T_{2s} and T_{2l} the short and long transverse relaxation time values. In biological tissues, the transverse magnetization decays with a short T_2 of about 0.5 to 3 ms and a longer T_2 of about 15 to 30 ms [70]. Since usually mono- and bi-exponential pools exist, the short/long component contribution can deviate from the 3:2 ratio of relative T_2 contribution. Conversely, only a mono-exponential T_1 is measured in practice due to the small short fraction of T_{1s} and closer relaxation values of T_{1s} and T_{1l} . A change in the interaction between sodium nucleus and its environment can be observed in altered relaxation times and in the relative contributions of the mono-exponential and bi-exponential pools [64], [69], [72].

3.3.2 Quantification of the total sodium content

To quantify the total sodium concentration (TSC) of biological tissue, the signal intensity of the tissue is compared to the signal of an externally placed calibration standard of known Na^+ concentration. This strategy relies on the linearity between signal and concentration. However, the fast decay of the short T_2 in biological tissue introduces a bias if data acquisition is run with an echo time (TE) that is relatively long compared to the short T_2 . This is because the short T_2 accounts for 60 % of the total ^{23}Na signal. Standard sequences fully sample the k-space on a Cartesian grid, which leads to relatively long TEs. Normally these TEs are longer than the ^{23}Na T_{2s} causing signal loss. Boada *et al.* [73] measured errors *in vivo* larger than 20 % in the TSC if the TE was longer than 2 ms.

This bias can be partially overcome by the application of ultra-short echo time (UTE) sequences that use echo times below 0.5 ms. The reduction of the TE can be achieved by different k-space sampling schemes such as sampling on centre-out radial lines (4.6.3). However, TSC might not be sufficient to monitor Na⁺ homeostasis *in vivo* due to a lack of differentiation between the extra- and intracellular Na⁺. The next section of this chapter explains the three methods to selectively gain information about the “intracellular” sodium with a focus on multiple quantum filters.

3.3.3 NMR techniques to probe sodium in different compartments

Sodium alterations in the intra- and extracellular compartments can be probed using shift reagents, inversion recovery sequences, and multiple quantum filters. Paramagnetic compounds, so-called shift reagents (SR), can induce frequency shifts of a nuclear spin. Several SR have been proven to not cross the cell membrane and thereby create a large shift in the resonance frequency of only the extracellular sodium [74]. These SR studies used injections of anionic complexes of Dy(PPP_i)₂⁷⁻ [75], Dy(TTHA)³⁻ [76]–[78], and Tm(DOTP)⁵⁻ [79]–[82] in skeletal muscle, heart, and brain. They clearly distinguish the intra- from the extracellular sodium resonances, but due to their toxicity after decomposition, SR are only used in animal studies.

The inversion recovery (IR) technique is a non-invasive alternative for SR. This technique takes advantage of T₁ relaxation differences of the sodium nucleus in different compartments. It is based on the assumption that the T₁ relaxation time of the extracellular sodium is significantly longer than the T₁ of the intracellular sodium. An appropriate inversion time (TI) can be selected to suppress the signal from the extracellular Na⁺ pool:

$$TI = \ln\left(\frac{2}{1 + e^{-TR/T_1}}\right) \times T_1$$

The IR method, however, allows only a weighting towards intracellular sodium signal. It can still have significant contributions from the extracellular compartment, because the IR pulse does not completely eliminate the extracellular ²³Na signal due to possible differences in T₁. So far, no SR experiment has investigated the contributions of the extracellular ²³Na. To date, only IR ²³Na NMRI monitored the intracellular weighted ²³Na signal in myopathies including muscular channelopathies and DMD [14], [83] (3.4.2).

The third method for intracellular sodium analysis consists of multiple quantum filters (MQF). As discussed above, the relaxation behaviour of motionally restricted sodium ions becomes bi-exponential, which can be detected by MQF sequences [84], [85]. Thus, MQF select signal arising from Na⁺ ions of restricted movement. These filters usually consist of three RF pulses and depending on their amplitude and phases, DQC or TQC are generated [86]. However, the resulting signal is only

a small fraction of the maximum single quantum signal, thus MQF suffer from poor signal intensities.

Figure 21 shows the basic MQF pulse sequence with corresponding coherence transfer pathways.

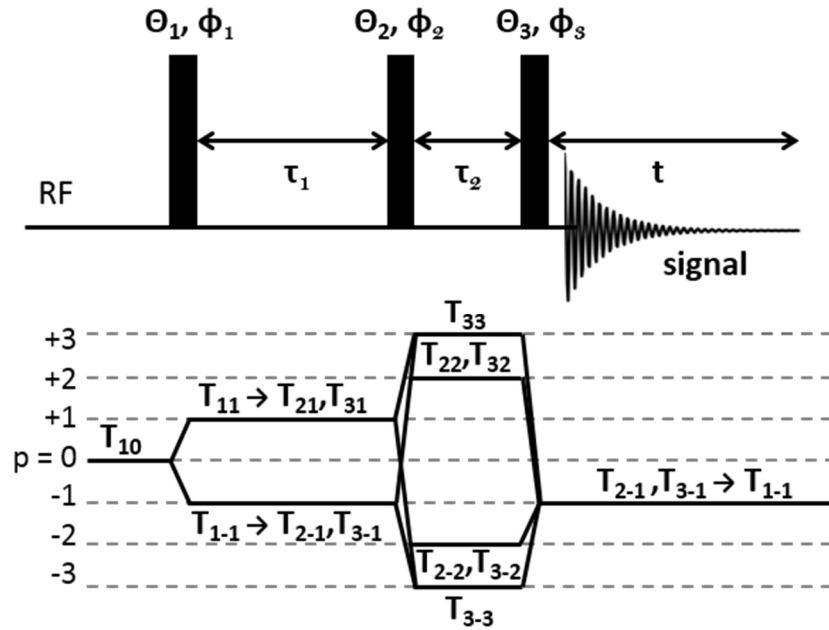


Figure 21: Schema of multiple quantum filter RF diagram with corresponding coherence order transfers and tensors $T_{l,p}$. A typical MQF sequence consists of three RF pulse of angle Θ and phase Φ . By proper phase cycling, DQC and TQC are selected and detected at the end of the third RF pulse.

Table 6: Irreducible spherical tensor operators for spin $I = 3/2$. Values taken from [70].

Irreducible spherical tensor operator	Spin 3/2	Definition
T_{00}	1	Identity
T_{10}	I_z	Longitudinal magnetization
$T_{1\pm 1}$	$\pm \frac{1}{\sqrt{2}} I_{\pm}$	Rank 1 single quantum coherence
T_{20}	$\frac{1}{\sqrt{6}} (3I_z^2 - I(I+1))$	Quadrupolar magnetization
$T_{2\pm 1}$	$\pm \frac{1}{2} [I_z, I_{\pm}]_+$	Rank 2 single quantum coherence
$T_{2\pm 2}$	$\frac{1}{2} I_{\pm}^2$	Rank 2 double quantum coherence
T_{30}	$\frac{1}{\sqrt{10}} (5 I_z^3 - (3I(I+1)-1) I_z)$	Octopolar magnetization
$T_{3\pm 1}$	$\pm \frac{1}{4} \sqrt{\frac{3}{10}} [5 I_z^3 - I(I+1) - \frac{1}{2} I_{\pm}]_+$	Rank 3 single quantum coherence
$T_{3\pm 2}$	$\frac{\sqrt{3}}{4} [I_z, I_{\pm}^2]_+$	Rank 3 double quantum coherence
$T_{3\pm 3}$	$\pm \frac{1}{2\sqrt{2}} I_{\pm}^3$	Rank 3 triple quantum coherence

A commonly used formalism to describe the complex processes during MQF sequences is based on the irreducible spherical tensor operator basis T_{1p} where l denotes the rank and p the order (or coherence) of the tensor with $abs(p) \leq l$. These tensors are defined by the spin operators I_z and $I_{\pm} = I_x \pm i I_y$ representing the spin angular momentum components along the three Cartesian axes. Table 6 lists the irreducible spherical tensor operators used to describe the density operator for spin of 3/2 (operator describing quantum state of entire sampl/system) [65].

In general, the signal intensity in a MQF experiment is the sum of all contributions of all possible coherence transfer pathways. All coherence pathways start at $p = 0$ and end at the detectable $p = -1$. Each coherence pathway can be described by its quantum numbers p and l (Figure 21). In the following theoretical analysis, the evolution of the tensor operator T_{1p} under the influence of RF pulses and transverse relaxation is discussed under on-resonance condition (no B_0 inhomogeneities). The signal intensity for a spin of quantum number l after the filter is a superposition of the signals from different coherence pathways $S_{l,p}(t)$ and depends on the preparation time τ_1 and evolution time τ_2 , the receiver phase Ψ , the RF pulse phases ϕ_1, ϕ_2, ϕ_3 , and the flip angle of the RF pulses $\theta_1, \theta_2, \theta_3$. The recorded signal is generally given by a sum of complex signals with amplitudes A and phases Ψ [87]:

$$S(t) = \sum_{l=0}^{2l} \sum_{p=-l}^l S_{l,p}(t) = \sum_{l=0}^{2l} \sum_{p=-l}^l e^{-i\psi_{l,p}} A_{l,p}$$

The phase factor $\psi_{l,p}$ consist of contributions of the RF pulses and receiver phases as well as phases accumulated during the preparation and evolution time:

$$\psi_{l,p} = \psi_{l,p}(\tau_1, \tau_2, \phi_1, \phi_2, \phi_3, \Psi) = \Phi_{l,p}(\phi_1, \phi_2, \phi_3, \Psi) + \Delta_{l,p}(\tau_1, \tau_2)$$

The amplitude $A_{l,p} = A_{l,p}(\tau_1, \tau_2, \theta_1, \theta_2, \theta_3, t)$ of the coherence pathways consist of contributions of the RF pulses that can be calculated via the Wigner rotation matrix elements $d_{p',p}^l$ and relaxation functions $f_{p',p}^l(t)$ during preparation, evolution, and acquisition time t .

Using to the tensor operator T_{1p} formalism, two rules help to understand the different events taking place during the MQF sequence. First, a non-selective RF pulse changes the coherence p only within the limits of $|p| \leq l$. Second, the rank l changes solely due to relaxation and modulation by quadrupolar, dipolar, or J-coupling, conserving the current coherence value p [88]. J-coupling refers to the indirect spin-spin coupling over bonding electrons that is independent of the applied magnetic field (see [65] or [64] for a detailed explanation). Thus, the general evolution of the tensor operator under an RF pulse of flip angle θ and phase ϕ is given by [89]:

$$T_{lp} \xrightarrow{\theta(I_y \cos \Phi - I_x \sin \Phi)} \sum_{p'=-l}^l T_{lp} d_{p',p}^l(\theta) e^{-i \Delta p \Phi}$$

Where p' is the new coherence order, $\Delta p = p' - p$ the change of order under the influence of the pulse. Note that the rank of the tensor remains unchanged. The Wigner rotation matrix elements $d_{p',p}^l$ are listed in [90]. The first RF pulse of angle θ_1 and phase ϕ_1 flips the longitudinal magnetization T_{10} into the transverse plane resulting in a transverse magnetization $T_{1\pm 1}$. The tensor operator T_{lp} further changes under the influence of quadrupolar relaxation, which changes the rank but conserves the order. SQC with different ranks ($T_{2\pm 1}$, $T_{3\pm 1}$) evolve during the so-called preparation time τ_1 . The evolution of $T_{1,1}$ under the influence of transverse relaxation and residual quadrupolar interaction (RQI) during τ_1 is given as [91]:

$$T_{11} \xrightarrow{\text{Relaxation} + \text{RQI}} f_{1,1}^1(t) T_{11} + f_{2,1}^1(t) T_{21} + f_{3,1}^1(t) T_{31} \quad [1]$$

With the relaxation functions $f_{p',p}^l(t)$:

$$f_{1,1}^1(t) = \frac{1}{5} \left[3 e^{-t/T_{2s}} \cos(\omega_Q t) + 2 e^{-t/T_{2l}} \right] \quad [2]$$

$$f_{2,1}^1(t) = f_{1,2}^1(t) = \sqrt{\frac{3}{5}} \left[e^{-t/T_{2s}} i \sin(\omega_Q t) \right] \quad [3]$$

$$f_{3,1}^1(t) = f_{1,3}^1(t) = \frac{\sqrt{6}}{5} \left[e^{-t/T_{2s}} \cos(\omega_Q t) - e^{-t/T_{2l}} \right] \quad [4]$$

Where T_{2s} and T_{2l} are the short and long T_2 , respectively, and $2\omega_Q$ the quadrupolar coupling. The relaxation functions $f_{p',p}^l(t)$ for spin-3/2 nuclei can be found in [92]. By looking at equations [1] and [3], one sees that in isotropic liquids, only odd rank tensors $T_{3\pm 1}$ are formed due the absence of RQI ($\overline{\omega_Q} = 0$). In anisotropic media, the quadrupolar coupling does not average to zero leading to the formation of an even rank tensor $T_{2\pm 1}$. A second pulse of angle θ_2 and phase ϕ_2 converts the SQC into double and triple quantum coherences ($T_{2\pm 2}$, $T_{3\pm 2}$, and $T_{3\pm 3}$). The MQCs evolve with their characteristic relaxation times during the evolution time τ_2 , which should be kept very short to prevent their decay. These coherences are then quickly read out by applying a third pulse of angle θ_3 and phase ϕ_3 to convert the DQC and TQC into SQCs $T_{2,-1}$ and $T_{3,-1}$, which evolve under relaxation or quadrupolar coupling during acquisition time t into the detectable $T_{1,-1}$ rank.

A MQF experiment is realized with a proper phase cycling scheme so that out of the 21 possible coherence pathways only the desired ones are detected. During TQF experiments, the first RF pulse creates first order coherences ($p = \pm 1$), which the second pulse converts into triple quantum coherences ($p = \pm 3$).

The selection of the coherences is done by acquiring N repetitions with different RF pulse and receiver phases. Their signals are then summed up so that the phases of the desired coherences add

up while the phases of undesired coherences cancel out one another. For TQF ($p = \pm 3$), the sequence usually consists of a six-phase cycling scheme with following flip angles and phases [93]:

$$\phi_1 = \alpha_1 + \frac{k\pi}{3}, \quad \phi_2 = \alpha_2 + \frac{k\pi}{3}, \quad \phi_3 = 0$$

$$\Psi = k\pi, k = 0, 1, 2, 3$$

Initial phases are commonly set to $\alpha_1 = 30^\circ$ and $\alpha_2 = 120^\circ$. With this cycle scheme, only four components ($l = \pm 1, p = \pm 3$) are conserved in the measured TQF signal:

$$S^{TQ}(t) = \sum_{l=-1}^1 \sum_{p=-3}^3 S_{l,p}(t) = |S_{-1,-3}^{TQ} + S_{-1,+3}^{TQ} + S_{+1,-3}^{TQ} + S_{+1,+3}^{TQ}|$$

The TQF signal can be then calculated as:

$$S^{TQ}(\theta_1, \theta_2, \theta_3, \tau_1, \tau_2, t) = f_{3,1}^1(\tau_1) f_{3,3}^3(\tau_2) f_{3,1}^1(t) F_{33}(\theta_1, \theta_2, \theta_3, \tau_1, \tau_2)$$

With the relaxation functions $f_{3,1}^1(\tau_1)$, $f_{3,3}^3(\tau_2)$, and $f_{3,1}^1(t)$, as well as the factor F_{33} . In case the evolution time τ_2 is chosen as short as possible ($\tau_2 \approx 50 \mu s$), the relaxation during the evolution time can be neglected ($f_{3,3}^3(\tau_2) \approx 1$). If the quadrupolar coupling is sufficiently strong, the relaxation functions can be simplified to:

$$f_{3,1}^1(\tau_1) f_{3,1}^1(t) \propto (\cos \omega_Q \tau_1 e^{-\tau_1/T_{2s}} - e^{-\tau_1/T_{2l}}) (\cos \omega_Q t e^{-t/T_{2s}} - e^{-t/T_{2f}})$$

The factor F_{33} depends on the flip angle ($\theta_1 = \theta_2 = \theta_3$) and includes normalization factors arising from Wigner rotation matrix elements [89]:

$$F_{33} = d_{1,0}^1(\theta) [d_{3,1}^3(\theta) + d_{3,-1}^3(\theta)]^2$$

The Wigner rotation matrix elements for double and triple quantum filtered coherence pathways are summarized in [90]:

$$d_{1,0}^1(\theta) = \frac{1}{\sqrt{2}} \sin(\theta), \quad d_{3,1}^3(\theta) = \frac{\sqrt{15}}{8} \sin^2(\theta) (1 + \cos(\theta)), \quad \text{and} \quad d_{3,-1}^3(\theta) = \frac{\sqrt{15}}{8} \sin^2(\theta) (1 - \cos(\theta))$$

Using the Wigner coefficients, the FID obtained after TQF sequence is proportional to [70]:

$$S^{TQ}(\tau_1, t, \omega_Q) \propto \frac{15}{16} \sin^5(\theta) \left(e^{-\frac{\tau_1}{T_{2l}}} - \cos(\omega_Q \tau_1) e^{-\frac{\tau_1}{T_{2s}}} \right) \left(e^{-\frac{t}{T_{2l}}} - \cos(\omega_Q t) e^{-\frac{t}{T_{2s}}} \right)$$

Where θ is the flip angle of the 2nd and 3rd RF pulse, τ_1 the preparation time, t the acquisition time, T_{2s} and T_{2l} the short and long transverse relaxation times, respectively, and ω_Q residual quadrupolar interaction frequency. Thus, the FID after TQF consists only of one term originating from T_{31} .

In biological tissues, the residual quadrupolar interaction can be greater than the fast T_2 relaxation rate (regime $\omega_Q \gg 1/T_{2f}$). In that case, two kinds of DQC are contributing to the signal: even rank ($T_{2\pm 2}$) and odd rank DQC ($T_{3\pm 2}$) (see equation [1]). For DQF ($p = \pm 2$), the commonly used parameters comprise a four-phase cycling scheme [94]:

$$\phi_1 = \phi_2 = \frac{k\pi}{2}, \phi_3 = 0$$

$$\Psi = k\pi, k = 0,1,2,3$$

With this cycle scheme, only four components ($l = \pm 1, p = \pm 2$) are conserved in the measured DQF signal:

$$S^{DQ}(t) = \sum_{l=-1}^1 \sum_{p=-2}^2 S_{l,p}(t) = |S_{-1,-2}^{DQ} + S_{-1,+2}^{DQ} + S_{+1,-2}^{DQ} + S_{+1,+2}^{DQ}|$$

The DQC signal can be then calculated with the relaxation functions and normalization factors arising from Wigner rotation matrix elements [90]:

$$S^{DQ}(\theta_1, \theta_2, \theta_3, \tau_1, \tau_2, t)$$

$$= S^{DQ,even}(\theta_1, \theta_2, \theta_3, \tau_1, \tau_2, t) + S^{DQ,odd}(\theta_1, \theta_2, \theta_3, \tau_1, \tau_2, t)$$

$$= f_{21}^1(\tau_1) f_{22}^2(\tau_2) f_{21}^1(t) F_{22}(\theta_1, \theta_2, \theta_3, \tau_1, \tau_2)$$

$$+ f_{31}^1(\tau_1) f_{23}^2(\tau_2) f_{31}^1(t) F_{32}(\theta_1, \theta_2, \theta_3, \tau_1, \tau_2)$$

Thus, the FID obtained after DQF sequence is proportional to (again assuming $f_{2,3}^2(\tau_2) \approx 1$, $f_{2,2}^2(\tau_2) \approx 1$ and sufficiently strong quadrupolar coupling) [95]:

$$S^{DQ}(\tau_1, t, \omega_Q) \propto -\frac{3}{2} \sin^3(\theta) \sin(\omega_Q \tau_1) e^{-\frac{\tau_1}{T_{2s}}} \sin(\omega_Q t) e^{-\frac{t}{T_{2s}}}$$

$$+ \frac{3}{8} \sin^3(\theta) (3 \cos^2 \theta - 1)^2 \left(e^{-\frac{\tau_1}{T_{21}}} - \cos(\omega_Q \tau_1) e^{-\frac{\tau_1}{T_{2s}}} \right) \left(e^{-\frac{t}{T_{2s}}} - \cos(\omega_Q t) e^{-\frac{t}{T_{2s}}} \right)$$

The observed decay is thus a sum of two terms: the first term represents the formation of second rank tensor $T_{2,-1}$ and the second term results from the third rank tensor $T_{3,-1}$. For isotropic solutions ($\overline{\omega_Q} = 0$), the term for the $T_{2,-1}$ tensor disappears.

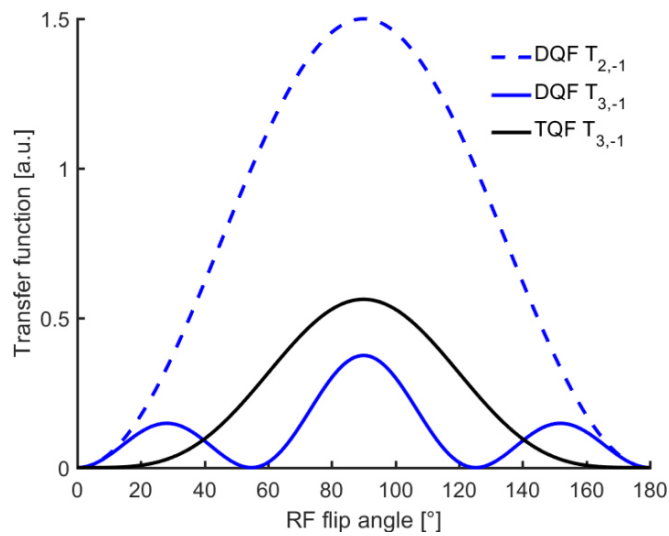


Figure 22: Dependency of the transfer functions of second rank tensor $T_{2,-1}$ for DQF and of third rank tensor $T_{3,-1}$ for DQF and TQF on the flip angle in MQF experiments. At the magic angle (54.7°) only the contribution of $T_{2,-1}$ is detected by the DQF.

Figure 22 demonstrates the effect of the flip angle (FA) on the double and triple quantum coherences using the transfer functions of T_{2-1} and of T_{3-1} for the DQF ($\frac{3}{2} \sin^2(\theta)$ and $\frac{3}{8} \sin^2(\theta) (3 \cos^2 \theta - 1)^2$, respectively) and the transfer function T_{3-1} for the TQF ($\frac{9}{16} \sin^4(\theta)$). In the case of RQI and $\theta_1 = 90^\circ$ and $\theta_2 = \theta_3 = 54.7^\circ$ (known as the magic angle), the DQF comprises only of the $T_{2\pm 1}$ term that originates from molecules experiencing anisotropic motion [91]. Thus, DQF spectra with a magic angle (DQF-MA) give an indication of order in the tissue or in other words, they represent sodium ions in anisotropic motion due to their binding to ordered structures [95].

While performing MQF experiments, one has to choose carefully the parameters. MQF signal intensities are highly dependent on the preparation time. Each tissue has a characteristic preparation time resulting in maximum signal intensity. For TQF sequences, the preparation time τ_1 can be optimized as in [84] to maximize the signal using the short and long relaxation components:

$$\tau_{1,opt}^{TQF} = \frac{\ln\left(\frac{T_{2l}}{T_{2s}}\right)}{\frac{1}{T_{2s}} - \frac{1}{T_{2l}}}$$

The optimal evolution time can be also evaluated empirically by stepwise increasing τ_1 for a series of acquisitions. For DQF-MA sequences, the optimum preparation time can be calculated using the strength of quadrupolar coupling and the short relaxation component [96]:

$$\tau_{1,opt}^{DQF-MA} = \frac{1}{\omega_Q} \tan^{-1}(\omega_Q T_{2s})$$

Several research groups have demonstrated that MQF methods can be used to study tissue samples including tumour growth in brain, liver damage, spinal disc, and myocardial infarction [97]–[101]. However, one big drawback of MQF remains their sensibility to magnetic field inhomogeneity. In the presence of B_0 offsets, signal loss occurs because of destructive interference between the different coherence pathways contributing to the MQF signal. Thus, B_0 and B_1 field variations across the volumes sample have been proven to introduce a significant bias and lead to unwanted signal loss [102], [87], [103]. Nowadays, TQF is preferred over the DQF, because it has a theoretical 50 % larger signal amplitude [84], [89]. Several methods have been develop based on TQF to increase the poor SNR in still moderate acquisition times and compensate the B_0 inhomogeneity sensitivity [104]–[106]. For example, an extra 180° RF pulse can be applied after the first RF pulse at $t = \tau_1/2$ to refocus the spin in presence of prominent magnetic field inhomogeneity [88]. Also a combination of SQF and TQF method named SISTINA (Simultaneous Single quantum and Triple quantum NMR Imaging of ^{23}Na) has been developed in an interleaved fashion to allow simultaneous acquisition of TQF and TSC weighted images providing more information for analysis of pathologies [107].

Finally, the motivation behind the application of MQF remains the separation of the signals from different compartments (intra- vs. extracellular sodium pool). SR experiments investigated the contribution of the extracellular Na^+ to the MQF signal. The proportion of TQF signal arising from the extracellular sodium pool was between 30 to 60 % depending on the experimental set-up [108]–[111]. Nevertheless, the TQF signal possesses a linear correlation with $[\text{Na}_i]$ [109], which suggest the TQF as a non-invasive tool to monitor intracellular sodium alterations. The *ex vivo* DQF signal shows also dominant contribution from the extracellular sodium pool during SR experiments with FA of 90° [112]. If the FA was set to the magic angle, the *ex vivo* DQF-MA spectrum acquired with SR showed exclusively extracellular sodium in the perfused mouse heart [110].

3.4 Applications of NMR in the dystrophic skeletal muscle

In the 1980s, Murphy and his colleagues [113] analysed for the first time systematically several muscle disorders including DMD, LGMD, FSHD, and poliomyelitis by NMRI. They were able to see common patterns of muscle abnormalities including changes in the muscle size and muscle replacement by fat. Since then, different NMR methods have been increasingly utilised to evaluate the disease processes in dystrophic muscles. The following section highlights the use of NMR as outcome measure (3.4.1) followed by initial ^{23}Na NMR studies on muscular dystrophies (3.4.2).

3.4.1 NMR-based outcome measures in the dystrophic skeletal muscle

Dystrophic muscles suffer from important fatty infiltration since fatty tissue replaces progressively the muscle tissue. Either chemical shift based imaging methods (Dixon) or single-voxel ^1H spectroscopy can be used to quantify lipid concentrations of muscular dystrophy patients (4.2) [12], [114]–[123]. Regardless of the used method, intramuscular lipid fractions in DMD patients are higher than in the healthy control group while the fraction increases in a sigmoidal fashion with age of the patient [116], [124]–[126] (Figure 23). In the quadriceps, the mean fat fraction (FF) increased by an average of 5 % per year starting from an age between three and four years, whereas a cut-off value for mean FF of 50 % predicted loss of ambulation [123]. In the forearms, non-ambulant DMD patients showed a much faster progression of fatty infiltration when compared to ambulant DMD patients [121], [125]. On a one-year corticosteroids treatment, the fatty infiltration progression was significantly slowed down for young boys (aged 5 - 6.9 years) [12]. These studies demonstrated the drawback of high inter- and intra-individual variability of the disease progression. The different onset and non-linear progression of the disease necessitate additional prognostic indices based on other measures than fat fraction determination.

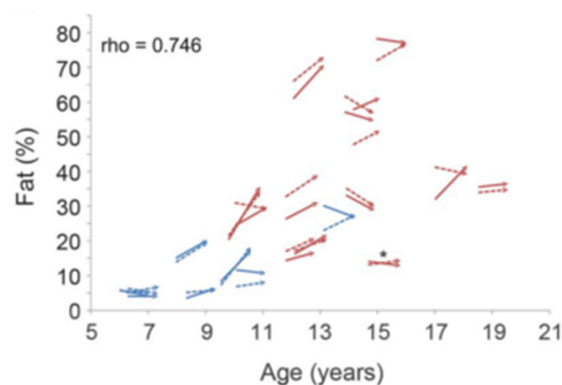


Figure 23: Dixon-based fat fraction plotted against the age at baseline and one-year follow up. The FF in the upper limb correlated with age. Ambulatory patients are represented in blue, non-ambulant in red. Adapted from [125].

The second frequently used quantitative approach to study muscular structure and compositions is T_2 mapping (4.4) [127]. Elevated water T_2 values, commonly interpreted as an

indicator of disease activity, observed in dystrophic skeletal muscles are linked to a variety of non-specific events like oedema, inflammation, or necrosis that precede the actual muscle replacement by fat. Although, there is a big effort to establish T_2 as an outcome measure in trials, so far no consensus exists regarding the T_2 measurement method. Studies report different number of echoes and TEs. Most importantly, the T_2 decay is mainly fitted to a mono-exponential model resulting in a global T_2 . However, the presence of fat in chronically affected muscle complicates the fitting approach: since fat possesses a much longer transverse relaxation time than tissue water, a mono-exponential fit of non-fat-suppressed signal decays result in a global T_2 reflecting predominantly the degree of fat infiltration [115], [128]–[130]. The global T_2 increases with age in muscles of DMD boys due to the increased fat fraction [115], [126]. This bias masks possible underlying alterations in muscle water T_2 . Thus, more sophisticated models for water T_2 measurement have been proposed taking into account the prominent fat infiltration in the dystrophic muscle tissue [131]. Various multi-exponential models can be used to fit the signal decay with at least two components (fat and water). A tri-exponential model with two components for fat and one for water was previously introduced [16]. Other models do not rely on exponential curves but instead use exact trajectories of spin echoes and stimulated echoes to represent the evolution of the magnetization signal during the multi-echo experiment. The EPG formalism has been proposed to model the T_2 relaxometry [132]. By assuming a multi-component model representing fat and water in muscle tissue, a water T_2 can be estimated [15].

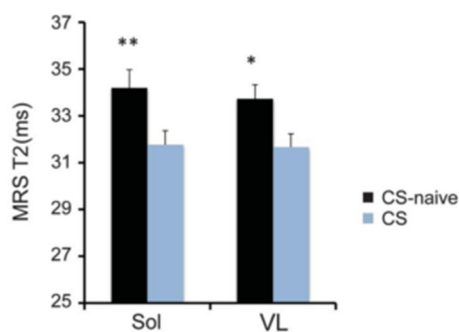


Figure 24: ^1H NMRS based water T_2 values for the soleus and vastus lateralis muscles were lower in CS boys compared to CS-naïve boys. CS corticosteroid treatment. Adapted from [12].

In DMD patients, the water T_2 was always elevated compared to healthy boys but decreased with age [115], [121]. The muscle water T_2 was however not abnormally elevated in the less severe form BMD [133]. In the upper arm of ambulatory and non-ambulatory boys, the water T_2 values also correlated with functional tests [125]. Finally, DMD patients on corticosteroid treatment demonstrated lower muscle water T_2 than DMD boys without corticosteroids suggesting decreased inflammation/muscle damage [12] (Figure 24). These water T_2 values seemed even to be too sensitive to the therapeutic effects of steroid treatment since they almost dropped to values of

healthy subjects. This could hamper the detection of beneficial effects of any additional intervention in patients that are routinely treated with steroids.

Besides the structural changes, dystrophic muscles show also metabolic changes that can be assessed by NMRS. It is considered that metabolic and subcellular changes occur even before structural changes such as fatty infiltration and fibrosis. Therefore, metabolic alterations could serve as a valuable biomarker in muscle diseases. Metabolic ratios obtained by ^1H spectroscopy were decreased in patients with DMD when compared with controls [134]. The reduced trimethylammonium/water ratio might be related to loss of muscle mass. The reduced total creatine/water ratio suggests an abnormality in membrane and energy metabolism. ^{31}P NMRS has been applied to measure the concentration of phosphorylated metabolites and intracellular pH in the sarcoplasm of muscles at rest and during and after exercise. Wokke *et al.* [53] published recently a significantly elevated PDE (phosphodiester)/ATP ratio detected by ^{31}P NMRS in BMD prior to any fat infiltration (Figure 25). Elevated PDE/ATP levels could indicate membrane anomalies more precisely an increase in the turnover of membrane phospholipids. Their findings evoke that PDE/ATP ratios assessed by ^{31}P NMRS could be a useful parameter to monitor the muscle membrane damage in early state of disease and before structural changes occur.

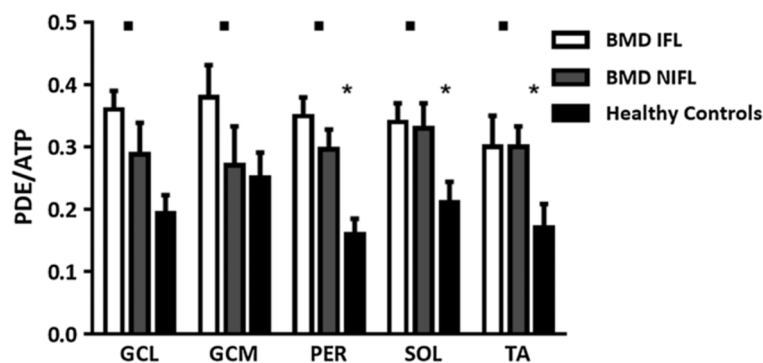


Figure 25: PDE/ATP ratios are increased in leg muscles in BMD patients with non-increased fat levels (NIFL) and increased fat levels (IFL) compared to healthy controls. * significantly higher PDE/ATP in BMD NIFL compared to controls. ■ significantly higher PDE/ATP in BMD IFL compared to controls. GCL gastrocnemius lateralis, GCM, gastrocnemius medialis, PER, peroneus, SOL soleus, and TA tibialis anterior [53].

Compared to healthy controls, DMD patients also showed higher pH, Pi (inorganic phosphorus)/PCr (phosphocreatine) ratios, and PDE/ATP ratios in leg muscles indicating anomalies in energy and phospholipid metabolism [124], [135]. In dystrophic muscle, increases in the pH could be used as a marker of the membrane leakiness and the impairment of ionic intracellular homeostasis. Reduced PCr/ATP levels could indicate a loss of metabolic activity/contractile tissue. In the forearm of DMD patients, metabolic and pH anomalies were present at early age and the slope of degeneration in metabolic ratios increased several fold after loss of ambulation [121]. Another study with female carriers of DMD or BMD revealed a higher Pi/PCr ratio during exercise and a lower post-

exercise recovery of PCr/Pi ratio indicating impairments in muscle energy metabolism not only in the patients but also in female carriers who live a normal life [136]. Elevated Pi/PCr ratios indicating higher ADP levels relate to a dysregulation of the mitochondrial oxidative phosphorylation control or unusual energy demand to preserve the ionic homeostasis. A recently published study investigated the origin of the alkaline pH in DMD by comparing the chemical shift of carnosine in the ^1H spectrum with the chemical shift of the Pi in the ^{31}P spectrum [137]. The pH based on ^{31}P was increased whereas the pH based on ^1H was not systematically increased in DMD compared to controls (Figure 26). They concluded that in the group where both pH values were increased, the alkaline change originated from the intracellular compartment reflecting ionic dysregulation. For the second group with normal intracellular pH (normal ^1H -based pH), the increased ^{31}P pH might, as suggested by the authors, reflect an expansion of the interstitial volume fraction that is often seen during fibrotic changes.

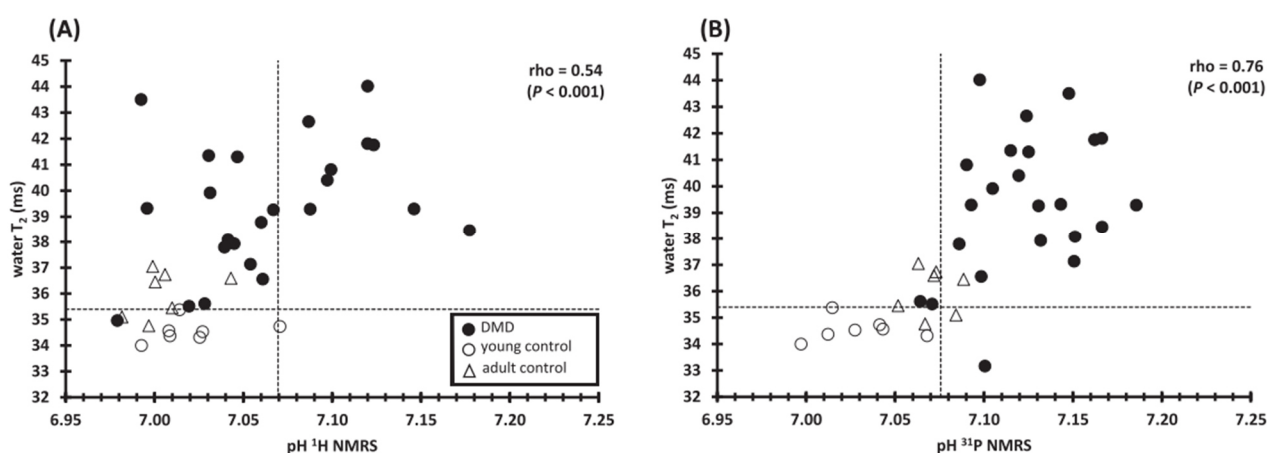


Figure 26: Correlations between the water T_2 and ^1H -based pH (A) or the ^{31}P -based pH (B). A group of DMD patients had normal ^1H -measured pH values but elevated ^{31}P -based pH and increased water T_2 cut-off value: mean value plus two standard deviation in young healthy group [137].

Although the majority of quantitative NMR studies focuses on DMD/BMD among muscular dystrophies, others studies investigated the fat infiltration and/or metabolic changes in more rare MD including LGMD 2I [138], [139] and FSHD [140]–[142]. Finally, a multicentre longitudinal study with more than 100 DMD patients proved the feasibility of implementing a standardized protocol to establish the sensitivity of NMR biomarkers including global T_2 mapping and fat quantification across multiple vendor platforms [126]. Alterations in the FF, water T_2 , and metabolic ratios as shown in these studies proved that NMR could be a powerful outcome measure for clinical trials. However, a predictive and sensitive NMR outcome measure, which is more specific to physiological or biochemical changes at early disease evolution, still has to be established. In this manner, ^{23}Na NMR could track appearing alterations in the ion distribution that precede any macroscopic degenerative changes in muscle tissue. Thus, ^{23}Na NMR presents itself as a promising tool for an early evaluation of muscle dystrophies.

3.4.2 ^{23}Na NMR research in muscle dystrophies

Since ^{23}Na NMR is still a research tool and not widely used in clinics, only few studies investigated the sodium homeostasis in MDs by ^{23}Na NMR. In 2000, Constantinides *et al.* [143] reported an up to 70 % increase of the sodium signal intensity in affected muscles of myotonic dystrophy patients when compared with unaffected muscle groups (Figure 27). These results were in line with a previous ^{23}Na TQF spectroscopy study of myotonic dystrophy patients, which quantified the disease progression by measuring Na^+ /water ratio and ^{23}Na T_2 relaxation times [144]. The total sodium levels in the patients increased by up to two fold when compared to healthy subjects. Both the Na^+ /water ratio and the sodium short T_2 tended to increase as the disease progresses indicating a correlation between ^{23}Na NMR parameters and disease severity.

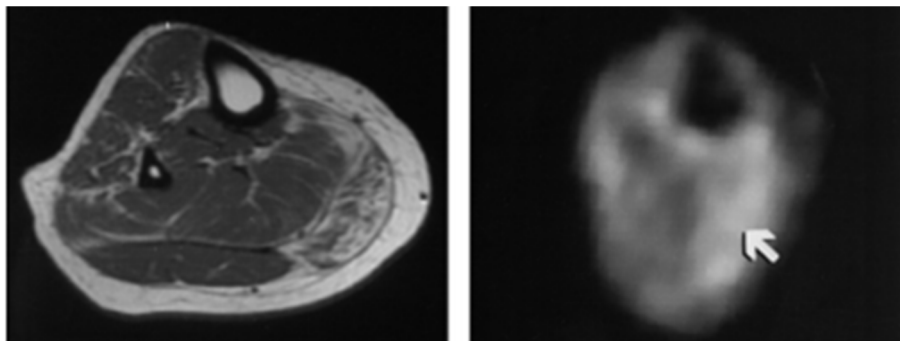


Figure 27: ^1H (left) and ^{23}Na NMR (right) image of a patient with myotonic dystrophy. Significant elevations in normalized ^{23}Na signal intensities were measured in the patient (up to 70 % compared to not affected side). Adapted from [143].

These initial studies suggested *in vivo* measurement of TSC and ^{23}Na relaxation behaviour as a promising tool for the study of physiological and pathophysiological processes in the skeletal muscle with possible clinical application in early disease stages. Since then, only few studies have been performed on patients with MD. Eleven patients with DMD were examined by ^1H NMRI and ^{23}Na density-adapted 3D radial NMRI sequence (see 4.6.3 for ^{23}Na sequence) [14]. DMD boys demonstrated higher muscular fat content and oedema-like changes than in volunteers. The patients furthermore demonstrated considerably increased TSC with an average of 38.4 mmol/L compared to age-matched control group with an average TSC of 25.4 mmol/L. In DMD patients, the ^{23}Na IR signal intensity was also increased to 0.77 a.u. compared with 0.50 a.u. in volunteers. The IR signal intensity and TSC were slightly higher in the older than in the younger DMD patients, whereas patients without glucocorticoid medication demonstrated higher sodium values than treated patients. Seven patients were then re-examined about seven months later with the same NMR protocol [60]. At the second visit, the ^{23}Na IR signal intensity and TSC remained constant as did the oedema-like changes and fat content. They further suggested that elevated muscular sodium concentration in DMD could cause muscle oedema, which was present in all participating DMD patients. If the oedema is mainly osmotic rather than inflammatory, diuretics could replace the glucocorticoid treatment, which

demonstrates grave adverse effects such as weight increase, osteoporosis, and cortisone-induced cardiomyopathy [145].

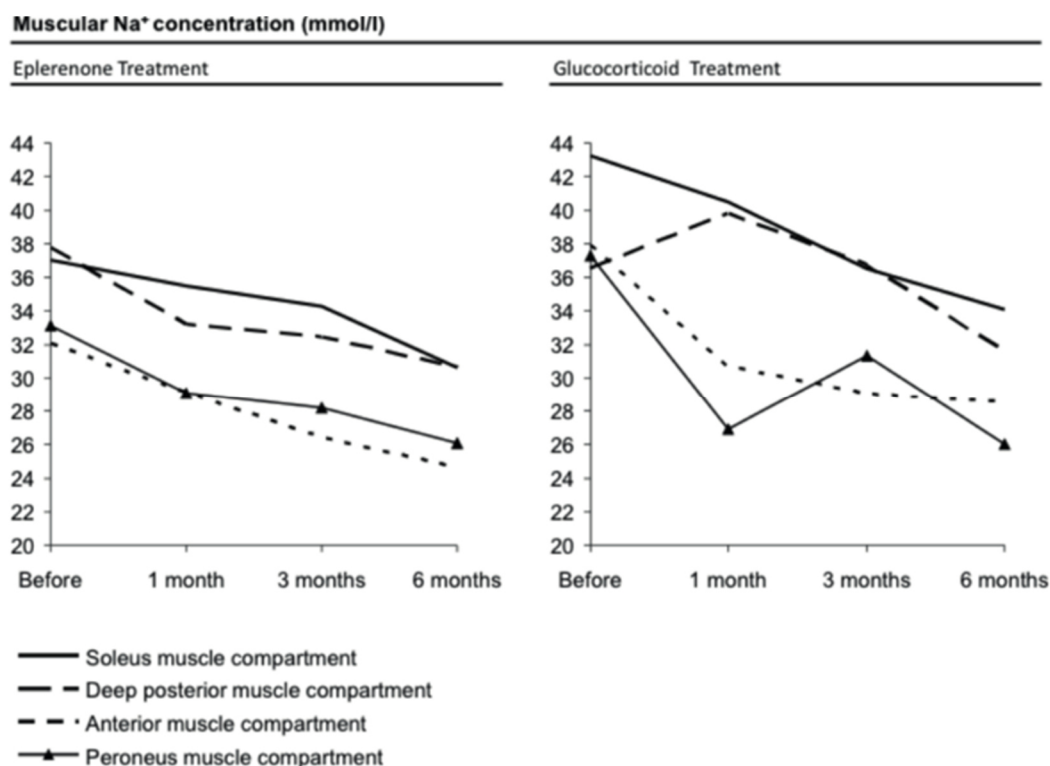


Figure 28: Temporal changes of TSC in DMD patients before and after start of treatment. While the first patient (on the left) underwent eplerenone treatment, the second patient (on the right) was under glucocorticoid treatment. Both DMD patients were seven years old. ²³Na signals were normalized using one phantom filled with 51.3 mM NaCl in 5 % agarose [145].

In a pilot study, they therefore addressed the question if the treatment of the dual overload of sodium ions and water has a beneficial effect on the dystrophic process. One DMD patient, who had so far no glucocorticoid therapy, started the treatment with eplerenone, a diuretic drug with a high repolarising power [146]. During seven months of treatment, the cytoplasmic sodium and water overload decreased slightly paralleled with increased muscle strength and mobility (Figure 28). They concluded that the diuretic treatment has a beneficial effect and oedema should be treated before the deleterious fatty degeneration takes place. In line with this observation, another two DMD boys were examined by ¹H and ²³Na NMRI, one with glucocorticoid and the other with eplerenone treatment [145]. The TSC and ²³Na IR signal intensity decreased during the six-month treatment in both treated DMD boys at roughly 20 %, whereas the fatty infiltration remained constant. The muscular water content was more reduced in the boy with eplerenone treatment. Nevertheless, the clinical abilities of both DMD patients were mostly constant. These studies confirmed that ²³Na NMRI detects the sodium overload in dystrophic muscles and could serve as a valuable tool in follow-up studies.

One of the big limitations of these initial studies are the small number of subjects. Due to the low to very low incidence of MD, patient recruitment is a lengthy and difficult task. Furthermore, clinical ^{23}Na NMR is still in its infancy. So far, these studies demonstrated only the feasibility to quantify changes of sodium homeostasis in different muscle pathologies with known sodium impairments. In general, no consistency exists as to the ^{23}Na quantification. Studies on muscle TSC quantification report different echo times and repetition times. The sodium nuclei however possess ultra-short and bi-exponential relaxation behaviour, which makes specialized (UTE) NMRI sequences for quantification necessary. Absolute TSC quantification is subjected to confounding effects of T_1 , T_2 relaxation, and B_1 inhomogeneities. Thus, tissue and reference signals require corrections for T_1 saturation and T_2 decay if not taken into account in the experimental design. Furthermore, the calibration of the signal should be standardized for reproducibility between different sides. In literature, one can find signal calibration approaches based on one to four standard phantoms with different concentrations of NaCl and with or without agarose. However, agarose phantoms mimic better the bi-exponential relaxation behaviour of skeletal muscle tissue.

Other concerns affect the origin of the signal and interpretation of the results. In patients with a significant fat infiltration, partial volume effects may lower the measured TSC, since fat tissue has lower sodium concentrations than muscle tissue. This has not yet been taken into account. Also, intra- and extracellular sodium cannot be currently unambiguously distinguished without the use of toxic shift reagents. The intracellular weighted sodium signal is commonly obtained by IR experiments in human. Nevertheless, the contribution of the extracellular ^{23}Na signal in this approach remains unclear. Another interesting contribution would be a combination of measured alterations of Na^+ levels with metabolic changes. Adding ^{31}P NMRS or ^1H NMRS to the ^{23}Na protocols could help to better understand the underlying pathophysiological changes.

^{23}Na NMR started at standard clinical field strength below 3 Tesla, but nowadays several studies have been carried out at (ultra-) high magnetic fields, which potentially offers an increased spatial resolution and faster scanning. The 3D density-adapted projection reconstruction sequence used in the DMD studies quantifies the TSC within less than ten minutes with a nominal spatial resolution of $5 \times 5 \times 5 \text{ mm}^3$ at 3T [83]. At 7T, the feasibility of performing a 3D gradient-echo radial ^{23}Na image of human skeletal muscle with a spatial resolution of $4 \times 4 \times 4 \text{ mm}^3$ has been demonstrated with an acquisition time of less than seven minutes [147]. Another group published a time-efficient interleaved ^{23}Na and ^1H imaging approach consisting of Dixon and T_2^* mapping sequences as well as TSC and ^{23}Na IR sequences [148]. Their protocol was completed within 30 minutes at 7T, which allows new promising clinical protocols within a relevant timescale. To make

this recent development of ^{23}Na NMR possible, many challenges have been tackled that are caused by the low SNR in biological tissues. Besides, ^{23}Na spectroscopy could provide a fast approach to distinguish fast and slow relaxing sodium ions if exact localization of signal is not important. Nevertheless, the main issue remains: to be successful in clinical settings, ^{23}Na NMR needs to add value by providing complementary information relating to evolution of disease or therapeutic effect.

Methods for quantitative NMR acquisitions in the skeletal muscle

This chapter introduces the NMR sequences and the corresponding postprocessing tools that have been implemented and used during the course of the thesis. After the description of the hardware (4.1), I will briefly describe ^1H imaging and spectroscopy sequences for fat fraction (4.2), global T_1 (4.3) and muscle water T_2 (4.4) quantification. Furthermore, two different approaches to measure the muscle tissue pH are explained in few words (4.5). Finally, ^{23}Na NMR spectroscopy and imaging sequences are presented to assess the sodium distribution in healthy and dystrophic skeletal muscle. A short, non-localized ^{23}Na spectroscopic protocol, which includes FID, TQF, and inversion-recovery Look-Locker (IR-LL) sequences, will be introduced in more detail (4.6.1) as well as the DQF-MA sequence (4.6.2) that was applied on healthy skeletal muscle. Then, a density-adapted 3D radial sequence is presented for fast ^{23}Na imaging of the leg (4.6.3).

4.1 Hardware

4.1.1 NMR scanners

The human NMR experiments were performed on the 3T whole-body NMR scanner (TIM TRIO; upgraded to PRISMA FIT in January 2015; SIEMENS Healthineers, Erlangen, Germany) at the Institute of Myology in Paris. Experiments in Erlangen were performed using the 3T whole-body NMR scanner (Magnetom SKYRA; SIEMENS Healthineers, Erlangen, Germany) at the Imaging Science Institute at the University Hospital Erlangen. All animal experiments were conducted using a small-animal NMR scanner (Bruker Pharma Scan 7T, bore diameter 16 cm using ParaVision Version 6) located at the Institute of Myology in Paris.

4.1.2 Coils

At 3T, ^{23}Na NMR sequences were first acquired with a homemade linear volume ^{23}Na knee coil (inner diameter 16 cm with a length of 15 cm). From 2016 onwards, ^{23}Na NMR acquisitions were performed with a new ^{23}Na knee coil showing a higher B_1 homogeneity (inner diameter 18 cm with a length of 16 cm; Stark Contrast, Erlangen, Germany). While proton acquisitions were performed with a 15-channel ^1H knee coil (SIEMENS Healthineers, Erlangen, Germany).

At 7T, a whole-body 38 mm-linear ^1H coil (Bruker, Billerica, USA) was used for the ^1H sequences as well as for anatomical reference imaging and B_0 -mapping for X-nuclei acquisitions. ^{23}Na NMR sequences were acquired with a homemade saddle-shaped ^{23}Na transceiver coil (inner

diameter 10 mm, length 10 mm). A homemade saddle-shaped ^{31}P coil with 8 mm diameter and 10 mm length was used to acquire ^{31}P spectra of the murine leg. During the murine ischemia experiments, the lower leg was scanned using a homemade saddle-shaped ^1H coil (10 mm diameter and 10 mm length).

4.2 Fat quantification

The fat content of the skeletal muscle was measured to evaluate the disease progression in dystrophic muscles. The so-called Dixon method named after its inventor was used for the clinical study on DMD patients [149]. This commonly used imaging method quantifies the fat content in skeletal muscle and relies on the chemical shift between fat and water signal. Since no Dixon method was implemented on the 7T preclinical machine, we measured the fat fraction in murine muscle by localized ^1H spectroscopy.

4.2.1 ^1H spectroscopy

^1H spectroscopy is the gold standard for fat quantification. In tissue, the ^1H NMR spectra is dominated by the water peak as the other ^1H containing metabolites have a more than 1000 fold lower concentration. Water suppression techniques like VAPOR (variable power and optimized relaxation delays) suppress completely or partially the water resonance. Figure 29 displays a water suppressed ^1H spectrum from the murine skeletal muscle with different lipid resonances. The signals between 0.8 and 2.8 ppm (Lipid $-\text{CO}-\text{CH}_2-(\text{CH}_2)_n$ and lipid $-(\text{CH}_2)_n$ and $-(\text{CH}_3)$) originate from methylene and methyl protons of triglycerides or fatty acids [150]. Downfield relatively to the water signal at 4.7 ppm, olefinic protons resonate between 5.3 and 5.7 ppm (Lipid $-\text{HC}=\text{CH}-$).

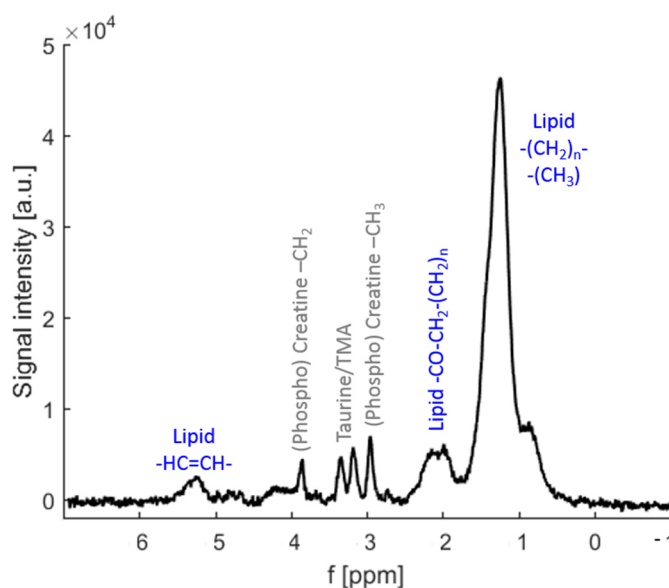


Figure 29: Typical localized *in vivo* ^1H NMR spectra from a murine skeletal muscle (acquired at 7T) with water suppression showing the different resonances originating from lipids.

In our murine experiments, two ^1H spectra were obtained: one with water peak suppression using VAPOR (variable power and optimized relaxation delays) and an unsuppressed water spectrum. The area under the curve was integrated for each of the three lipid peaks from the water suppressed spectrum. In the unsuppressed spectrum, the area under the water peak was integrated. The values of water and lipids were divided with $\text{factor}_{\text{corr}}$ to correct for T_1 relaxation effects due to the short repetition time:

$$\text{factor}_{\text{corr}} = \left(1 - e^{-\frac{TR}{T_1}}\right)$$

Where T_1 is the longitudinal relaxation time of fat and muscle (T_1 of fat 535 ms and T_1 of muscle 1684 ms, obtained at 7T from T_1 measurements) and TR the repetition time of the experiment. Fat ratios for each voxel were then calculated using the lipid and fat peaks:

$$\text{Fat ratio} = \frac{\text{Area}_{\text{Lipid 1}} + \text{Area}_{\text{Lipid 2}} + \text{Area}_{\text{Lipid 3}}}{\text{Area}_{\text{Lipid 1}} + \text{Area}_{\text{Lipid 2}} + \text{Area}_{\text{Lipid 3}} + \text{Area}_{\text{H}_2\text{O}}}$$

Where Lipid 1 corresponds to the lipid signals in the range of $\sigma = 0.8 - 1.8$, Lipid 2 to the signal in the range of $\sigma = 2 - 2.8$, and Lipid 3 to the olefinic protons ($\sigma = 5.3 - 5.7$).

4.2.2 Dixon

The Dixon method [149] relies on the chemical shift difference between water and fat that is used to generate phase differences. Originally, two gradient echo images are acquired with different TEs (2-point Dixon): one with fat and water signals in phase at the centre of the echo (IP) and another with a different TE so that the fat and water signals are out-of-phase (OP).

$$IP = W + F \quad \text{and} \quad OP = W - F$$

W and F are the signal contributions from water and fat, respectively. The sum and difference for each pixel of the in- and out-of-phase images result in a water (W) and fat image (F):

$$\frac{IP+OP}{2} = \frac{(W+F)+(W-F)}{2} = W \quad \text{and} \quad \frac{IP-OP}{2} = \frac{(W+F)-(W-F)}{2} = F$$

In off-resonance conditions, the classical the 2-point Dixon approach is prone to errors in the decomposition of F and W images. Today, several modified approaches overcome B_0 inhomogeneity-related artefacts including the 3-point Dixon that was used in our studies [151]. Images are acquired with three different echo times [151], generally in - out - in conditions, so B_0 maps can be obtained to correct water and fat signals for each pixel. The corresponding fat fraction maps (FFmap) are generated by computing the ratio between the fat signal and the sum of water and fat signal:

$$\text{FFmap} = \frac{F\text{map}}{(F\text{map} + W\text{map})}$$

Figure 30 shows the fat map (Fmap) and the water map (Wmap) with the resultant FFmap obtained in the calf of a young woman.

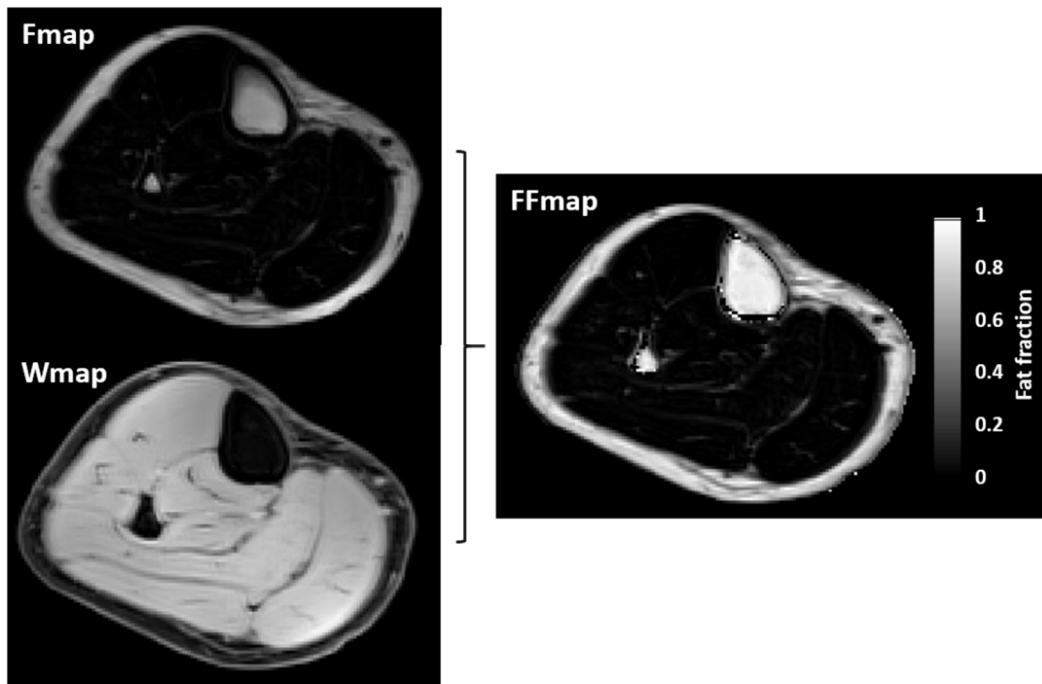


Figure 30: The fat fraction map (FFmap) are generated by computing pixel wise the ratio between the fat map (Fmap) and the sum of water map (Wmap) and fat map (Fmap) based on the 3-point Dixon approach.

4.3 Fast T_1 measurement

The muscle longitudinal relaxation time represents a fundamental tissue property that can change in the course of different pathological processes. For example, T_1 time lengthens with interstitial expansion as a result of oedema or fibrosis and shortens in the presence of fat. The spatially resolved quantification of T_1 , so called T_1 mapping, represents thus a promising tool to investigate muscle diseases. Due to the impractical long acquisition times with the gold standard inversion-recovery method [152], fast acquisition scheme have been used in our study. For the characterization of the murine dystrophic muscle, we acquired a fast spin echo sequence, namely RARE, at different repetition times.

4.3.1 Fast spin-echo sequence

The Rapid Acquisition with Relaxation Enhancement (RARE) sequence is based on multiple spin-echoes (Figure 31). Thereby, n 180° pulses are applied after every excitation RF pulse leading to n echoes. After each refocusing pulse, the echo undergoes a different amount of phase-encoding, so that each echo can be used as different line in the k-space of an image. With a RARE factor of eight, a multiple-echo sequence with eight echoes contributes eight phase-encoded lines to a single image or four phase-encoded lines if two images are acquired. This approach reduces the number of required excitations and thus also the acquisition time. However, each line has a different echo time hence T_2 weighting, which limits the acceleration that can be achieved for quantitative mapping. As a trade-

off, we acquired our images with a RARE factor of eight. Before the echo train, a saturation recovery module using a spoiler gradient of 4.2 ms duration is launched. For the T_1 mapping, we acquired 19 images with the RARE sequence with different TRs: 54.6, 100, 200, 300, 400, 500, 600, 700, 800, 1000, 1300, 1600, 2000, 2400, 2900, 3400, 4000, 5000, and 6500 ms. The total acquisition time was less than eight minutes. In each pixel, the T_1 value was then computed using a mono-exponential model:

$$S(TR) = A \left[1 - e^{-\frac{TR}{T_1}} \right]$$

Where $S(TR)$ is the signal for a given repetition time TR, T_1 the longitudinal relaxation time, and A the thermal equilibrium magnetization.

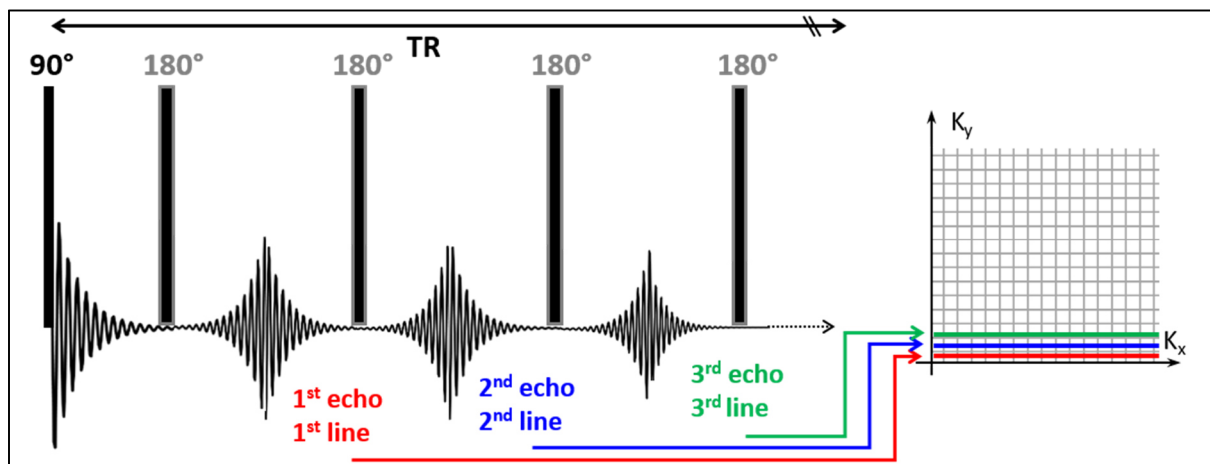


Figure 31: General diagram of the RARE sequence showing the RF-pulse sequence and sampling scheme of the k-space. The individual echoes are used to fill the lines of the k-space of a single image.

4.4 Water T_2 measurement

Elevated water T_2 values are linked to a variety of non-specific events like oedema, inflammation, or necrosis. Commonly, the T_2 decay of the signal obtained with a multi-spin echo sequence is fitted to a mono-exponential model resulting in a global T_2 . However, the presence of fat in chronically affected muscles complicates the interpretation of the extracted T_2 , because fat possesses a much longer transverse relaxation time than tissue water. Thus, mono-exponential fitting of non-fat-suppressed signal decays results in elevated global T_2 values that predominantly reflect the degree of fat infiltration in MD patients. For this reason, we used a tri-exponential model that accounts for water and fat signal to characterise the disease activity of dystrophic muscles.

4.4.1 Advanced models for water T_2 mapping

The T_2 relaxation times are commonly extracted from so-called T_2 maps. We generated water T_2 maps from a standard multi-slice multi-echo sequence (MSME). During the NMR experiment, several echoes (between 17 and 32) were recorded after the RF excitation pulse by a spin-echo train

to measure the transverse magnetization in several slices during the same TR (Figure 32). The echo amplitudes are steadily decreasing in intensity due to coherence losses between the nuclei spins of the sample representing the decay of T_2 . A theoretical model is then fitted to the resulting amplitudes of the echo train.

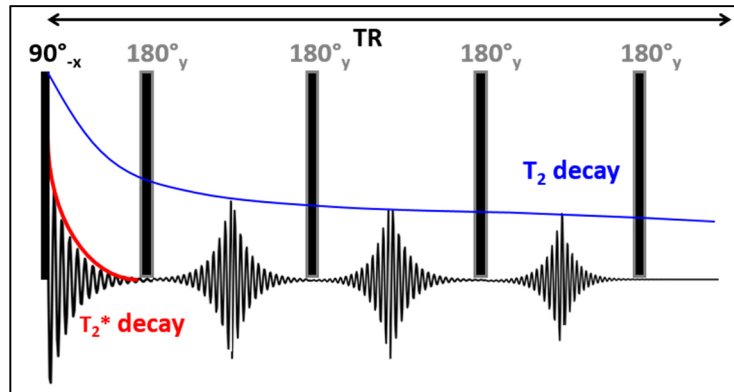


Figure 32: The spin echo pulse sequence consists of an initial 90° RF pulse followed by train of 180° RF pulses and results in multiple spin echo formations.

We computed the water T_2 value in each pixel using the tri-exponential model introduced by Azzabou *et al.* [16]. This approach determines the water T_2 since the multi-exponential model accounts for the water and fat components.

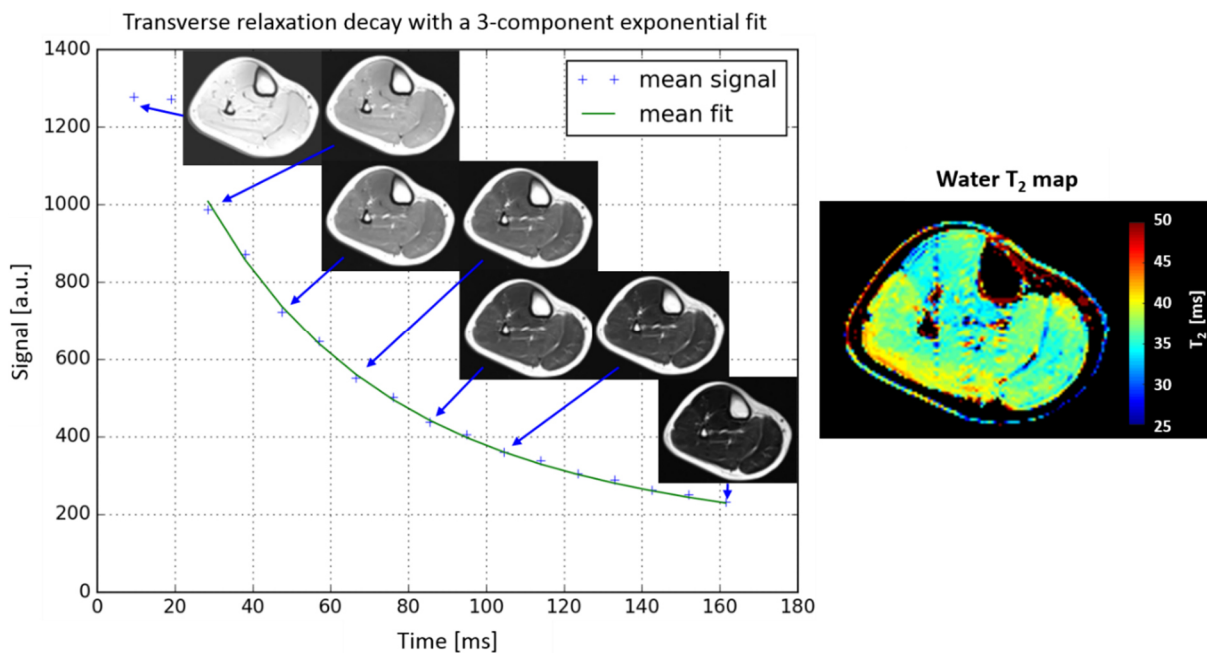


Figure 33: Plot of ^1H T_2 -decay curve of muscle tissue obtained for a healthy subject. Examples of images acquired at different echo times are assigned to the relaxation curve. The green line fitting the blue points corresponds to the tri-component exponential fit without the two first points. T_2 values are calculated pixel wise to compute the corresponding T_2 map.

Figure 33 presents one example of the ^1H T_2 decay curve fit and corresponding water T_2 maps obtained in a young woman. The signal decay is fitted with the following three-component model:

$$S(TE) = A_f \left[c_l e^{\frac{-TE}{T_{2fl}}} + c_s e^{\frac{-TE}{T_{2fs}}} \right] + A_m \left[e^{\frac{-TE}{T_{2m}}} \right]$$

Where $S(TE)$ is the signal for a given echo time TE . T_{2fl} and T_{2fs} are the long and short T_2 times of the two fat components, respectively. T_{2m} is the T_2 of the muscle water component. A_f and A_m are the two coefficients reflecting the proportion of fat component and muscle water in the signal, respectively. c_l and c_s are coefficients of the bi-exponential model of fat. The choice of a bi-exponential model for the fat signal was due to better fitting results than with a mono-exponential model, thus had no physiological reasons. The fat parameters were fixed to $T_{2fl} = 544$ ms and $T_{2fs} = 81$ ms, $c_l = 0.33$ and $c_s = 0.67$, according to previous measures on the subcutaneous fat of healthy volunteers. The parameters T_{2m} , A_f and A_m are computed excluding the first two echoes to minimize the impact from stimulated echoes. Additionally, fat fraction maps can be calculated as the ratio between the fat proton density and the sum of the water and fat proton densities:

$$FF = \frac{A_f(c_l + c_s)}{A_f(c_l + c_s) + 1.8 A_m}$$

The water signal was corrected with a factor of 1.8 for multi-slice acquisitions to take into account the magnetization transfer process [16].

4.4.2 Multi-component water T_2 relaxation evaluation using ISIS-CPMG

Changes in the water T_2 value as obtained from the above-described water T_2 maps are non-specific and reflect overall (patho-) physiological alterations in any anatomical compartment. A combination of the basic spectroscopic CPMG sequence with volume selection techniques permits an evaluation of multi- T_2 relaxation behaviour of tissue water. Studies based on such techniques have already demonstrated a multi-exponential behaviour of T_2 relaxation in skeletal muscle [153]–[155]. In tissue, we would expect water molecules in at least two different environments. On one hand, “bound” water, which is in strong electrostatic dipole-dipole interactions with macromolecules, shows increased correlations times due to the restricted movement. On the other hand, “free” water, which can be found in the so-called bulk aqueous phase, is far enough from the these macromolecules leading to hydrogen bonding characteristics closer to pure water. Proton exchanges between bound and bulk water pools could then affect the entire tissue relaxation characteristic. Indeed, several studies observed three different fractions in the spin-echo decay of tissue water protons [153], [156]–[158]; one “short” component ($T_2 < 10$ ms with a fraction of less than 15 %), an “intermediate” component (T_2 between 20 and 50 ms with a fraction around than 80 to 90 %), and a “long” component ($T_2 > 100$ ms with a fraction of less than 15 %). While the short component is commonly attributed to “bound” water, the intermediate and long components correspond to the bulk water pool. During the course of this work, the multi- T_2 relaxation of skeletal muscle tissue was characterized using the ISIS-CPMG method that was implemented by Araujo *et al.* at the Institute of

Myology [17]. With this method, we can gain insight in the water distribution within muscle tissue (intracellular, interstitial, and vascular compartment).

Figure 34 shows the RF pulse diagram of the CPMG sequence with a preceding ISIS localization module. In order to assure a complete selection of a volume of interest, the sequence has to be repeated eight times while three orthogonal slices of the ISIS module are selectively inverted. In the first loop, no inversion occurs, then from loop two to four, the three orthogonal slices are inverted, one by one (Acqu 2, Acqu 3 and Acqu 4). In loop five to seven, two of the three orthogonal slices are inverted per acquisition loop, varying the selected duo of slices (Acqu 6 and Acqu 7) and finally, all three orthogonal slices are inverted in loop 8 (Acqu 8). In each loop, a CPMG pulse train is launched just after the ISIS localization and fat-suppression module.

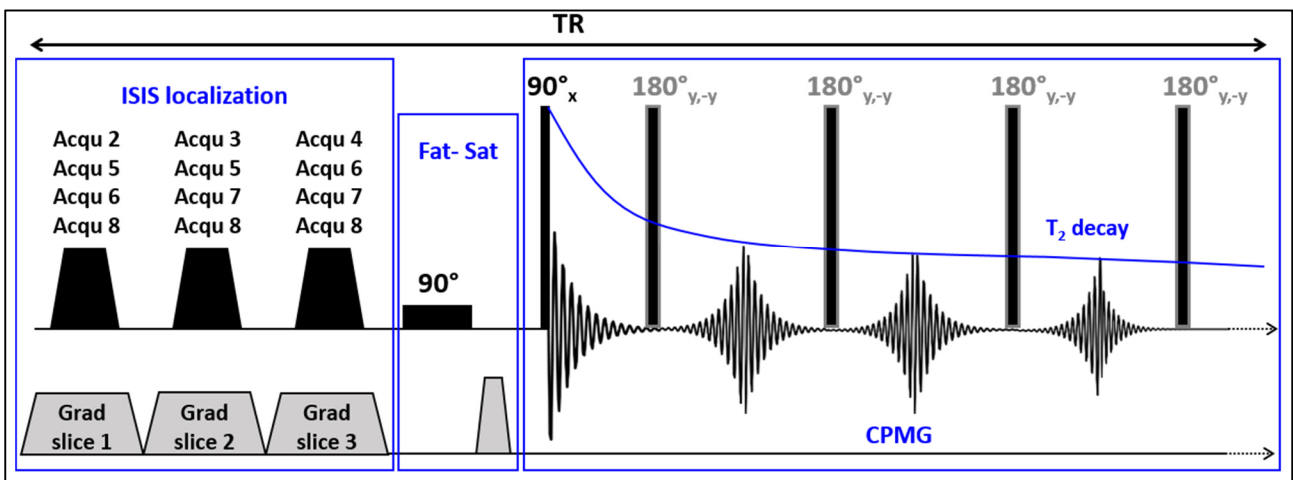


Figure 34: General diagram of the ISIS-CPMG method showing the RF-pulse sequence and slice-selecting gradient. Signal localization is achieved by the ISIS method using inversion pulses that are selectively turned on following an eight-step combination (Acqu 1 to 8). A fat-suppression module is launched just after the ISIS module to suppress the unwanted signal from intramuscular lipids. Then, the signal of the CPMG echo train is acquired.

^1H T_2 spectra were obtained from the signal decay curves by the deconvolution method presented in the study of Araujo *et al.* [17] (Figure 35). The transverse relaxation decay can be described by the following matrix equation:

$$Y = A \times P + E$$

Where Y is the vector containing the signal amplitudes at each echo time, P is the unknown vector containing the relative fraction of protons with a decay constant T_2 . A is a matrix containing the echo times and a number of possibly observable T_2 values. E is the vector containing the corresponding measurement error. A solution for the ill-posed Laplace transform inversion problem can be solved using a regularized minimization approach:

$$P = \min_{P \geq 0} \{ \|Y - A \times P\|_2 + \alpha \|P\|_2 \}$$

Where α is the L_2 - norm regularization parameter controlling the smoothness of the solution. Using a non-negative least-mean squares algorithm, spectra of the different T_2 contributions were extracted. In skeletal muscle tissue, the proton T_2 spectrum contained typically two separated T_2 pools with relative fractions and T_2 values representing fast and slow relaxing components. Since two peaks were systematically observed in healthy subjects, we also compared the results to a non-linear bi-exponential fit in the following studies. This approach allows estimating confidence intervals for the calculated T_2 values and fractions, which are difficult to assess using the T_2 spectrum approach. Araujo *et al.* [17] attributed the short T_2 component (T_2 around 30 ms) to the relaxation behaviour of water in exchange between the intracellular and interstitial spaces and the long T_2 component ($T_2 > 100$ ms) to the relaxation of water within the vascular space.

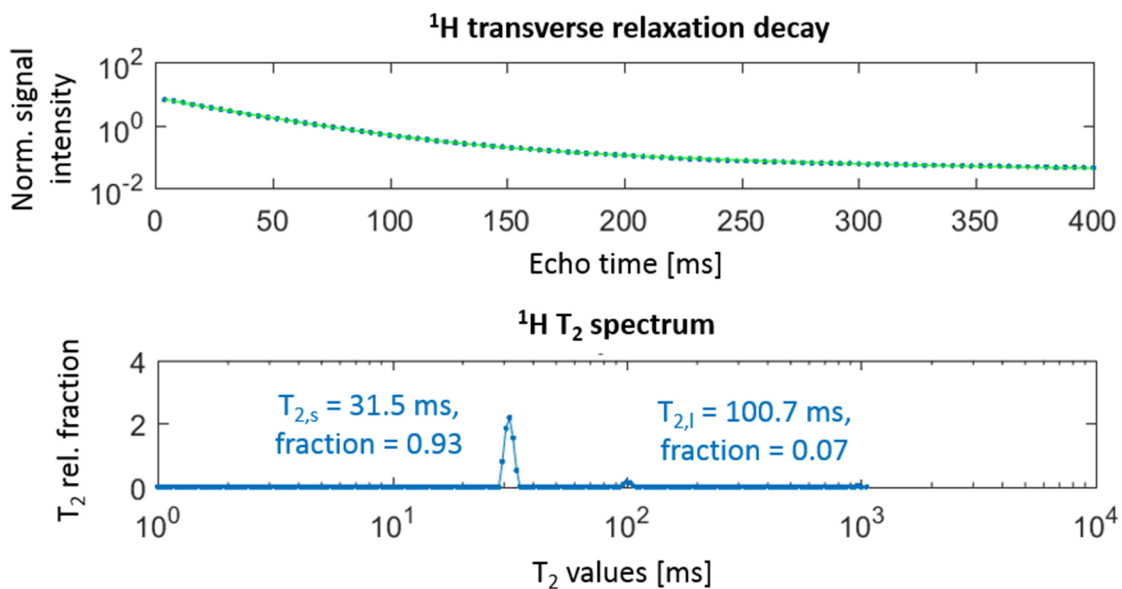


Figure 35: Plot of ^1H T_2 -decay curve obtained from the gastrocnemius medialis muscle of a healthy, male subject. The green line fitting the blue points corresponds to the fitted curve resulting from the regularized inversion solution using a nonnegative least-square method. The corresponding T_2 spectrum shows two distinct T_2 components characterized by their relative fraction and T_2 value. Typical values in accordance with literature were observed: $T_{2,s} = 31.5$ ms with relative fraction of 0.93 and $T_{2,l} = 100.7$ ms with relative fraction of 0.07.

4.5 pH measurement

Two different techniques were used to measure the pH of the dystrophic skeletal muscle tissue. The classic approach based on ^{31}P spectroscopy was used on the preclinical 7T scanner. Since no ^{31}P NMR coil was available in Erlangen, we had to measure the pH based on ^1H spectra in the course of the DMD study.

4.5.1 ^{31}P spectroscopy

Several resonances such as Pi and γ -ATP are sensitive to physiological parameters including the pH. Assuming a pH-independence of PCr, measurement of the chemical shift difference between Pi and PCr represents one of the most used pH determination method in skeletal muscle (Figure 36).

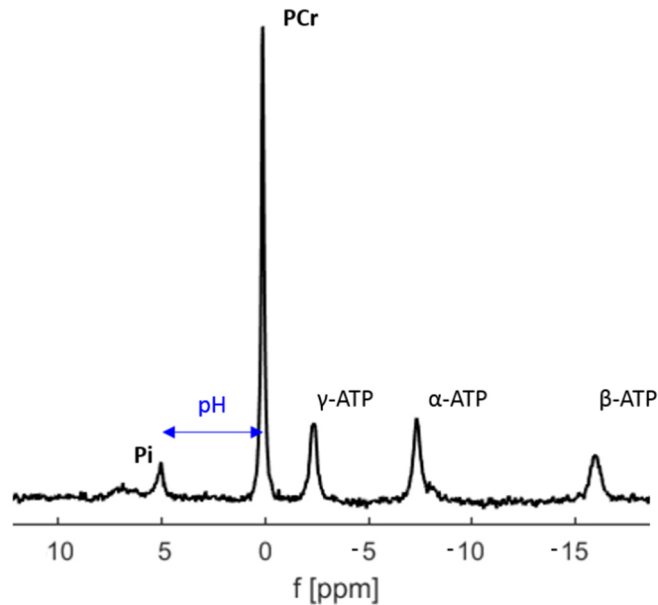


Figure 36: Typical *in vivo* ^{31}P NMR spectrum from a murine skeletal leg (non-localized acquisition at 7T) showing relevant ^{31}P containing metabolites such as adenosine triphosphate (ATP), phosphocreatine (PCr), and inorganic phosphate (Pi). By measuring the chemical shift difference between the Pi and PCr resonances, the pH can be determined.

The pH can be measured using the PCr resonance as reference peak using the modified Henderson-Hasselbach equation [64]:

$$pH = pKa + \log \left(\frac{\delta - \delta_{Hmetab}}{\delta_{metab} - \delta} \right)$$

Where pKa is the logarithm of the equilibrium constant for the exchange between the protonated and unprotonated form of the metabolite and δ_{Hmetab} and δ_{metab} the chemical shift of the protonated and unprotonated form of the metabolite, respectively. Based on pH calibration curves, values for pKa, δ_{Hmetab} , and δ_{metab} have been calculated for different metabolites that show a dependence on the pH. In our case, the chemical shift difference δ_{Pi} between the Pi and PCr resonances was used for pH measurement, resulting in the equation [159]:

$$pH = 6.75 + \log \left(\frac{3.27 - \delta_{Pi}}{\delta_{Pi} - 5.69} \right)$$

The cytosolic pH is commonly measured from the chemical shift difference between the Pi and PCr. However, in dystrophic muscles a second more alkaline resonance (Pi_b) at 0.3 ppm downfield from the cytosolic Pi (Pi_a) was observed [160]. Whereas the Pi_a peak has an intracellular origin, the origin of observed Pi_b remains uncertain. It could be either resulting from leaky dystrophic myocytes or from an increased interstitial space, thus being from extracellular origin [137].

4.5.2 ^1H spectroscopy

The pH can also be measured using ^1H NMRS exploiting the carnosine metabolite that resonates on the left side of the water signal (Figure 37). In resting muscle, carnosine can be found

only in the sarcoplasm, since extracellular carnosine is quickly degraded [137]. In the ^1H spectrum, the resonances of carnosine are visible at around 7 and 8 ppm ($-\text{C}_4\text{-H}$ and $-\text{C}_2\text{-H}$, respectively). Both resonances are sensitive to pH changes and based on their chemical shifts the intracellular pH can be measured using the water resonance as reference. We used the chemical shift difference $\delta_{\text{C}_2\text{-H}}$ between the $-\text{C}_2\text{-H}$ and residual water resonances to determine the pH [161]:

$$\text{pH} = 6.81 + \log \left(\frac{8.57 - \delta_{\text{C}_2\text{-H}}}{\delta_{\text{C}_2\text{-H}} - 7.65} \right)$$

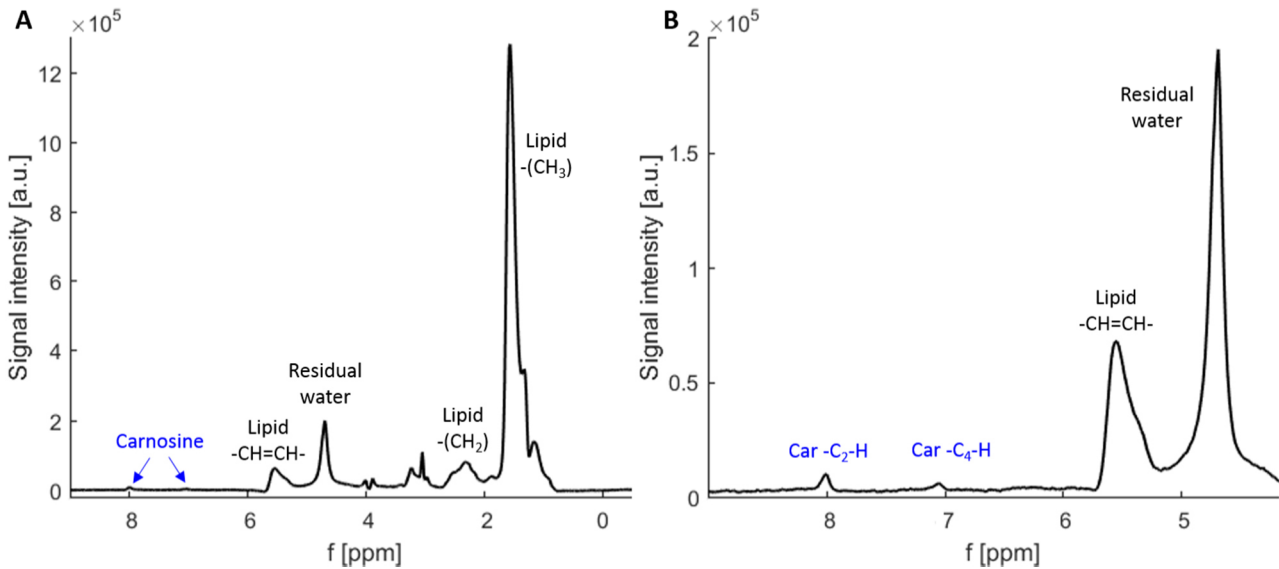


Figure 37: Typical localized *in vivo* ^1H NMR spectra from a voxel within the gastrocnemius muscle of a healthy human subject (acquired at 3T) **A**) with imperfect water suppression. **B**) In ^1H NMR, intracellular pH measurement is based on the shift between the carnosine peaks at around 8 and 7 ppm and the water peak (zoom of A).

4.6 ^{23}Na NMR methods for sodium quantification

4.6.1 Development of a non-localized ^{23}Na NMR protocol

In general, ^{23}Na NMR imaging sequences have long acquisition times that prevents their frequent application in clinical settings. Therefore, we implemented a non-localized ^{23}Na spectroscopy protocol for skeletal muscle characterization that can be added to clinical studies since the acquisition time was limited to about 15 minutes.

Three different sequences for seven sodium indices

This multi-parametric protocol aims to derive quantitative indices reflecting the sodium distribution and interactions with macromolecules in the skeletal muscle, in particular the intracellular sodium content and the extracellular volume fraction.

Before ^{23}Na NMR acquisition, a B_1^+ calibration sequence using rectangular pulses determined the reference voltage for a 90° excitation pulse (Figure 38). A set of forty FIDs was acquired ($\text{TR}/\text{TE} =$

300/0.2 ms, number of experiments (NEX) = 5, FA = 90°, bandwidth (BW) = 2.5 kHz, vector size = 128 points) with step-wise increased transmitter voltage (from $0.6 \times V_0$ to $1.4 \times V_0$, $V_0 = 100$ V). The voltage corresponding to the highest signal intensity was then applied as the reference voltage for the entire ^{23}Na NMR protocol.

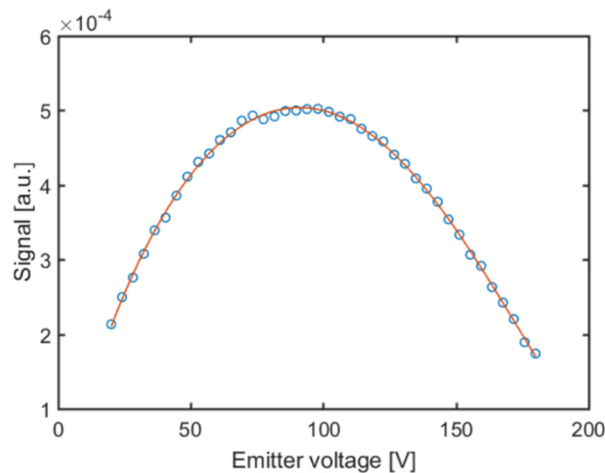


Figure 38: Voltage calibration for the ^{23}Na NMR protocol: the RF voltage to produce a 90° FA was determined by increasing stepwise the emitter voltage. The voltage resulting in the highest signal intensity was used for the ^{23}Na protocol acquisition.

Figure 39 depicts the RF pulse sequences of the non-localized ^{23}Na protocol that includes FID, TQF, and IR-LL sequence. The FID was acquired with a relatively long TR of 300 ms to allow full signal recovery after excitation. After a 90° excitation pulse, the signal decay was acquired with a short delay time of 200 μs to collect the signal from the fast T_2 component. For phantom studies, the receiver BW was set to 2 kHz with a vector size of 256 points. 400 averages lead to a total acquisition time of two minutes. After data reconstruction, the area under the curve was calculated from the FID spectra in order to derive the total sodium signal. In addition, T_2^* spectra were first obtained from the temporal decay of the FID by the T_2^* deconvolution method presented in the study of Araujo *et al.* [17] (Figure 40, see paragraph 4.4.2). The ^{23}Na T_2^* -decay curve was fitted using a nonnegative least-square method to extract T_2^* spectra. In biological tissue, the T_2^* spectrum contained systematically two separated T_2 pools with relative fractions and T_2^* values representing the fast and slow relaxing components. Since two peaks were thoroughly observed, a bi-exponential model was used in our studies to fit the ^{23}Na transverse relaxation decay, which allowed estimating confidence intervals. Thus, the FID sequence gives rise to the FID signal in arbitrary units (a.u.), a short T_2^* and long T_2^* in the order of few ms, as well as their relative fractions.

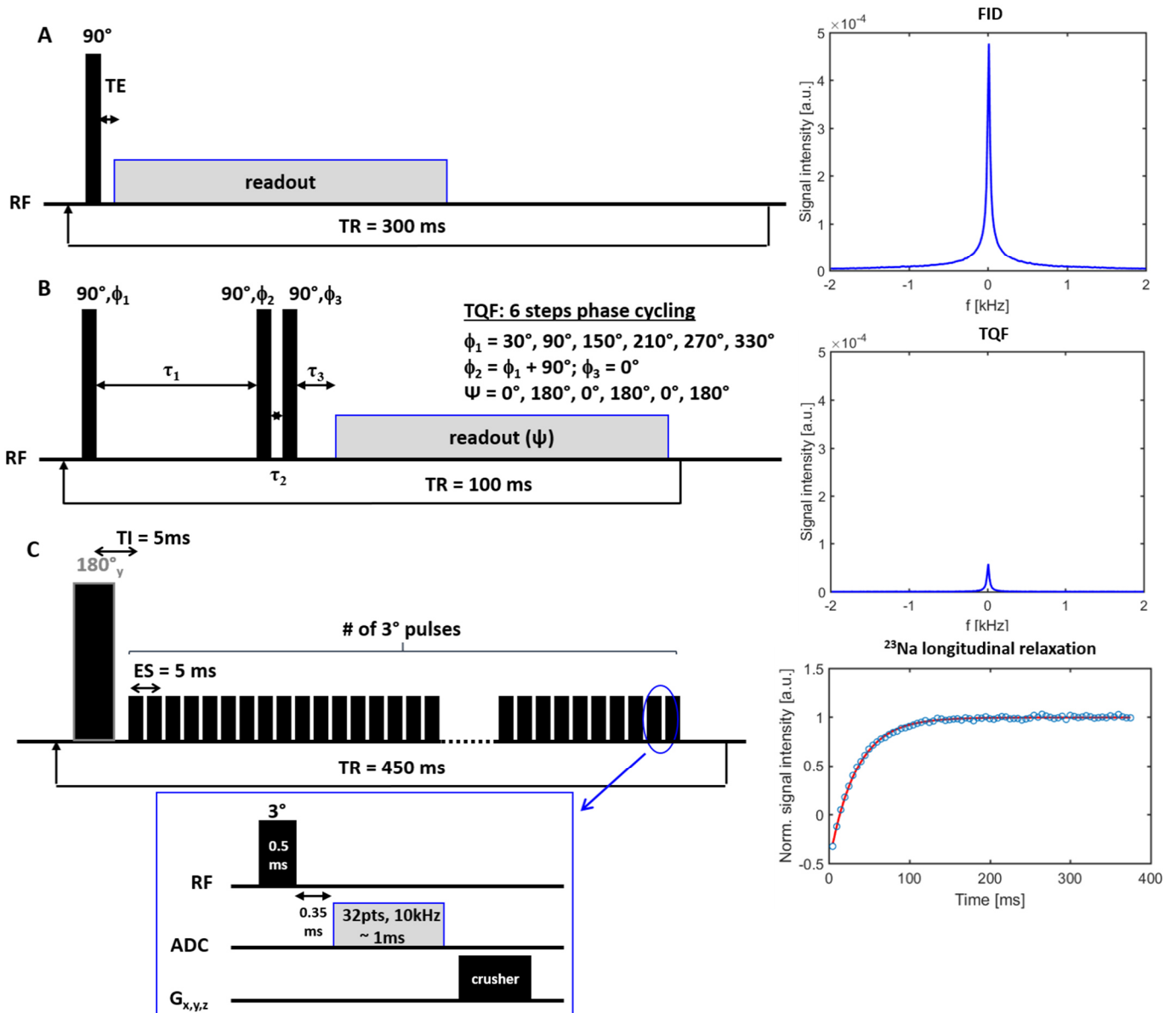


Figure 39: RF sequence diagram for ^{23}Na spectroscopy protocol that includes non-localized A) FID, B) TQF and C) IR-LL sequences. Next to the sequence diagram, corresponding human in vivo spectra are plotted for the FID and TQF sequence (acquired at 3T). Note the difference in the signal intensities between the FID and TQF signal. The IR-LL data was fit with a mono-exponential model to obtain a global T_1 of the leg. TE echo time, TR repetition time, ϕ_1 , ϕ_2 , ϕ_3 phase of pulses, TI inversion time, ES echo spacing.

The selection of TQC (Figure 39B) was realized by a six-step phase cycling scheme [104] with three 90° excitation pulses of different phases ($\phi_1 = 30^\circ, 90^\circ, 150^\circ, 210^\circ, 270^\circ$, and 330° ; $\phi_2 = \phi_1 + 90^\circ$; $\phi_3 = 0^\circ$). To increase the SNR, the number of repetitions was set to 3000 using a receiver BW of 2 kHz and a vector size of 256 points. To limit the acquisition time to five minutes, a TR of 100 ms was chosen. After reconstruction, the area under the curve was calculated from the TQF spectra in order to derive the signal of motionally restricted sodium ions. Additionally, the TQF/FID signal ratio was calculated indicating the distribution of ions between motionally restricted compartment and the total sodium pool.

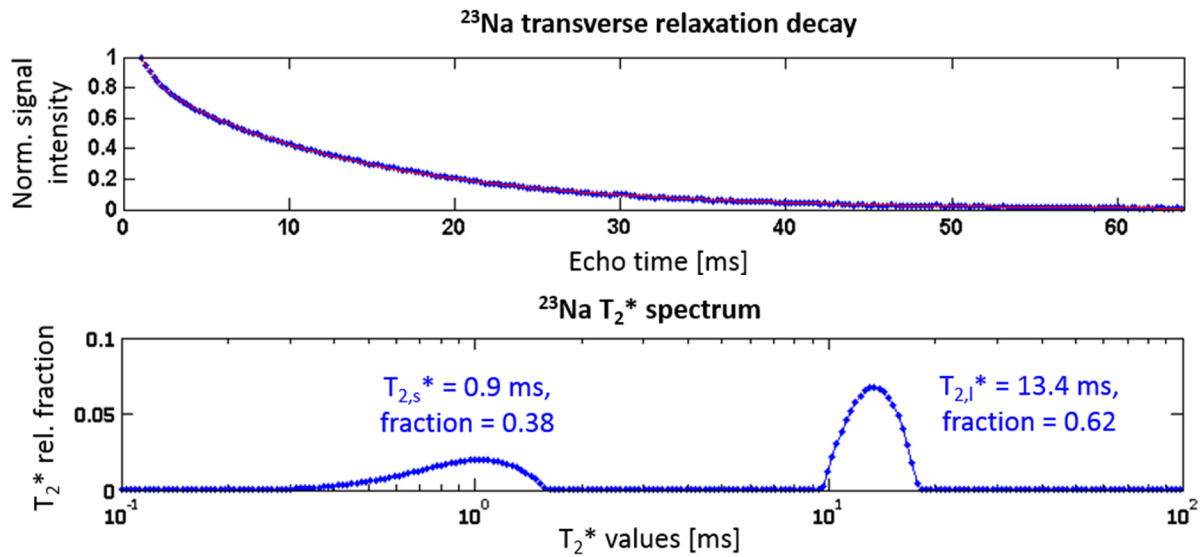


Figure 40: Plot of ^{23}Na T_2^* -decay curve obtained for a healthy subject. The violet line fitting the blue points corresponds to the fitted curve resulting from the regularized inversion solution using a nonnegative least-square method. The corresponding T_2^* spectra shows two distinct T_2^* components characterized by their relative fraction and T_2^* value. Typical values in accordance with literature were observed: $T_{2,s}^* = 0.9$ ms with relative fraction of 0.38 and $T_{2,l}^* = 13.4$ ms with relative fraction of 0.62.

To measure the global ^{23}Na T_1 , the inversion-recovery Look-Locker sequence was acquired (Figure 39C). After the inversion pulse, a series of α° excitation RF pulses is applied to probe the apparent longitudinal relaxation. The echo train was performed with 75 equally distributed TI ranging from 5 ms to 375 ms, a FA of 3° and a short acquisition time of 1 ms with an acquisition BW of 10 kHz and a vector size of 32 points. In total, 950 echo train experiments were acquired with a TR of 450 ms resulting in a total acquisition time of seven minutes. T_1 relaxation time was estimated from the IR-LL sequence by a mono-exponential model of the signal recovery at different time-points after magnetization inversion.

Validation of the sequences in phantoms

A validation on phantoms of the ^{23}Na protocol was performed on the 3T scanner in Paris. TQF experiments were performed with $\tau_1 = 11$ ms, $\tau_2 = 200$ μs , and $\tau_3 = 350$ μs . The test included phantoms with same size, but different agarose (0.2, 0.5, 1, and 2 %) or NaCl (80, 120, 140, 160, and 200 mM) concentrations (Figure 41). As expected, the FID signal increases with higher NaCl concentrations ($R = 0.984$), which represents the increasing number of sodium ions within the phantom. The FID signal decreases with higher agarose concentrations, in other words in higher motionally restricted media. This observation is due to the bi-exponential relaxation behaviour under conditions of restricted mobility ($R = -0.911$). In contrast, the TQF signal increases with higher agarose concentration since it originates from motionally restricted sodium ions ($R = 0.998$). The global T_1 value shortens, due to the bi-exponential relaxation behaviour if the agarose concentration

is increased ($R = -0.985$). These in vitro observations were in line with previous studies performed on agarose or gelatine gels [162].

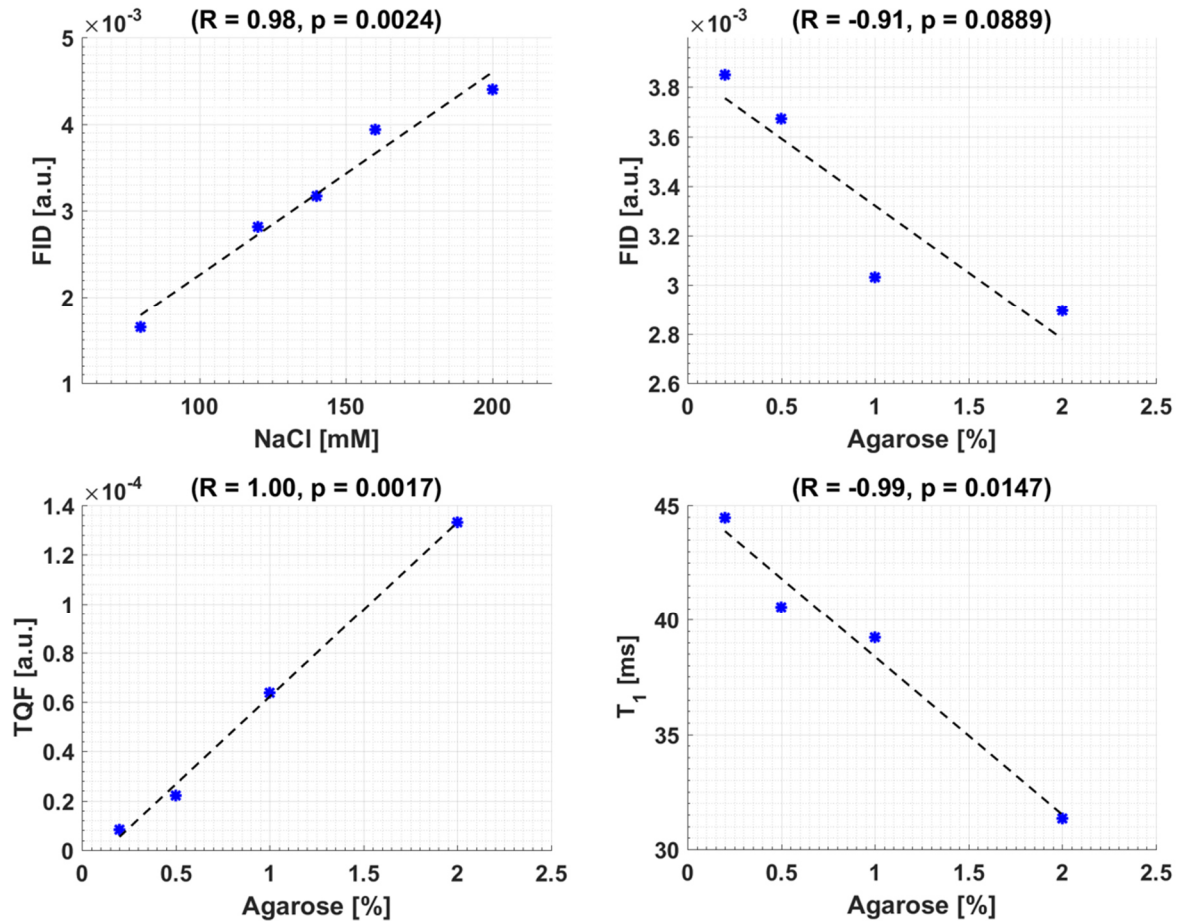


Figure 41: Correlation of FID signal with different concentrations of NaCl and correlations of FID signal, TQF signal, and T_1 value with different concentrations of agarose.

To calibrate and quantify the non-localized ^{23}Na signals, a calibration phantom containing a shift reagent (TmDOTP $^{5-}$) was placed next to the leg during ^{23}Na acquisition. This SR phantom was filled with 140 mM NaCl and 24 mM TmDOTP $^{5-}$. The signal calibration steps and its evaluation are explained in more detail in 5.2. The ^{23}Na non-localized NMR protocol was also transferred from the human clinical scanner to the preclinical scanner for animal investigations.

4.6.2 Double quantum filter with magic angle sequence

To investigate quadrupolar interactions between the ^{23}Na nuclei and their environment, a DQF-MA sequence (3.3.3) was implemented at the clinical scanner in Erlangen.

The slowly tumbling ^{23}Na nuclei in an anisotropic environment were measured with at the magic angle 54.7° (Figure 42). The DQF-MA was realized by a 4-steps-phase cycling scheme with the magic angle for the second and third RF pulse to suppress unwanted signal of third-rank DQC ($\Theta_1 = 90^\circ$, $\Theta_2 = \Theta_3 = 54.7^\circ$, $\phi_1 = 0^\circ, 90^\circ, 180^\circ$, and 270° ; $\phi_2 = \phi_1$; $\phi_3 = 0$). To increase the SNR, the number of

repetitions was set to 2000 using a receiver BW of 5 kHz and a vector size of 256 points. To allow full relaxation a TR of 200 ms was chosen. After reconstruction, the area under the curve was calculated from the DQF-MA spectra in order to derive the signal of sodium ions in anisotropic motion. Additionally, the DQF-MA/TQF signal ratio was calculated indicating the fraction of motionally restricted ions in an anisotropic environment.

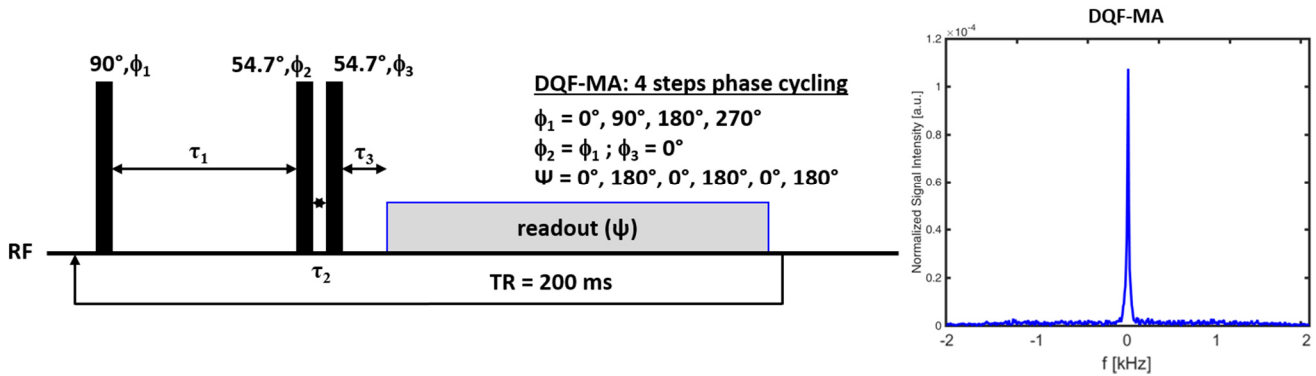


Figure 42: RF sequence diagram for ^{23}Na DQF-MA spectroscopic sequence. Next to the sequence diagram, corresponding human in vivo spectrum is plotted (acquired at 3T). TR repetition time, ϕ_1, ϕ_2, ϕ_3 phase of pulses.

4.6.3 Fast ^{23}Na NMR imaging sequences

With the above-introduced non-localized protocol, the spatial information of the ^{23}Na signal is lost. During this PhD, we set up a collaboration with a German team in Erlangen to assess ionic disturbances in the dystrophic muscle of DMD patients. They have developed a fast NMR ^{23}Na imaging sequence for skeletal muscle tissue characterization. Here, the theory of this sequence will be briefly introduced followed by a presentation about ^{23}Na NMRI signal calibration.

Density-adapted 3D radial projection pulse sequence

Because the sodium nucleus exhibits a bi-exponential relaxation with a fast component of around 1 ms in biological tissues [143], dedicated NMR pulse sequences with very short TEs are needed to record the complete relaxation behaviour. This reduction of the TE is achieved by different k-space sampling schemes such as sampling on centre-out radial lines (Figure 43B). The excitation pulse is followed immediately after a required hardware-dependent delay (e.g. 50 μs) by the signal acquisition. In a conventional radial gradient readout, the centre of k-space is more densely sampled as less points are acquired in the outer part due to the homogenous sampling speed of each radial spoke. This decreases the already poor SNR of the ^{23}Na signal [13]. An inhomogeneous sampling scheme can result in an increase of image noise, since the SNR efficiency η is defined as [163]:

$$\eta = \frac{\sigma_{i,hom}}{\sigma_{i,inhom}}$$

Where $\sigma_{i,\text{hom}}$ and $\sigma_{i,\text{inhom}}$ are the standard deviations in image space for homogenous and inhomogeneous sampling densities, respectively. Thus, by manipulating the readout gradient during signal acquisition, the sampling scheme is changed from an inhomogeneous to a more homogenous distribution of the sampling density of the k-space.

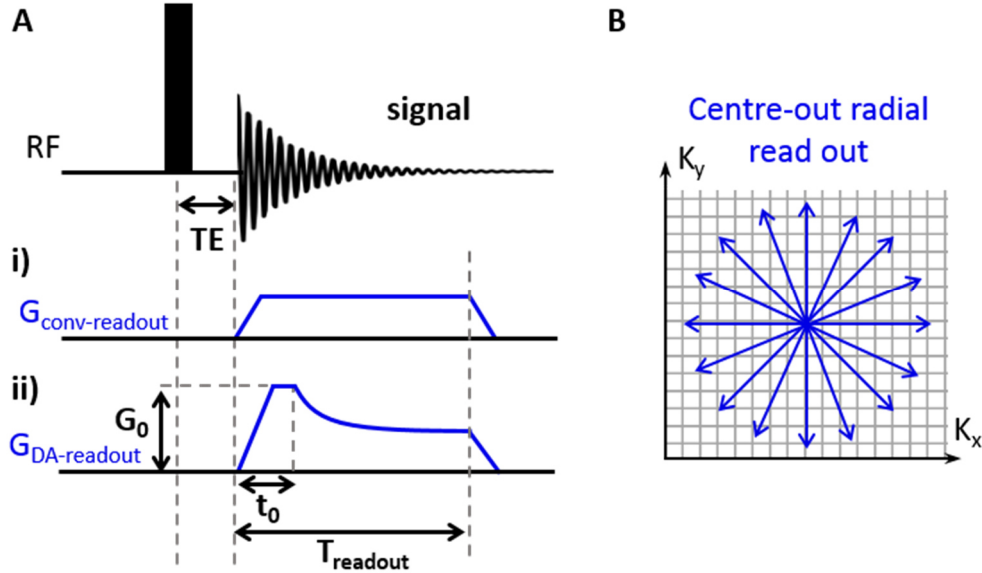


Figure 43: **A)** RF pulse and gradient diagram of the 3D radial sequence with i) a conventional gradient readout and ii) a density-adapted gradient readout. The conventional gradient readout uses a constant gradient strength after the gradient ramp, while the density-adapted readout gradient consists of three parts: (1) the gradient ramp, (2) a trapezoidal part with gradient strength G_0 , and (3) a density-adapted part that starts after t_0 allowing in the following constant sampling density in the outer part of the k-space. **B)** Radial sampling scheme of the k-space: without density-adapted sampling, the centre of k-space is more densely sampled than the outer part. By manipulating the readout gradient, the sampling velocity is slowed down in the outer part of k-space leading to a more homogenous sampling scheme.

Therefore, Nagel *et al.* [18] introduced a density-adapted 3D radial projection pulse sequence (DA-3DPR). Changes in the sampling density are achieved by manipulating the readout gradient during data acquisition (Figure 43A). As aforementioned, it is desirable to achieve a uniform sampling density throughout the k-space. However, due to hardware limitations (maximal possible gradient amplitude and slew rate), gradients cannot be designed in such a way that the averaged sampling density of k-space is constant. Thus, the density-adapted approach starts with an inhomogeneous sampling density during the ramp and the trapezoidal part with gradient strength G_0 . The period t_0 , corresponding to the time needed for the ramp and trapezoidal part, is kept as short as possible. Then, uniform sampling can be achieved for k-space by slowing down the sampling velocity in the outer part of k-space by reducing the amplitude of the readout gradient. The gradient strength after t_0 is described by:

$$G(t) = k_0^2 G_0 (3\gamma k_0^2 G_0 (t - t_0) + k_0^3)^{-2/3}$$

Where k_0 is the radius of the k-space at t_0 and γ the gyromagnetic ratio. The homogenous distribution of the sampling points after t_0 leads to a reduced image noise and consequently to an increased SNR. Additionally, k-space positions are sampled ahead of time compared to conventional radial sampling techniques. Therefore, less signal has decayed due to T_2 relaxation for each k-space position. This causes less image blurring since high-spatial frequencies (i.e. edges, details) stored at the periphery of k-space are sampled faster [18]. Please refer to the publication for further explications about the optimization of the parameters such as the readout time, G_0 , and t_0 .

In vivo application of the density-adapted 3D radial projection pulse sequence

Two DA-3DPR sequences were parameterized at the 3T scanner in Erlangen; one DA-3DPR sequence to quantify TSC and another DA-3DPR sequence including an IR preparation pulse to obtain an intracellular weighted sodium signal (ICW). For the TSC acquisition, the acquisition time was reduced using a short TR of 50 ms leading to a T_1 weighting. An ultra-short TE of 0.3 ms was achieved. The FA was set to 80° to match the Ernst angle of skeletal muscle tissue. Radial sampling was performed with 8264 projections and 384 averages per projection. The readout used a gradient amplitude G_0 of 7.89 mT/m (t_0 0.5 ms), a gradient slew rate of 170 T/m/s, and a readout window length of $T_{\text{readout}} = 10$ ms to achieve a nominal spatial resolution of $3 \times 3 \times 15$ mm³. The gradient parameters were previously optimized for *in vivo* imaging [18]. A gradient spoiler after each readout with duration of 5.1 ms was used to spoil residual transverse magnetization. The acquisition time to obtain a single 3D TSC data set was 6 min 53 s. To obtain ICW images, an inversion pulse (pulse length of 1 ms) with a TI of 34 ms was applied to suppress the signal from “free” sodium nuclei originating from a liquid environment. Other parameters were TR = 124 ms, TE = 0.3 ms, and FA = 90° . Radial sampling was performed with 4760 projections and 384 averages per projection. The signal was read out with a gradient amplitude G_0 of 4.61 mT/m (t_0 0.5 ms), a gradient slew rate of 170 T/m/s, and a readout window length of $T_{\text{readout}} = 20$ ms to achieve a nominal spatial resolution of $4 \times 4 \times 20$ mm³ followed by a gradient spoiler of 5.1 ms. The acquisition time to obtain a single 3D ICW data set was 9 min 50 s.

For anatomical reference imaging, a ¹H FLASH (Fast low angle shot magnetic resonance imaging) sequence was acquired using the body coil for magnetization excitation and signal reception. These images were used to visualize blood vessels, which exhibit high sodium concentrations and should be avoided during the sodium quantification of the skeletal muscle tissue. Furthermore, anatomical reference images helped to delineate different muscle groups during regions-of-interest (ROI) determination. FLASH sequences were obtained with the following parameters: 24 slices with TE = 4.77 ms, TR = 308 ms, and a resolution of $1 \times 1 \times 5$ mm³. Two averages

and a FA of 90° were applied to increase the SNR, which was intrinsically low due to the shielding of the ^{23}Na volume coil (acquisition time (T_{acq}) = 2 min).

For ^{23}Na signal quantification, external calibration phantoms were placed next to the leg (Figure 44). After reconstruction of the ^{23}Na images, the sodium signals were calibrated using the signal intensities of the reference phantoms. Exploiting the known NaCl concentration of the calibration standards (20 mM and 40 mM NaCl) and the background noise (0 mM NaCl) allowed the calibration and quantification of the TSC and ICW signals originating from the skeletal muscle tissue. The DA-3DPR sequences were acquired *in vivo* on healthy subjects ($n = 6$, five females, age 26.6 ± 3.4 years) with four calibration standards of different NaCl and agarose concentrations (Table 7).

Table 7: Composition of calibration phantoms used for ^{23}Na imaging.

Calibration phantom	NaCl [mM]	Agarose [%]
1	40	0
2	40	4
3	20	0
4	20	4

Figure 44 depicts the higher spatial resolution of the ^1H images (A) compared to the DA-3DPR ^{23}Na images of the leg without (B) and with (C) the IR pulse. The DA-3DPR ^{23}Na images (B) show increased total sodium signal in the blood vessels (Table 8). Furthermore, a non-negligible sodium signal arises from the subcutaneous fat. The calibration standards with sodium concentration of 40 mM (1 without agarose and 2 with agarose) appear with an about twice higher signal intensity than those with 20 mM (3 without agarose and 4 with agarose). The agarose standards appear lighter than the saline solution due to the decreased T_1 .

Table 8: Signal intensities of calibration phantoms (1, 2, 3, and 4), muscle, blood, and subcutaneous fat in DA-3DPR ^{23}Na images and DA-3DPR ^{23}Na images with IR preparation pulse ($n = 6$).

ROI	DA-3DPR [a.u.]	DA-3DPR with IR [a.u.]
1	0.018 \pm 0.002	0.002 \pm 0.001
2	0.024 \pm 0.002	0.012 \pm 0.001
3	0.009 \pm 0.001	0.001 \pm 0.000
4	0.014 \pm 0.001	0.008 \pm 0.001
Muscle	0.011 \pm 0.002	0.006 \pm 0.001
Blood	0.022 \pm 0.004	0.008 \pm 0.001
Sub. fat	0.007 \pm 0.001	0.003 \pm 0.002

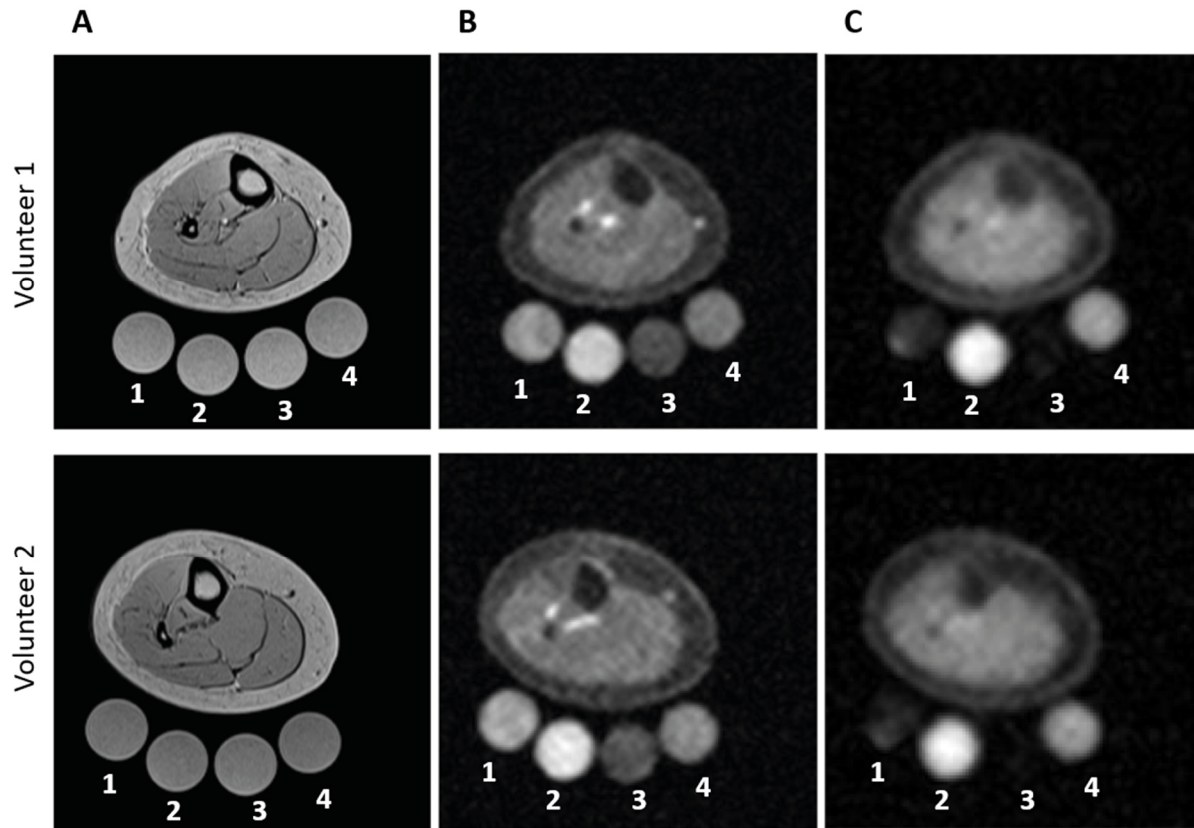


Figure 44: Images of two healthy female volunteers. **A)** T_1 weighted ^1H image of right leg with corresponding **B)** DA-3DPR ^{23}Na image and **C)** DA-3DPR ^{23}Na image with IR pulse (TI 34 ms). Four calibration standards are shown at the bottom of the leg with sodium concentration of 20 mM (3) and 40 mM (1) and with 4 % agarose and 20 mM (4) and 40 mM (2) mimicking Na^+ with restricted mobility.

The DA-3DPR ^{23}Na images with IR pulse (C) demonstrate the suppression of sodium signal originating from a non-restricted environment since the signal from the calibration standards without agarose (1 and 3) vanishes. A small signal contribution still arises from the lateral part of phantom 1 due to B_1 inhomogeneities. In volunteer 1, the signal originating from the blood vessel in the medial part was also not completely suppressed. Furthermore, only a very small sodium signal arises from the subcutaneous fat. These observations were partly in line with previous studies performed *in vivo* [83], where no signal intensity in the saline solution tube and a suppression of the intravascular sodium ions in ^{23}Na -IR image were reported.

For quantification purpose, TSC and ICW maps were calculated based on the signal intensities and known concentration of the reference tubes. The TSC maps were calculated with the agarose phantoms (2 and 4), since they reflect better the muscle tissue properties (restricted environment). The signal of the calibration references and the noise were fitted by a linear model, which was used to calculate the concentration maps (Figure 45). A linear polynomial model was fit was used to obtain the calibration curve:

$$f(x) = a_1 x + a_2$$

Where a_1 and a_2 are the fitting constants that are used to calculate the TSC and ICW maps pixel wise by calibrating the signal intensity of the DA-3DPR ^{23}Na images:

$$TSC = \frac{p_{im} - a_2}{a_1}$$

Where p_{im} is a pixel of the DA-3DPR ^{23}Na image. The ROIs were traced on the ^1H images on the lower leg and the reference tubes (Figure 46) and automatically registered to the ^{23}Na TSC and ICW maps. For ICW signal calibration, we assigned 0.5 to phantom #2 and 1 to phantom #4 to obtain relative ICW values in a.u..

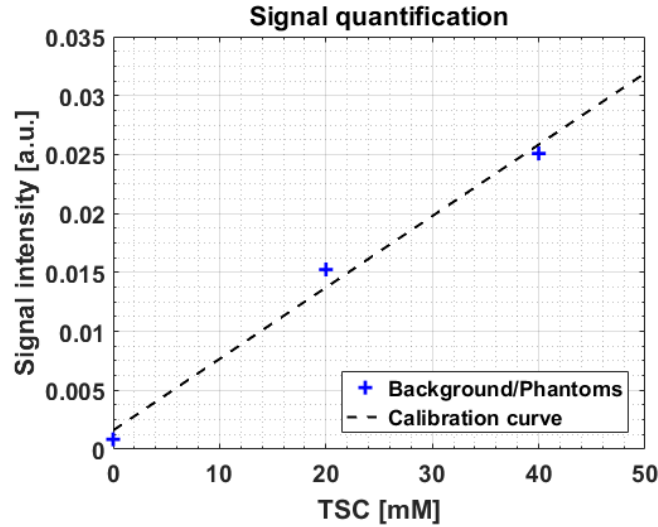


Figure 45: ^{23}Na signal calibration using two reference phantoms with 20 mM and 40 mM NaCl in 4 % agarose and the background noise. Based on the calibration curve, TSC and ICW maps are calculated pixel-wise.

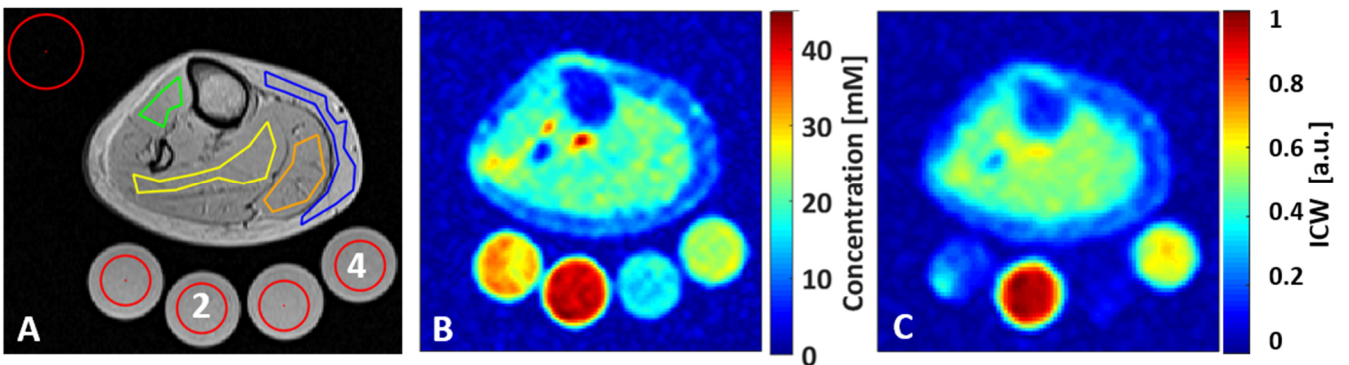


Figure 46: ^{23}Na signal calibration of the leg. **A)** ROIs are drawn manually on the ^1H image in TA (green), SO (yellow), GM (orange), subcutaneous fat (blue), in the calibration standards, and in the background (red). **B)** TSC map and **C)** ICW map were calculated based on the calibration curve using the agarose phantoms (2 and 4) and the background noise.

The average TSC and ICW values of healthy subjects were calculated for the tibialis anterior (TA), soleus (SO) and gastrocnemius medialis (GM) muscles as well as the subcutaneous fat (Table 9). The TSCs and ICW values were lower in the TA than the posterior muscle of the leg. The subcutaneous fat exhibits a non-zero sodium signal in the TSC and ICW maps confirming the

previously made visual observation. This fact should be taken into account for the TSC quantification of muscle in patients where an increased fat fraction is known to be present in skeletal muscle tissue such as in DMD patients. In other studies, a mean TSC of 24 ± 2 mM (healthy subjects) was calculated by linear extrapolation using only one reference tube with 51.3 mM NaCl and 5 % agarose gel [83]. Nevertheless, we suggest using at least two reference phantoms of different NaCl concentration with agarose that mimics the relaxation behaviour of muscle tissue as well as the background noise to obtain a more precise calibration curve for proper ^{23}Na quantification. An additional saline phantom should be used to verify the efficiency of the liquid suppression in the DA-3DPR ^{23}Na images with IR pulse.

Table 9: Measured TSC and ICW of healthy volunteers ($n = 6$) of the TA, SO, and GM muscle as well as the subcutaneous fat. Values presented as mean and SD (standard deviation).

ROI	TSC [mM]	ICW [a.u.]
TA	15.3 \pm 2.7	0.39 \pm 0.03
SO	17.6 \pm 1.4	0.50 \pm 0.02
GM	17.5 \pm 1.4	0.43 \pm 0.03
Sub. fat	7.7 \pm 0.7	0.15 \pm 0.04

4.7 Post-processing tools and statistical analysis

All ^1H and ^{31}P NMR spectra were processed using jMRUI [164]. The FF, water T_2 , and T_1 maps were processed using Python reconstruction codes. ROIs were drawn on specific muscles using the free-ware segmentation software ITK-SNAP [165]. ISIS-CPMG and ^{23}Na NMR data processing was carried out using Matlab (MathWorks, Inc., Natick, MA).

Data were analysed and expressed as mean and standard deviation (SD). Statistical analysis was performed in SPSS (SPSS 22, SPSS Inc. Chicago, IL).

Characterization of healthy skeletal muscle tissue by ^{23}Na NMR

This chapter summarizes several experiments investigating the healthy skeletal muscle by ^{23}Na NMR. In a proof of concept study, we induced acute changes in extracellular volume fraction in skeletal muscle tissue of healthy volunteers. We then compared the sensitivity to track these changes of a standard ^1H T_2 imaging method to the fast ^{23}Na NMR spectroscopy protocol (4.6.1). Using an external reference phantom, we validated an approach to quantify *in vivo* the ^{23}Na signal of the ^{23}Na NMR spectroscopy protocol (5.2). Furthermore, the impact of prolonged ischemia on the ^1H T_2 and ^{23}Na signals of skeletal muscle was studied in mice where the physiological paradigm could be extended up to 40 minutes (5.3). The last part of this chapter is dedicated to investigate the environment of sodium ions in skeletal muscle tissue using MQF sequences (5.4).

5.1 Monitoring the variations of ^{23}Na NMR signals during different vascular filling conditions in comparison to ^1H T_2 alterations

After the *in vitro* evaluation of the fast ^{23}Na spectroscopic protocol (4.6.1), a proof of concept study investigated its sensitivity to monitor changes in extracellular volume fraction in skeletal muscle tissues. In order to evaluate the ability of ^{23}Na spectroscopy to detect changes in the Na^+ distribution between intra- and extracellular compartments, different experiments were conducted *in vivo*. First, the effect of a short-term ischemia on the Na^+ bio-distribution in the leg muscle was monitored. Then, measurements were performed on the same lower leg muscles under different vascular filling conditions to manipulate the ratio of intra-/extracellular contributions to the Na^+ pool and to test the ability to detect it by multi-parametric ^{23}Na NMR. The sensitivity of the three non-localized ^{23}Na sequences were compared to that of a standard ^1H T_2 mapping method to these different conditions.

5.1.1 Materials and methods

Subjects and study design

Sodium NMRS and proton NMRI were performed on 28 healthy volunteers (aged 28.2 ± 8.4 years, 13 women and 15 men) as part of a methodology protocol approved by the local ethics committee (Comité de Protection des Personnes Ile de France VI). Before data acquisition, written informed consent was obtained from all subjects. Subjects underwent one of the two protocols described below. The first group of seven volunteers participated in protocol 1 dedicated to investigate the effect of a short-term ischemia on the sodium distribution in skeletal muscle (group

1). The other 21 volunteers were assigned to group 2 ($n = 14$) and group 3 ($n = 7$), which underwent protocol 2 with either ^{23}Na NMR (group 2) or ^1H T_2 (group 3) acquisitions to compare the sensitivities of the two methods to detect acute changes in intra-/extracellular volume fractions.

Protocol 1

^{23}Na NMR spectra were acquired during a short ischaemia in the right calf of group 1 (Figure 47). Prior to the NMR acquisition a medical cuff was placed above the knee and the subjects rested supine on the bed during 30 minutes. Then the cuff was connected to a circuitry pressurized at 250 mmHg to block instantaneously and completely the arterial inflow and the venous outflow. The cuff pressure was manually controlled from the outside of the magnet room by the manipulator using a mercury manometer (MERCUREX+; Spengler, Antony, France) combined with a fast switch valve system. During the 15-minute ischaemia, sodium homeostasis was monitored with series of short ^{23}Na sequences.

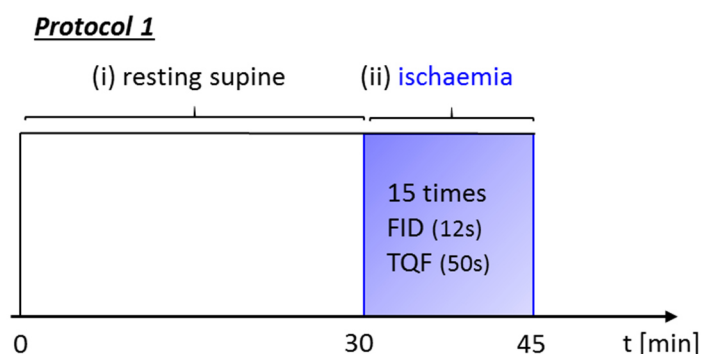


Figure 47: Timeline of the ischemia protocol (protocol 1): (i) After 30 min supine rest, (ii) the medical cuff placed above the knee was rapidly inflated and the acquisition of the sodium spectra started.

Protocol 2

^{23}Na NMR spectra and ^1H NMR images of group 2 and 3 were acquired under three different vascular filling conditions: (i) vascular draining, (ii) vascular filling, and (iii) normal condition. The protocol timeline for the data acquisition is presented in Figure 48. These vascular conditions were imposed while the subject remained still in supine position inside the scanner. Vascular draining was initiated by wrapping an elastic compression band from toes to the knee. Then a medical cuff, placed over the knee, was inflated at 250 mmHg to block completely the arterial inflow and the venous outflow. The elastic compression band was then removed from the leg while keeping the cuff pressure high and after centring the leg in the magnet, the first set of data was acquired. Next, the cuff pressure was decreased to 60 - 70 mmHg in order to fill the capacitance vessels. After a five-minute interval to allow for a stabilized vascular filling condition, another NMR data acquisition was performed. Finally, the cuff was fully released and again five minutes were given, this time to resume normal perfusion regime and the last series of NMR sequences was acquired.

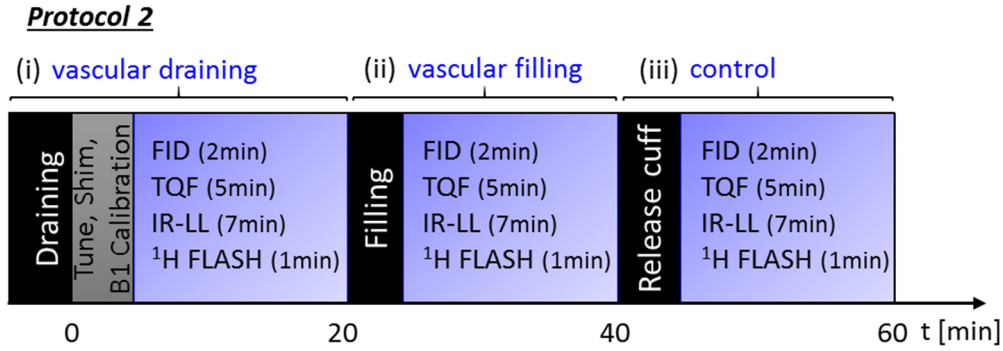


Figure 48: Timeline of the vascular filling conditions (protocol 2): (i) vascular draining was first applied with the calf positioned in the coil followed by the NMR acquisition (non-localized ^{23}Na spectroscopic and ^1H imaging acquisition or by ^1H MSME acquisition). (ii) After vascular filling during a 5-minute interval initiated by a reduced cuff pressure, another NMR acquisition was launched. (iii) Normal condition: the pressure of the cuff was completely released and after a 5-minute break, the final sodium NMR and proton imaging were performed.

NMR sequences

For group 1 and 2, ^{23}Na NMRS sequences were acquired with the linear volume ^{23}Na leg coil. To minimize the leg movement, foam pads were inserted between the leg and the coil. The ^{23}Na spectroscopy part consisted in FID, TQF, and IR-LL sequences with a total acquisition time of 14 minutes for the second protocol. The sequences were acquired with the parameters as described in 4.6.1, except of a reduced vector size of 128 points for the FID and TQF. For group 1 the number of averages for the FID and TQF were reduced to acquire the two sequences with a temporal resolution of 1 min. The FID had 40 averages ($T_{\text{acq}} = 12$ s) and the TQF 500 averages ($T_{\text{acq}} = 50$ s).

Changes in the leg volume between the different vascular filling conditions were monitored with a 3D FLASH sequence covering the whole calf using the body coil for magnetization excitation as well as signal reception. This sequence was acquired with the following parameters: TE/TR = 2.78/65 ms, matrix size = $250 \times 250 \times 50$ mm³, spatial resolution = $2.6 \times 2.6 \times 5$ mm³, and $T_{\text{acq}} = 1$ min.

For group 3, proton images were acquired with the 15 channel ^1H knee coil (Figure 49A). Foam pads were inserted between the leg and the coil to minimize leg movements. To measure proton T_2 weighted signal intensities and proton T_2 values, a MSME sequence was acquired with 17 different TEs: 8.5 - 144.5 ms, TR = 3000 ms, 5 slices with matrix size = $192 \times 192 \times 10$ mm³, spatial resolution = $1.5 \times 1.5 \times 10$ mm³, and $T_{\text{acq}} = 3$ min.

Analysis of ^{23}Na and ^1H NMR data

Sodium data were processed as described in 4.6.1. We obtained the following ^{23}Na indices: FID signal, TQF signal, TQF/FID ratio, short T_2^* fraction, short and long T_2^* , and global T_1 . Total muscle volume estimation was performed on ImageJ [166] from the ^1H FLASH images. ROIs were

manually drawn around the leg on 23 slices. Leg volumes were then calculated based on the exported ROIs (leg area x slice thickness).

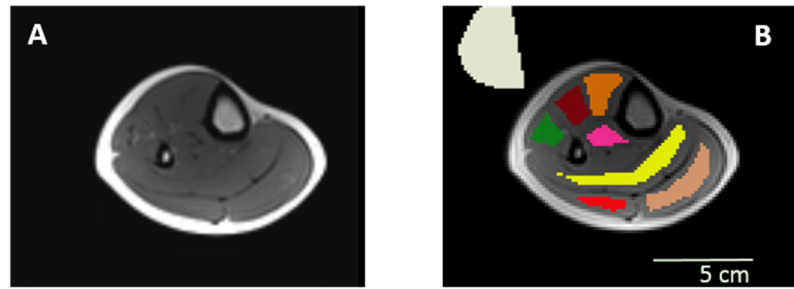


Figure 49: Standard ^1H T_2 imaging: **A**) a cross-sectional $T_2\text{w}$ image ($TE = 34$ ms); **B**) The ROIs used for analysis were traced within the muscles (TA orange; ED brown; TP pink; PL green; SO yellow; GL red; GM beige; Background noise grey).

Proton T_2 weighted signal intensities and proton T_2 values were measured from the MSME sequences. ROIs were manually traced inside specific muscles (see Figure 49B; ED extensor digitorum, GL gastrocnemius lateral, GM gastrocnemius medial, PL peroneus longus, SO soleus, TA tibialis anterior, TP tibialis posterior). Proton T_2 weighted ($T_2\text{w}$) signal intensities were calculated as a mean signal intensity of each ROI in the $T_2\text{w}$ image at TE of 34 ms and the T_2 maps were produced via a standard mono-exponential fit [64].

Statistical analysis

Percentages of change of each parameter as compared to the control condition were determined. Statistical analysis was performed using ANOVA with repeated measures and Bonferroni post-hoc tests for pairwise comparisons to evaluate significant differences between the different conditions. Pearson correlations analysed the relationship between the variables. In all statistical tests, $p < 0.05$ was considered statistically significant.

5.1.2 Results

Impact of ischemia on ^{23}Na NMR signal

Figure 50 shows the evolution of the FID and TQF signals as well as the TQF/FID ratio during the 15-minute ischemic period. The signals have been normalized using the first time point as a reference. The normalized FID signal changes with time by -2 ± 2.7 %, not significant with repeated measures ANOVA. The normalized TQF signal was found to progressively decrease over time (-6 ± 1.7 % at the end of the experiment). Repeated measures ANOVA indicated a significant decrease of the TQF signal after 15 minutes of ischemia ($p < 0.05$). The TQF/FID thus decreased by 4.1 ± 2.6 % (not significant).

5.1 Monitoring the variations of ^{23}Na NMR signals during different vascular filling conditions

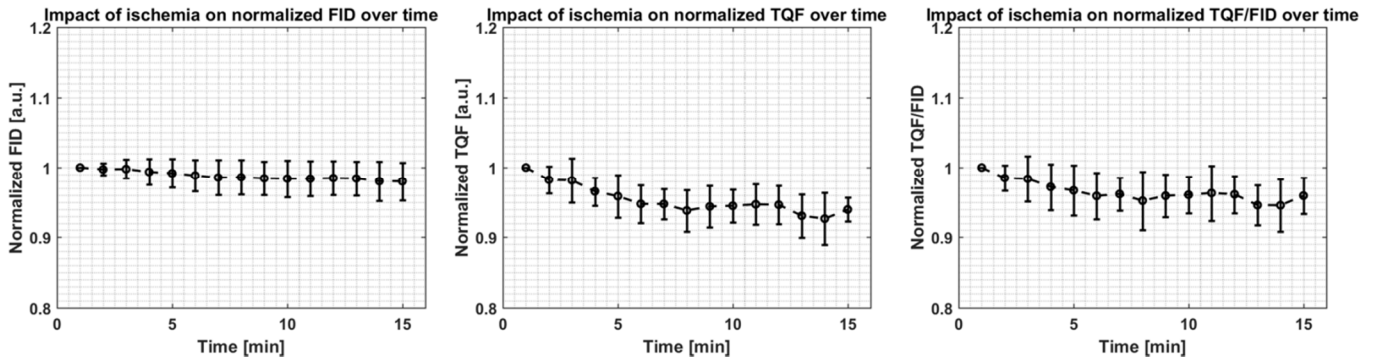


Figure 50: The effect of short-term ischemia *in vivo* in skeletal muscle measured by ^{23}Na NMR.

Vascular filling changes monitored by ^{23}Na NMR

Figure 51A displays the different sodium indices obtained by ^{23}Na NMR in one volunteer of the group 2 under each vascular filling condition. As depicted, the FID, TQF signal, and T_1 relaxation curves were modified in response to extracellular volume changes. The FID signal decreased from 8.2×10^{-3} a.u. for the control condition to 7.4×10^{-3} a.u. while draining and increased to 9.7×10^{-3} a.u. under vascular filling. The TQF signal showed a different behaviour with a decrease from 5.5×10^{-5} a.u. to 5.4×10^{-5} a.u. during vascular filling and increases to 5.8×10^{-5} a.u. during vascular draining. The T_1 relaxation time showed a parallel behaviour as the FID signal, by dropping from 34.3 ms to 33.7 ms during draining and rose to 37.0 ms during filling. After deconvolution, two well-resolved Na^+ pools could be identified for each vascular filling condition on the T_2^* spectra. One slice of the ^1H FLASH volume is presented in Figure 51B, with the manual delineation of the leg. For this subject, the leg muscle volume was 1175 cm^3 during vascular draining, 1273 cm^3 during vascular filling, and 1180 cm^3 under control conditions.

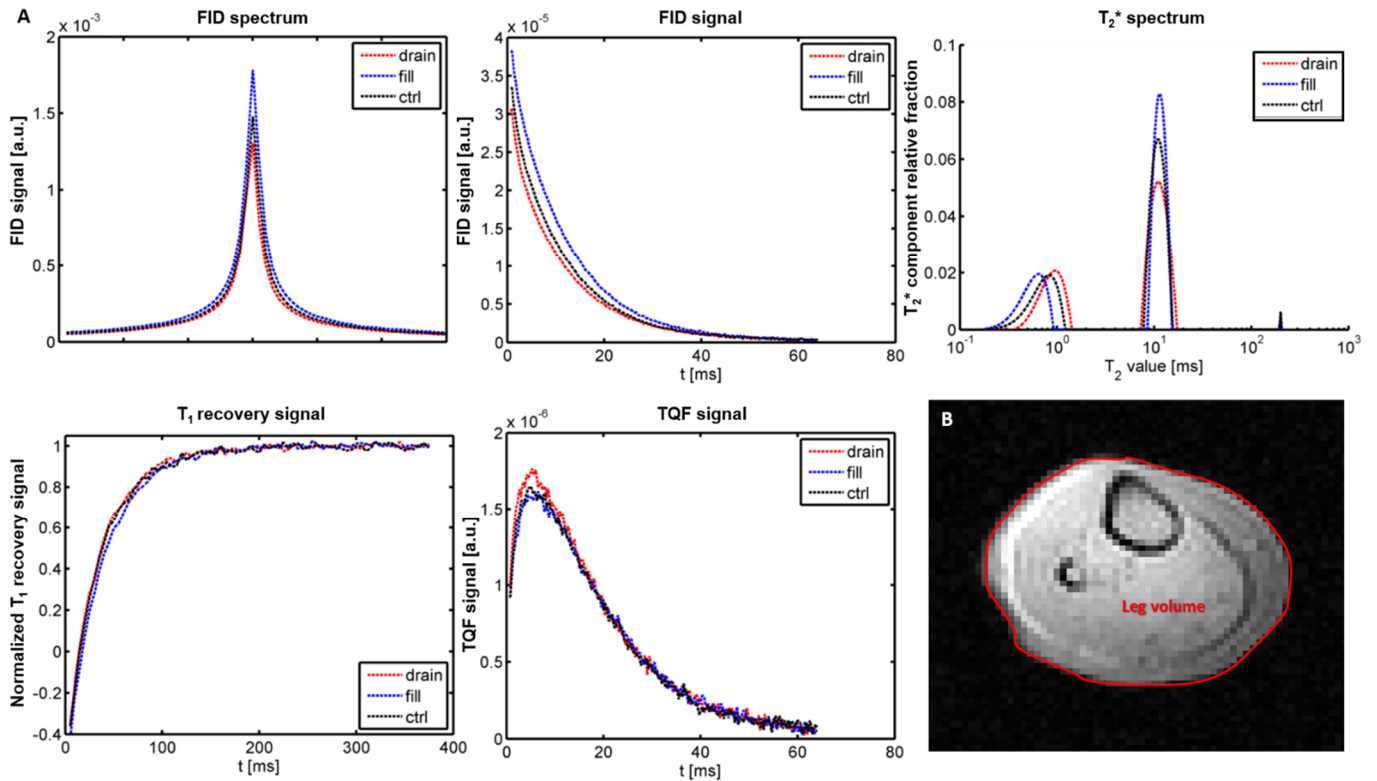


Figure 51: The sodium FID, TQF, and T_1 recovery signals measured in a healthy young 22-year-old female volunteer under different vascular filling conditions. **A)** The FID signal in the time domain is Fourier transformed to obtain the FID spectrum, which gives then the T_2^* spectrum by a T_2^* deconvolution of the FID signal decay. The T_2^* spectrum is plotted with logarithmically scaled abscise. The plots show the characteristic course of the vascular draining (red), vascular filling (blue), and control (black) conditions. **B)** The drawn ROI on the FLASH image of the right calf of the volunteer were used for the volume calculations.

Figure 52 summarizes the mean values of the different indices extracted from the ^{23}Na spectroscopic sequences and the leg volume of all subjects under the three different vascular filling conditions. Repeated measures ANOVA tests revealed significant variations of all the parameters between the three conditions ($p < 0.05$). At rest, the mean sodium FID signal was $2.5 \pm 0.3 \times 10^{-3}$ a.u., the global sodium T_1 was 33.8 ± 2.2 ms, the sodium TQF signal $1.6 \pm 0.3 \times 10^{-4}$ a.u., and the TQF/FID ration $6.3 \pm 1.0 \times 10^{-2}$. Mean ^{23}Na short T_2^* and long T_2^* were $T_{s,2}^* = 0.8 \pm 0.2$ ms and $T_{l,2}^* = 12.4 \pm 1.8$ ms with mean fraction of 32 % and 68 %, respectively. Over all subjects, the mean leg volume at rest was 995.7 ± 160.2 cm 3 .

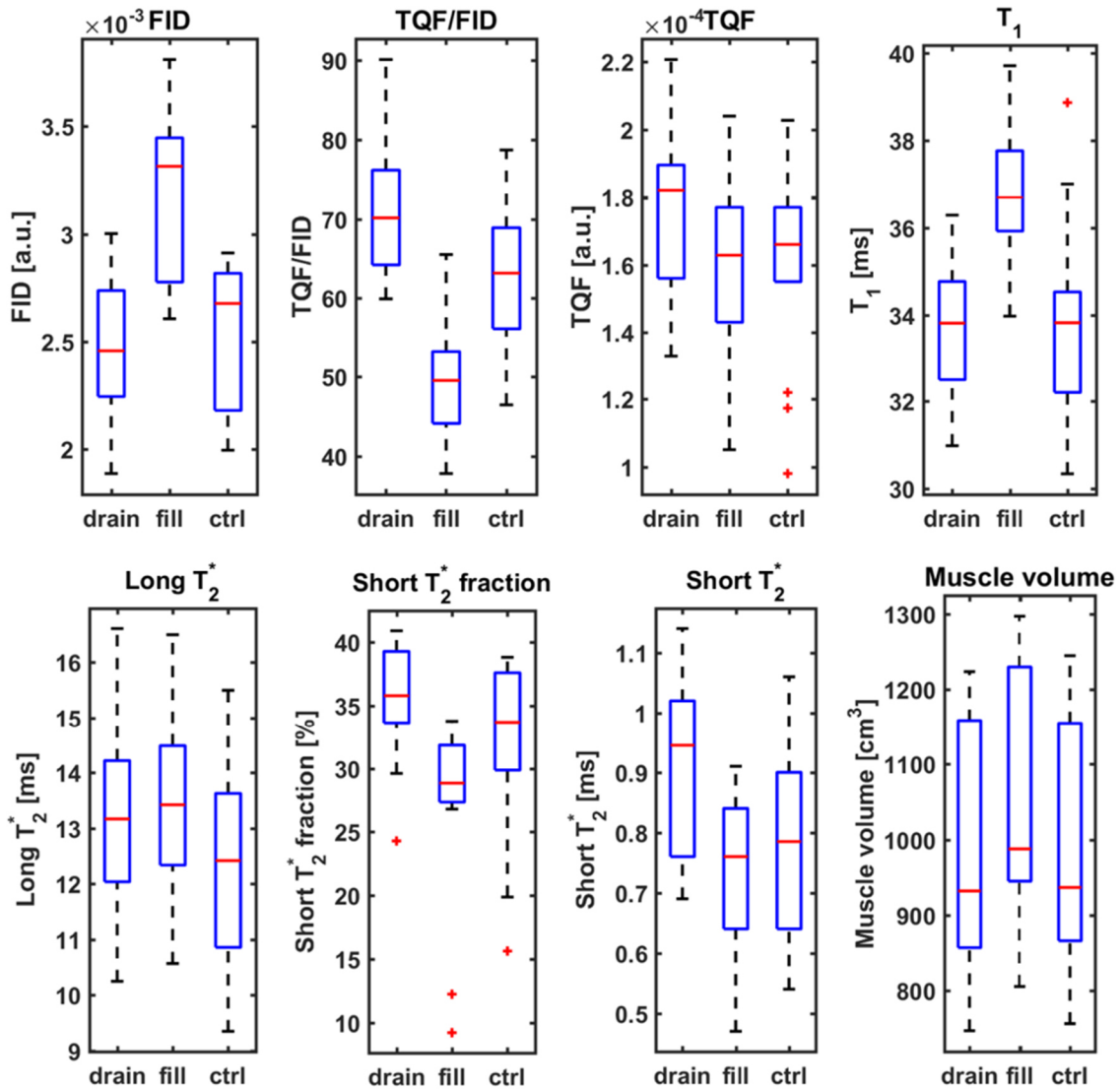


Figure 52: Evolution of different ^{23}Na parameters (FID signal, TQF/FID ratio, TQF signal, T_1 value, long T_2^* signal, short T_2^* fraction, and short T_2^* signal) and leg volume under three different vascular filling conditions (vascular draining: drain, vascular filling: fill, and control condition: ctrl). The boxes have lines at the lower quartile, median (red), and upper quartile with the length of the whiskers specified as 1.5 times the interquartile range. The red crosses mark outliers of the datasets.

All measured changes of the ^{23}Na variables and leg volume were calculated as percentage of change between the vascular filling or draining condition and the control condition (Figure 53). The ^{23}Na FID signal was non-significantly decreased under the drainage condition ($-3.8 \pm 7.4\%$) and significantly increased in the filling conditions ($+22.7 \pm 3.2\%$; $p < 0.05$), compared with the control condition. The opposite trend was observed for the short T_2^* fraction and the TQF/FID ratio, which both raised significantly during vascular draining ($+13.0 \pm 15.3\%$ and $+13.1 \pm 6.1\%$ respectively; both $p < 0.05$) and significantly decreased with vascular filling as compared to normal conditions ($-18.2 \pm 23.0\%$ and $-23.4 \pm 4.9\%$ respectively; both $p < 0.05$). In parallel, the long T_2^* value was significantly increased during draining and filling ($+6.4 \pm 5.6\%$; $p < 0.05$, $+7.9 \pm 4\%$; $p < 0.05$ respectively). The short T_2^* value increased significantly during vascular draining ($+18.0 \pm 14.7\%$; $p < 0.05$) and tends to

decrease during the filling condition ($-6.4 \pm 9.8 \%$). TQF signal was significantly higher with vascular draining ($+9.3 \pm 9.9 \%$; $p < 0.05$) and did not vary during vascular filling ($-0.7 \pm 5.7 \%$). On the contrary, significant increase was observed for global T_1 values and muscle volume during vascular filling (respectively $+8.2 \pm 3.1 \%$ and $+5.5 \pm 2.0 \%$; $p < 0.05$) while no significant alterations were detected during vascular draining (respectively $-0.2 \pm 3.5 \%$ and $-1.7 \pm 1.8 \%$).

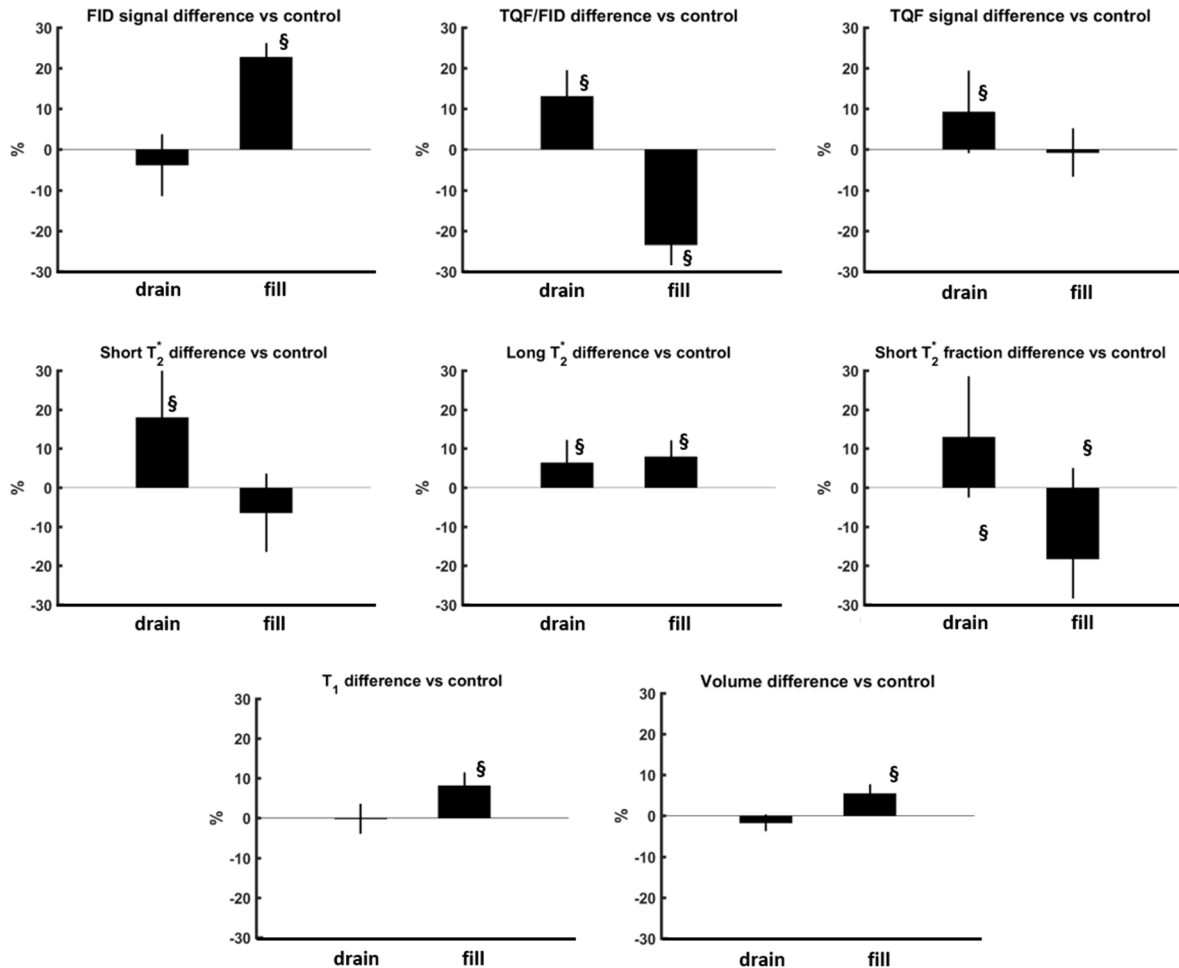


Figure 53: The percentages of change of the ^{23}Na parameters under vascular filling and vascular draining conditions compared with the control condition ($\$: p < 0.05$).

The changes in the FID signal and in muscle volume were significantly correlated ($R = 0.53$, $p < 0.001$), whereas no significant correlation was observed between the TQF signal changes and the muscle volume ($R = 0.17$, $p < 0.001$). Significant linear dependences between the TQF/FID ratio and T_1 values ($R = -0.53$, $p < 0.001$) and all the T_2^* parameters (short T_2^* fractions: $R = 0.78$; short T_2^* : $R = 0.77$; and long T_2^* : $R = 0.52$, $p < 0.001$). Figure 54 depicts a selection of correlations from different ^{23}Na parameters and the leg volume.

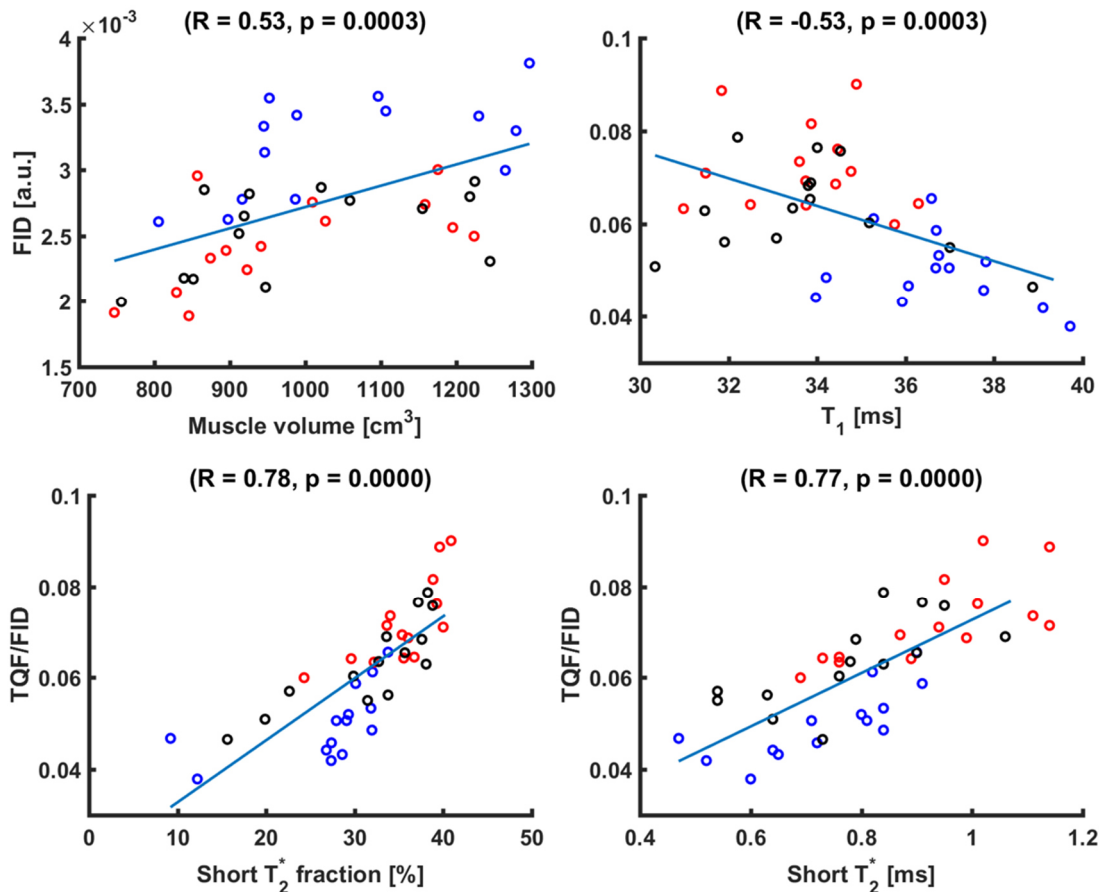


Figure 54: Correlation between FID signal and volume and between TQF/FID ratio and T_1 value. Additionally, highly significant correlations between TQF/FID ratio and short T_2^* fraction and short T_2^* values were detected. Data acquired under vascular draining and vascular filling are depicted as red and blue circles, respectively. Black circles represent the data points collected during the control condition.

Vascular filling changes monitored by ^1H NMR

The same vascular filling paradigm was applied to investigate the sensitivity of ^1H T_2 imaging to detect the extracellular volume fraction changes. Proton T_2 values and proton $T_2\text{w}$ signal intensities were measured for different muscles, from which a mean value over all muscles was determined. At rest, the mean T_2 was 43.3 ± 1.7 ms and the mean $T_2\text{w}$ intensity was 547.3 ± 16.3 a.u. Besides all measured changes of the ^1H T_2 and ^1H $T_2\text{w}$ intensities were calculated as percentage of change between the vascular filling or draining condition and the control condition. Only two muscles changed significantly their T_2 during the three conditions as determined by one-way ANOVA ($p < 0.05$). Post-hoc Bonferroni test disclosed that the T_2 augmented significantly in the ED and the TP muscles during vascular filling compared to the control condition (1.7 ± 1.2 % and 1.6 ± 0.9 % respectively). Furthermore, repeated measures ANOVA tests revealed significant variations of the $T_2\text{w}$ intensities between the three conditions for three muscles (ED, GL, and TA; $p < 0.05$). Post-hoc tests using the Bonferroni correction revealed that the $T_2\text{w}$ intensities of the ED and TA muscles increased significantly during vascular filling (3.8 ± 1.8 % and 4.8 ± 1.4 % respectively) compared to

the control condition, whereas the T_2w intensity of the GL muscle increased significantly during vascular draining (4.2 ± 2.5 %; $p < 0.05$) and shows no significant variation during the filling condition (1.0 ± 1.7 %; $p = 0.5$). The mean T_2 and the mean T_2w intensity taken over all muscles did not significantly differ between vascular filling conditions (one-way ANOVA test, Figure 55).

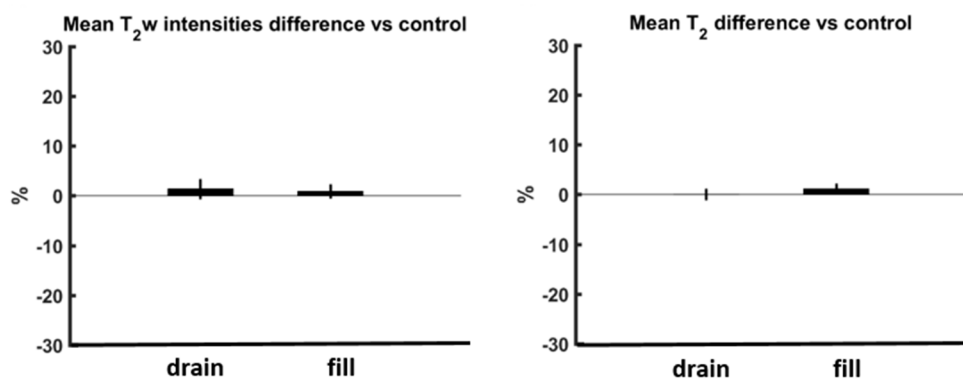


Figure 55: The percentages of change of the mean T_2w signal intensities and the mean T_2 for all muscles under the vascular filling and vascular draining conditions compared with the control condition

5.1.3 Discussion

The intent of this study was to assess whether ^{23}Na NMR could monitor acute changes in the extracellular volume fraction and compare the sensitivity of this method to standard proton T_2 imaging.

15-minute ischemia

In the first part of our study, we investigated the effect of a short-term ischemia on the sodium distribution in human skeletal muscle. This was an important preliminary step to make sure that the interpretation of the ^{23}Na signal changes during the vascular volume manipulations would not be complicated by concurrent alterations of the intracellular Na^+ distribution. Contrary to earlier findings in the ischemic heart [167], the total sodium content did not significantly vary within this short period of blood flow interruption. This can easily be understood considering the huge energy demand difference between the two organs in baseline conditions. Still, the TQF signal within the skeletal muscle tissue was decreased by approximately 6 % after the 15-minute ischemia.

The same ischemic protocol was already used in our laboratory to study its impact on muscle oxygenation and perfusion. The ADP concentration increased by 7 % compared to the resting state after 6 minutes of ischemia indicating already a slight impairment of the muscle ATP metabolism [168]. A reduced activity of the Na-K ATPase would result in an increased intracellular sodium content as well as cell swelling. Regarding the ^{23}Na nucleus, this effect would translate in an increase of the TQF signal [71], [169]. In our situation, the small decrease in TQF signal that was observed

during the 15-minute ischemia is contra-intuitive and was further investigated on animal models, where this ischemic paradigm was prolonged to 40 minutes (5.3).

Extracellular volume fraction changes

We then investigated the sensitivity of non-localized ^{23}Na spectroscopy to monitor acute changes in the extracellular volume fraction including vascular draining and vascular filling. We hypothesized that the rapid inflation of the air cuff above the knee to 250 mmHg does instantaneously stop the blood circulation, and has no further high impact on the intracellular sodium concentration during the protocol. We considered the alterations of the ^{23}Na signals being mainly due to changes of the extracellular volume fractions, or modification of interactions with macromolecules within the skeletal muscle tissue.

First, although the FID signal sums extra- and intracellular sodium content, changes in the extracellular volume could be clearly detected with this sequence. To our knowledge, only one group before us has performed a ^{23}Na NMRS study of the human skeletal muscle during short ischemic periods. Binzoni *et al.* analysed the interstitial fluid displacement in the gastrocnemius during short ischemic cycles. In their study, FID signal decreased during ischemia, followed by a rapid sodium increase during the hyperaemic reperfusion phase, which they attributed to volume changes in extracellular fluids [170]. In our work, we confirmed this hypothesis by the significant correlation observed between the muscle volume estimated with ^1H imaging and the ^{23}Na FID signal.

Besides, slowly tumbling Na^+ content in the muscle tissue was measured by acquisition of TQF spectra. Theoretically, as the TQF preparation filters out first and second order coherences, only ^{23}Na experiencing quadrupolar interactions are highlighted. The TQF signal is often associated to the sodium pool bound to macromolecules in the intracellular matrix. Changes in TQF signal are thus interpreted as modifications of intracellular Na^+ concentration or intracellular volume fraction. However, some studies have already demonstrated that the ^{23}Na TQF signal has contributions from the intra- as well as the extracellular Na^+ pool. In previous work, the proportion of the total TQF signal originating from the extracellular compartment was found to be between 30 % and 60 % of total TQF signal [109], [110], [171]. The TQF arising from the extracellular space is likely a result from ^{23}Na nuclei being in close interaction with the macromolecules, which could explain the large correlation between TQF signal variations and intracellular Na^+ content generally reported. Our results identified a small but significant increase of TQF signal under vascular draining as compared to control condition ($+9.3 \pm 9.9$ %), while no significant changes were noticed between vascular filling and control condition. This observation tends to confirm the hypothesis that part of TQF signal

reflects the ^{23}Na nuclei within the interstitial space, which is *a priori* the only compartment experiencing large modifications during our physiological paradigm. The increase of TQF signal likely reflects a more important interaction between ^{23}Na nucleus and interstitial macromolecules caused by the additional drainage with the elastic band.

Longitudinal and transverse relaxation time variations were evaluated during this protocol. Mono-exponential T_1 recovery and bi-exponential T_2^* decay behaviours were observed in the calf muscle tissues. This corresponds to what is generally observed in skeletal muscle [172], and is explained by a two-component model in fast-exchange regime with a pool of Na^+ ions within bulk isotropic medium and a pool of Na^+ ions bound to macromolecules experiencing quadrupolar interactions. Global ^{23}Na T_1 relaxation times were significantly increased during vascular filling but this parameter did not allow differentiating between vascular draining and control conditions. This parameter was not the most sensitive index to discriminate between the three vascular filling conditions of our physiological paradigm.

Mean T_2^* skeletal muscle tissue sodium relaxation times at rest were $T_{s,2}^* = 0.8 \pm 0.2$ ms (mean fraction of about 32 %) and $T_{l,2}^* = 12.4 \pm 1.8$ ms. These results are in agreement with previous findings. For example, at 1.5T in the skeletal muscle, Constantinides *et al.* found short and long T_2^* equal to 0.5 ± 2.1 ms and 12.3 ± 1.9 ms, respectively [143]. The short T_2^* fraction was increased during draining, decreased during vascular filling, and correlated significantly with the TQF/FID ratio. This confirms that the variation of the Na^+ content bound to macromolecules and experiencing quadrupolar interactions could be efficiently monitor with our spectroscopic protocol. Finally, the TQF/FID ratio was found to be the most robust and sensitive index to discriminate between the three conditions.

Comparison of ^{23}Na and ^1H NMR

Proton T_2 values in the muscle are elevated in different physiological and pathological scenarios such as necrosis and intracellular or interstitial oedema [127]. Methodological efforts improve the precision of the T_2 maps [15], [16], but yet reliable interpretation of the data remains limited by the lack of specificity of the measure to the different underlying mechanism [127], [155], [173]. In our study, we observed no significant changes of the mean T_2 or the mean T_2w signal intensity during vascular draining or vascular filling. Only three muscles showed significant alterations of the signal intensity or T_2 in one of the two conditions as compared to the control condition. More sophisticated proton multi-compartment T_2 methodologies have been applied and demonstrated a better sensitivity to extracellular volume variations. Using a localised proton ISIS-

CPMG sequence and a three-sites two-exchange model, authors provided quantitative information about histological tissues compartmentation and water exchange rates [17]. However, signal originating from lipids can hamper such a proton approach. The bias due to fat signal contamination can be avoided by using ^{23}Na NMR, which represents an advantage for the characterization of cell viability in chronically affected muscle tissues.

Despite significant changes in ^1H NMR parameters of some muscles during vascular volume changes; the ^{23}Na NMR approach seems to be much more sensitive to monitor acute changes in extracellular volume fractions. This can have an impact for monitoring the pathological alterations of patient groups showing alterations in the tissue cellular volume fraction (2.3).

Limitations

Problems arising with the ^{23}Na NMR method are low SNR and strong sensitivity of the TQF signal intensity on B_0 and B_1 inhomogeneities [105]. Depending on the organ, sensitivity of ^{23}Na NMR is 3000 to 20000 times smaller than the one of ^1H [174]. For a sufficient SNR, sodium imaging requires generally long acquisition times [83], [175]. TQF sequences suffer from even lower SNR (~1 order of magnitude lower than TSC sequences) and hence impose acquisition times incompatible with clinical use on patients [176]. Although promising, these imaging sequences should be further optimized to be frequently applied in clinical trials or natural history studies, since reduced acquisition time and patient comfort represent important issues when designing NMR protocols.

Furthermore, concerns about absolute concentrations constitute the major limitation of this NMRS method for a direct application to longitudinal monitoring of Na^+ during disease natural history studies or long-term clinical trials. We report this approach as highly sensitive to detect subtle modifications of sodium content or biodistribution when assessment is performed within a single spectroscopic session. Since the NMR signal does not only depend on spin concentration, but also on coil quality factor, on B_1^+ and B_0 field, all these parameters have to be taken into account for quantification. So far, phantoms with known Na^+ concentrations have been used as external references to quantify the sodium content *in vivo* in several ^{23}Na NMR imaging studies [14], [72], [143], [177]. This idea was extended to our protocol by using an external phantom containing a shifting reagent to resolve the peak of the phantom separately and is presented in the next section (5.2). Even then, the B_0 and B_1 field inhomogeneities issue has to be carefully addressed, which is not a trivial task.

Moreover, due to the non-localized approach, sodium pools from other tissue such as skin, tendons, and ligaments contributed to a certain extent to our results. Although its contribution is

obviously smaller than the one of skeletal muscle given the size difference of the organs, its real impact on our findings is still to be studied. One possible solution would be to use localized spectroscopy methods. Nevertheless, classical schemes such as point resolved spatially localized spectroscopy (PRESS) [178] would lead to too long TEs by preventing the acquisition of fast decaying ^{23}Na signals. Another localised method, namely ISIS [67], would be an alternative to acquire the sodium spectra including the short ^{23}Na T_2^* components in a defined region.

5.2 Signal quantification for non-localized ^{23}Na NMR spectroscopy

For the next step towards a successful implementation in (pre-) clinical protocols, we evaluated an approach to calibrate and quantify the ^{23}Na signal from the non-localized spectroscopy protocol. A standardized and reliable approach is a pre-requisite to quantify the signals either to compare two distinct groups or to monitor muscle response to interventions in the course of longitudinal studies.

5.2.1 Materials and methods

Study design and NMR protocol

The right calf of 19 healthy volunteers (aged 29.5 ± 9.7 years, seven women and twelve men) was scanned at 3T (PRISMA; SIEMENS Healthineers, Erlangen, Germany) under different vascular filling conditions (see protocol 2 in 5.1.1). The leg was placed inside the coil on a holder with a SR phantom (24 mM TmDOTP⁵⁻ in 140 mM NaCl) to calibrate the FID and TQF signal originating from the leg (Figure 56A). The FID and TQF signals were acquired with the same parameters as in 5.1.1 with NEX = 100 ($T_{\text{acq}} = 1$ min) and NEX = 1500 ($T_{\text{acq}} = 2$ min 30 s), respectively. Additionally, a 3D 3-point Dixon sequence was performed at the end of the control condition using the body coil for magnetization excitation and signal reception with the following parameters: TR = 10 ms, 2 x 2 TEs = 2.75/3.95 ms and 2.75/5.15 ms, FA = 3° and 64 slices of 5 mm thickness and resolution = 1.3 x 1.3 mm². The slices were centred in the iso-centre at the magnet ($2 \times T_{\text{acq}} = 1$ min 36 s).

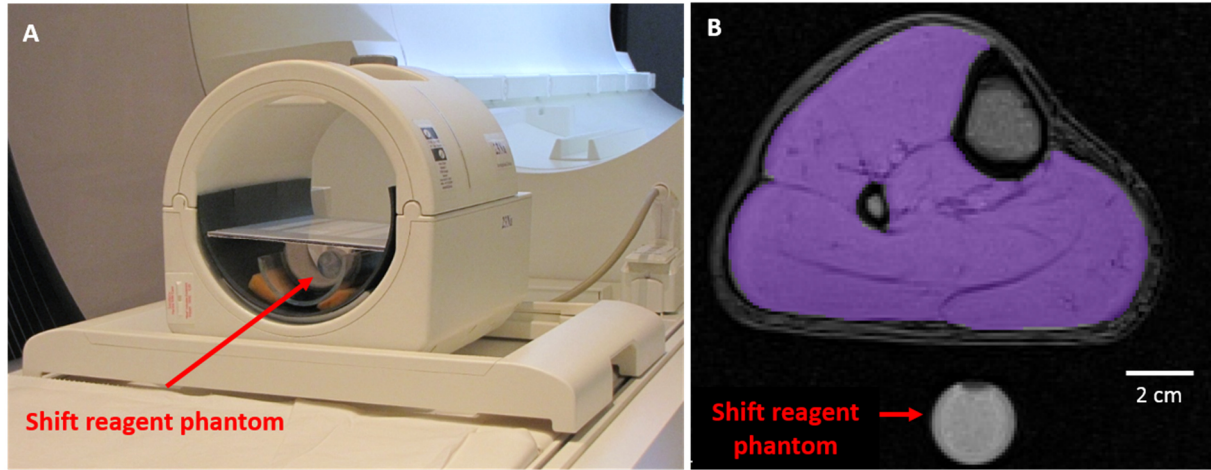


Figure 56: Calibration of the *in vivo* ^{23}Na signal: **A)** Costume-made linear volume ^{23}Na leg coil with the leg holder and shift reagent phantom used as external reference. **B)** Dixon image ($TE = 2.75$ ms) of the leg and SR phantom. The ROI used for volume analysis was traced over all muscles (in violet) excluding bone, skin, and subcutaneous fat.

Quantification of ^{23}Na NMR signals

^{23}Na NMR spectra were processed as described in 5.1.1. Total muscle volume estimation was performed on the water maps derived from the 3-point Dixon images. ROIs were manually drawn on the muscle excluding bones on the 31 central slices (Figure 56B) to cover the whole leg inside the coil. Muscle volumes were calculated based on the exported ROIs (muscle area \times slice thickness) for each slice that was acquired inside the ^{23}Na coil.

The muscle volume ($\text{volume}_{\text{FID,leg}}$) per slice derived from the water map was then weighted with the spatial ^{23}Na coil sensitivity in the z-direction that was obtained by *in vitro* ^{23}Na imaging of a NaCl filled bottle (Figure 57). The six central ^1H slices were weighted with a factor one. The more lateral the slices, the lower was the weighting factor, as the coil sensitivity decreases drastically at the periphery of the coil. The TSC of the corrected leg volume was calculated on the known volume and Na^+ concentration of the SR phantom as following:

$$TSC = \frac{[\text{SR}] \times \text{volume}_{\text{SR}}}{\text{FID}_{\text{SR}}} \times \frac{\text{FID}_{\text{leg}}}{\text{volume}_{\text{FID,leg}}}$$

Where $[\text{SR}]$ is the concentration of NaCl in the SR phantom (24 mM), $\text{volume}_{\text{SR}}$ the volume of the SR phantom (56 ml), and FID_{SR} and FID_{leg} the ^{23}Na signal originating from the SR phantom and leg, respectively. For ICW, leg volume was weighted with the coil sensitivity to the fourth power due to the FID signal dependency of $\sin^4(\theta)$ after triple quantum filtering (3.3.3) to obtain the sensitivity-weighted volume $\text{volume}_{\text{TQF,leg}}$. The ICW of the volume corrected leg was calculated using the FID signal from the SR phantom as followed:

$$ICW = \frac{[\text{SR}] \times \text{volume}_{\text{SR}}}{\text{FID}_{\text{SR}}} \times \frac{\text{TQF}_{\text{leg}}}{\text{volume}_{\text{TQF,leg}}}$$

Where $[\text{SR}]$ is the concentration of NaCl in the SR phantom (24 mM), $\text{volume}_{\text{SR}}$ the volume of the SR phantom (56 ml), and FID_{SR} and TQF_{leg} the FID and TQF ^{23}Na signal originating from the SR phantom and leg, respectively.

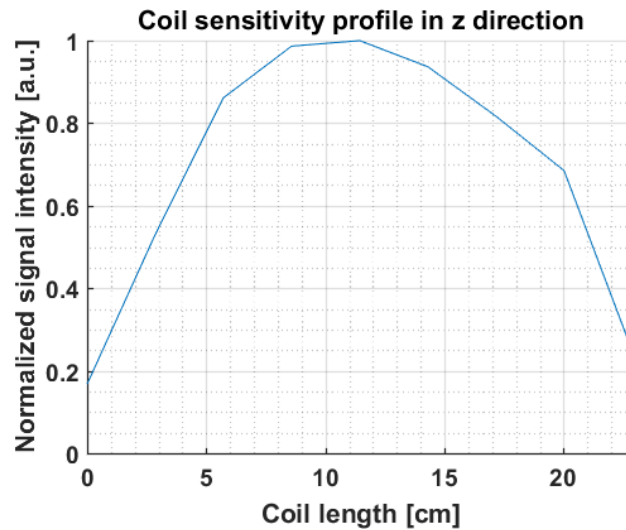


Figure 57: Sensitivity profile of the ^{23}Na coil along the length measured on a 140 mM NaCl containing bottle with a diameter of 9 cm.

Statistical analysis

Statistical analysis was performed using ANOVA with repeated measures and Bonferroni post-hoc tests for pairwise comparisons to evaluate significant differences between the different conditions. Pearson correlations analysed the relationship between the variables. In all statistical tests, $p < 0.05$ was considered statistically significant.

5.2.2 Results

Figure 58 shows the FID and TQF spectre acquired on one subject at control condition. The SR peak is only visible in the FID spectrum since the TQF filters the signal from motionally non-restricted environment out.

Figure 59 summarizes the mean values of ^{23}Na FID and TQF signals and the calculated TSC and ICW of all subjects under the three different vascular filling conditions. Repeated measures ANOVA tests revealed significant variations of all the parameters between the three conditions ($p < 0.05$). At rest, the mean sodium FID signal originating from the leg was 0.075 ± 0.013 a.u., the mean sodium FID signal originating from the SR was 0.007 ± 0.001 a.u. and the sodium TQF signal 0.0056 ± 0.0005 a.u.. The mean TSC of the leg was 14.99 ± 1.99 mM and the mean ICW 1.54 ± 0.12 a.u..

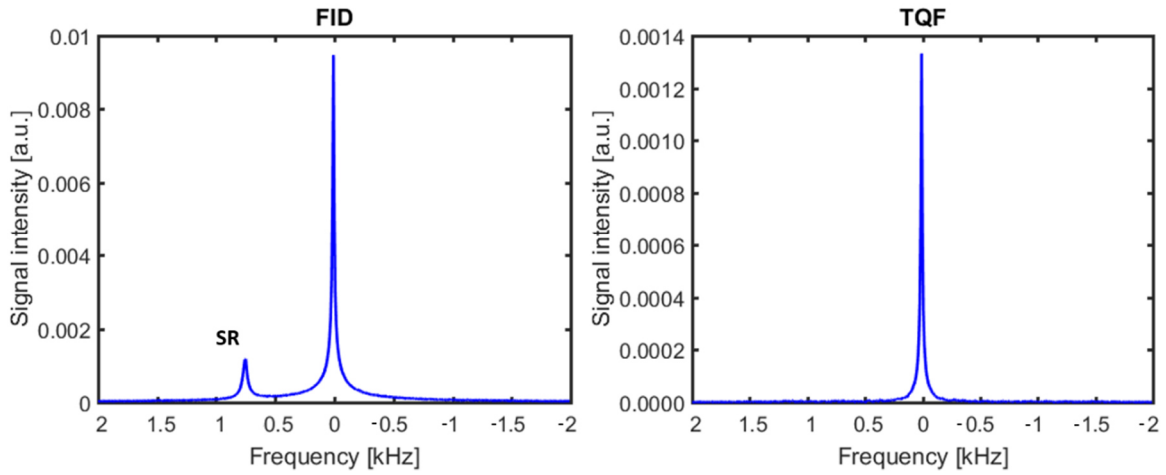


Figure 58: The sodium FID and TQF signals measured in a healthy young 23-year-old female volunteer at control condition. Notice the presence at around 0.7 kHz of the SR in the FID spectrum and its absence in the TQF spectre.

During vascular draining, the FID signal changed by $3.09 \pm 4.93\%$ and the TQF signal increased significantly by $2.6 \pm 1.41\%$ ($p < 0.05$). TSC changed by $1.3 \pm 6.15\%$ and ICW increased by $2.6 \pm 1.41\%$ ($p < 0.05$). During the vascular filling, FID increased significantly by $15.89 \pm 4.39\%$ ($p < 0.05$), TQF changed by $0.27 \pm 1.18\%$, TSC by $20.76 \pm 4.92\%$ ($p < 0.05$), and ICW by $0.27 \pm 1.18\%$ ($p < 0.05$).

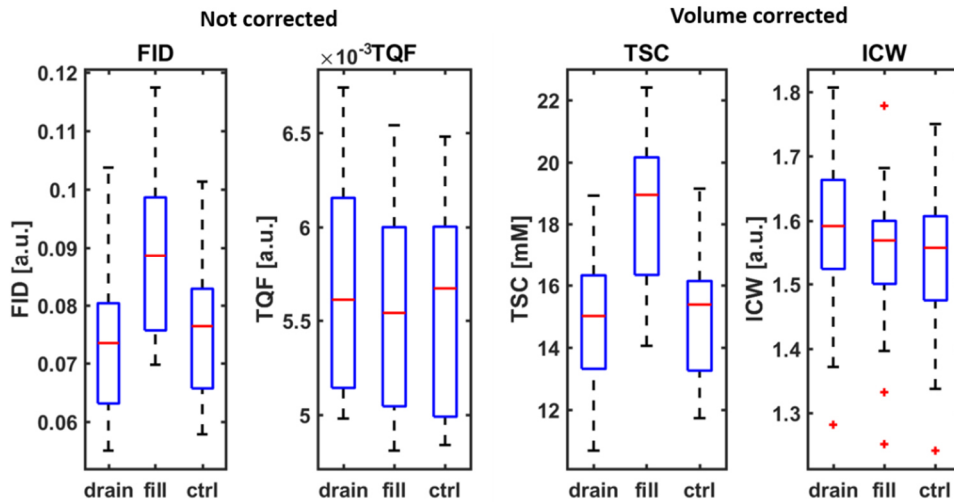


Figure 59: Evolution of ^{23}Na FID signal and TQF signal before volume correction under three different vascular filling conditions (vascular draining: drain, vascular filling: fill, and control condition: ctrl). Based on the ^{23}Na signals, TSC and ICW values were calculated for the three different vascular filling conditions taking the muscle volume and coil sensitivity into account. The boxes have lines at the lower quartile, median (red), and upper quartile with the length of the whiskers specified as 1.5 times the interquartile range. The red crosses mark outliers of the datasets.

The changes in the FID and TQF signals correlated significantly with the muscle volume ($R = 0.56$ and $R = 0.78$, respectively; both $p < 0.005$). Figure 60 illustrates the independence of muscle volume after the volume and coil-sensitivity correction step of the sodium indices. TSC and ICW showed both no correlation with the muscle volume ($R = 0.11$ with $p = 0.4$ and $R = -0.16$ with $p = 0.22$, respectively).

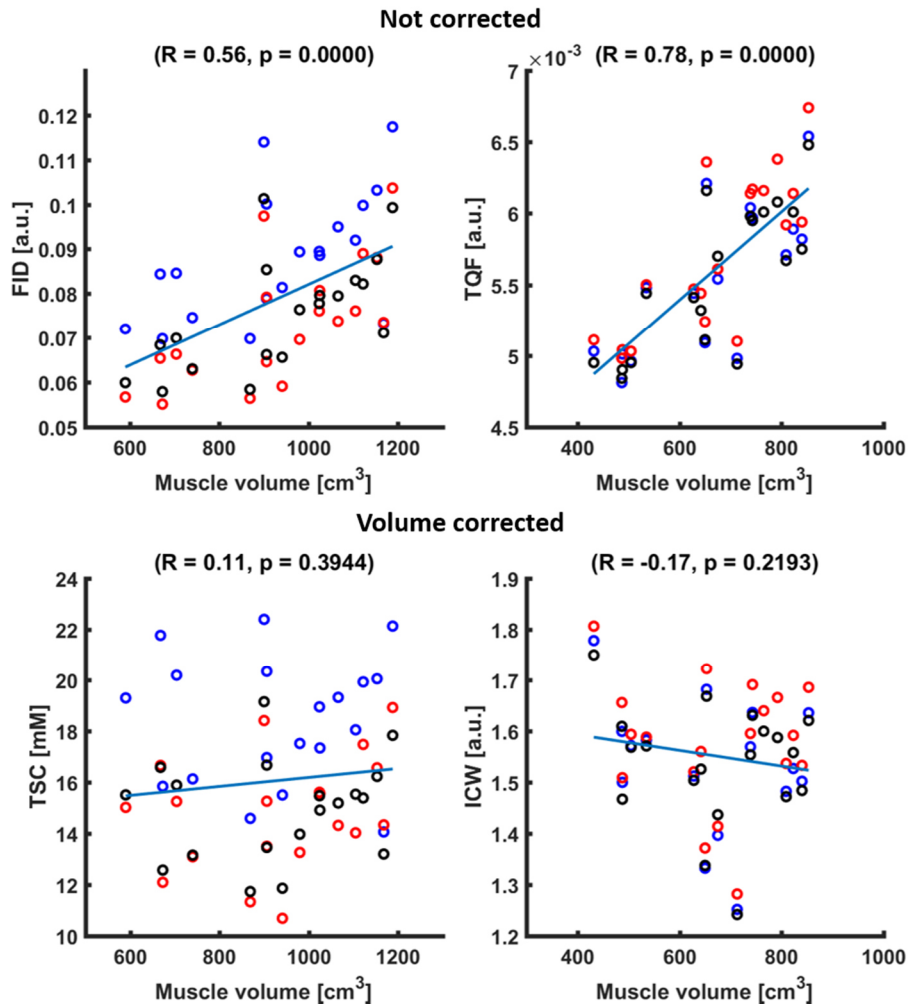


Figure 60: Important correlations of ^{23}Na FID and TQF signal with muscle volume were detected. After correction, TSC and ICW showed no correlation with the muscle volume. Data acquired under vascular draining and vascular filling are depicted as red and blue circles, respectively. Black circles represent the data points collected during the control condition.

5.2.3 Discussion

The intent of this study was to establish a method to calibrate the non-localized ^{23}Na signals, which can then be applied to quantify changes in the sodium content or distribution. An external calibration phantom with known sodium concentration and doped with SR was used to calibrate the ^{23}Na signals originating from the leg. To evaluate the method, we choose the same physiological protocol as in 5.1 to change the sodium content and distribution in the leg.

In 5.1, we reported a mean ^{23}Na FID signal of $2.5 \pm 0.3 \times 10^{-3}$ a.u. and a mean ^{23}Na TQF signal of $1.6 \pm 0.3 \times 10^{-4}$ a.u. at rest, which are more than an order smaller than the values measured during the quantification study. This is due the NMR system upgrade from TIM TRIO to PRISMA that took place between the two studies. Additionally, the Laboratory obtained a new ^{23}Na knee coil with a higher B_1 homogeneity. However, the percentage of change between the vascular filling or draining conditions and the control condition of the FID and TQF remained similar after the system change.

Under the TIM TRIO and the old ^{23}Na coil, the ^{23}Na FID signal was non-significantly decreased under the drainage condition ($-3.8 \pm 7.4 \%$) and significantly increased in the filling conditions ($+22.7 \pm 3.2 \%$; $p < 0.05$), compared with the control condition. TQF signal was significantly higher with vascular draining ($+9.3 \pm 9.9 \%$; $p < 0.05$) and did not vary during vascular filling ($-0.7 \pm 5.7 \%$). After the upgrade and with the new ^{23}Na coil, the FID signal changed by $-3.09 \pm 4.93\%$ under the vascular draining condition and increased significantly by $+15.89 \pm 4.39 \%$ ($p < 0.05$). In parallel, TQF signal increased significantly by $+2.6 \pm 1.41 \%$ ($p < 0.05$) during draining and did not vary during vascular filling ($0.27 \pm 1.18 \%$). The smaller changes in the TQF signals in the current study go hand in hand with much smaller SD and thus leading to significant increase of the TQF signal during draining compared to the control condition as it was observed before. Thus, the current study underlines also the reproducibility of the proposed non-localized ^{23}Na protocol.

The non-localized NMR signal depends highly on the charge present in the coil. This can be seen for example in the high correlation between the SR signal having a constant NaCl concentration and the muscle volume ($R^2 = 0.9$). The recorded signals thus have to be corrected for the changing load that is the volume of the leg inside the coil. As explained in 5.1.3, we considered that the muscle tissue is the main source of the sodium signal and we thus decided to take the muscle tissue volume from the water map to correct for the coil load. The TQF showed a higher correlation ($R = 0.78$) with the muscle tissue volume than the FID signal ($R = 0.56$). This might be partly because the ^{23}Na FID signal arises also from the subcutaneous fat and blood vessels, the latter exhibiting much higher sodium concentrations than skeletal muscle tissue. During the coherence pathway filtering, these contributions from freely moving sodium ions are suppressed and the ^{23}Na TQF signal might arise primarily from the skeletal muscle (3.3.3). TQF imaging of the leg has indeed shown an excellent suppression of intravascular ^{23}Na signal (8.2, not yet published).

After the signal calibration that takes the coil sensitivity and the muscle volume into account, the calculated TSC and ICW values showed no correlation anymore with the muscle volume. They nevertheless exhibited the same changes under the three different vascular filling conditions as the uncorrected ^{23}Na signals. An average TSC of 15 mM is in close accordance with the TSC values measured by NMRI in 4.6.3 (15.3 to 17.6 mM depending on the muscle).

5.3 Impact of prolonged ischemia in murine skeletal muscle monitored by ^{23}Na and ^1H NMR

In 5.1, we reported non-significant changes in the ^{23}Na FID signal in the human leg during a 15-minute ischemia, whereas the ^{23}Na TQF signal decreased by more than 5 % at the end of the ischemic period. We further wanted to investigate the behaviour of the ^{23}Na signals on an animal model, where we could prolong the ischemic paradigm to 40 minutes and compare it to ^1H T_2 changes.

5.3.1 Materials and methods

Study design and NMR protocol

The NMR study was performed on male C57BL6 mice, which were bought from the Jackson Laboratory. The study was approved by the French Ministry of Higher Education and Research according to the European directive 2010/63/EU. The rodents received food and drink ad libitum.

The C57BL6 mice were investigated at an age of three months. Animals were initially anesthetized with 4 % isoflurane, before we placed subcutaneous surgical threads above the knee of their left leg. The mice were then positioned onto the custom-made bed and their legs were centred at the iso-centre of the magnet. Ischemia was then achieved by a compression with the threads that were connected to a 500 g weight outside the magnet to completely block blood flow. During the NMR protocol, animals continued to be under anaesthesia using a breathing mask (1.5 – 2 % isoflurane in O_2 at 1.5 l/min) and held on a heating pad at 42 °C to keep their body temperature constant. Animal respiration was monitored externally during imaging with a breathing surface pad.

The lower legs of four other mice were scanned using the ^1H protocol, which consisted of imaging and localised spectroscopy sequences to measure global and water T_2 . MSME imaging was performed using the following parameters: 32 echoes with TE = 5.15 - 164.82 ms, TR = 3500 ms, resolution = 0.2 x 0.2 mm², slice thickness = 1 mm, and T_{acq} = 2 min 20 s. In addition, the ISIS-CPMG sequence, which has been implemented on the 3T clinical scanner [17], was also programmed on the 7T preclinical scanner by combining the existing CPMG sequence of Bruker with the ISIS module. T_2 spectra of the TA muscle were obtained with the following parameters: 500 echoes with echo space (ES) = 1 ms, TR = 4 s, voxel size = 1.5 x 1.5 x 5 mm³, NEX = 2, acquisition BW = 50 kHz and data points = 32, and T_{acq} = 1 min 4 s.

The lower legs of four other mice were scanned using the ^{23}Na protocol, which comprised non-localized FID and TQF sequences. The FID was acquired with the following parameters:

acquisition delay = 50 μs , TR = 200 ms, NEX = 250, FA = 90°, BW = 10 kHz, vector size = 300, and T_{acq} = 50 s. TQF experiments used following parameters: τ_1 = 4 ms, TR = 200 ms, NEX = 600, FA = 90°, BW = 10 kHz, vector size = 300, and T_{acq} = 2 min. At the beginning and after ischemia, a FLASH sequence was acquired to track a possible leg movement and visualize the blocking of the blood vessels (1 slice with FA = 10°, TE = 2.6 ms, TR = 7.3 ms, resolution = 0.1 x 0.1 mm², slice thickness = 1 mm, NEX = 200, BW = 50 kHz, and T_{acq} = 2 min 11 s).

Analysis of ^{23}Na and ^1H NMR data

The T_2 values obtained from the MSME were quantified by manually tracing ROI within muscle groups (anterior, medial, and posterior region). Due to the absence of fat-infiltration, the T_2 decay of the MSME sequence was calculated with a mono-exponential fit (excluding first two echoes) to obtain the global T_2 . The ISIS-CPMG T_2 decay was fitted with a bi-exponential model resulting in a short and long T_2 value and their relative fractions. The ^{23}Na FID and TQF signals were processed as described in 4.6.1. The signal intensities were normalized to their first time point.

Statistical analysis

Statistical analysis was performed using ANOVA with repeated measures and Bonferroni post-hoc tests for pairwise comparisons to evaluate significant differences during the course of the ischemia. A $p < 0.05$ was considered statistically significant.

5.3.2 Results

FID signal, TQF signal, and TQF/FID ratio were modified during the course of the ischemia (Figure 61), with the FID signal increasing by around 5 %, the TQF signal decreasing on average by 10 %, and the resulting TQF/FID ratio decreasing by 15 % after 40 minutes of ischemia. The TQF/FID ratio changed significantly from start to end of ischemia ($p < 0.05$). The leg movement due to the heavy external weight during the course of the ischemia was negligible small.

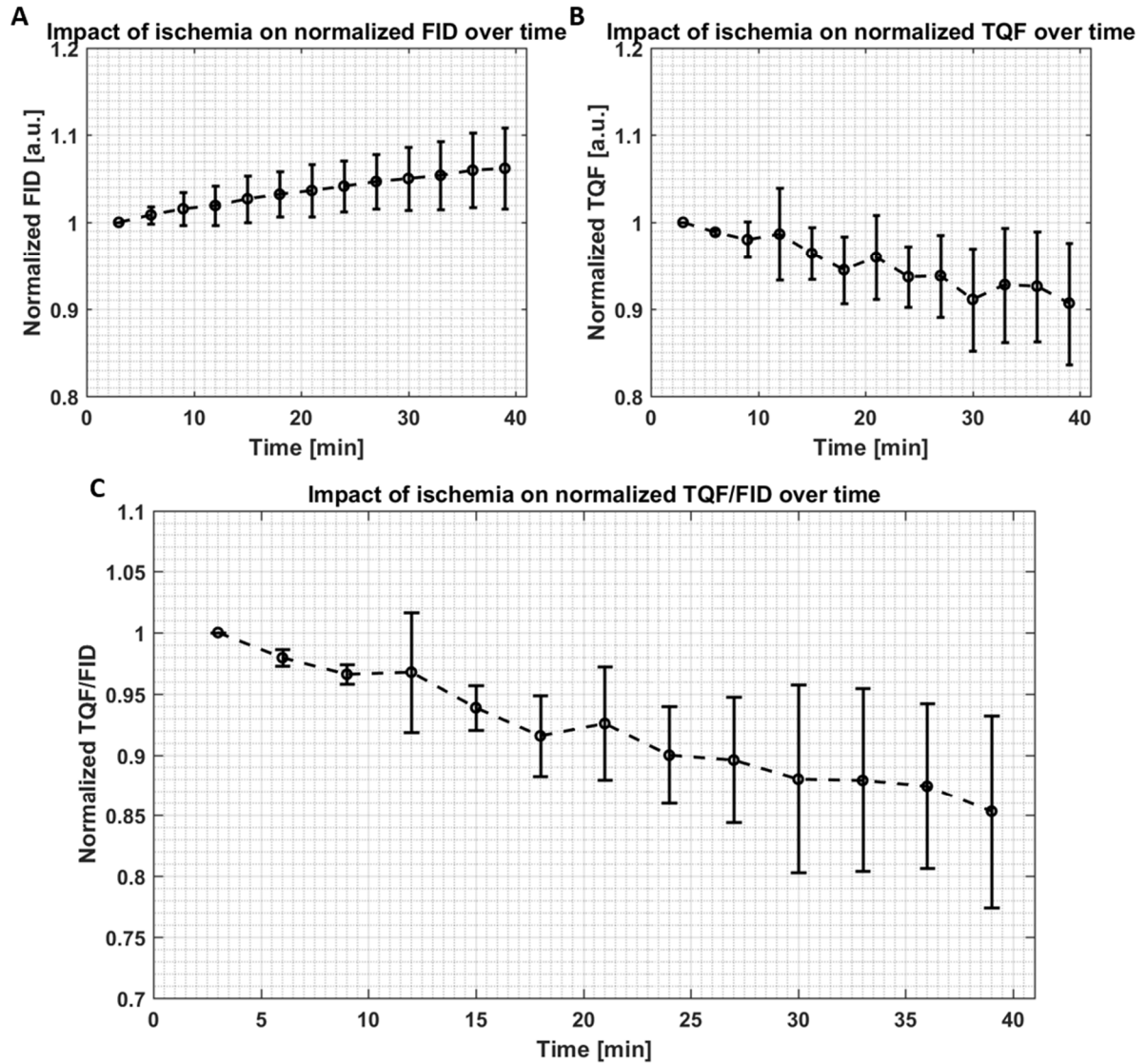


Figure 61: The effect of prolonged ischemia *in vivo* in skeletal muscle measured by ^{23}Na NMR. Evolution of the **A)** ^{23}Na FID signal, **B)** ^{23}Na TQF signal, and **C)** TQF/FID ratio during a 40-minute ischemia in skeletal muscle tissue (normalized with first time point, presented as mean with SD bars, $n = 4$).

In the same time course, the mean (weighted over all muscles) of the global ^1H T_2 increased significantly from 26.3 ± 1.6 ms to 29.3 ± 1.3 ms (Figure 62A, $p < 0.05$). Besides, the ISIS-CPMG T_2 decay exhibited an increase in water short T_2 from 25.0 ± 0.5 ms to 27.9 ± 0.4 ms ($p < 0.05$) with constant water long T_2 (beginning 92.8 ± 19.7 ms vs end 90.5 ± 6.3 ms) and stable relative fractions (beginning 94.9 ± 1.7 % vs end 93.7 ± 1.1 %) (see Figure 62B-D).

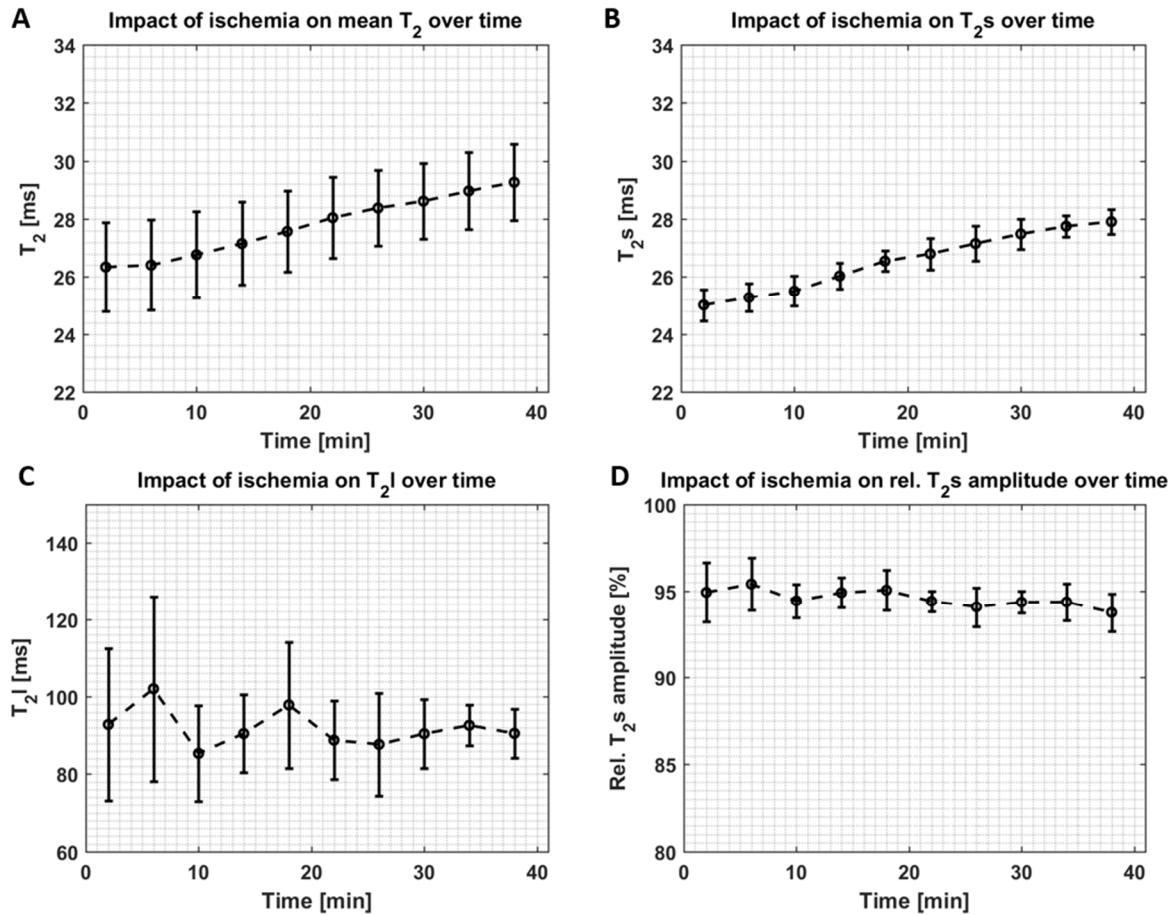


Figure 62: The effect of prolonged ischemia *in vivo* in skeletal muscle measured by ^1H NMR. Evolution of **A)** the mean T_2 of the leg muscles measured by a MSME sequence during ischemia and of **B)** the short and **C)** long T_2 with **D)** the relative short T_2 amplitude obtained by a biexponential fit of the ISIS-CPMG signal decay during ischemia (presented as mean with SD bars, $n = 4$).

5.3.3 Discussion

The ^{23}Na data are in line with our former ischemia experiments carried out in humans (5.1). While the FID seemed to be stable during the short ischemia in human, the total sodium signal yet increased after 40 minutes by around 5 % in mice. In the same time course, the TQF signal decreased by around 10 %. These observations in mice demonstrated that the sodium distribution was altered since the TQF/FID ratio declined while global and short T_2 of ^1H increased and the relative volume fraction of the short T_2 stayed constant during the whole period of ischemia.

Ten years ago, Babsky *et al.* [179] studied the effect of prolonged global ischemia on Na^+ concentrations in rat skeletal muscle *post mortem* over four hours. In their work, the total Na^+ measured by an FID was unchanged compared to the pre-ischemic level during the first two hours of ischemia followed by a significant increase afterwards by 8 to 16 %. Since the sodium concentration in extracellular space, which makes up about 23 % of the tissue [180], is more than 10 fold higher than the sodium concentration in the intracellular space, more than 75 % of the tissue ^{23}Na signal

originates from the extracellular space. To monitor changes in the intracellular sodium concentration, they acquired the ^{23}Na FID signal using a shift reagent in a second group of rats to separate the intra- from the extracellular ^{23}Na signals. Ischemia caused a progressive increase in the $[\text{Na}^+]_i$ but only after the first hour of ischemia, with a parallel decrease of the extracellular sodium concentration. They reasoned that the cessation of the Na-K ATPase function and influx of Na^+ causes the three-fold increase of $[\text{Na}^+]_i$.

In SR experiments with rats, another group reported also that the intracellular sodium concentration increased monotonically six-fold during eleven hours of ischemia [181]. During the first 90 minutes of ischemia the total ^{23}Na signal increased by 10 %. While the extracellular ^{23}Na signal increased slightly during the first 30 minutes and remained then constant, the $[\text{Na}^+]_i$ doubled to its original value decreasing the transmembrane sodium gradient. They explained the initial total ^{23}Na signal increase by an augmentation of the extracellular fluid and correlated the peak area temporally and quantitatively with the decrease in the total peak area of the ^{31}P NMR spectrum. During ischemia, energy stores are mainly used to maintain membrane potential and ion compartmentalization [182]. Creatine phosphate, which acts as buffer in skeletal muscle under absence of oxygen and free fatty acids, is depleted to maintain an adequate rate of ATP production necessary for the activity of the Na-K ATPase. In concurrent ^{31}P and ^{23}Na NMR experiments [78], the intracellular sodium and phosphorus signals in rat leg muscle were monitored during ischemia. The phosphorylation potential was falling slowly until a critical value that was linked to the energetic failure of the Na-K ATPase triggering an increase of the intracellular sodium signal. The ^{31}P spectra showed the effects of ischemia with an increase of the P_i peak and decrease of the PCr peak while intracellular acidosis gradually increased. After more than one hour, high-energy phosphorus metabolites were depleted and ATP started to decrease while the intracellular sodium initially at a constant level started to increase. Although, this study used different SR and ischemic protocols with most of the time only one animal, it illustrated that the intracellular ^{23}Na signal stays during ischemia initially constant until the cessation of the Na-K ATPase function. We cannot be sure if we already reached this critical point after 40 minutes of ischemia with the mice. Interleaved or at least consecutive ^{31}P and ^{23}Na NMR acquisition would have been necessary to exclude clearly the failure of the Na-K ATPase. Our laboratory previously communicated a PCr depletion of around 60 % in mice during a 30-minute ischemia [183]. This observation could indicate that ATP stores are still buffered during the present time course, which likely ensured the activity of the Na-K ATPase.

In this study, we additionally monitored the effect of prolonged ischemia on skeletal muscle tissue by ^1H NMR to get an idea about changes in the fluid distribution. Histology has related the

increased global ^1H T_2 values during ischemia to muscle fibres swelling and interstitial spaces widening [184]. Additionally, the increase in short water T_2 with constant relative fractions points to a redistribution of water within the extravascular compartment [17]. The parallel changes in ^1H and ^{23}Na indices suggest that they are coupled or at least related, and likely reflect cell swelling with a stable vascular volume.

The observed decrease in the TQF/FID seems to be first contra intuitive as we expect raising or at least stable intracellular sodium concentrations (and TQF/FID ratio). Although, the TQF sequence is frequently termed as intracellular weighted, it also has significant contributions from the extracellular space (3.3.3). FID experiments with SR and TQF experiments therefore do not see exactly the same sodium species. In general, the ^{23}Na TQF/FID ratio depends on the local Na^+ concentration, the water compartment size, as well as on the number of accessible “binding” sites. Filtering by TQF leaves only the Na^+ pool subjected to interactions with macromolecules, partly but yet not exclusively found in the intracellular matrix [110]. Thus, despite the possible increase in intracellular sodium concentration and decreasing transmembrane sodium gradient [181], which we cannot completely exclude, a redistribution of extravascular water between interstitial and intracellular spaces was likely to decrease sodium-protein interactions as a result of the higher mobility while the number of accessible “binding” sites probably stayed constant. Consequently, quadrupolar interactions decreased and so did the TQF ^{23}Na signal, and the TQF/FID ^{23}Na ratio. For further experiments, it would be interesting to combine the present protocol first with SR and second with ^{31}P NMR acquisitions for a better understanding of the underlying mechanisms.

5.4 Double- and triple-quantum filtered ^{23}Na NMR in human resting skeletal muscle tissue

^{23}Na NMRI has been used as a tool to determine the TSC in healthy and diseased tissues (3.4.2). Efforts have been also made to distinguish the intracellular from extracellular ^{23}Na signal. Nevertheless, the complete potential of ^{23}Na NMR still needs to be exploited since by using dedicated sequences insights in the Na^+ molecular environment can be assessed. The quadrupole interactions between the ^{23}Na nuclei and their environment lead to different transitions between the four energy levels (3.3.3).

DQF [91] and TQF [144] NMR methods have been proposed to exclusively detect Na^+ ions within motional restricted areas. Moreover, DQF-MA only detects signal from Na^+ interacting with anisotropic structures, e.g. fibres [95]. Changes in the order could present a useful marker in some pathologies. While TQF sequences have been already applied several times on human subjects to

study for example the brain [107], [176], [185] and muscle [144] tissue, the use of DQF-MA ^{23}Na NMR is even less exploited.

Here, we compared both methods, DQF-MA and TQF, to characterize the microstructure of human muscle tissue. As in the aforementioned section of the thesis, non-selective FID sampling was conducted to enable fast data acquisition. Moreover, we wanted to establish reference values of lower leg muscle tissue of a healthy population.

5.4.1 Materials and methods

Nine healthy volunteers (aged 24.7 ± 1.7 years, four women and five man) were scanned at the Institute of Radiology in Erlangen. Data were acquired on the right calf after a resting period of 30 minutes in supine position to avoid important fluid distributions during NMR acquisition due to postural changes.

The FID was acquired with the following parameters: TR = 300 ms, NEX = 200, time delay = 200 μs , BW = 5 kHz, vector size = 256 pts, and $T_{\text{acq}} = 1$ min. The TQF experiments used following parameters: $\tau_1 = 3$ ms, $\tau_2 = 50$ μs , and $\tau_3 = 300$ μs , TR = 200 ms, NEX = 1500, BW = 5 kHz, vector size = 256 pts, and $T_{\text{acq}} = 5$ min. The evolution time τ_1 was optimized to 3 ms based on the T_2 values measured in 5.1 as in [84]. The DQF-MA experiments used following parameters: $\tau_1 = 5$ ms, $\tau_2 = 50$ μs , and $\tau_3 = 300$ μs , TR = 200 ms, NEX = 2000, BW = 5 kHz, vector size = 256 pts, and $T_{\text{acq}} = 6$ min 40 s. The preparation time τ_1 was chosen according to previous *in vivo* DQF-MA FID measurements, which pointed out a maximum at 5 ms [186].

After reconstruction of ^{23}Na spectra, the area under the curve was calculated from the FID, the TQF and the DQF-MA spectra to derive the FID signal, the TQF signal, the DQF signal, and thus their ratios. The temporal decay of the total ^{23}Na signal acquired by a FID was fitted by a bi-exponential model taking the noise B into account to obtain short T_2^* , long T_2^* , and short T_2^* fraction F:

$$s^{FID}(t) = A \left(F e^{\frac{-t}{T_{2l}}} + (1 - F) e^{\frac{-t}{T_{2s}}} \right) + B$$

Also the temporal TQF signal decay was fitted by a characteristic signal equation assuming negligible quadrupolar coupling [187]:

$$s^{TQF}(t) = A \left(e^{\frac{-t}{T_{2l}}} - e^{\frac{-t}{T_{2s}}} \right) + B$$

Where B is again the noise, T_{2s} and T_{2l} the short and long transverse relaxation times. The ratios and fitting values were expressed as mean and SD.

5.4.2 Results

The TQF and DQF-MA signals are one and two orders of magnitude smaller than the FID signal (Figure 1Figure 63), respectively. The mean TQF/FID ratio representing the fraction of slowly tumbling ions out of the total sodium pool was calculated to be 0.095 ± 0.009 . Moreover, the DQF-MA/TQF ratio describes the fraction of the slowly tumbling sodium ions that are actually bound to ordered structures. This mean ratio was estimated as 0.097 ± 0.035 . Thus, only a very small fraction (DQF-MA/FID = 0.009 ± 0.004) of sodium ions can be found in ordered environments.

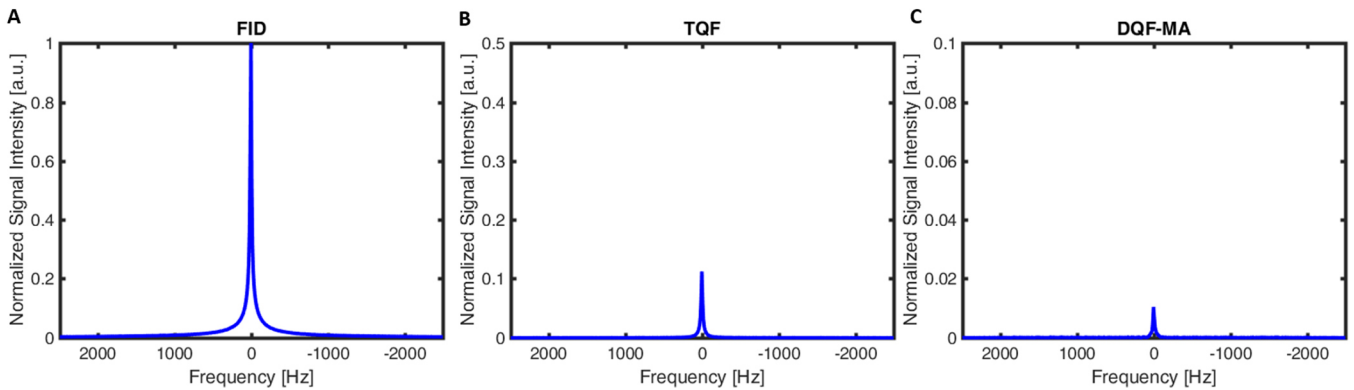


Figure 63: Examples of **A)** FID signal, **B)** TQF signal, and **C)** DQF-MA signal acquired on one volunteer showing the important differences in signal intensity between the three techniques.

Figure 64 shows examples of temporal decays of the FID and TQF signals acquired on one volunteer and their corresponding fit to derive the short and long T_2 values. For the FID, a mean short T_2 of 1.01 ± 0.2 ms with a relative fraction of 0.336 ± 0.003 and a mean long T_2 of 11.98 ± 1.19 ms were obtained. The TQF fitting resulted in a mean short T_2 of 1.74 ± 0.08 ms and a mean long T_2 of 12.99 ± 1.49 ms.

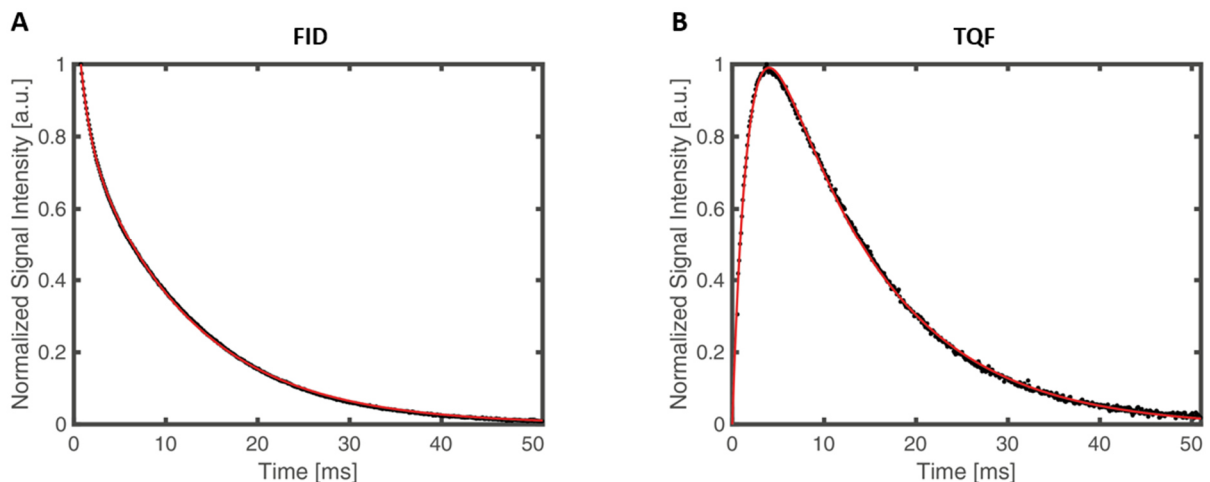


Figure 64: Example of **A)** normalized FID and **B)** normalized TQF signal decays acquired on one volunteer. The resulting fit curves are shown in red.

5.4.3 Discussion

In this work, ^{23}Na DQF and TQF NMR examined the tissue microstructure of human lower leg. As described in 3.3.3, MQF sequences have been used to select sodium signals from different molecular environments. Tsang *et al.* [188] nicely illustrated the signal evolution using the spherical tensor operator notation during the TQF and DQF-MA experiment. In biological tissues, the TQF signal results from bi-exponential relaxation and residual time-averaged quadrupole interactions. On the other hand, the DQF-MA sequence only produces signal in the presence of residual time-averaged quadrupole interactions (originating from ordered structures). In 1995, residual time-averaged quadrupole interactions were reported in DQF spectra of human skeletal muscle tissue and brain [91]. This was the first *in vivo* observation indicating the existence of sodium ions in anisotropic motion because of their binding to ordered structures.

The low DQF-MA/TQF ratio in the present study underlined that only a very small fraction of slowly tumbling Na^+ are bound to ordered structures in calf muscle tissue. Similar observations have been made in the heart muscle, where SR-aided and SR-free TQF and DQF spectra were acquired during ischemia [71]. They reported a TQF/DQF ratio of 3.55 to 4.56 for the SR-free MQF spectra (resulting in DQF/TQF around 0.21 to 0.28). Although not reported, we would expect a lower DQF-MA/TQF ratio, as the third-rank tensor contributions are filtered out at the magic angle. In the SR-aided experiments, TQF spectra showed contributions from the intra- and extracellular space, while DQF-MA signal was recorded only from the extracellular space since the intracellular DQF spectrum contains solely contributions of third-rank tensor that are filtered out by the magic angle excitation [189]. Moreover, our reported DQF-MA/TQF fraction of about 0.1 in muscle might be even smaller than calculated due to field inhomogeneities and the non-localized approach. Phantom experiments demonstrated that in presence of B_0 inhomogeneities, unwanted signal from Na^+ nuclei exhibiting bi-exponential decay cannot be completely suppressed in DQF imaging [188]. On the other hand, B_0 inhomogeneities can lead to loss of SNR for TQF sequences, which should be nevertheless not crucial for field strengths below 4.7T [103]. Additional inaccuracy to the measured signals can also occur because of B_1 inhomogeneities especially for the DQF-MA.

The short and long T_2 values from the FID and TQF fits showed a good agreement with literature values [143], [144]. Thus, the values could be used as references for clinical studies as they could change during (patho-) physiological events. Alterations in the transversal relaxation times or their relative fraction in skeletal muscle have been already reported after exercise [72] and during vascular filling/draining (5.1 and 5.2).

^{23}Na NMR sequences present research tools to enhance the sodium contrast that are so far used especially in the field of brain, cardiac, and tumour imaging [70]. Dedicated MQF techniques

generate contrast by filtering signal of different molecular environments without using invasive and toxic SR agents. Still, the validity and clinical utility are in question and more studies have to be performed to justify the effort of relaxation-based ^{23}Na NMR for tissue characterization. Both, ratios and T_2 values might be useful to study structural changes in muscle pathologies. By using TQF and DQF-MA sequences, the order of the skeletal muscle tissue and dynamics of motionally restricted sodium ions can be non-invasively probed. Exploring possible variations with disease may be particularly interesting in MD, where changes in the membrane structure take place.

5.5 Conclusion

Na^+ holds a central position in the fluid homeostasis and thus the cell volume regulation as it accounts for 90 to 95 % of all solutes in the extracellular fluid while being the only cation exerting significant osmotic pressure [190]. The idea of performing ^{23}Na spectroscopy to assess homeostasis and cell viability *in vivo* is not novel and dates back to the 1980s [78], [191]. However the spectroscopic approach seems to be nowadays left aside by most research groups currently focusing their efforts on improving spatial resolution of ^{23}Na images by taking advantage of high field NMRI [177], [192], [193]. At the beginning of this chapter, we showed that biophysically relevant information related to the physiological status of skeletal muscle tissue could be acquired in less than 15 minutes, at the expense of losing the spatial information. Thanks to the high SNR of this spectroscopic approach, we were able to monitor several ^{23}Na NMR variables while filling or draining the vascular compartment. On the other hand, the standard ^1H signal intensities and the ^1H T_2 , which are usually used to characterize disease activity, have been found less sensitive to the extracellular volume fraction alterations when compared to the ^{23}Na parameters.

As demonstrated in our study changes in extracellular volume fraction are traceable by using non-localized ^{23}Na NMR spectroscopy. This approach allows the monitoring of total and intracellular weighted ^{23}Na signal, in addition to the distribution of Na^+ in a time compatible with clinical investigation. This biophysical information can be used to assess ion homeostasis and cell integrity in skeletal muscle. In the context of neuromuscular disorders, these variables offer new options to investigate ion channel leakage, membrane integrity, or even fibrosis formation.

For such longitudinal or comparative studies, signal calibration is indispensable. That is why we showed that despite the loss of spatial resolution the ^{23}Na signal of the proposed spectroscopic protocol can be quantified using an external calibration phantom doped with SR. This method allows the calibration and quantification of TSC and ICW. A successful signal calibration then permits the extension of current clinical protocols with a short ^{23}Na protocol to unlock questions regarding the Na^+ homeostasis and volume fraction changes. Consequently, the proposed non-localized multi-

parametric ^{23}Na approach could represent a powerful tool to describe the onset phase of diseases, revisit several aspects of their pathogenesis, and ultimately monitor treatment in a novel non-invasive fashion.

As shown in human and mice, ^{23}Na NMR indices can give insights into the volume fraction changes and the tissue microstructure of skeletal muscle tissue. Thus as next step, I studied the impact of increased membrane permeability of the dystrophic muscle on different ^{23}Na spectroscopic indices and compared these measurements with more established biomarkers as the proton T_2 and fat fraction.

Preclinical studies of the murine dystrophic muscle

6.1 Murine models for muscular dystrophies

The heterogeneous group of MD is associated to different genetic mutations (2.5). Numerous animal models demonstrating similar phenotypes as observed in men have been identified or generated. Among the different species, murine models are the most widespread due to the short gestational and maturation time, the availability, and relatively low cost. Murine models represent a valuable tool to study the role of membrane proteins and the pathological progress of myopathies. Additionally, animal models are used nowadays in many preclinical trials to test possible therapeutic interventions. Therapeutic interventions for human muscle disorders are predominantly validated on murine models of homologous or analogous human disease. In several murine models the feasibility to restore a functional protein by gene transfer, genome editing, or exon skipping approaches has been demonstrated [194], [195]. Still, the success rate of translating preclinical trials in human clinical trials remains low [196]. Several limitations to translate data obtained from mouse to man exist, such as the difference in scale, growth, and response to pathological processes [197]. Nevertheless, NMR techniques can be used as a tool to characterize non-invasively animal models and to evaluate the impact of an intervention. On the other hand, new NMR methods can be validated on well-described murine models. The specificity of the NMR techniques to monitor certain pathologies can be endorsed with murine models as they represent a very homogenous group exhibiting a usually stable phenotype across strains. They also provide an easy access to histology to compare the sensitivity of the NMR approach with the underlying pathological changes.

The *mdx* mouse is the most popular animal model for DMD. It was first described in 1984 as having a muscular dystrophy with a spontaneous mutation in the X chromosome (stop codon in exon 23). The *mdx* model is similar to DMD patients as they lack dystrophin and share biochemical and histopathological features such as increased plasma levels of creatine kinase [198]. However, the phenotype is less severe than in human patients. The regenerative cycles exhaust in DMD at an early age leading to increased fibrosis, fatty infiltration, and premature death due to respiratory and heart failure [36]. On the opposite, the murine muscle shows cycles of degeneration and regeneration even during adult life. The high degree of fibrosis in DMD is only reproduced in the diaphragm muscle of *mdx* mice but not in their limb muscles [199]. The lifespan of *mdx* mice is hence only very fairly shortened. Despite intensive research on the *mdx* model, it is still unclear why the disease progression is much milder in comparison to DMD patients [200].

For LGMD2B, two murine models have been so far described with spontaneous mutations: the *A/J* strain with a retrotransposon insertion in dysferlin intron 4 and the *SJL/J* strain with a deletion of dysferlin exon 45 [201]. Several backcrossed strains carrying one of these mutations have been developed to improve the dysferlin-deficient murine model. One inbred strain is the *BLAJ* mouse, where the *A/J* mutation was introduced into the *C57Bl/6J* background strain in the laboratory of Isabelle Richard at Généthon [194]. The phenotype is generally mild with an onset at two months characterized by centronucleated fibres and areas of inflammation. Similar as in LGMD2B patients, proximal muscles are more severely affected than distal muscles. As described in 2.4, repeated muscle contractions lead to small membrane damages that are usually quickly resealed by the Ca⁺-dependent repair mechanism involving also the dysferlin protein. Biondi *et al.* [202] studied the effect of exercise in the *BLAJ* model, which demonstrated a delayed membrane repair, typically seen in dysferlinopathies. They also exhibited dual effects of exercise: while eccentric exercise provokes extensive myoinjuries, non-eccentric exercise improved muscle strength and limited the disease progression in *BLAJ* mice. A virus-mediated gene transfer therapy in *BLAJ* mice led to a widespread but weak expression of the dysferlin protein [194]. The treated mice showed a restored membrane repair capacity, however the systematic injections improved only partly histological and functional features of the dysferlinopathy. This underlines that the dysferlin function is not only involved in the membrane repair, but has also other not-yet elucidated roles in cell function.

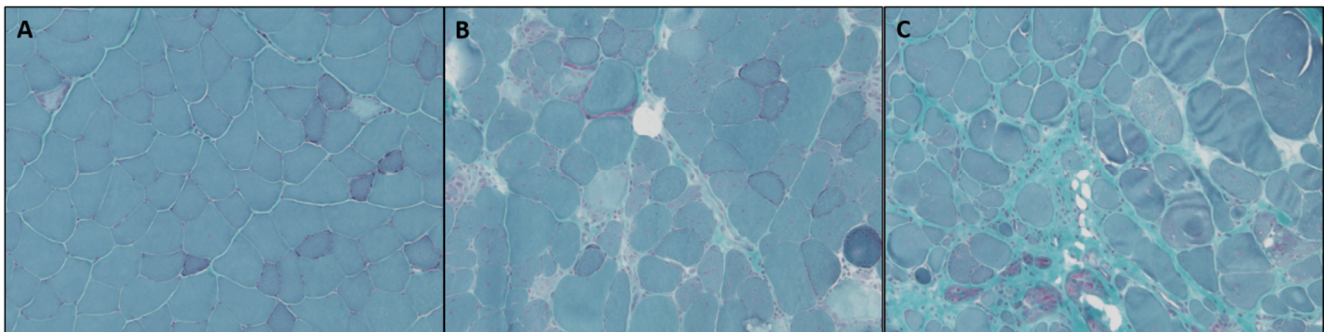


Figure 65: Histology of the quadriceps muscle of *MMex38* mice at **A)** 12 weeks, **B)** 20 weeks, and **C)** 60 weeks of age. The dystrophic phenotype worsens with age. Stained with Gomori's trichrome. Provided by V. Schöwel.

Another dysferlin-deficient murine model, called *MMex38*, has been recently generated by Verena Schöwel and co-workers [203]. The *MMex38* mouse model (B6; 129P2-Dysftm1.1Mdc) has a missense mutation in exon 38 of the *DYSF* gene. It has been shown that a missense mutation *DYSF* p.L1341P in the human dysferlin gene causes dysferlin protein misfolding leading to characteristics of a protein misfolding disease in a well-studied, large family cohort [204]. Thus, they developed the first knock-in dysferlin-deficient model analogous to the human mutation (target T>C mutation in murine *DYSF* exon 38 leading to *DYSF* p.L1360P (dysferlin isoform 2, NP_001071162.1)). The missense mutation in *MMex38* leads to a dystrophic phenotype in three-month-old mice with a continuous

disease progression in later life (Figure 65). In young mice, a number of necrotic and regenerating fibres are visible (centronucleated fibres). The number of necrotic fibres is increasing significantly with age accompanied with fat infiltration and increased connective tissue. On protein level, the missense-mutated dysferlin is prematurely degraded. This protein misfolding leads to amyloid formation in aged muscle as seen in patients. Like the *BLAJ* model, the *MMex38* displays significant endurance impairments on the treadmill and a delayed myofibre membrane resealing [Jakub Malcher *et al.* 2018 under revision].

The objective of the current preclinical study was to characterize the skeletal muscle tissue of the *MMex38* mice by standard NMR methods. This dysferlin-deficient model was already described by histology, but not by NMR yet. Thus, a NMR protocol for thighs and legs was implemented that consisted of T₁ weighted anatomical imaging, ¹H T₂ and T₁ measurements, fat fraction quantification and ³¹P NMRS. These ¹H NMR data were compared to the more described *BLAJ* model and wild-type mice.

In a protocol extension, different murine models of MD were used to validate novel NMR approaches. ISIS-CPMG and ²³Na NMR spectra were acquired in skeletal muscle tissue of *MMex38*, *mdx* and wild-type mice. We compared their sensitivity and specificity to detect pathological alterations in dystrophic muscle to standard NMR methods. Furthermore, histology was performed to confirm the extent of pathological features.

6.2 Materials and methods

Murine models and study design

The NMR protocols included four different murine strains. The dysferlin-deficient *BLAJ* and *MMex38* mice were bred in the *Max-Delbrück-Centrum für Molekulare Medizin*, Berlin and the dystrophin-deficient *mdx* mice were obtained from *UMS 28-Nouvelle Animalerie commune*, Paris. *C57BL10* mice served as wild-type (WT) for the dysferlin-deficient and *mdx* mice and were bought from the *Janvier Laboratory*. The study was approved by the *French Ministry of Higher Education and Research* according to the European directive 2010/63/EU. Mice received food and drink ad libitum. NMR acquisitions were performed on 1-year-old female mice (*MMex38* n = 10, *BLAJ* n = 4, *mdx* n = 10, and WT n = 10).

NMR protocol

Animals were initially anesthetized with 4 % isoflurane before placed onto a custom-made bed. The biggest circumference of the legs was centred in the body coil at the iso-centre of the

magnet. During the NMR scanning, animals continued to be under anaesthesia using a breathing mask (1.5 – 2 % isoflurane in O₂ at 1.5 l/min) and held on a heating pad at 42°C to keep their body temperature constant. Animal respiration was monitored externally during NMR acquisition with a breathing surface pad.

All animals experienced to the first part of the study. The ¹H NMR protocol for leg and thigh included T₁-weighted high-resolution for anatomical images, multi-spin echo for T₂ measurement, fast spin echo for T₁ measurement, and localized ¹H NMRS for fat quantification. The anatomical images were acquired with a RARE sequence (TR/TE = 3500/5.5 ms, FA = 90°, RARE factor = 8, 23 axial slices with resolution = 0.1 mm × 0.1 mm² and slice thickness = 0.5 mm, slice gap = 1mm, and T_{acq} = 2 min 30 s). For the evaluation of disease activity, muscle water T₂ values were measured by a non-fat suppressed MSME imaging sequence with: 37 different TEs = 4.0 - 149.3 ms, TR = 750 ms, FA = 90°, acquisition BW = 200 kHz, 3 axial slices, resolution = 0.125 × 1.25 mm² and slice thickness = 1 mm, and T_{acq} = 13 min for legs/T_{acq} = 17 min for thighs). T₁ values were measured by a RARE sequence with 19 different TRs = 54.6 - 6500 ms, TE = 5.5 ms, excitation/refocusing FA = 90°/180°, RARE factor = 8, acquisition BW = 200 kHz, 1 axial slice, resolution = 0.125 × 1.25 mm² and slice thickness = 1 mm, and T_{acq} = 8 min for legs/T_{acq} = 10 min for thighs). Finally, PRESS sequences were acquired at two voxel locations to quantify the fat content in muscle (TE/TR = 15/1505 ms, voxel size = 2 × 2 × 3 mm³ with 0.61 Hz/point spectral resolution, spectral BW = 5 kHz and 4096 data points, 200 averages, and T_{acq} = 5 min). The voxels were positioned in the anterior and in the posterior part of both the right leg and the right thigh. For a good spectral quality, manual shimming was performed to obtain a linewidth of water that was below 30 Hz. The duration of the ¹H NMR protocol was about three hours per animal including repositioning and shimming.

For six *MMex38*, six *mdx*, and six WT, additional ³¹P spectra were acquired on the right leg. Non-localized ³¹P spectrum of the murine leg was acquired with TE/TR = 0.05/2500 ms, 200 μs hard pulse excitation with FA = 60°, spectral BW = 6009 Hz and 1026 data points, 720 averages, and T_{acq} = 30 min. The power setting was used from preceding calibration experiments. For a good spectral quality, B₀ mapping and additionally shimming was performed to obtain a linewidth of water that was below or equal to 70 Hz.

The same mice also underwent a ²³Na NMR protocol. A small cylindrical vial (2 mm diameter and 10 mm length) containing a solution of 140 mM NaCl doped with 24 mM TmPOPT⁵⁻ was fixed to in the ²³Na coil next to the leg. Bulk susceptibility of the TmDOTP⁵⁻ solution shifted the resonance frequency by 37 ppm allowing discrimination from the signals of the hindlimb and the calibration phantom. The RF power to produce a 90° FA angle was determined by increasing the transmit power

stepwise (between 0.6 and 2.5 W). The ^{23}Na protocol comprised non-localized FID, TQF, and IR-LL sequences as presented in 4.6.1. The FID was acquired with the following parameters: acquisition delay = 50 μs , TR = 200 ms, NEX = 250, BW = 10 kHz, vector size = 256 points, and T_{acq} = 50 s. TQF experiments were performed with following parameters: $\tau_1/\tau_2/\tau_3$ = 4/0.05/0.05 ms, TR = 200 ms, NEX = 600, BW = 10 kHz, vector size = 256 points, and T_{acq} = 2 min. The ^{23}Na T_1 values were obtained from the IR-LL with the following parameters: acquisition delay = 200 μs , TR = 200 ms, 55 echoes with ES = 5 ms, NEX = 400, BW = 10 kHz, vector size = 30 points, and T_{acq} = 50 s.

Finally, for the six *mdx* and six WT mice, the protocol was expanded by acquiring ISIS-CPMG sequences. ^1H T_2 spectra were obtained with the following parameters: 500 with ES = 1 ms, TR = 4 s, voxel size = 1.5 x 1.5 x 5 mm^3 , NEX = 2, BW = 50 kHz and data points = 32, and T_{acq} = 1 min 4 s. The voxel positions in the thigh and leg were the same as for the PRESS acquisitions.

Analysis of NMR data

To assess the muscle trophicity in dysferlin-deficient mice, cross sectional areas (CSA) of the quadriceps were drawn on the contractile tissue on the T_1 -weighted images avoiding the complete fat-replaced parts of the muscle (Figure 66A). For T_1 and T_2 measurements, ROIs were manually traced on the right and left leg and thigh within muscle compartment on MSME images (Figure 66B).

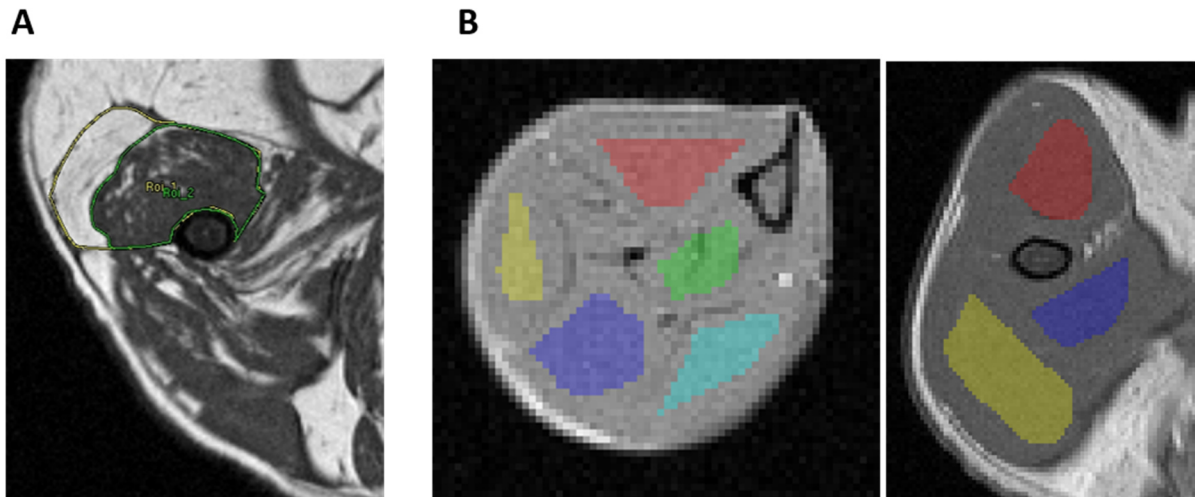


Figure 66: **A)** Representative T_1 -weighted image of the thigh of a *MMex38* mouse. CSA of the quadriceps were drawn on the contractile tissue avoiding the complete fat-replaced parts of the muscle (ROI_2). **B)** Representative axial MSME image (at TE 4 ms) of the left leg and thigh of a WT mouse. The overlay represents the manually traced ROIs in the different muscle compartments. Leg: Ant. (red) = TA/EDL, med. (green) = TP, and pos. (yellow, blue and turquoise) = gastrocnemius, plantaris muscles; Thigh: ant. (red) = quadriceps, med. and pos. (yellow and blue) = biceps femoris and gluteus maximus.

T_1 values were fitted to a mono-exponential model. FF and water T_2 values were measured using a tri-exponential analysis [16] with noise compensation due to the low SNR at higher TE. The

noise correction took into account the Rician noise of the background to calculate the true image intensities for the fit [205]:

$$\check{A} = \sqrt{|M^2 - \sigma^2|}$$

Where \check{A} is the corrected image pixel intensity, M the measured pixel intensity and σ the background noise. Global T_1 , FF, and water T_2 were determined as mean value of pixels within the drawn ROI with a confidence interval less than 10 [206]. The heterogeneity of muscle T_2 was assessed by the coefficient of variation (CV) across ROIs. In addition, the percentage of pixels with a water T_2 higher than 36.7 ms were computed and reported as elevated T_2 . This threshold was determined from the mean value plus two SD of water T_2 values of the WT mice.

The ^1H NMR spectra were processed with a 5 Hz Lorentzian apodization and manual zero and first order phasing correction. The water peak was set to 4.7 ppm. The amplitudes of three peak clusters in the proton spectra used for the fat ratio calculation as described in 4.2.1 (Figure 67).

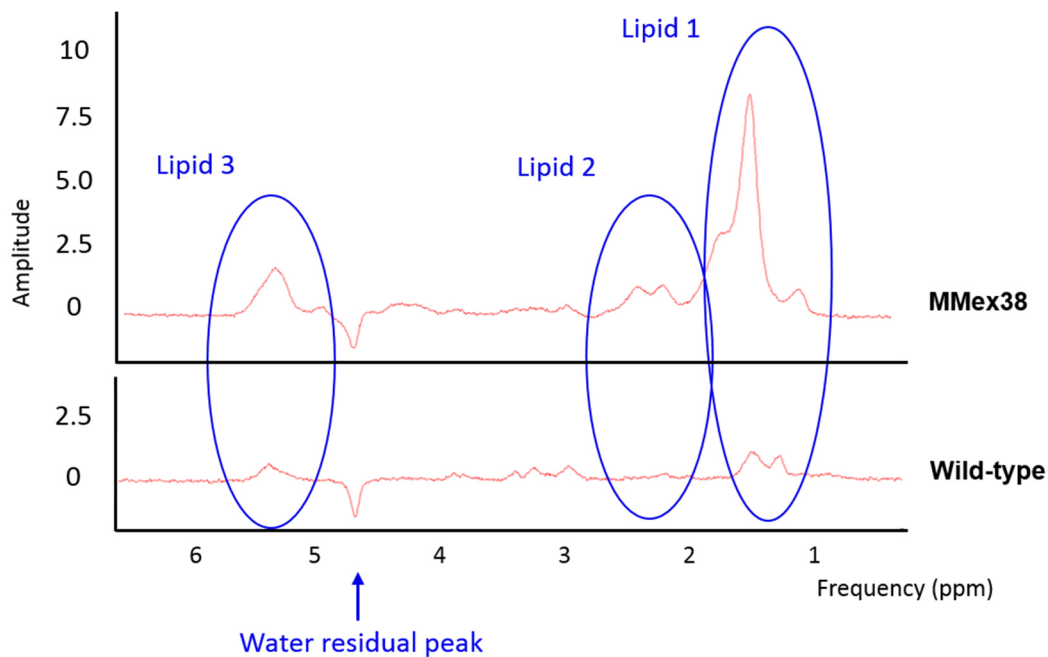


Figure 67: ^1H NMR spectra with water suppression in the calf of a MMex38 and a WT mouse. Lipid 1 was assigned to methylene protons at $\Delta\text{ppm} = 0.8 - 1.8$, Lipid 2 to α - or β -methylene protons at $\Delta\text{ppm} = 2 - 2.8$, and Lipid 3 to olefinic protons at $\Delta\text{ppm} = 5.3 - 5.7$. Note the residual peak of water at 4.7 ppm.

The ^{31}P NMR spectres were smoothed with a 10 Hz Lorentzian filter followed by manual zero and first order phase correction. The resonances of PDE, P_i , PCr, and the three phosphate groups of ATP (γATP , αATP and βATP) were fitted with the AMARES algorithm from jMRUI. The pH was determined from the chemical shift between PCr and P_i according to the modified Henderson-Hasselbalch equation (4.5.1). All ^{31}P resonance integrals were corrected for saturation effects using a fully relaxed spectra with $\text{TR} = 18$ s. The broad, small peak at the phosphomonoesters (PME)

resonance was recorded, but not quantified since it was not detected in all mice. Only ^{31}P spectra with a linewidth of PCr below or equal to 30 Hz were accepted for the analysis.

The ISIS-CPMG T_2 decay was fitted with a bi-exponential model resulting in a short and long T_2 value and their relative fractions. The ^{23}Na signals were calibrated with the leg volume and SR peak as described in 5.2. We obtained four different ^{23}Na indices: FID, TQF, TQF/FID ratio, and global T_1 value. No T_2^* values were fitted due to the signal contamination of the SR phantom leading to signal superimposition of the relaxation decay.

Histology

After NMR acquisition, animals assigned to the extended protocol were euthanized by cervical dislocation under full anaesthesia. The anterior and posterior muscles of the right leg and thigh were harvested and preserved in formaldehyde solution (4 % in phosphate buffer saline). The samples were stained with hematoxylin and eosin (H&E) for a qualitative evaluation of the muscle tissue. Three transversal sections were cut in the proximal, medial, and distal part of the muscles, which were viewed at 10x magnification.

Statistical analysis

A non-parametric Kruskal-Wallis test with Dunn post-hoc multiple comparisons was used to evaluate the different NMR variables. ^{31}P and ^{23}Na NMR data were analysed using a single-factor ANOVA with a Bonferroni post hoc analysis. ISIS-CPMG data were analysed using Student's t-test as this measure was only performed in two groups. Spearman-rank correlations analysed the correlation between the parameters. Statistical significance was considered at $p < 0.05$.

6.3 Characterisation of a novel dysferlin-deficient murine model by NMR

Anatomical imaging

At 1 year of age, intramuscular fat infiltration could be clearly visualized on T_1 -weighted images of the thigh of both dysferlin-deficient murine models (Figure 68). Thighs of *MMex38* showed heavily fat infiltrated muscle in the posterior medial muscle group as well as completely fat replaced muscles in the quadriceps. The T_1 -weighted images of *BLAJ* mice showed also hyperintensities in the thigh muscles; however, the quadriceps was less severely affected than in *MMex38*. The CSA of the quadriceps was significantly decreased in *MMex38* ($18.4 \pm 2.8 \text{ mm}^2$, $p < 0.05$) and *BLAJ* ($16.1 \pm 2.3 \text{ mm}^2$, $p < 0.05$) compared to WT ($22.2 \pm 0.5 \text{ mm}^2$). On the contrary, leg muscles looked very homogenous in both models of dysferlin-deficiency. Thus, there was no visual difference between the leg of dysferlin-deficient mice and WT.

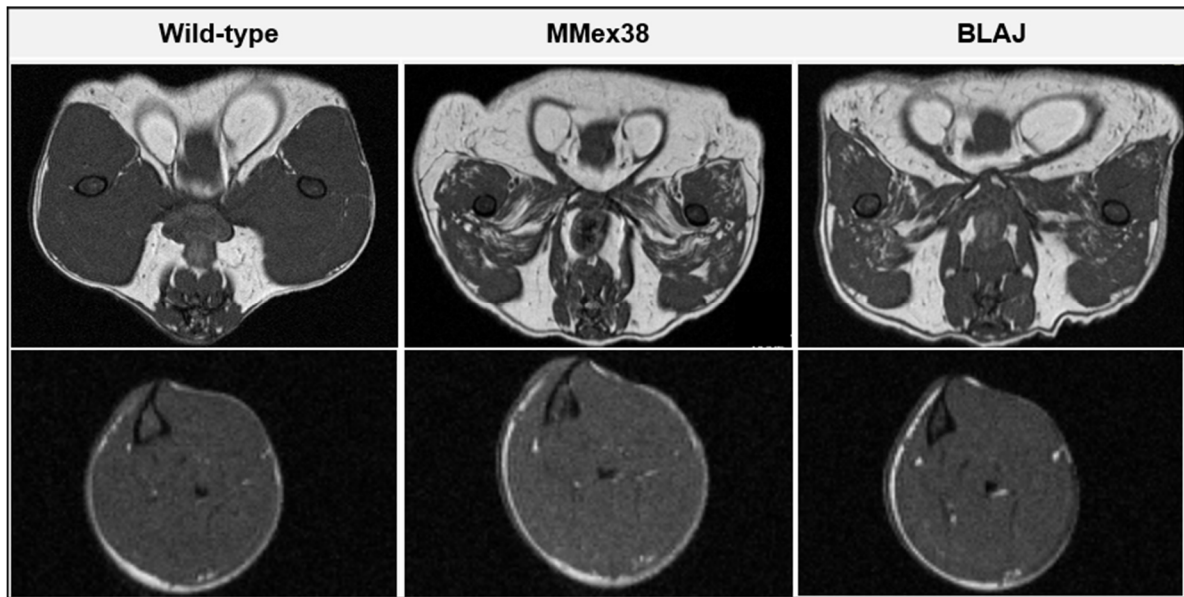


Figure 68: T_1 -weighted images of the thigh and leg of WT, *MMex38*, and *BLAJ* mice. The images showed highly fat infiltrated muscles in the thighs of both dysferlin-deficient mouse models. Parts of the quadriceps of *MMex38* were systematically replaced by fatty tissue.

^1H T_2 and T_1 mapping

Figure 69 plots the T_1 values of the different muscle compartments. The mean T_1 in thighs and legs of *MMex38* was 1.70 ± 0.07 s, for the *BLAJ* 1.73 ± 0.06 s, and for the WT 1.76 ± 0.07 s. The difference in T_1 of the hindlimb muscles was only significant between the *MMex38* and WT. This results from the significantly decreased T_1 values in the posterior medial compartment of the thigh.

Water T_2 values and FF of the leg and thigh muscles are plotted in Figure 70 and Figure 71, respectively. The mean FF in thigh and leg of *MMex38* was 0.13 ± 0.07 , for the *BLAJ* 0.11 ± 0.05 , and for the WT 0.08 ± 0.01 with a significant difference between the dysferlin-deficient models and WT ($p < 0.05$). While the leg muscles were not affected, the thigh muscles exhibited increased FF. NMR detected also increased water T_2 in the calf and thigh muscles of *MMex38* and *BLAJ* mice reflecting an ongoing disease activity. The mean water T_2 of *MMex38* and *BLAJ* was 27 ± 3 ms and for the WT 24 ± 1 ms with a significant difference between the dysferlin-deficient models and WT.

Elevated water T_2 and CV of water T_2 of the leg and thigh muscles are plotted in Figure 72 and Figure 73, respectively. Dysferlin-deficient mice showed a much higher ratio of pixels with elevated water T_2 (*MMex38* global mean of 50 ± 28 % and *BLAJ* global mean of 50 ± 32 %) than WT (Global mean of 15 ± 8 %). The mean water T_2 CV of *MMex38* and *BLAJ* was 0.13 ± 0.02 and 0.12 ± 0.02 , respectively. This ratio was significantly higher than the one of WT with 0.01 ± 0.01 . The high T_2 heterogeneity in dysferlin-deficient mice indicates tissue disorganization in the muscle tissue.

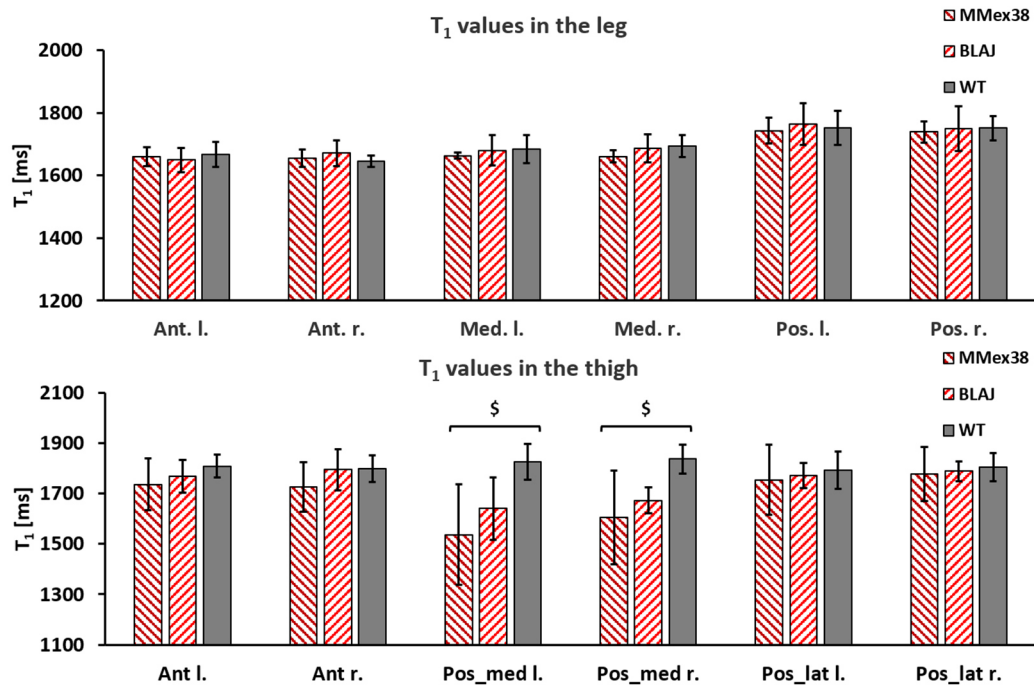


Figure 69: T_1 values of WT and dysferlin-deficient MMex38 and BLAJ mice: No significant differences were seen in the leg between the strains. In the thigh, the dysferlin-deficient mice showed decreased T_1 values in the medial posterior compartment compared to WT (MMex38 $n = 10$, BLAJ $n = 4$, and WT $n = 10$; $\$$: $p < 0.05$).

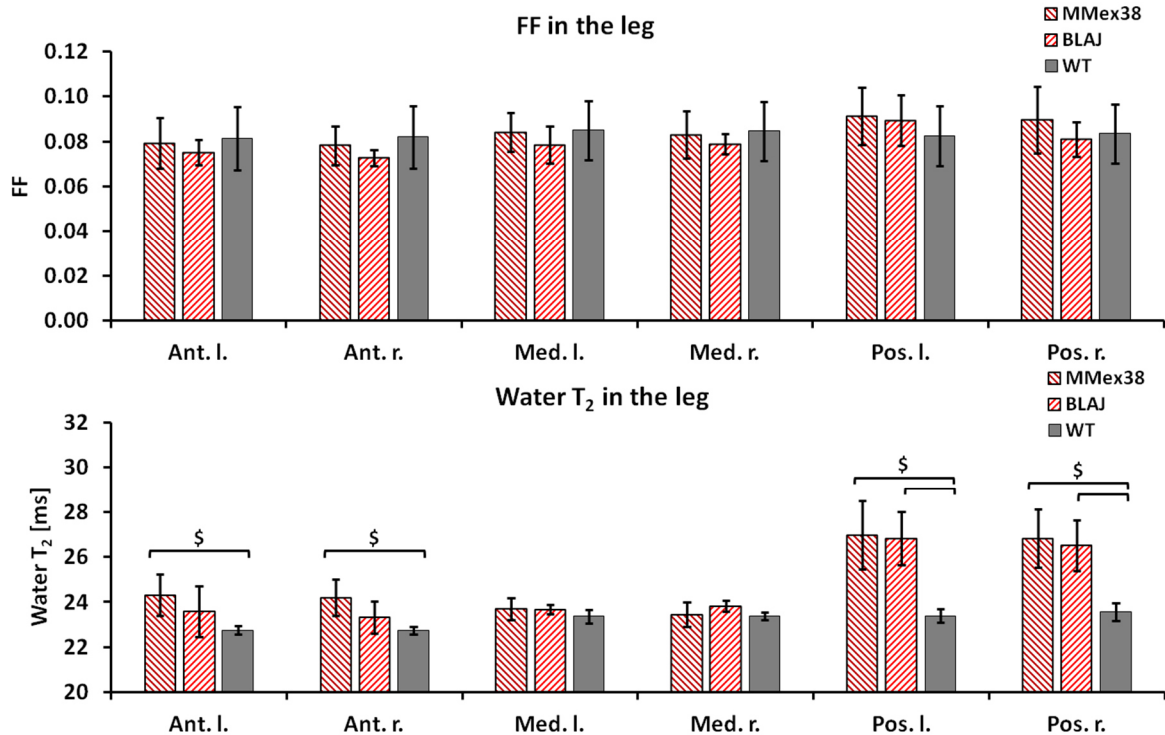


Figure 70: Fat fraction and water T_2 values measured in the leg of WT and dysferlin-deficient MMex38 and BLAJ mice: No significant differences were seen in the FF between the strains. Dysferlin-deficient mice showed increased water T_2 values in the anterior and posterior compartment compared to the (MMex38 $n = 10$, BLAJ $n = 4$, and WT $n = 10$; $\$$: $p < 0.05$).

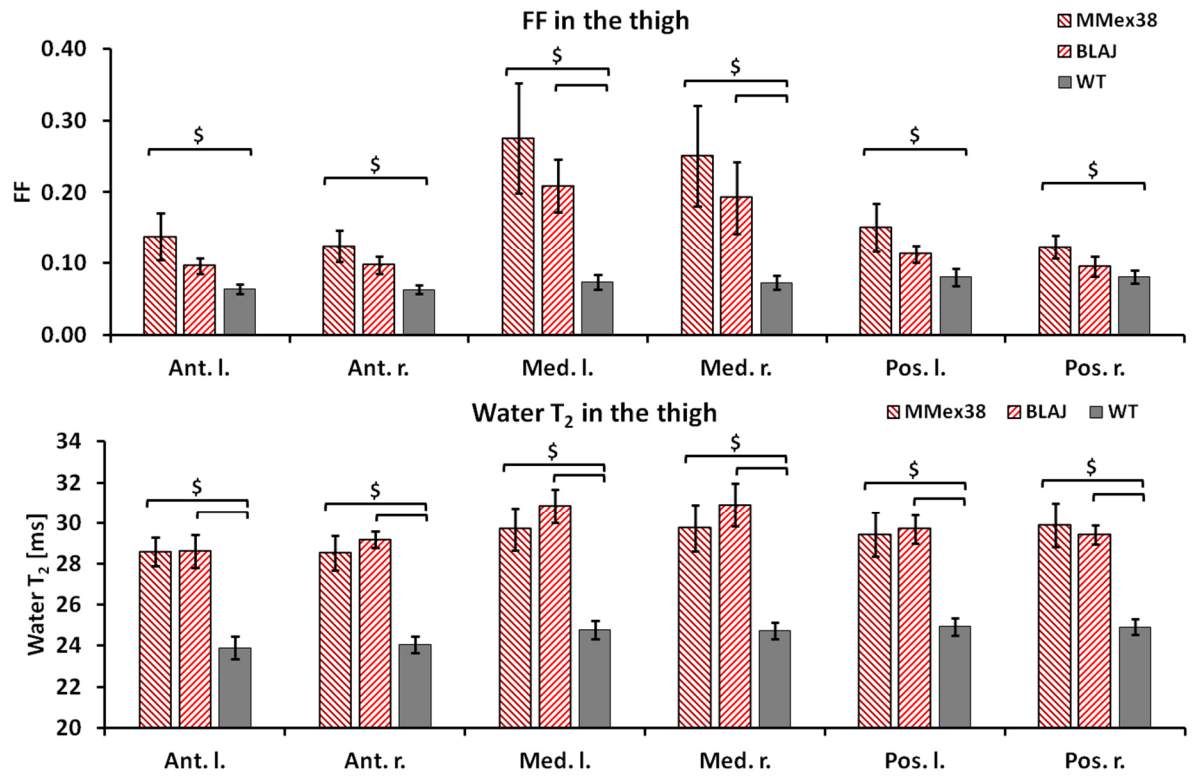


Figure 71: Fat fraction and water T_2 values measured in the thigh of WT and dysferlin-deficient MMex38 and BLAJ mice: Dysferlin-deficient mice showed systematically increased FF and water T_2 values compared to WT (MMex38 $n = 10$, BLAJ $n = 4$, and WT $n = 10$; \$: $p < 0.05$).

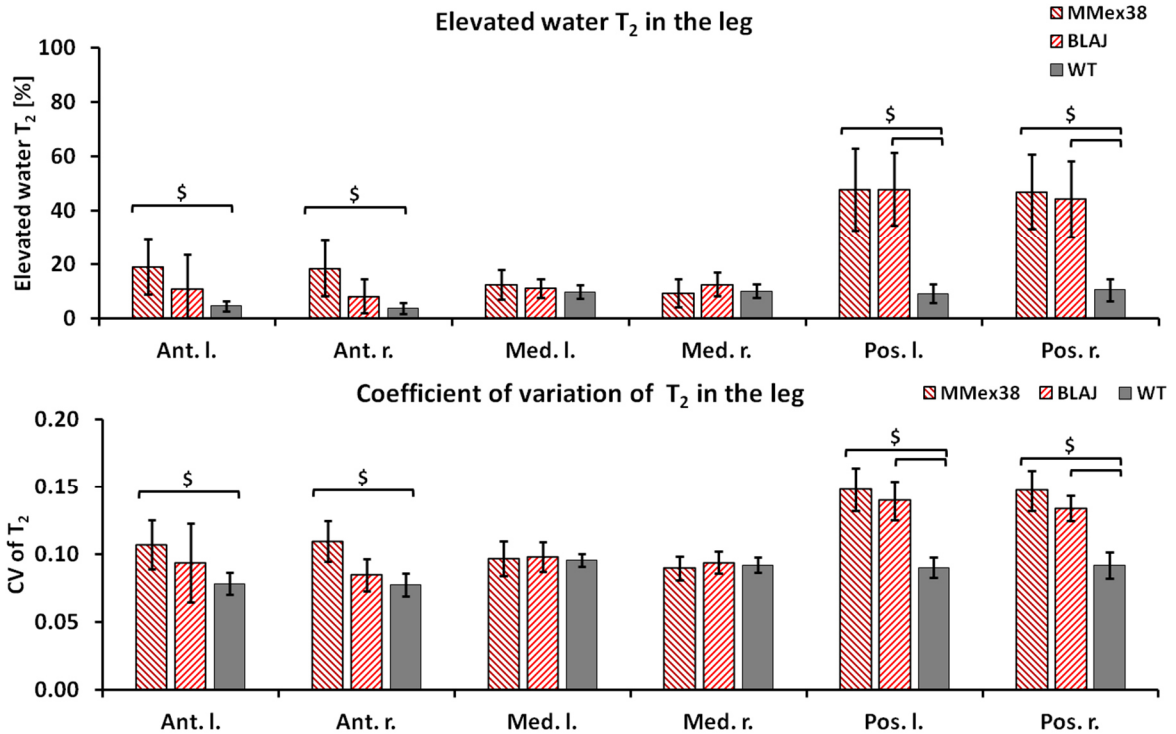


Figure 72: Elevated water T_2 and water T_2 CV measured in the leg of WT and dysferlin-deficient MMex38 and BLAJ mice: Dysferlin-deficient mice showed a higher percentage of elevated water T_2 values as well as higher CV in the anterior and posterior compartment compared to WT (MMex38 $n = 10$, BLAJ $n = 4$, and WT $n = 10$; \$: $p < 0.05$).

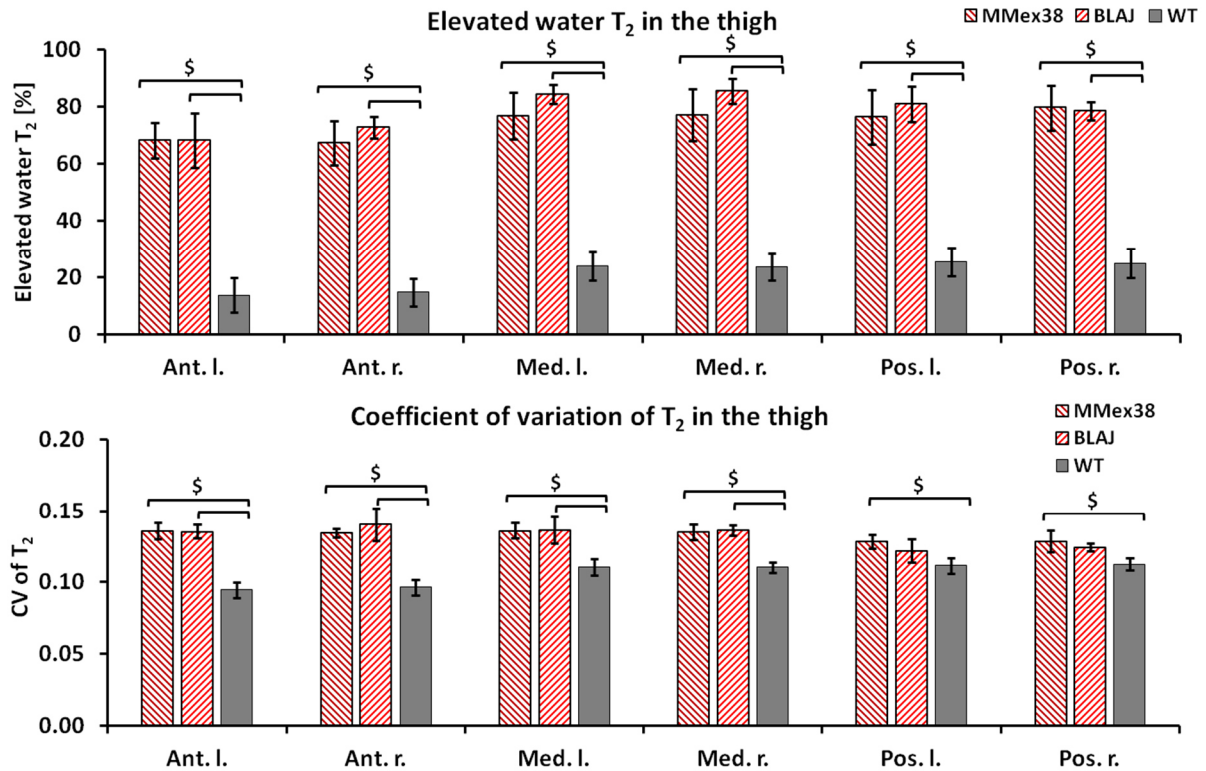


Figure 73: Elevated water T_2 and water T_2 CV measured in the thigh of WT and dysferlin-deficient MMex38 and BLAJ mice: Dysferlin-deficient mice showed higher percentage of elevated water T_2 values as well as higher CV compared to WT (MMex38 $n = 10$, BLAJ $n = 4$, and WT $n = 10$; \$: $p < 0.05$).

^1H NMR spectroscopy

The localized ^1H spectroscopy showed a significant accumulation of lipids in thigh and calf of MMex38 and BLAJ compared with WT (Figure 74). The fat ratio in the thigh muscles was higher in MMex38 than in BLAJ mice.

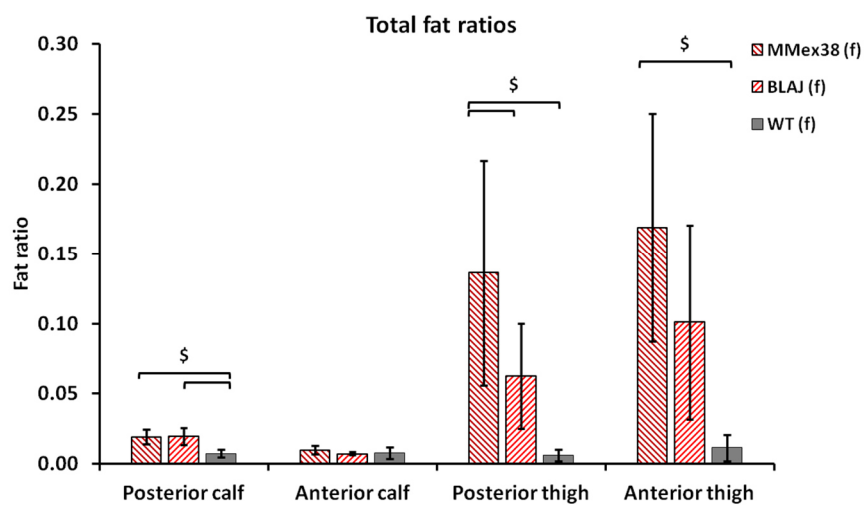


Figure 74: Fat ratios measured by ^1H spectroscopy in the leg of WT and dysferlin-deficient MMex38 and BLAJ mice: Dysferlin-deficient mice showed higher fat ratios especially in the thigh muscles compared to WT (MMex38 $n = 10$, BLAJ $n = 4$, and WT $n = 10$; \$: $p < 0.05$).

³¹P NMR spectroscopy

Figure 75 presents the non-localized spectra of *MMex38* and WT mice with the assigned phosphate resonances. Metabolic ratios were calculated with the Pi, PCr, and ATP peaks (Table 10). In *MMex38*, the PCr/ATP ratio tended to be lower and the Pi/ATP ratio higher than in WT (both not significant). The pH was significantly higher in *MMex38* than in WT (7.16 ± 0.09 vs 7.06 ± 0.06). In contrast to WT, four out of six spectra of *MMex38* mice showed a clear peak at the PME resonance. None of the phosphor metabolite ratios correlated with the fat fraction (all $R^2 < 0.05$).

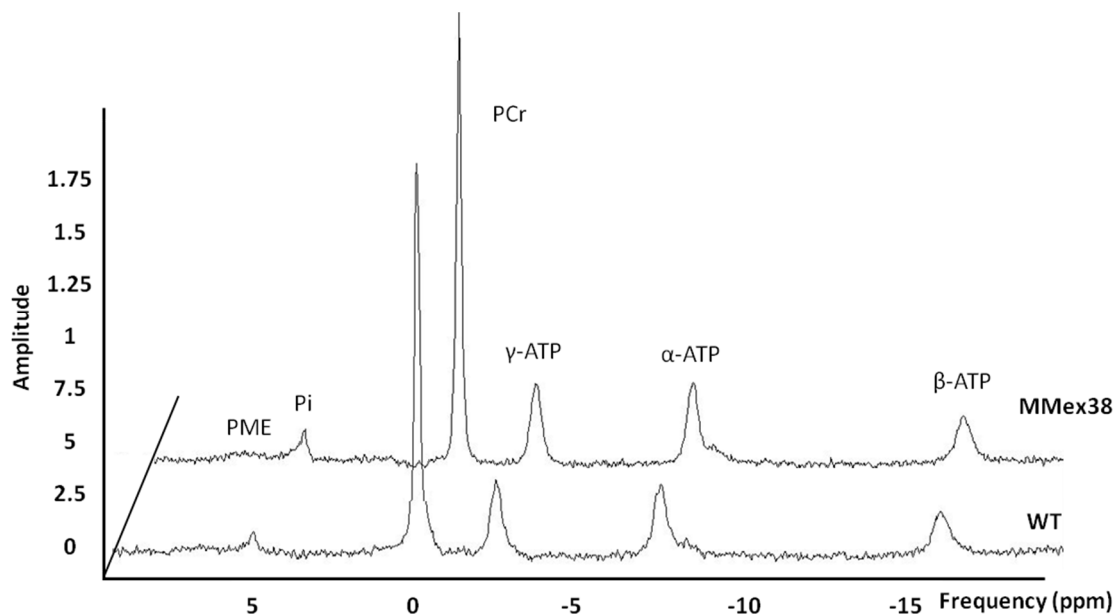


Figure 75: Resting ³¹P spectra (TR 2.5 s) acquired of the right leg are shown for *MMex38* and WT. Peaks were assigned to PME (around 6 ppm), Pi (4.95 ppm), PCr (0 ppm), and the γ - (-2.4 ppm), α - (-7.5 ppm), and β -phosphate (-16 ppm) of ATP. Each spectra represents an average of 720 FIDs over 30 minutes.

Table 10: Mean values \pm SD for the different phosphate metabolites in WT and *MMex38* (*MMex38* $n = 6$ and WT $n = 5$). Only the pH was significantly increased ($\$$: $p < 0.05$).

	Pi/PCr	Pi/ATP	PCr/ATP	pH
<i>MMex38</i>	0.11 \pm 0.03	0.29 \pm 0.06	2.70 \pm 0.45	7.16 \pm 0.09 [§]
WT	0.09 \pm 0.02	0.27 \pm 0.09	3.08 \pm 0.30	7.06 \pm 0.06

6.4 Results of standard NMR protocol for *mdx* model

Anatomical imaging

At 1 year of age, the T_1 -weighted images of the thigh of *mdx* mice showed few hyperintensities in the muscle tissue (Figure 76). No hyperintensities in the muscle tissue were visible in the leg muscles.

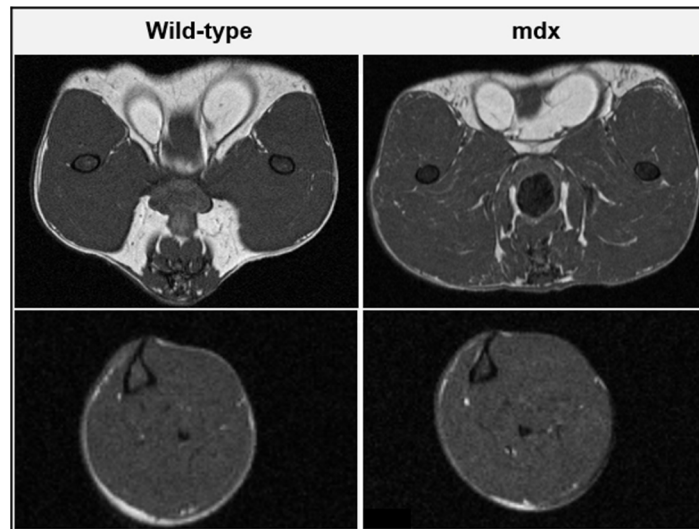


Figure 76: T_1 -weighted imaging showed slightly fat infiltrated muscles in the thigh of *mdx* compared to WT.

1H T_2 and T_1 mapping

The mean T_1 value of *mdx* was 1.77 ± 0.03 s and for the WT 1.76 ± 0.06 s. Significantly increased T_1 values were found only in the anterior and medial compartment of the leg of *mdx* when compared to WT (Figure 77).

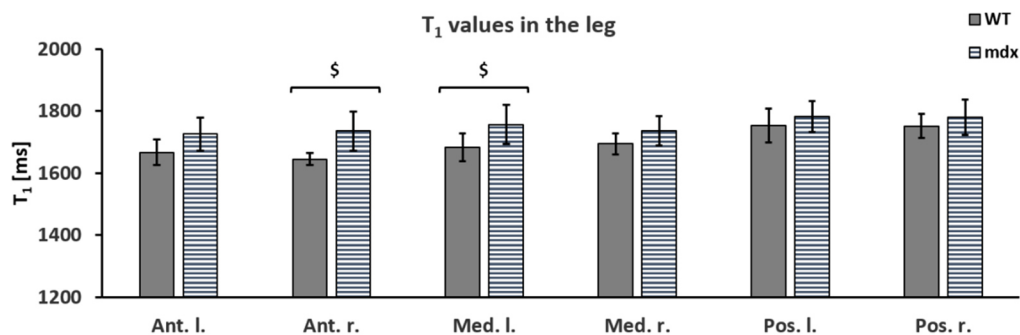


Figure 77: T_1 values of the WT and *mdx* mice: Significant differences were seen in the leg between the strains ($\$: p < 0.05$).

The mean FF of *mdx* was 0.09 ± 0.01 and for the WT 0.08 ± 0.01 . No muscle compartment in *mdx* showed a significant increase in FF. NMR detected increased water T_2 in the calf and thigh muscles of *mdx* reflecting an ongoing disease activity (Figure 78). The mean water T_2 of *mdx* was 26.2 ± 1.7 ms and for the WT 24 ± 0.8 ms with a significant overall difference between the two strains ($p < 0.05$).

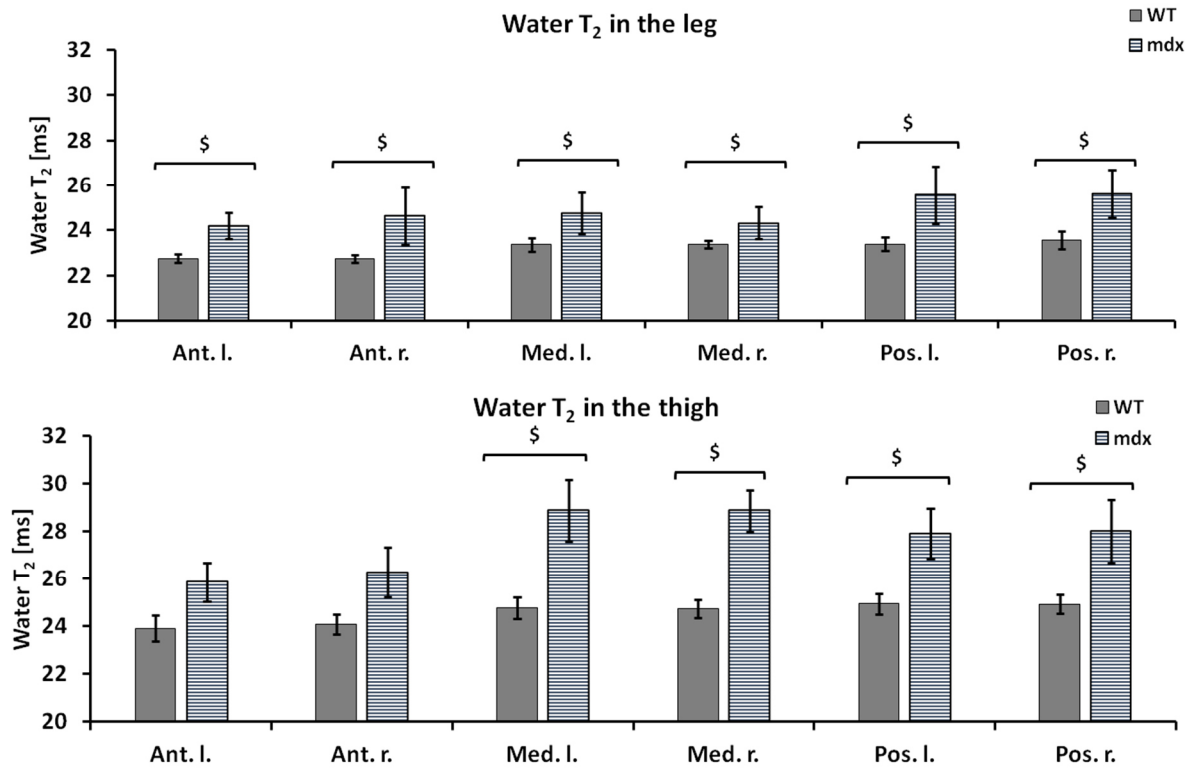


Figure 78: Water T₂ values measured in the leg and thigh of the WT and mdx mice: Mdx mice showed increased water T₂ values in several muscle compartments compared to WT (§: p < 0.05).

Elevated water T₂ and water T₂ coefficient of variations of the leg and thigh muscles are plotted in Figure 79 and Figure 80, respectively. Mdx mice showed a higher ratio of pixels with elevated water T₂ (Global mean of 42 ± 20 %) than WT (Global mean of 15 ± 8 %). The mean water T₂ CV of mdx and WT was 0.12 ± 0.01 and 0.10 ± 0.01, respectively (p < 0.05).

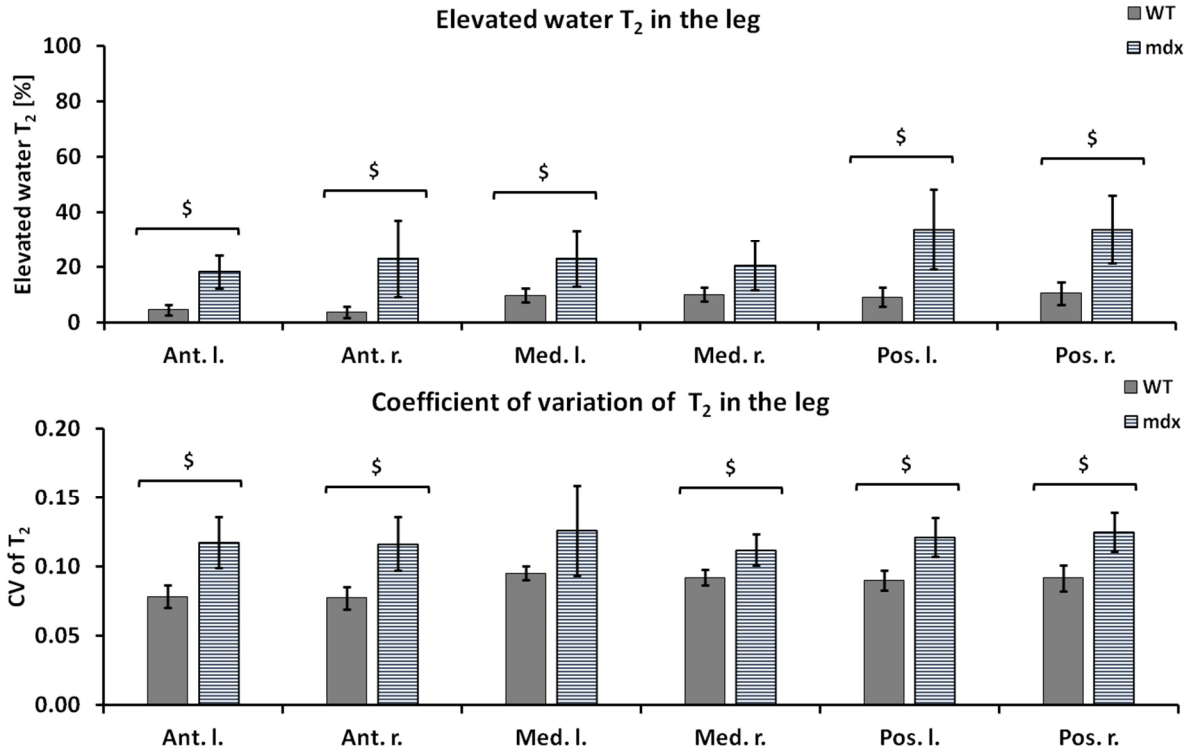


Figure 79: Elevated water T_2 and water T_2 CV measured in the leg of WT and mdx mice: mdx showed a higher percentage of elevated water T_2 values as well as higher CV in the anterior and posterior compartment compared to WT ($\$$: $p < 0.05$).

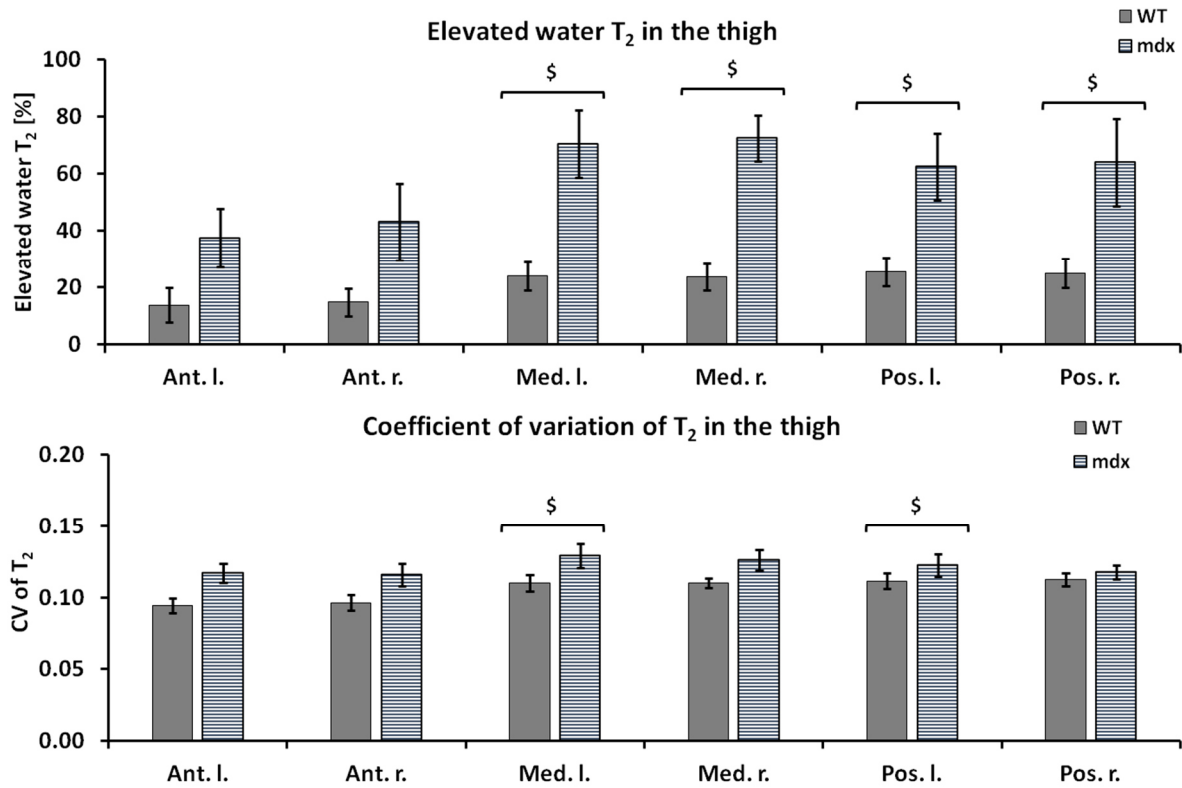


Figure 80: Elevated water T_2 and water T_2 CV measured in the leg of WT and mdx mice: mdx showed a higher percentage of elevated water T_2 values as well as higher CV in the anterior and posterior compartment compared to WT ($\$$: $p < 0.05$).

¹H NMR spectroscopy

The localized ¹H spectroscopy showed a trend of elevated lipid ratios in *mdx*, that remained not significant compared with WT (Anterior leg: *mdx* 0.007 ± 0.005 and WT 0.007 ± 0.004; posterior leg: *mdx* 0.010 ± 0.003 and WT 0.005 ± 0.002; anterior thigh: *mdx* 0.014 ± 0.008 and WT 0.011 ± 0.009; posterior thigh: *mdx* 0.018 ± 0.008 and WT 0.005 ± 0.004).

³¹P NMR spectroscopy

Figure 81 presents the non-localized spectra of *mdx* and WT. The mean of PCr/ATP and Pi/ATP were elevated compared to the WT (Table 11; both not significant). The pH was higher in *mdx* than in WT (7.14 ± 0.09 vs 7.06 ± 0.06). In contrast to WT, three out of five spectra of *mdx* mice showed a clear peak at the PME resonance.

Table 11: Mean values ± SD for the different phosphate metabolites in WT and *mdx* (n = 5 mice per group). No significant alterations were observed.

	Pi/PCr	Pi/ATP	PCr/ATP	pH
<i>mdx</i>	0.11 ± 0.04	0.36 ± 0.11	3.29 ± 0.28	7.14 ± 0.09
WT	0.09 ± 0.02	0.27 ± 0.09	3.08 ± 0.30	7.06 ± 0.06

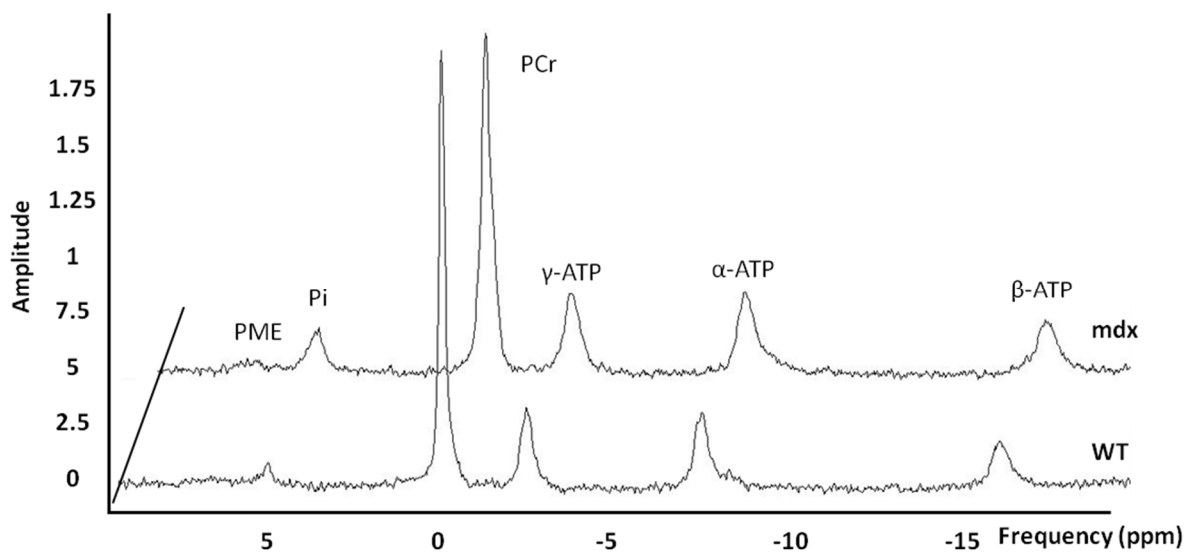


Figure 81: Resting ³¹P spectra (TR 2.5 s) acquired on the right leg are shown for *mdx* and WT mice. Peaks were assigned to PME (around 6 ppm), Pi (4.95 ppm), PCr (at 0 ppm), and γ- (-2.4 ppm), α- (-7.5 ppm), and β- (-16 ppm) ATP. Each spectrum represents an average of 720 FIDs over 30 minutes.

6.5 Validation of new NMR outcome measures on dystrophic murine models

In this subchapter, I present the results of the ISIS-CPMG and ^{23}Na NMR acquisitions as well as the histological features. The new NMR indices are compared to the outcome measures of the standard protocol.

ISIS-CPMG

Figure 82 presents the results of this bi-exponential fit as mean of average and SD of the relative short T_2 amplitude and short and long T_2 values. A significant increase in the short T_2 was observed in *mdx* compared to WT.

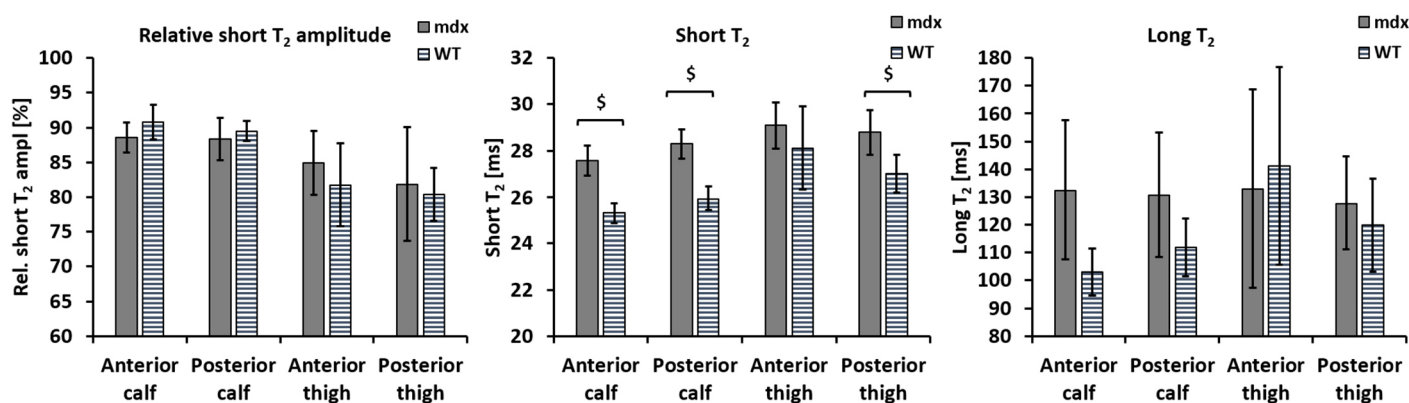


Figure 82: Results obtained from the bi-exponential fit for the relative short fraction and short and long T_2 values in WT and *mdx* ($n = 6$ mice per group). Short T_2 s were increased in the thigh and anterior compartment of the leg compared to the WT ($\$: p < 0.05$).

^{23}Na NMR spectroscopy

During the course of the ^{23}Na acquisitions of *MMex38*, the SR evaporated out of the small vial making a signal calibration impossible. Thus, only the TQF/FID ratio and T_1 values were calculated for *MMex38* and are presented in Table 12. The TQF/FID ratio was independent of the volume and considered to give a correct indication of sodium distribution in the leg between the two groups. The mean TQF/FID ratio was decreased in *MMex38* mice while the mean T_1 value was increased when compared to WT (both $p < 0.05$). An increased T_1 was accompanied with a decrease in the TQF/FID ratio (Figure 83).

Table 12: Mean values \pm SD of the ^{23}Na TQF/FID ratio and the ^{23}Na T_1 in WT and *MMex38* (*MMex38* $n = 6$, WT $n = 5$). Significant alterations were observed in the TQF signal and the T_1 values ($\$: p < 0.05$).

	TQF/FID	T_1 [ms]
<i>MMex38</i>	$0.157 \pm 0.043^\$$	$36.6 \pm 2.2^\$$
WT	0.212 ± 0.034	32.7 ± 2.6

For the ^{23}Na experiments in WT and *mdx*, a new vial for the SR reagent was used that was impermeable during the course of ^{23}Na acquisitions. Table 13 presents the calibrated FID and TQF signal as well as the TQF/FID ratio and T_1 values. The TQF/FID ratio were significantly increased in *mdx* mice when compared to WT. No significant changes were observed in the FID signal, the TQF signal and T_1 values between *mdx* and WT.

Table 13: Mean values \pm SD of the sodium indices measured in WT and *mdx*: FID signal, TQF signal, TQF/FID ratio, and the T_1 (*mdx* $n = 6$, WT $n = 5$). Significant alterations were observed in the TQF/FID ratio ($\$: p < 0.05$).

	FID [a.u.]	TQF [a.u.]	TQF/FID	T_1 [ms]
<i>mdx</i>	0.201 \pm 0.014	0.05 \pm 0.003	0.253 \pm 0.026 §	32.9 \pm 2.6
WT	0.208 \pm 0.031	0.044 \pm 0.008	0.212 \pm 0.034	32.7 \pm 2.6

As previously seen in *MMex38* mice, an increased T_1 was accompanied with a decrease in the TQF/FID ratio. Figure 83 illustrates the correlations of the TQF/FID ratio with the global sodium T_1 and the PCr/ATP ratio obtained by ^{31}P NMR. No further correlations between ^1H T_2 , ^{31}P , and ^{23}Na NMR parameters have been observed.

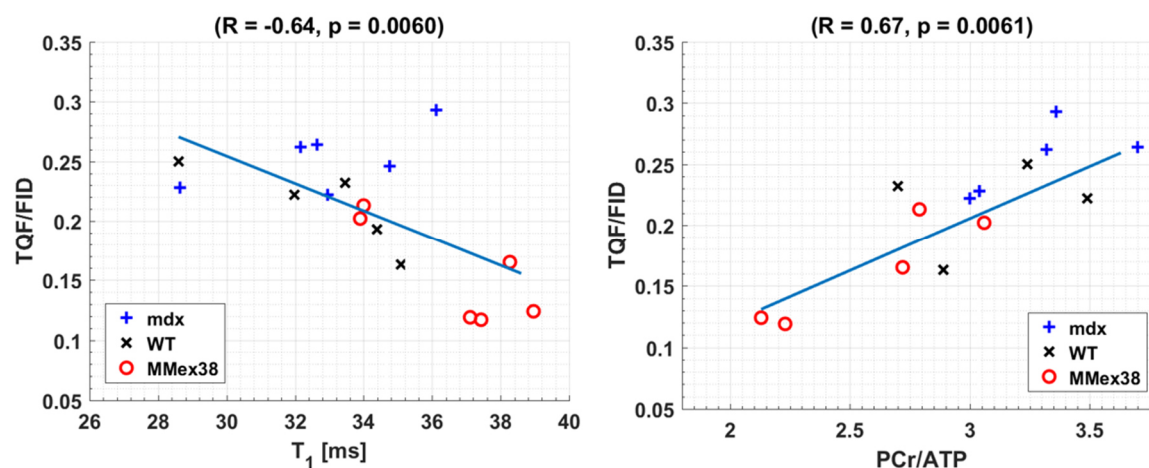


Figure 83: Correlation between the TQF/FID ratio and ^{23}Na T_1 values and PCr/ATP ratio (including *MMex38*, *mdx*, and WT mice).

Histology

To have a microscopic insight of the pathology present in the dystrophic muscles, H&E staining was performed. Consistent with the elevated fat ratios and increased disease activity (high T_2 values, high ratio of pixels with elevated T_2 , and high CV of T_2), the histological slices of *MMex38* contain a mix of inflammation, degenerating and regenerating fibres, and an accumulation of lipid droplets. These features are especially pronounced in the proximal muscles compared to distal muscles that are more spared (compare Figure 84 and Figure 85). Inflammation, necrosis or fatty infiltration were not observed in either of the WT muscles (Figure 86). The muscles of *mdx* mice also

showed typical histological features of a dystrophic muscle including centronucleated fibres. In the proximal muscles of *mdx* mice several accumulations of mononuclear cells and few lipid droplets were observed (Figure 87).

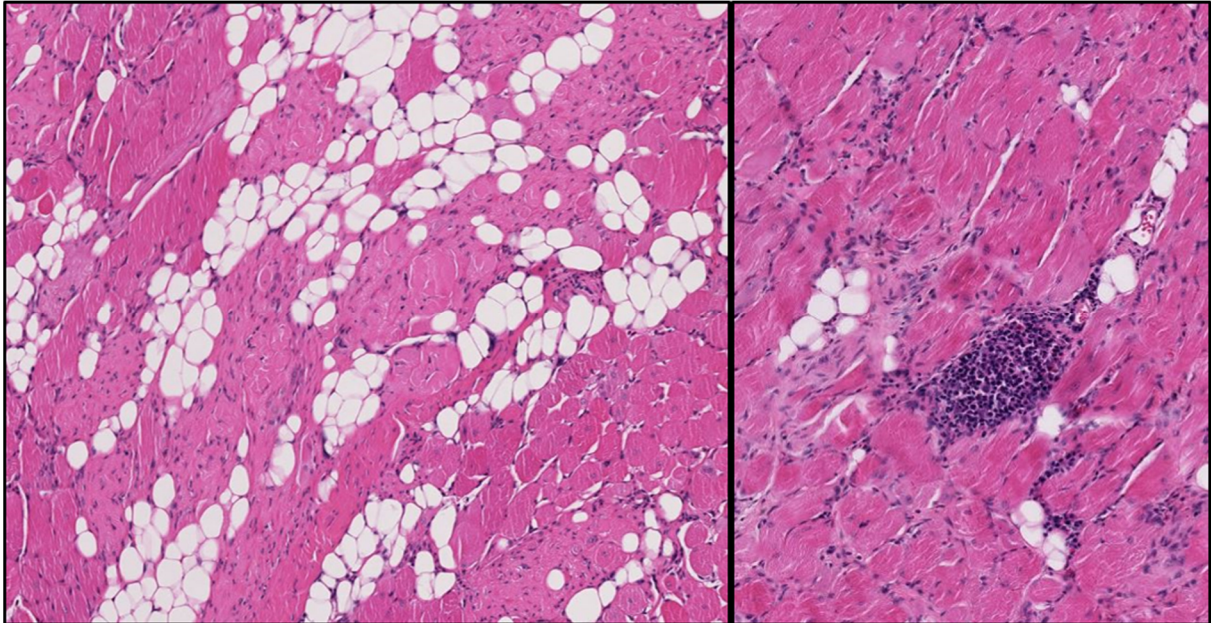


Figure 84: Visualisation of myofibre damage and mononuclear cell infiltration in the quadriceps of MMex38. H&E staining of the quadriceps muscle cross sections reveals the dysferlin-deficient pathological process. The images show centrally nucleated fibres indicating ongoing necrosis and recuperation and fatty tissue replacement. Several accumulations of mononuclear cells were observed in dysferlin-deficient muscle tissue (right).

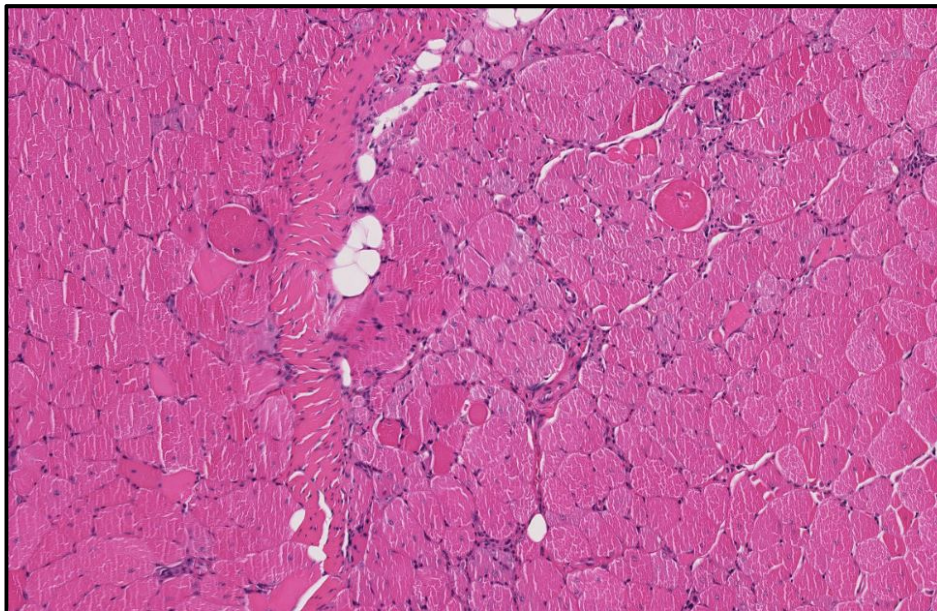


Figure 85: Visualisation of myofibre degenerating and regenerating fibres in the leg of MMex38. H&E staining of the tibialis anterior muscle cross sections reveals centrally nucleated fibres, some atrophic fibres and lipid droplets. Few areas are infiltrated by mononuclear cells.

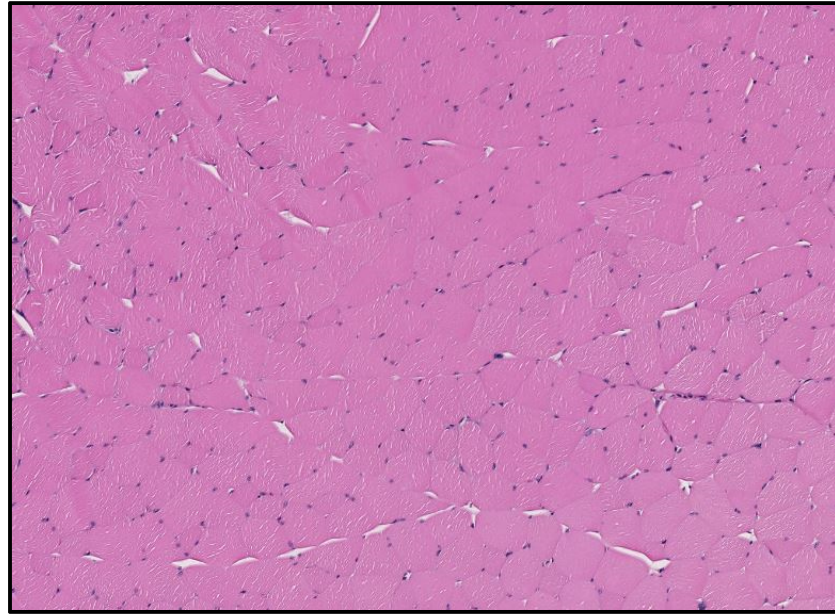


Figure 86: Visualisation of healthy myofibres in the quadriceps of WT. The images show neither centrally nucleated fibres nor lipid droplets in the muscle tissue.

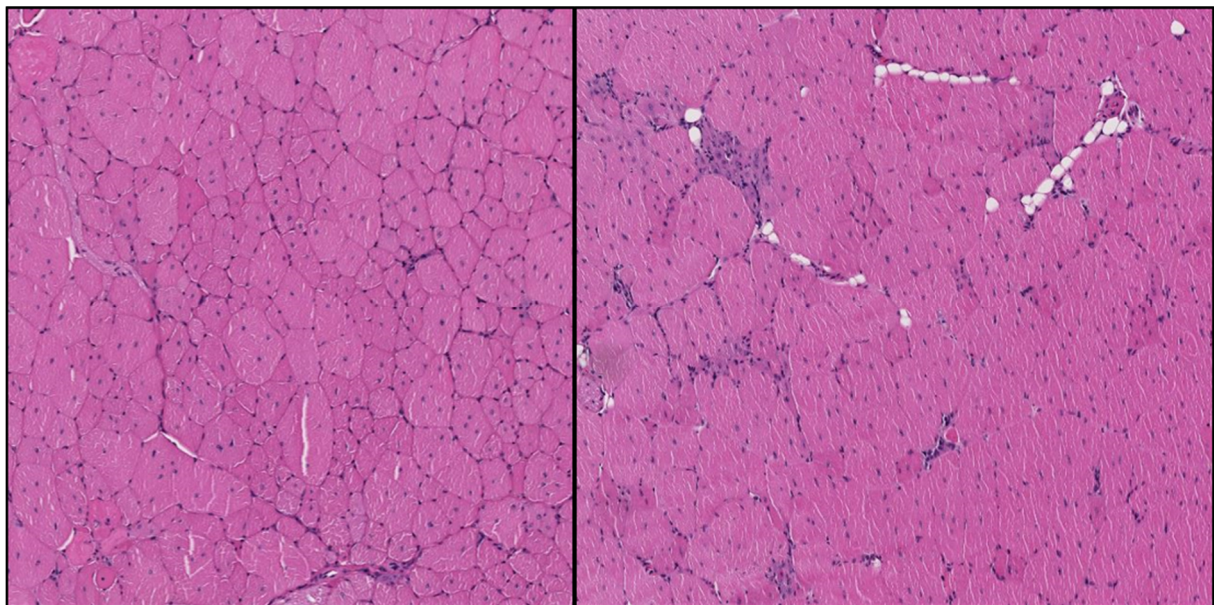


Figure 87: Visualisation of myofibre damage and mononuclear cell infiltration in the tibialis anterior (left) and quadriceps muscles (right) of mdx. The images show centrally nucleated fibres indicating ongoing necrosis and recuperation. In the quadriceps of mdx mice, several accumulations of mononuclear cells and few lipid droplets were observed.

6.6 Discussion

6.6.1 NMR characterization of the dysferlin-deficient murine models

Muscle dystrophies commonly exhibit a variety of pathological features that include muscle weakness, inflammation, loss of membrane integrity, necrosis, regeneration, and ultimately fat replacement. Here, we used a multi-parametric NMR approach to study the different underlying pathological processes. A standard NMR protocol was used to characterise the pathology of a novel

dysferlin-deficient murine model. The set of different NMR methods produced a variety of non-invasive measures that allow monitoring the disease progression and activity.

Quantitative NMRI and NMRS provided a variety of abnormal indices in thigh and leg muscles of both dysferlin-deficient animal models. The anatomical images indicated a very advanced disease progression in the proximal hindlimb muscles. The disease progression and activity was symmetrical between the left and right limbs. The visible fat infiltration in the thigh was confirmed by increased fat fraction measured by localized ^1H spectroscopy as well as by ^1H imaging. The reduced ^1H T_1 values in the medial posterior compartment of the thigh, which showed the highest FF of all muscle compartments based on MSME images, reflect also the presence of fat in the skeletal muscle tissue. Although T_1 mapping is spatially localized, it was less sensitive than the spectroscopic approach to detect fat accumulation. Localized ^1H NMR spectroscopy also detected a small but significant accumulation of lipids in the calf that was not detected by the fat fraction maps obtained by the tri-exponential fit of the MSME signal decay. The fat ratios tended to be higher in the *MMex38* murine model than the *BLAJ* model; however, a higher number of animals would be needed to confirm this observation. The reported increase of fatty tissue in the dysferlin-deficient mice is in accordance with previous study on *BLAJ*. Oil red O staining and electron microscopy revealed a significant lipid accumulation with areas of increased numbers of interstitial adipocytes within the myofibres of dysferlin-deficient mice [50]. Nagy *et al.* reported a progressive volume loss and fatty acid accumulation in the hip region observed by ^1H NMR in six to twelve-month-old *BLAJ* mice [207].

Alterations in water T_2 were monitored as they convey also information about the structural changes within the muscle. Both dysferlin-deficient murine models showed increased water T_2 values as well as high percentage of pixels with elevated water T_2 in leg and thigh muscles. No correlation existed between the water T_2 and fat fraction. Thus, the elevated water T_2 values reflect disease activity including inflammation, necrosis, and oedema. The coefficient of variation of water T_2 reflects the tissue heterogeneity and points to a tissue disorganization in dysferlin-deficient muscles [208]. Absence of correlation between T_2 heterogeneity and the amount of fatty infiltration reflects mechanism of tissue disorganization other than fat infiltration. The high heterogeneity in the dysferlin-deficient mice could be attributed for example to development of interstitial fibrosis or centronucleated fibres.

^1H NMR data demonstrated that leg muscles are less affected by fat infiltration, but exhibit already high disease activity. ^{31}P NMR was used to detect changes in dysferlin-deficient muscles before irreversible changes such as fatty infiltration occur. Thus, disturbances in energy metabolism were analysed in the dysferlin-deficient muscle of *MMex38*.

Energy metabolites quantified from ^{31}P NMRS also revealed a significantly higher pH in the leg of *MMex38*. Some, but not all *MMex38* mice also showed deficits in phosphocreatine. The decrease in the mean PCr/ATP ratio reflecting the energy state of muscle nevertheless was not significant due to the high SD. Human ^{31}P NMR data revealed significantly higher Pi/PCr and pH and significantly lower PCr/ATP in the tibialis anterior muscle of dysferlinopathy patients compared to control [209]. To the best of my knowledge, no ^{31}P NMR data was reported on dysferlin-deficient mice. A ^1H NMR study reported decreased creatine levels in the gluteus maximus of 6 month old *BLAJ* mice, but no data was reported for one year old mice [207]. Thus, our results are in agreement with these studies, although we did not find significant alterations for all the reported indices.

The NMR measures showed similar contrast between the two different dysferlin-deficient models, *BLAJ* and *MMex38*. However, the number of animals was very low and an increase in sample size would make the comparison more robust. Nevertheless, it seems that different mutations in the dysferlin gene lead to similar phenotype. So far, only very few NMR studies with dysferlin-deficient mouse models were presented providing insight into the pathophysiology. One reported as aforementioned a fatty acid accumulation and decreased creatine levels in the hip region of *BLAJ* mice [207]. Another study imaged the TA muscle of the *A/J* murine model after lengthening contractions [210]. In this longitudinal study, $T_2\text{w}$ imaging after contractions was performed up to 14 days. They reported, much higher increase in T_2 signal intensity in dysferlin-deficient muscles compared to control after injury relating their observation to the membrane repair impairments of the mouse model.

Finally, the reported disease progression and disease activity are consistent with the pathological changes observed in human dysferlin-deficient patients [209]. This study investigated several NMR outcome measures that could be used to study the efficacy of therapeutically interventions for human dysferlin deficiency. Furthermore, it would be interesting to study the effect of exercise in the dysferlin-deficient model by different NMR techniques. An eccentric exercise study in combination with ^1H T_2 , ^{31}P NMR, and ^{23}Na NMR could investigate the impairments of membrane repair in dysferlin-deficient muscles. However, due to time constraints this could not be performed yet.

6.6.2 NMR characterization of the dystrophin-deficient murine models

The anatomical images revealed the mild phenotype of the dystrophin-deficient murine model. DMD patients can compensate more or less for the disease process until an age of about five years. At this age, they present typical difficulties in their motor function such as climbing stairs.

Chronic muscle damage with inflammation, necrosis and oedema lead to the progressive muscle loss and replacement of muscle tissue by fibro-fatty tissue. In contrast, an active regeneration in *mdx* throughout their lifetime seems to counterweigh for the ongoing muscle damage. Thus, *mdx* skeletal muscle tissue does not resemble the one of DMD patients at an advanced stage of disease.

In the present study, no significant fat infiltration was detected by ^1H NMR in thigh or leg muscles. An increase in T_1 values in the anterior and medial muscles of the leg was paralleled with an increase in T_2 . As there was no correlation between the fat fraction and T_1 values, concurrent changes in T_1 and T_2 can point to oedema in the muscle tissue. Increases in T_1 were previously reported in GRMD dogs, a canine model for DMD [211]. The alterations in T_1 were related to changes in the water molecular dynamics that also increased the muscle T_2 , however on a smaller scale. *Mdx* mice showed increased water T_2 values as well as high ratio of pixels with elevated water T_2 in leg and thigh muscles. No correlation existed between the water T_2 and fat fraction. Thus, the elevated water T_2 values reflect disease activity including inflammation, necrosis, and oedema. The increased water T_2 heterogeneity in dystrophin-deficient muscles points to a tissue disorganisation. These changes in water T_2 have also been observed in DMD patients [121], [125]. So far, some studies reported T_2 changes in the *mdx* muscle. In 2013, a case study monitored temporal changes of the T_2 intensities in the leg of one *mdx* mouse [212]. A peak in muscle weakness and degeneration/regeneration was reported between the 2nd and 5th weeks of life. The heterogeneity of hyperintensities increased up to 13 weeks of age and then decreased. Vohra *et al.* further investigated age-related T_2 changes in hindlimb muscles of *mdx* mice [213]. They reported elevated global T_2 values and increased percentage of pixels with elevated T_2 (two times the SD) at all ages. Asynchronous and cyclical alterations in the global T_2 were observed in 20 to 60 week-old mice with a mean muscle T_2 peak at 7 - 8 weeks. Other studies used T_2 measurements to study the impact of downhill running and gene therapy in *mdx* mice [214], [215]. Although, these studies used a mono-exponential fit to determine the T_2 , their results reflect the inflammation and muscle damage present in *mdx* as the murine model shows no significant fatty infiltration.

We further analysed impairments in energy metabolism in murine dystrophic muscle by ^{31}P NMR. Several studies on DMD patients showed promising results to detect changes in dystrophin-deficient muscles before onset of irreversible changes such as fatty infiltration [53], [60], [121], [216]. In our study, the PCr/ATP and Pi/ATP ratio as well as the pH tended to be increased compared to the WT. However, no significant alterations were measured. In contrast to WT, three out of five spectra of *mdx* mice showed a clear peak at the PME resonance. No PDE peak was visible in the murine ^{31}P spectra as reported in dystrophic patients [53]. Increases in pH and Pi/ATP ratios are expected in

dystrophic muscles as they can serve as a marker of the membrane leakiness and the impairment of ionic intracellular homeostasis. The higher, but non-significant PCr/ATP ratio is first contra-intuitive, because dystrophic muscles have an increase in PCr/ATP reflecting a loss of metabolic efficiency [121]. Our observation that this ratio was not decreased was caused by two *mdx* mice, which seem to show no energy metabolism impairment. Thus, the presented results are pointing to the same direction as other ^{31}P NMR studies on dystrophic muscles [217]. Heier *et al.* studied the potential of ^{31}P spectroscopy on *mdx* as an outcome measure translatable to human clinical trials [218]. *Mdx* mice showed a lower PCr/ATP ratio and an increase in Pi/ATP compared to WT at six weeks of age. This difference between WT and *mdx* disappeared after about 10 weeks of age. Thus, the peak stage of muscle weakness and necrosis was paralleled with energy metabolism deficiency that later improved during recovery phase. However, this longitudinal study included only mice from six to twelve weeks of age. Nevertheless, the age of our *mdx* mice might be also an important reason why we did not observe any significant alterations in the energy metabolism.

6.6.3 Sensitivity of ^{23}Na NMR and ISIS-CPMG sequences to the dystrophic muscle

Our ^1H NMR data demonstrated that hindlimb muscles of *mdx* and *MMex38* exhibited active disease activity. In an extended NMR protocol, the murine models were used to test the sensitivity of the ISIS-CPMG method and our non-localized ^{23}Na protocol (4.6.1).

Regarding the T_2 ^1H relaxometry study using ISIS-CPMG, only the short T_2 was significantly increased in *mdx* compared to WT, whereas the long T_2 and the relative fraction seemed not to be impacted by the dystrophic disease process. The increase in short water T_2 with constant relative fractions points to an increase of water within the extravascular compartment [17]. Similar changes were observed in DMD patients (7.3).

We further analysed impairments in sodium homeostasis in murine dystrophic muscle by ^{23}Na NMR. ^{23}Na longitudinal relaxation times and ^{23}Na TQF/FID ratio was determined from a non-localized ^{23}Na NMR spectroscopy protocol. Due to the short T_1 relaxation time, we used a repetition time of 200 ms to determine the ^{23}Na signals at fully relaxed longitudinal relaxation conditions. Another study reported an increase of intracellular sodium levels in the myocardium during hypoxia, while the T_1 stayed constant [219]. This observation may indicate that ^{23}Na T_1 stays constant even when physiologically occurring alterations in the intracellular sodium concentrations occur. We reported here a significant decrease of the mean TQF/FID ratio and a significant increase of the T_1 in *MMex38* mice when compared to WT. In *in vitro* experiments (4.6.1), T_1 values decrease with increase of agarose due to bi-exponential relaxation behaviour. In our drain-filling paradigm in

human, we reported a decrease in the TQF/FID ratio paralleled with an increase in T_1 during the vascular filling condition. Thus, the present decrease in the ratio and increase in T_1 point towards oedema in *MMex38* mice. A similar observation has been described in brain tumours, where the percent of bound Na^+ ions was dramatically decreased and the ^{23}Na T_1 relaxation time were increased [220].

On the contrary, the ^{23}Na TQF/FID ratio was increased in *mdx* mice compared to WT. No alterations were observed in the ^{23}Na T_1 . This increase in the TQF/FID ratio can reflect the increased intracellular sodium concentration in *mdx* muscles. Elevated total sodium levels were measured in four-month old *mdx* mice using microelectrodes [221]. Based on intra- and extracellular volumes and sodium concentrations, the intracellular sodium concentration was calculated, which was approximately doubled in the *mdx* compared to WT. They suggested that the intracellular sodium concentration could be increased if Na-K ATPase is partially inhibited such as by a decrease in cellular ATP concentration in dystrophin-deficient cells [217]. The absence of dystrophin also changes the expression level and gating properties of the sodium channel Nav1.4 in *mdx* leading to increased sodium concentrations and enhanced cell death [61].

Important correlations have been found between ^{23}Na and ^{31}P NMR parameters. The sodium T_1 correlated with the sodium distribution merging data from *mdx*, *MMex38*, and WT mice. If the percent of bound Na^+ ions increases, then ^{23}Na T_1 relaxation time decreases due to the bi-exponential nature of the sodium nuclei. It is interesting to see, that the dystrophin- and dysferlin-deficient muscles do not seem to have the same ^{23}Na NMR features. While the *MMex38* mice showed an increase in T_1 and a decrease in TQF/FID, the *mdx* mice exhibited an increase in TQF/FID ratio with an unchanged T_1 . This might reflect different pathophysiological processes as increase in intracellular sodium concentration and water redistribution in the different tissue compartments.

The second important correlation was observed between PCr/ATP and the TQF/FID. In dystrophic muscle, reduced PCr/ATP levels could indicate a loss of metabolic activity/contractile tissue. Changes in both ratios could point to membrane leakiness/breakdown of membrane.

The histological samples confirmed the dystrophic pattern in the dysferlin-deficient disease process. H&E staining demonstrated the presence of central nuclei with a mix of inflammation, hypertrophic fibres, and myofibre degeneration and regeneration in *mdx* as well as in *MMex38*. The visual inspection of all slices indicates that *MMex38* show more intramuscular lipid droplets and a higher infiltration of mononuclear cells than *mdx*. These features are all signs of a dystrophic muscle, which were not observed in WT.

6.6.4 Limitations

The extended protocol only included six mice per group. I had also to discard some of the ^{23}Na and ^{31}P spectra as they were of insufficient quality to be used for the analysis. Thus, this further reduced the sample size and might be one reason while no significant alterations have been found in Pi/ATP and PCr/ATP ratios as well as ^{23}Na TQF signal. Furthermore, the ^{23}Na signals were not calibrated for *MMex38* mice due to the evaporation of the SR in course of experiment. For ^{31}P and ^{23}Na a non-localized approach was chosen to increase the spectral quality and reduce acquisition times. Thus, spatial information was lost. The leg was carefully placed inside the coils during different set-ups to assure a consistency between the acquisitions. Due to the non-localized approach, sodium pools from other tissue such as skin, tendons, and ligaments contributed to a certain extent to our results. Although its contribution is obviously smaller than the one of skeletal muscle given the size difference of the organs, its real impact on our findings remains unclear.

6.7 Conclusion

Several NMR based biomarkers were tested to monitor the disease process in dystrophin- and dysferlin-deficient murine muscle. Tissue properties changed according to the underlying pathological process, which was successfully monitored by NMR.

	Dystrophin-deficient murine models (mdx)	Human DMD
Disease activity	Water $T_2 \uparrow$	Water $T_2 \uparrow$
Disease progression	No fat infiltration	% Fat in different muscle groups
	Dysferlin-deficient murine models (MMex38, BLAJ)	Human LGMD 2B
Disease activity	Water $T_2 \uparrow$	Water $T_2 \uparrow$
Disease progression	% Fat in different muscle groups	% Fat in different muscle groups

Figure 88: Similarities and discrepancies of different NMR parameters between murine models and corresponding human myopathy.

Figure 88 summarizes water T_2 and fat fraction alterations in murine models and corresponding human dystrophies. The *mdx* model possesses signs of dystrophic muscle including increased water T_2 values and associated parameters, which reflect the ongoing disease activity. However, the hindlimb muscles of *mdx* show no important fat infiltration and muscle wasting resulting in a phenotype that is much less severe than in DMD patients. In contrast, an elevated

disease activity as well as disease progression reflected by the important fatty replacement were observed in the dysferlin-deficient murine models.

In summary, murine models provide researchers with an important tool to study the pathological process in dystrophic muscles and to test novel therapies. Moreover, NMR can be used as a non-invasive method providing outcome measures for muscle damage. In this context, few gene correction studies in *mdx* and LGMD mouse models have already implemented NMR techniques. After gene transfer, ^1H T_2 changes were observed to monitor the correction of sarcolemma integrity [215], [222]. These studies show the potential trend to use NMR outcome measure for muscle damage use in preclinical trials. Moreover, well-described animal models can be used to test the sensitivity of new NMR approaches before translation to human studies.

Characterization of the dystrophic muscle by quantitative ^{23}Na NMR and ^1H NMR in a clinical setting

7.1 Characterization of skeletal muscle of Duchenne muscular dystrophy patients by ^{23}Na NMR and ^1H NMR

DMD is a severe muscular dystrophy with chronic inflammation, ionic dysregulation, and exhaustion of regenerative capacities leading ultimately to progressive muscle wasting (2.5.2). Figure 89 summarises the main underlying pathological processes in dystrophin-deficient muscles that are relevant to this study. Several NMR methods have been proposed to monitor non-invasively the disease activity and progression; please refer to 3.4 for a discussion about the current state and problems of diverse NMR techniques commonly used to examine MDs. Here, we performed a longitudinal NMR study of skeletal muscle tissue of DMD patients at the University Hospital in Erlangen.

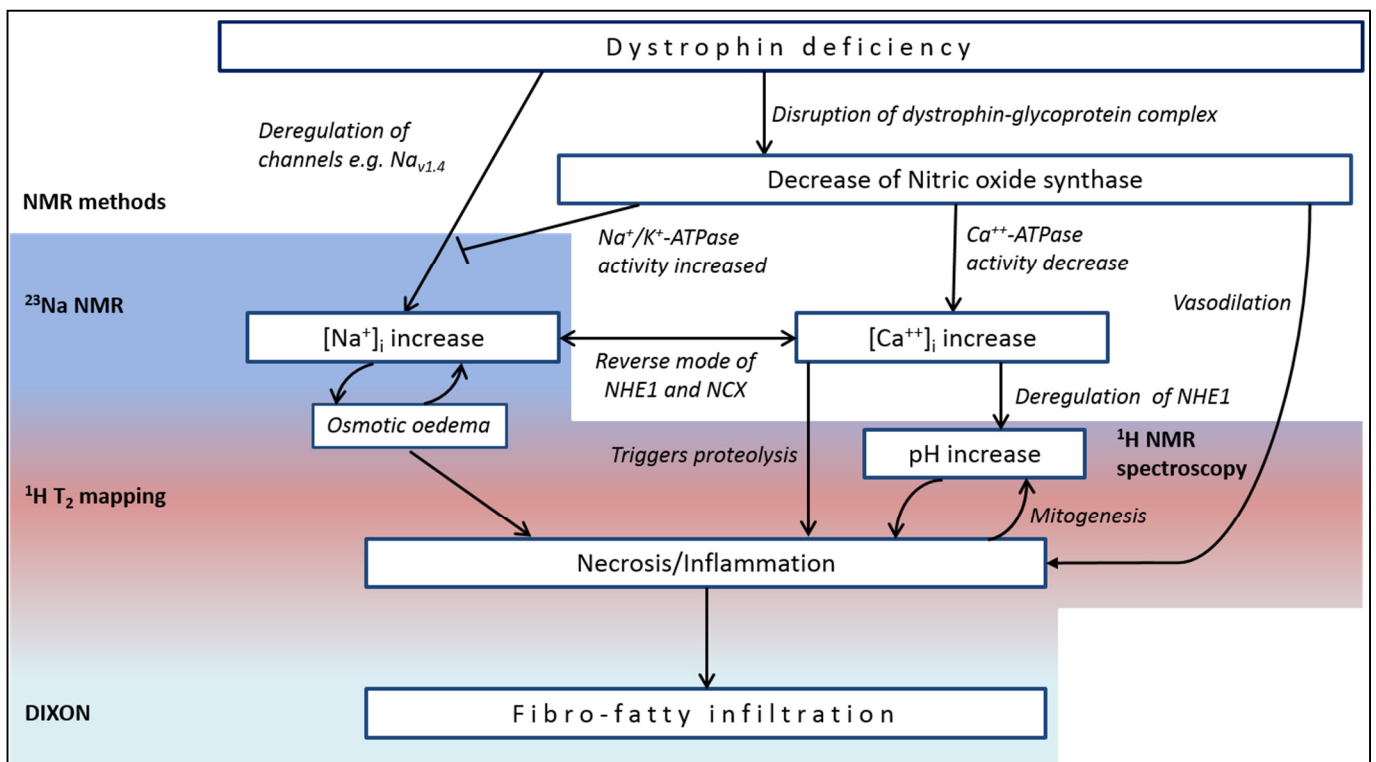


Figure 89: Schema of supposed underlying pathological processes in dystrophin-deficient muscle. While sodium and pH impairments occur at an early stage, the fibro-fatty infiltration presents the end stage of the disease leading to immobility at the beginning of the second decade of life. Different NMR methods are used to track the disease-related alterations including ^{23}Na NMR, ^1H T_2 mapping, ^1H spectroscopy, and Dixon techniques. Figure based on [59], [61], [63], [145], [223].

The objective of this study was to combine different NMR methods and to evaluate their sensitivity to monitor the pathological processes of the dystrophic muscle at an early stage of the disease. Thus, ambulant DMD boys were examined at baseline and after six months to monitor the disease progression of the leg muscles. The NMR protocol included fat quantification, which is the most commonly employed NMR outcome measure for monitoring the disease progression in DMD patients [9]. Furthermore, water T_2 measures were performed to monitor the disease evolution that precedes the fibro-fatty infiltration of the muscle tissue. ISIS-CPMG sequences were acquired for a more in-depth analysis of the T_2 relaxation behaviour. We further tested ^1H NMR-based pH and different ^{23}Na NMR indices (4.6) as potential sensitive and early indicators of dystrophic muscle.

7.2 Materials and methods

Subjects and study design

The ethic review board at the Friedrich-Alexander University approved the DMD NMR study (number: 250_16 Bc). A medical doctor provided participants and their legal guardian with clear information about the study and informed written consent was obtained before each exam. The medical history of each DMD patient was recorded; eleven boys with genetically confirmed diagnosis of DMD (age 8.3 ± 2.3 years) and one without genetically confirmed diagnosis of muscle dystrophy (age 16.5 years) were enrolled in the study (Table 14). Ten boys were under glucocorticoid treatment at the time of the NMR experiments. All boys showed clinical symptoms of muscle dystrophy; however, patient seven was still ambulant at 16 years of age, which indicates a milder form of muscle dystrophy. The inclusion criterion was the ability to stay still in the NMR scanner for the whole duration of the protocol. DMD patients were invited for a follow up visit at 6 months. To date, eight patients had their second visit. Twelve healthy boys (age 9.6 ± 2.3 years) were also recruited for one NMR examination as age-matched controls.

NMR protocol

A standardized protocol was implemented for the right lower leg. Subjects were lying feet first in supine position with the biggest circumference of the lower leg in the centre of the coil. The coil position was marked on the leg to ensure the same positioning of the leg between the different parts of the protocol. No anaesthesia was used and the children listened to audio files throughout the data acquisition while one relative was sitting next to them in the room. Nevertheless, we had to stop the NMR acquisition for patient 6 and 8 after the ^1H part since they were too restless. The total scan time was between 60 and 75 minutes including shim and time for positioning between the different parts of the protocol.

Table 14: List of participating DMD patients with age, diagnosis and therapy.

Patient	Age (years)	2 nd visit	Diagnosis	Glucocorticoid therapy	Additional pharmaceutical treatment
#1	6.1	Yes	Point mutation in Exon 39 (c.5530C>d)	Yes	Ataluren
#2	9.8	Yes	Deletion Exons 48-50	Yes	Metformin, Citrulline
#3	11.4	Yes	Mutation Exon 51 (c.7541dupA)	Yes	
#4	11.5	Yes	Deletion Exons 18-19	Yes	Idebenone
#5	11.3	Yes	Deletion Exons 48-50	Yes	
#6	5.6	No	Point mutation in Exon 12 (c.1375G>T)	Yes	Ataluren
#7	16.5	No	<i>No mutation found (histology)</i>	Yes	
#8	7.2	Yes	Deletion Exons 28-43	No	
#9	7.2	Yes	Deletion Exons 28-43	No	
#10	8.6	Yes	Point mutation in Exon 41	Yes	
#11	7.0	No	Deletion Exons 45 - 50	Yes	
#12	5.9	No	Point mutation in Exon 46 (c. 6762+1G>T)	Yes	

The ¹H NMR protocol consisted of a 3-point gradient echo Dixon sequence [151] for fat quantification, a MSME sequence for T₂ mapping and two localized spectroscopy sequences, PRESS [178] and ISIS-CPMG [17], to measure the intracellular pH and derive T₂ spectra, respectively. The 3D 3-point Dixon sequences were performed with the following parameters: TR = 10 ms, two times two TEs = 2.75/3.95 ms and 2.75/5.15 ms, FA of 3°, and 64 slices of 5 mm thickness and a resolution of 1.3 x 1.3 mm², whereas the middle slice was positioned at the iso-centre of the magnet (T_{acq} = 2 × 1 min 36 s). The MSME images were acquired with a TR of 3 s and 32 equally distributed TEs from 9.5 to 304 ms. Parallel imaging using GRAPPA [224] was performed with an acceleration factor of two (T_{acq} = 3 min 41 s). The central slice of the five slices with a slice thickness of 10 mm and a resolution of 1.4 x 1.4 mm² was positioned in the iso-centre. For the ¹H spectroscopy part, a localizer with 4 x 5 x 4 slices localised in the gastrocnemius muscles was performed to ensure a proper voxel positioning on the gastrocnemius medialis muscle. The voxel dimension of 30 x 9 x 30 mm³ was reduced to the muscle size if too big. PRESS sequences with and without water suppression peak were performed using a TR = 3 s and a TE = 30 ms and 64 and 16 averages, respectively (total T_{acq} = 4 min 24 s). The ISIS-CPMG sequence used the same voxel size and position than the PRESS sequences with TR = 10 s and 400 echoes with ES = 2 (T_{acq} = 2 min 40 s) [17].

For the ²³Na NMR part, two DA-3DPR [18] were acquired, one without an IR pulse to quantify TSC and the second one with an IR pulse to obtain the ICW signal (4.6.3). Prior to the image acquisition, a non-selective B₁⁺ calibration sequence using rectangular pulses determined the

reference voltage for a 90° excitation pulse of 500 μ s length. This voltage was then applied as the reference voltage for the entire ^{23}Na NMR protocol. For the TSC acquisitions following parameters were used: TE = 0.3 ms, TR = 50 ms, FA = 80° (Ernst angle), T_{readout} of 10 ms, and nominal spatial resolution = 3 x 3 x 15 mm³ (T_{acq} = 6 min 53 s). To obtain ICW images, an inversion pulse with a TI of 34 ms was applied to suppress the signal from sodium ions with relaxation times similar to sodium ions in pure saline solution. Parameters were: TR = 124 ms, TE = 0.3 ms, FA = 90°, T_{readout} = 20 ms, and nominal spatial resolution = 4 x 4 x 20 mm³ (T_{acq} = 9 min 50 s).

The sodium protocol was extended with three non-localized spectroscopy sequences: FID, TQF, and IR-LL that were introduced in 4.6.1. The FID sequence was acquired with the following parameters: TR = 300 ms, NEX = 200, time delay = 200 μ s, BW = 5 kHz, vector size = 256 pts, and T_{acq} 1 min. The TQF acquisition was realized with τ_1 = 3 ms, τ_2 = 200 μ s, and τ_3 = 300 μ s, TR = 100 ms, NEX = 1500, BW = 5 kHz, vector size = 256 pts, and T_{acq} 2 min 30 s. During the FID and TQF acquisition, a SR as described in 5.2 was placed next to the leg. The IR-LL sequence was acquired without SR phantom and with 80 different inversion times (from 5 ms to 400 ms), FA = 3°, TR = 450 ms, NEX = 500, BW = 10 kHz, vector size = 32 pts, and T_{acq} 3 min 45 s.

Analysis of ^{23}Na and ^1H NMR data

The T_2 decay of the MSME images was fitted by a three-exponential fit (4.4.1). ROIs were manually traced within leg muscles on MSME images (see Figure 90: tibialis anterior (TA), extensor digitorum (ED), peroneus longus (PL), tibialis posterior (TP), soleus (SO), gastrocnemius medialis (GM), and gastrocnemius lateralis (GL)). The ROIs were interpolated on the FF maps derived from the Dixon method.

FF and water T_2 were determined as mean value of pixels within the drawn ROI. Only pixels with a confidence interval less than 10 were used for the analysis. The heterogeneity of muscle T_2 was assessed by the CV of water T_2 across ROIs. In addition, the percentage of pixels with water T_2 higher than 40.3 ms were computed and reported as elevated T_2 . This threshold was determined from the mean value (35.73 ms) plus three SD (1.52 ms) of water T_2 values of controls.

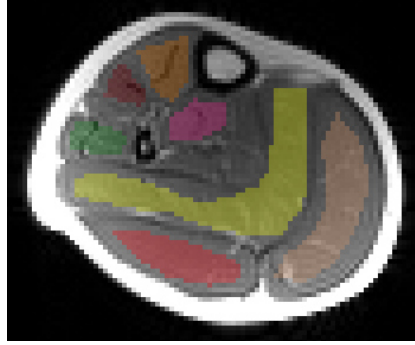


Figure 90: ROIs were traced manually on the leg muscles: Orange tibialis anterior (TA), bordeaux extensor digitorum (ED), green peroneus longus (PL), pink tibialis posterior (TP), yellow soleus (SO), red gastrocnemius medialis (GM), and salmon pink gastrocnemius lateralis (GL).

The water-suppressed and unsuppressed ^1H NMR spectra were aligned with the water frequency at 4.7 ppm. Then, resonances between 0 and 4 ppm were removed using the HLSVD (Hankel Lanczos Squares Singular Values Decomposition) algorithm followed by manual zero and first order phase corrections. The peak of the two carnosine resonances ($-\text{C}_2\text{-H}$ and $-\text{C}_4\text{-H}$) and the residual water peak were fitted with the AMARES algorithm (constraints for frequencies and linewidths, fixed phases, and Lorentzian line shapes). The pH was determined from the chemical shift between $-\text{C}_2\text{-H}$ and residual water resonance according to the modified Henderson-Hasselbalch equation (4.5.2). Only ^1H spectra with a sufficient high SNR and sufficient low peak linewidth (< 12 Hz) to enable proper $-\text{C}_2\text{-H}$ carnosine resonance fitting were accepted for the analysis.

The ISIS-CPMG T_2 curves were fitted with a biexponential model resulting in a short and long T_2 value and their relative fractions. After the ^{23}Na imaging reconstruction, the sodium signals were calibrated using the signal intensities of the background noise and two reference phantoms (20mM and 40mM NaCl in 4% agarose). TSC and ICW maps were computed as described in 4.6.3 and then corrected for the fatty infiltration. The mean TSC and ICW values per muscle were corrected with the corresponding FF derived from the Dixon method. Due to the non-negligible sodium signal of fat, the median values of the subcutaneous fat were computed on seven DMD patients and six age-matched controls (TSC of subcutaneous fat = 7.9 mM and ICW of subcutaneous fat = 0.17 a.u.) to correct together with the FF the TSC and ICW of the muscle tissue:

$$TSC_{muscle} = \frac{TSC - (TSC_{fat} \times FF)}{(1 - FF)} \quad \text{and} \quad ICW_{muscle} = \frac{ICW - (ICW_{fat} \times FF)}{(1 - FF)}$$

In the following, the fat-corrected TSC_{muscle} and ICW_{muscle} will be presented as TSC and ICW for the reader's comfort. The ^{23}Na NMRS signals were calibrated with the leg volume and SR peak as described in 5.2.1. We obtained different ^{23}Na indices: FID signal, TQF signal, TQF/FID ratio, and global T_1 value. No FID T_2^* values were fitted, because muscle ^{23}Na signal decay is superimposed by the SR phantom signal resulting in a noisy signal decay.

Statistical analysis

DMD and control groups were compared using Wilcoxon rank-sum tests, and the change between the two visits of the DMD patients were tested using Wilcoxon signed-rank tests. Repeated ANOVA taking the different muscles as intra-subject variable were performed for the overall changes in FF, T_2 , and ^{23}Na imaging data sets. Spearman-rank correlations analysed the correlation between the parameters. Statistical significance was set to $p < 0.05$.

7.3 Results

In the following, the results of the first visit of DMD patients will be presented in comparison with the control group. The second part is devoted to the longitudinal aspect of the study evaluating the NMR outcome measures obtained during the first and second visit of eight DMD boys.

7.3.1 Visit 1: DMD in comparison with control group

Fat fraction and ^1H T_2 mapping

Figure 91 shows typical water and fat images with the corresponding fat fraction maps acquired in the leg of DMD patients derived from the Dixon method. While the six-year-old DMD patient exhibited very low fat fraction in all muscles, the fat fraction was elevated in the muscles of the eleven-year-old DMD patient, who was not able to walk more than ten meters without human assistance.

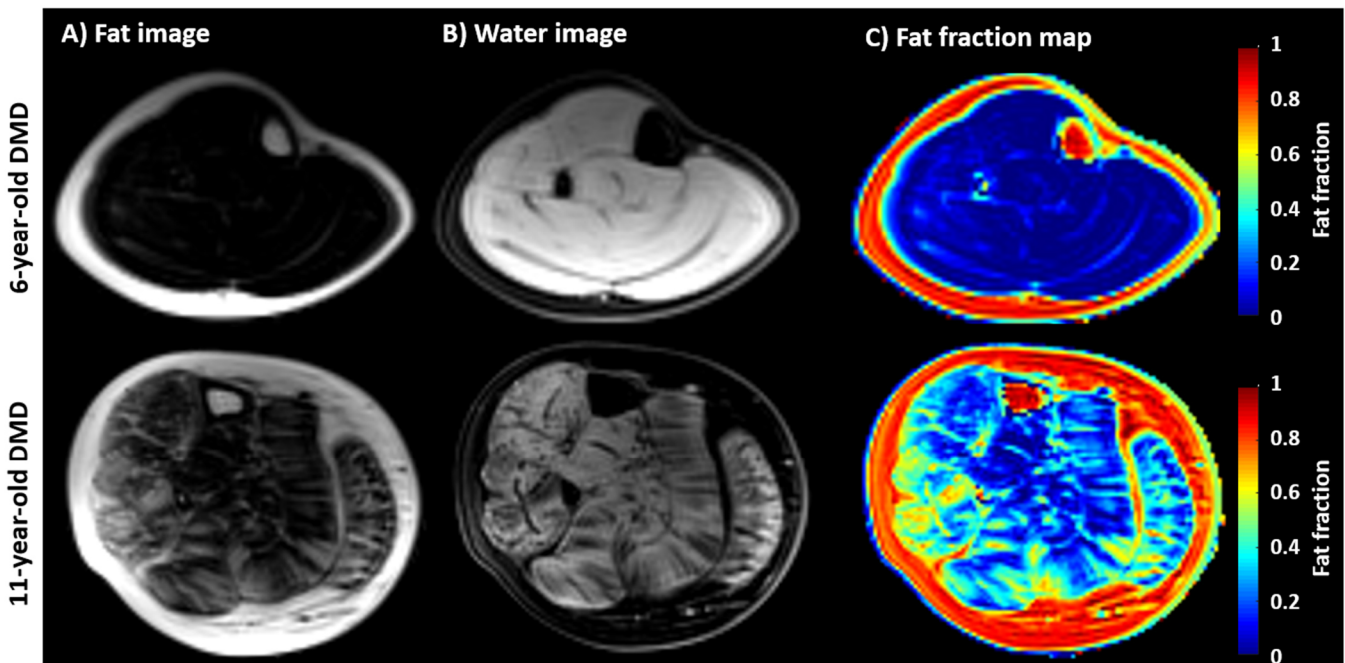


Figure 91: Examples of A) fat image B) water image, and C) fat fraction map in the leg of six- (Patient #1) and eleven-year-old (Patient #3) DMD patient derived from the Dixon method.

Table 15: ^1H imaging results. FF, water T_2 , percentage of voxels with elevated T_2 , and coefficient of variation of T_2 for DMD ($n = 12$) and control ($n = 12$) group per muscle and as mean over all muscles. $\$$: significant difference between DMD and control group ($p < 0.05$).

	FF	T_2 [ms]	Elevated T_2 [%]	$\text{CV } T_2$	
DMD	ED	0.081 \pm 0.077	35.2 \pm 1,5	7.4 \pm 11.3	0.083 \pm 0.027
	GL	0.185 \pm 0.168 $\$$	39.7 \pm 5.1 $\$$	46.7 \pm 33.1 $\$$	0.097 \pm 0.033
	GM	0.108 \pm 0.080 $\$$	39.2 \pm 2.0 $\$$	35.0 \pm 21.6 $\$$	0.097 \pm 0.039 $\$$
	PL	0.168 \pm 0.150 $\$$	35.9 \pm 3.4	15.2 \pm 17.1	0.098 \pm 0.039 $\$$
	SO	0.092 \pm 0.073 $\$$	39.5 \pm 3.6 $\$$	41.9 \pm 34.2 $\$$	0.087 \pm 0.027 $\$$
	TA	0.051 \pm 0.040 $\$$	38.1 \pm 2.8 $\$$	29.4 \pm 27.2 $\$$	0.093 \pm 0.023 $\$$
	TP	0.038 \pm 0.020	37.8 \pm 2.0 $\$$	22.6 \pm 19.7 $\$$	0.094 \pm 0.021
	mean	0.103 \pm 0.087 $\\$	37.9 \pm 3.1 $\\$	28.3 \pm 23.5 $\\$	0.093 \pm 0.030 $\\$
Control	ED	0.033 \pm 0.015	35.5 \pm 0.8	1.2 \pm 1.0	0.065 \pm 0.014
	GL	0.031 \pm 0.015	36.1 \pm 2.0	9.7 \pm 14.4	0.078 \pm 0.016
	GM	0.034 \pm 0.012	36.3 \pm 1.7	6.5 \pm 8.7	0.068 \pm 0.023
	PL	0.049 \pm 0.017	36.3 \pm 1.5	5.4 \pm 11.3	0.051 \pm 0.008
	SO	0.023 \pm 0.008	36.7 \pm 1.8	8.3 \pm 19.0	0.060 \pm 0.007
	TA	0.018 \pm 0.007	35.7 \pm 0.7	2.8 \pm 2.0	0.073 \pm 0.018
	TP	0.022 \pm 0.012	35.8 \pm 1.2	5.7 \pm 8.6	0.080 \pm 0.012
	mean	0.030 \pm 0.012	36.1 \pm 1.4	5.7 \pm 9.3	0.068 \pm 0.014

The mean fat fraction for all analysed muscles was 0.103 \pm 0.087 for DMD patients and 0.03 \pm 0.012 for age-matched controls (Table 15). Five out of seven examined muscles exhibited a significant increase in the FF. The GL muscle had the highest mean fat fraction in DMD patients and the tibialis posterior muscle had the lowest.

Figure 92 presents water T_2 maps with the corresponding anatomical images acquired in the leg of DMD patients and control estimated via the tri-exponential model. While the water T_2 was elevated in muscles of DMD patients even if they are still spared from fatty infiltration, the muscles of healthy control exhibit no elevated water T_2 . The mean water T_2 for all analysed muscles was 37.9 \pm 3.1 ms for DMD patients and 36.1 \pm 1.4 ms for age-matched controls (Table 15). The water T_2 values were significantly higher in DMD patients compared to controls for most leg muscles, except the ED and PL muscles. Furthermore, DMD showed significantly higher ratio of pixels with elevated T_2 values and an increased water T_2 coefficient of variation.

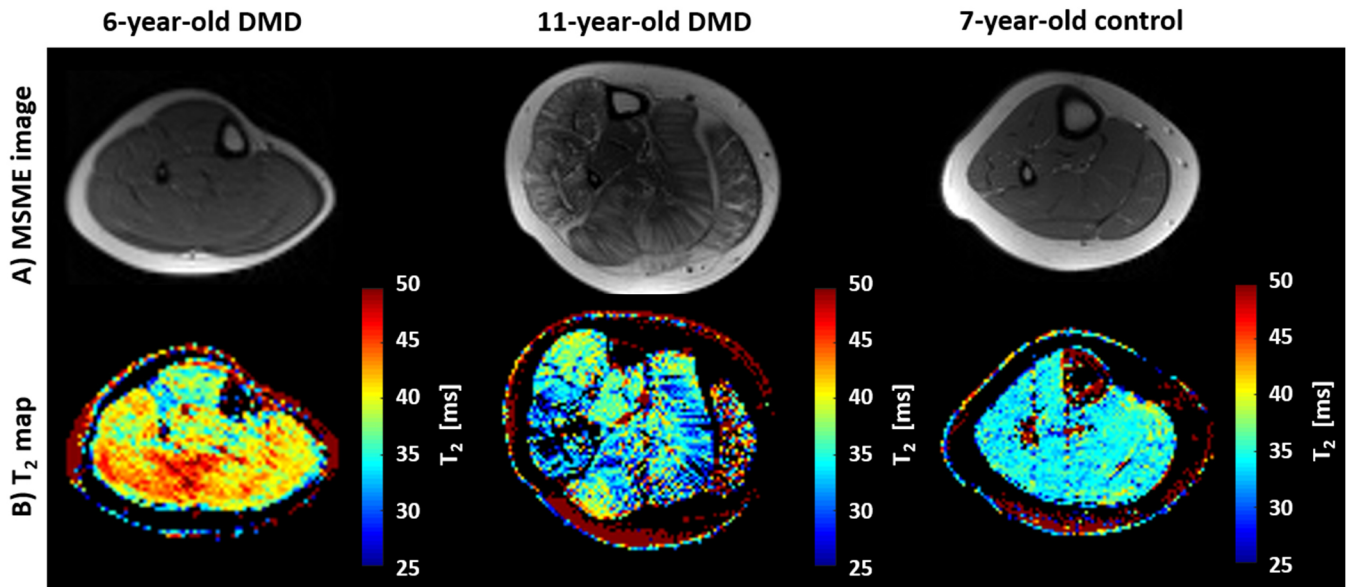


Figure 92: Examples of **A)** MSME images (at TE 9.5ms) and corresponding **B)** water T₂ maps in the leg of six- (Patient #1) and eleven-year-old (Patient #3) DMD patient as well as seven-year-old control.

The measured alterations in FF and water T₂ as a function of age are plotted in Figure 93. Both outcome measures demonstrate a highly intra- and inter-subject variability. While the FF of the youngest participating DMD patients lied in the normal range for most patient, their water T₂ values were already elevated. Older patients showed elevated FF. Increased water T₂ values can be observed in old and young DMD boys. The relatively low FF and water T₂ values of the sixteen-year old patient were in line with his preserved motoric ability to walk, which together points to a milder form of dystrophy.

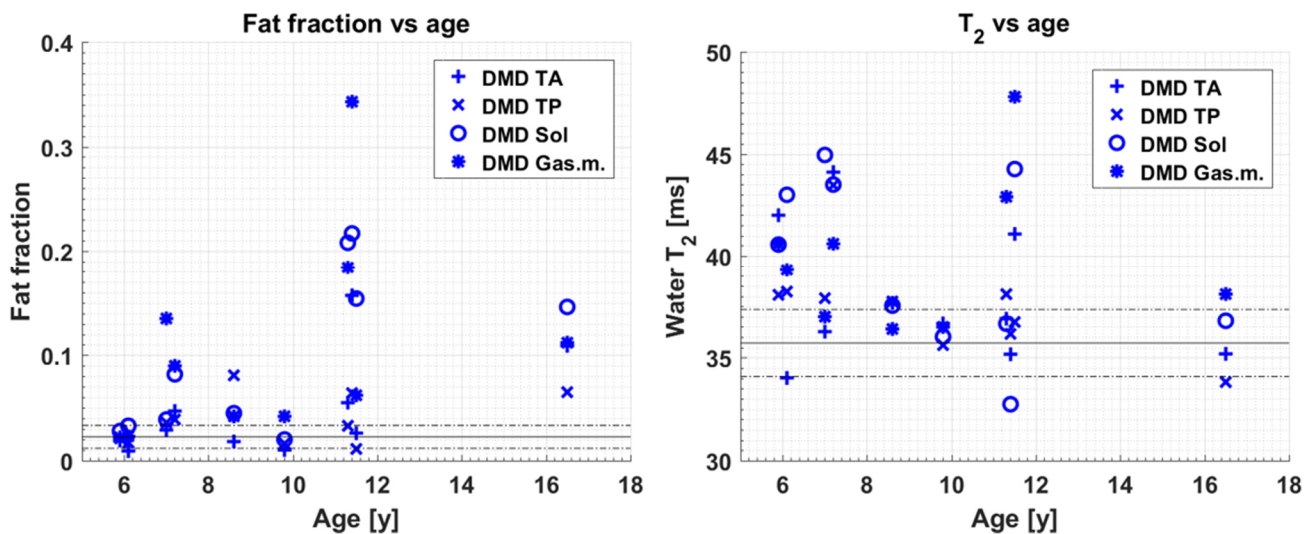


Figure 93: FF and water T₂ alterations for selected muscles of DMD patients plotted against the age. Dashed grey lines represent the mean ± SD of control cohort.

ISIS-CPMG: T₂ spectra

Results of the T₂ signal decay analysis showed a significant increase of the short T₂ values in DMD patients, when compared to control group (Table 16). The mean long T₂ value and the mean relative fraction of short T₂ were not-significantly decreased in DMD patients.

Table 16: ISIS-CPMG results. Relative fraction of short T₂, short T₂ and long T₂ values for the GM muscle of DMD (n = 10) and control group (n = 11). ‡: significant difference between DMD and control group (p < 0.05).

	DMD	Control
Rel. T _{2s} frac [%]	84 ± 9	88 ± 5
T _{2s} [ms]	33 ± 3 ‡	30 ± 2
T _{2l} [ms]	188 ± 47	205 ± 27

¹H NMRS based pH

The GM muscle showed a significantly increased pH (n = 9, mean 7.06 ± 0.03) compared to the control group (n = 12; 7.03 ± 0.02) (p = 0.02). The alterations in pH are plotted in Figure 94 against the age of the patients. Non-published data acquired at the NMR Laboratory at the Institute of Myology in Paris on a bigger DMD cohort point to a similar observation that the pH at the onset of the disease is close to normal values. As in the present study the pH then reaches a peak at an age of around eight to nine years to then usually decrease.

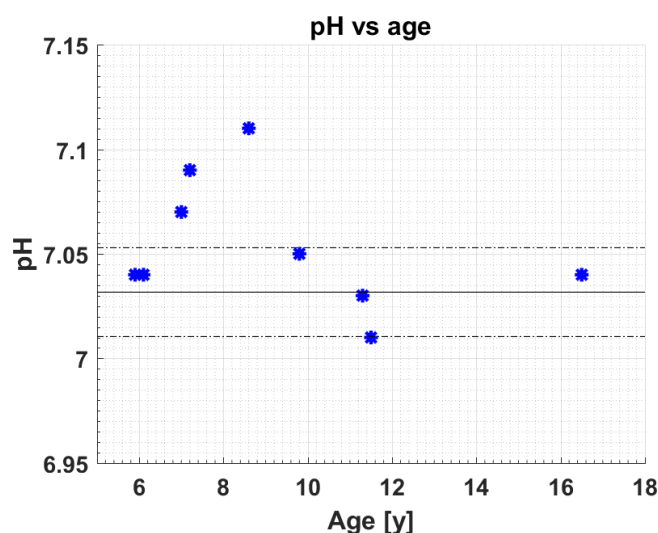


Figure 94: pH alterations for the GM muscle of DMD patients plotted against the age. Grey lines represent the mean ± SD (dashed line) of control cohort.

Sodium imaging

Before the fat correction, fat correlated negatively with TSC (R = -0.32) and ICW (R = -0.46) for DMD patients. This correlation vanished after considering the fat correction (TSC: R = 0.08 and ICW: R = 0.08). As demonstrated in Figure 95, TSC and ICW were elevated in DMD patients compared

to healthy boys. The mean TSC for all analysed muscles was 24.7 ± 4.5 mM for DMD patients and 16.7 ± 2.5 mM for age-matched controls (Table 17). The mean ICW for all analysed muscles was 0.69 ± 0.05 a.u. for DMD patients and 0.47 ± 0.04 a.u. for age-matched controls. The increase in TSC and ICW was significant in all examined leg muscles when compared to the healthy cohort. However, the ICW/TSC ratio did not differ between the DMD and healthy cohort.

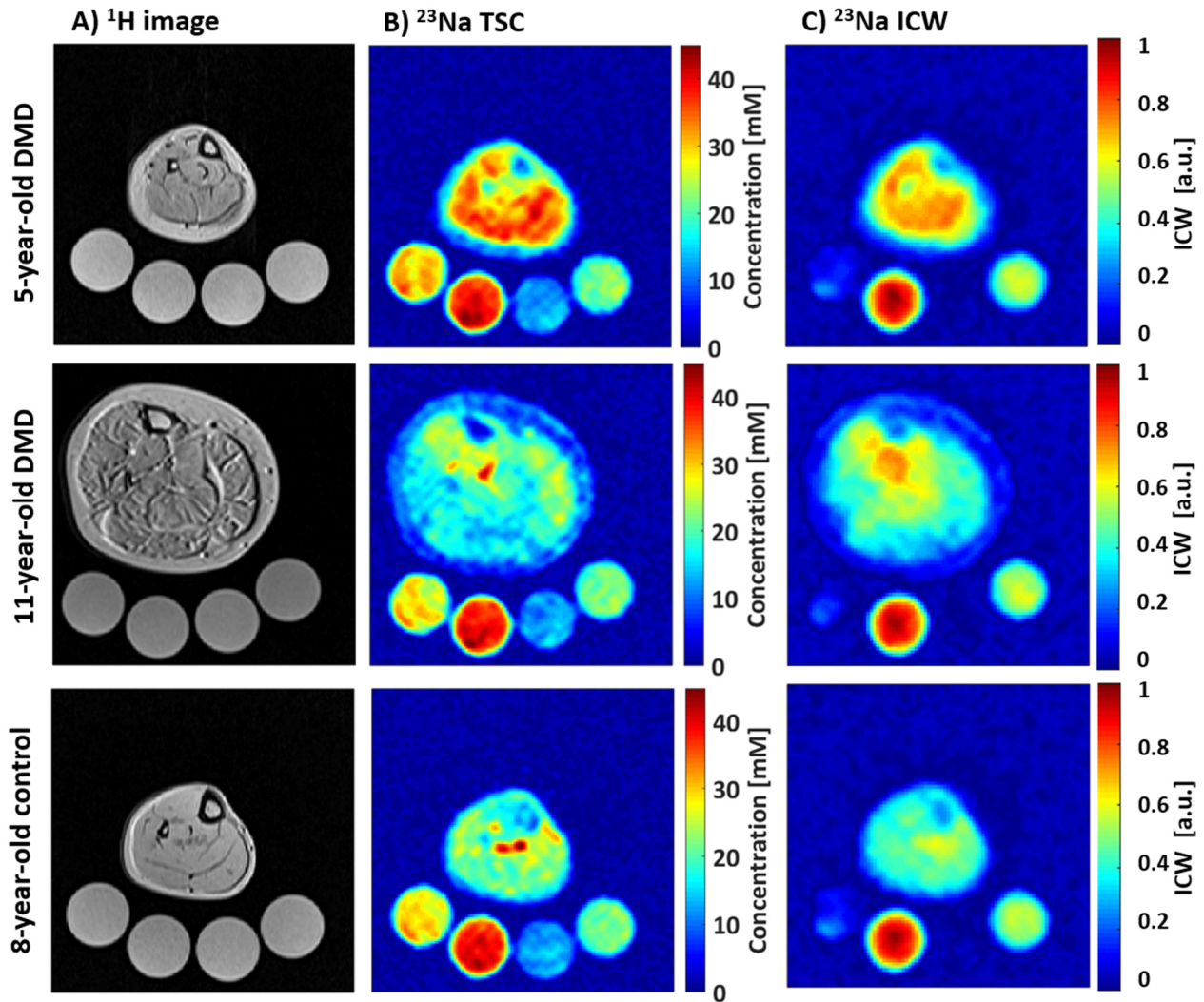


Figure 95: Examples of **A)** anatomical ^1H images and corresponding **B)** TSC and **C)** ICW maps in the leg of five- (Patient #12) and eleven-year-old (Patient #3) DMD patient as well as eight-year-old control.

Figure 96 depicts the alterations in TSC and ICW against the age of the patients. Moreover, the ^{23}Na indices were frequently abnormal in DMD even when water T_2 , FF, and pH remained in the normal range (compare Figure 93 and Figure 94 with Figure 96). DMD patients at all ages exhibited abnormally elevated sodium indices, whereas FF increased with age and the water T_2 and pH fluctuated during the course of disease. Figure 97 presents the ^1H T_2 , ^{23}Na TSC, and ^{23}Na ICW maps of patient 2 and 10. In their cases, the muscles exhibited normal ^1H T_2 and ^{23}Na TSC values, but elevated ^{23}Na ICW values.

Table 17: ^{23}Na imaging results. TSC, ICW, and their ratio for DMD ($n = 10$) and control group ($n = 12$) per muscle and as mean over all muscles. $\$$: significant difference between DMD and control group ($p < 0.05$).

		TSC [mM]	ICW [a.u.]	ICW/TSC
DMD	GM	25.2 \pm 4.2 $\$$	0.62 \pm 0.07 $\$$	0.026 \pm 0.004
	SO	26.1 \pm 6.7 $\$$	0.73 \pm 0.07 $\$$	0.028 \pm 0.004
	TA	23.5 \pm 4.1 $\$$	0.68 \pm 0.07 $\$$	0.028 \pm 0.002
	TP	24.0 \pm 2.8 $\$$	0.74 \pm 0.06 $\$$	0.030 \pm 0.003
	mean	24.7 \pm 4.5 $\$$	0.69 \pm 0.05 $\$$	0.028 \pm 0.003
Control	GM	18.0 \pm 2.8	0.46 \pm 0.06	0.027 \pm 0.004
	SO	17.8 \pm 2.3	0.51 \pm 0.06	0.029 \pm 0.003
	TA	14.7 \pm 1.8	0.41 \pm 0.06	0.029 \pm 0.002
	TP	16.2 \pm 2.9	0.49 \pm 0.09	0.031 \pm 0.003
	mean	16.7 \pm 2.5	0.47 \pm 0.04	0.029 \pm 0.003

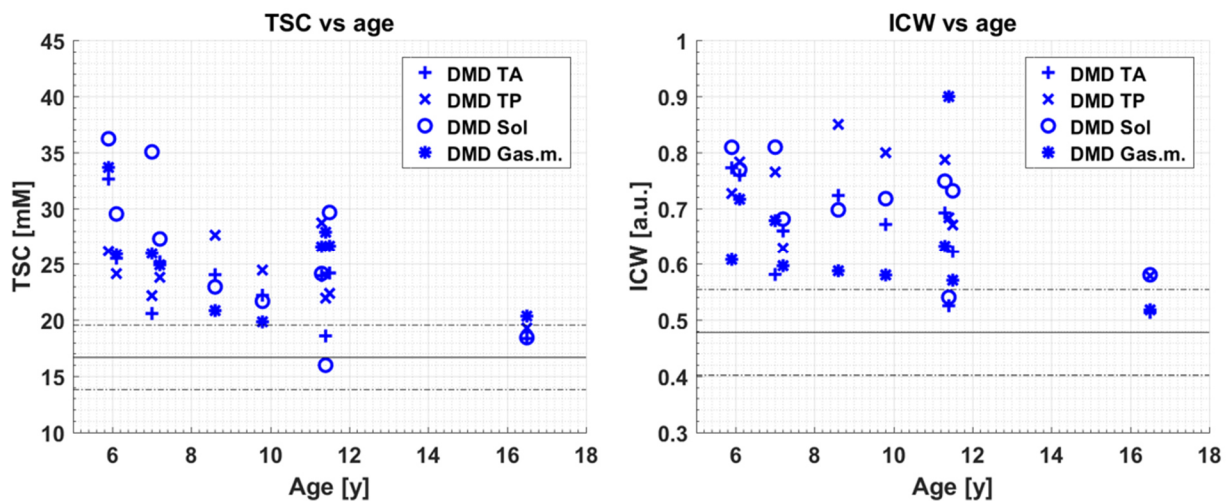


Figure 96: TSC and ICW alterations for different muscles of DMD patients plotted against the age. Grey lines represent the mean \pm SD (dashed line) of control cohort.

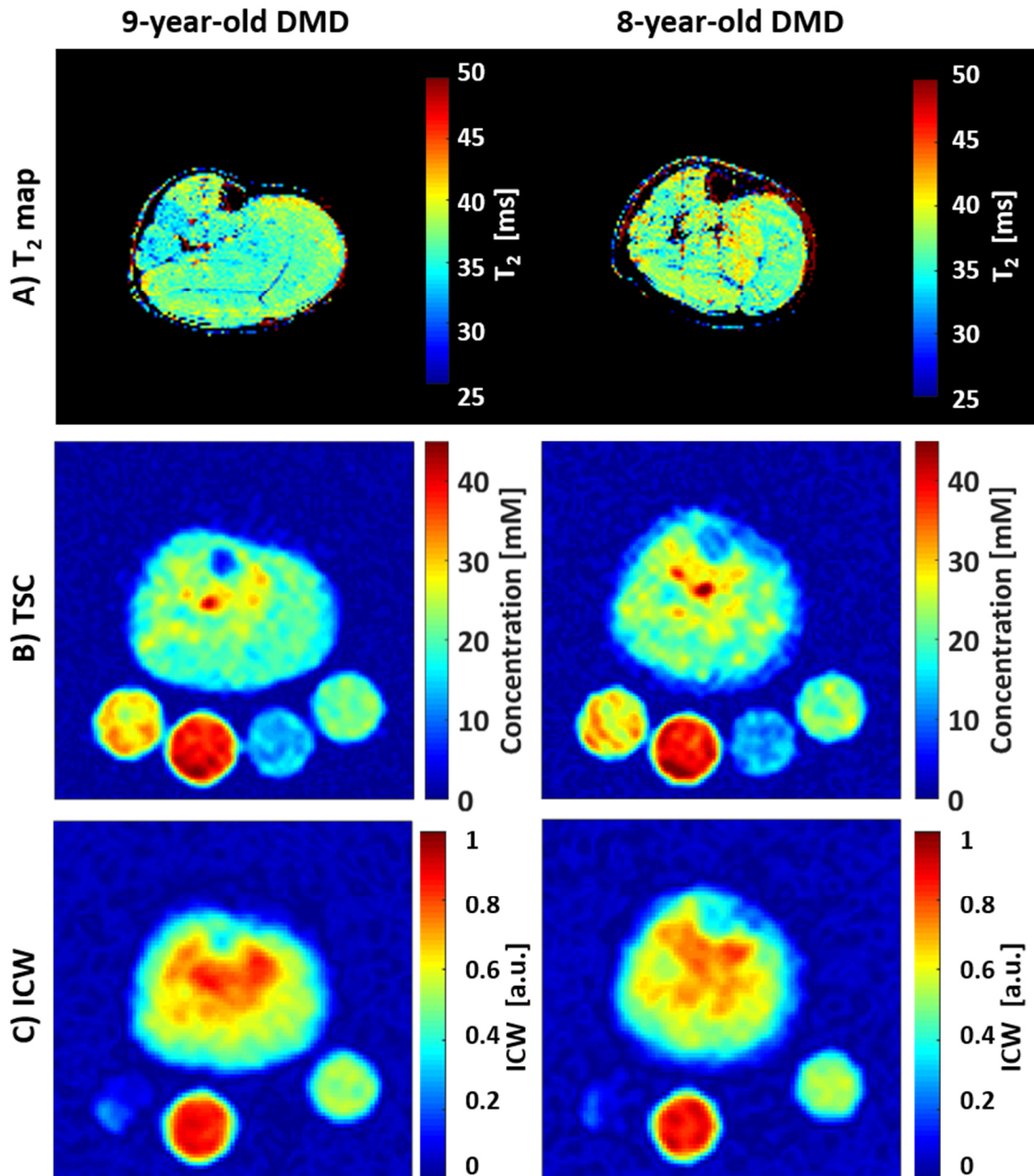


Figure 97: Examples of **A)** anatomical ^1H images and corresponding **B)** TSC and **C)** ICW maps of two DMD patients (#2 and #10). While the proton T_2 and ^{23}Na TSC maps present muscles with values in a normal range, the ICW signals are elevated.

Sodium spectroscopy

After calibrating the ^{23}Na signals according to 5.2.1, the FID and TQF were still dependent on the leg volume. Thus, only their ratio and the global T_1 value are presented in Table 18. While the TQF/FID ratio was found to be significantly increased in DMD patients ($p = 0.01$), no alterations were observed for the T_1 , when compared to the healthy cohort. The alterations in TQF/FID are plotted in Figure 98 against the age of the patients.

Table 18: ^{23}Na spectroscopy results. Non-localized TQF/FID ratio and global T_1 value of DMD ($n = 9$) and control group ($n = 10$). \S : significant difference between DMD and control group ($p < 0.05$).

	DMD	Control
TQF/FID	0.11 ± 0.01 \S	0.09 ± 0.02
T_1 [ms]	32.5 ± 2.3	33.1 ± 1.9

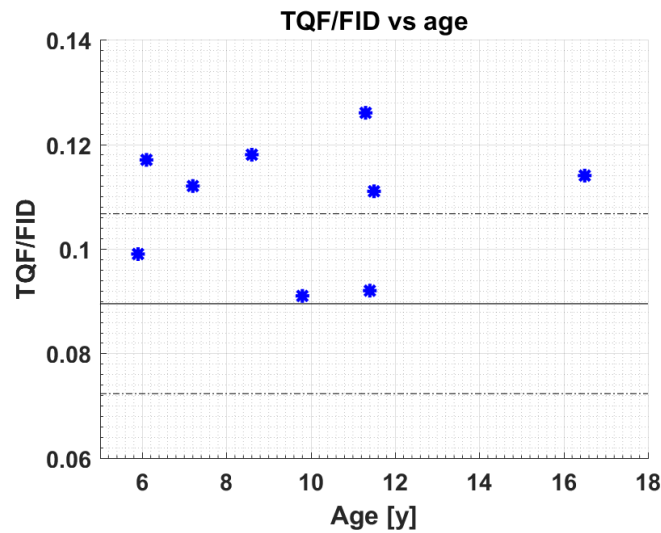


Figure 98: TQF/FID alterations in the leg of DMD patients plotted against the age. Grey lines represent the mean \pm SD (dashed line) of control cohort.

Correlation of different outcome measures

Figure 99 presents the correlations between the ^{23}Na imaging parameters and water T_2 . While TSC augmented with increased water T_2 values ($R = 0.64$, $p < 0.001$), ICW values were also elevated in DMD patients with normal water T_2 values ($R = 0.34$, $p = 0.0014$).

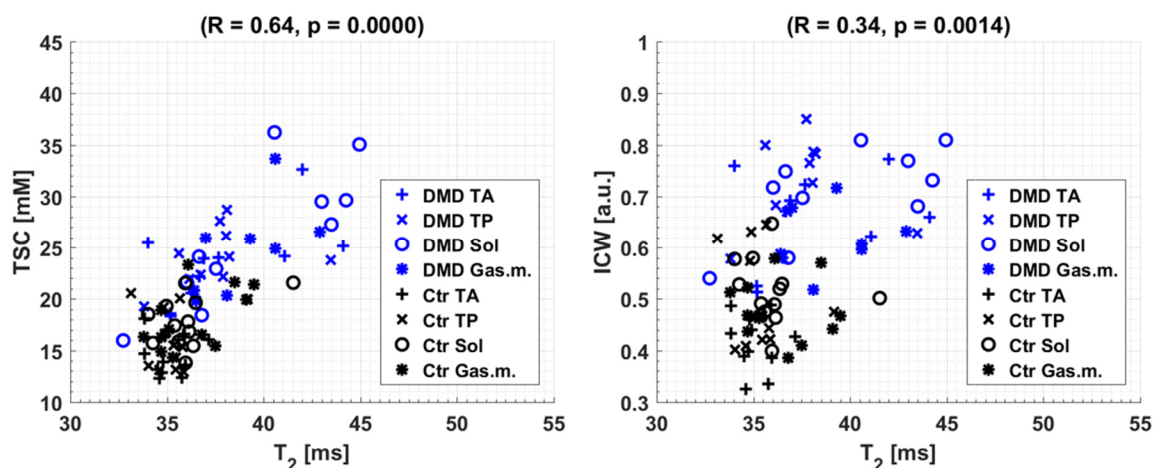


Figure 99: Correlations of the TSC and ICW sodium signal with water T_2 : significant correlations between water T_2 and TSC as well as ICW. Ctr control.

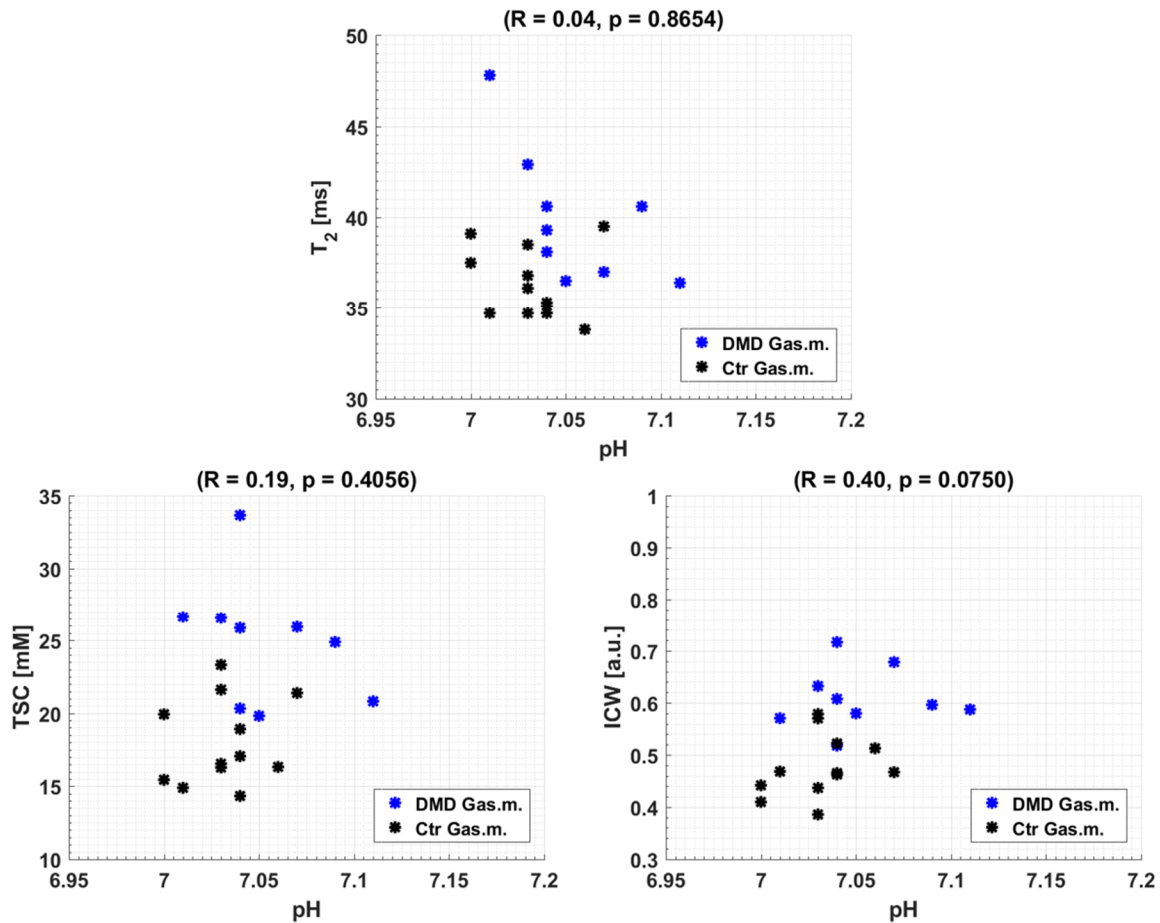


Figure 100: Correlations of water T₂, TSC, and ICW with pH. Ctr control.

Figure 100 presents the correlations between the pH and the water T₂ as well as the ²³Na imaging indices. The highest correlation was found between the ICW and pH (R = 0.4, p = 0.08).

7.3.2 Baseline and six-month follow up of DMD patients

Eight DMD patients were scanned a second time after an average of 6 months (25.0 ± 2.4 weeks passed after the first visit). While the FF stayed constant or increased, water T₂ values fluctuated between the two visits. Figure 101 presents the evolution of FF and water T₂ for the SO and TA muscles. Table 19 presents the values for FF, water T₂, TSC, and ICW at baseline and six-month follow up as well as the percentage difference (delta). These outcome measures remained increased. The mean value of all muscles of FF increased from 0.07 ± 0.07 to 0.09 ± 0.09. The mean water T₂ was 38.9 ± 3.8 ms at baseline and 39.2 ± 3.9 ms after six months. TSC and ICW (n = 7) were 24.3 ± 3.1 mM and 0.69 ± 0.09 a.u. at baseline, and 27.7 ± 7.4 mM and 0.71 ± 0.15 a.u. during the follow-up, respectively.

Table 19: FF, water T_2 , TSC, and ICW across time in DMD patients for GM, SL, TA, and TP muscle ($n = 8$ for FF and T_2 , $n = 7$ for TSC and ICW). †: significant difference between 1st and 2nd visit ($p < 0.05$).

		FF	T_2 [ms]	TSC [mM]	ICW [a.u.]
GM	baseline	0.10 ± 0.11	39.1 ± 5.4	25.3 ± 2.6	0.69 ± 0.11
	6 months	0.12 ± 0.14	39.6 ± 2.9	26.8 ± 7.7	0.67 ± 0.17
	delta [%]	1.8 ± 9.6	2.1 ± 47.6	2.9 ± 22.3	-4.0 ± 28.2
SO	baseline	0.10 ± 0.08	39.1 ± 4.1	24.6 ± 4.8	0.71 ± 0.09
	6 months	0.12 ± 0.11	40.5 ± 4.8	28.9 ± 8.8	0.79 ± 0.15
	delta [%]	3.50 ± 12.2	11.7 ± 22.2	13.8 ± 25.9	8.8 ± 19.1
TA	baseline	0.04 ± 0.05	38.0 ± 3.1	23.3 ± 2.6	0.66 ± 0.07
	6 months	0.07 ± 0.06 †	38.3 ± 3.0	25.3 ± 5.9	0.70 ± 0.14
	delta [%]	1.0 ± 9.2	45.0 ± 38.8	6.3 ± 24.9	5.0 ± 22.4
TP	baseline	0.03 ± 0.02	38.0 ± 2.4	23.8 ± 2.5	0.70 ± 0.09
	6 months	0.04 ± 0.04	38.4 ± 5.0	25.3 ± 5.6	0.68 ± 0.12
	delta [%]	0.5 ± 10.5	10.4 ± 58.3	4.0 ± 18.7	-3.4 ± 19.9
mean	baseline	0.07 ± 0.07	38.6 ± 3.8	24.3 ± 3.1	0.69 ± 0.09
	6 months	0.09 ± 0.09	39.2 ± 3.9	26.6 ± 7.0	0.71 ± 0.15
	delta [%]	1.7 ± 1.3	17.3 ± 19.0	6.8 ± 4.9	1.6 ± 6.3

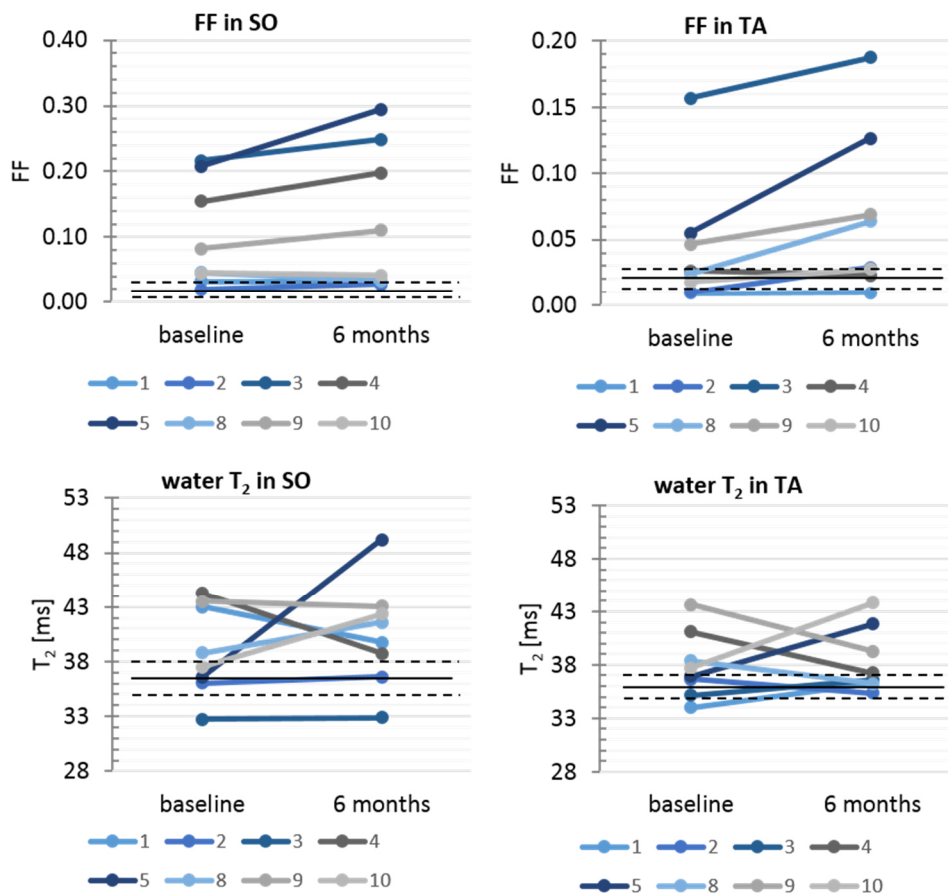


Figure 101: FF and water T_2 at baseline and 6 months follow up of the SO and TA muscles for the eight DMD patients (Patient #1, #2, #3, #4, #5, #8, #9, and #10). Black lines represent the mean \pm SD (dashed line) of control cohort.

Figure 102 presents the evolution of TSC and ICW for the SO and TA muscles. Four out of the seven patients showed an increase in TSC and ICW in SO and TA muscles. For the other three, these values either stayed stable or decreased between the two visits. TSC and ICW values are increased during both visits when compared to the healthy cohort. For Patient #8, no ^{23}Na values are plotted since the NMR acquisition was stopped after the ^1H part during his first visit.

TQF/FID ratio obtained from the ^{23}Na spectroscopy part did not vary between the two visits (0.11 ± 0.01 for both visits, $n = 6$). The mean pH was 7.06 ± 0.04 at baseline and 7.07 ± 0.04 after six months ($n = 7$). At baseline, the relative short T_2 fraction derived from the ISIS-CPMG data sets was 84 ± 9 , the short T_2 33 ± 3 ms, and the long T_2 188 ± 47 ms. After six months, the relative short T_2 fraction was 87 ± 7 , the short T_2 34 ± 4 ms, and the long T_2 171 ± 42 ms (the latter with $p < 0.05$, probably due to the high SD).

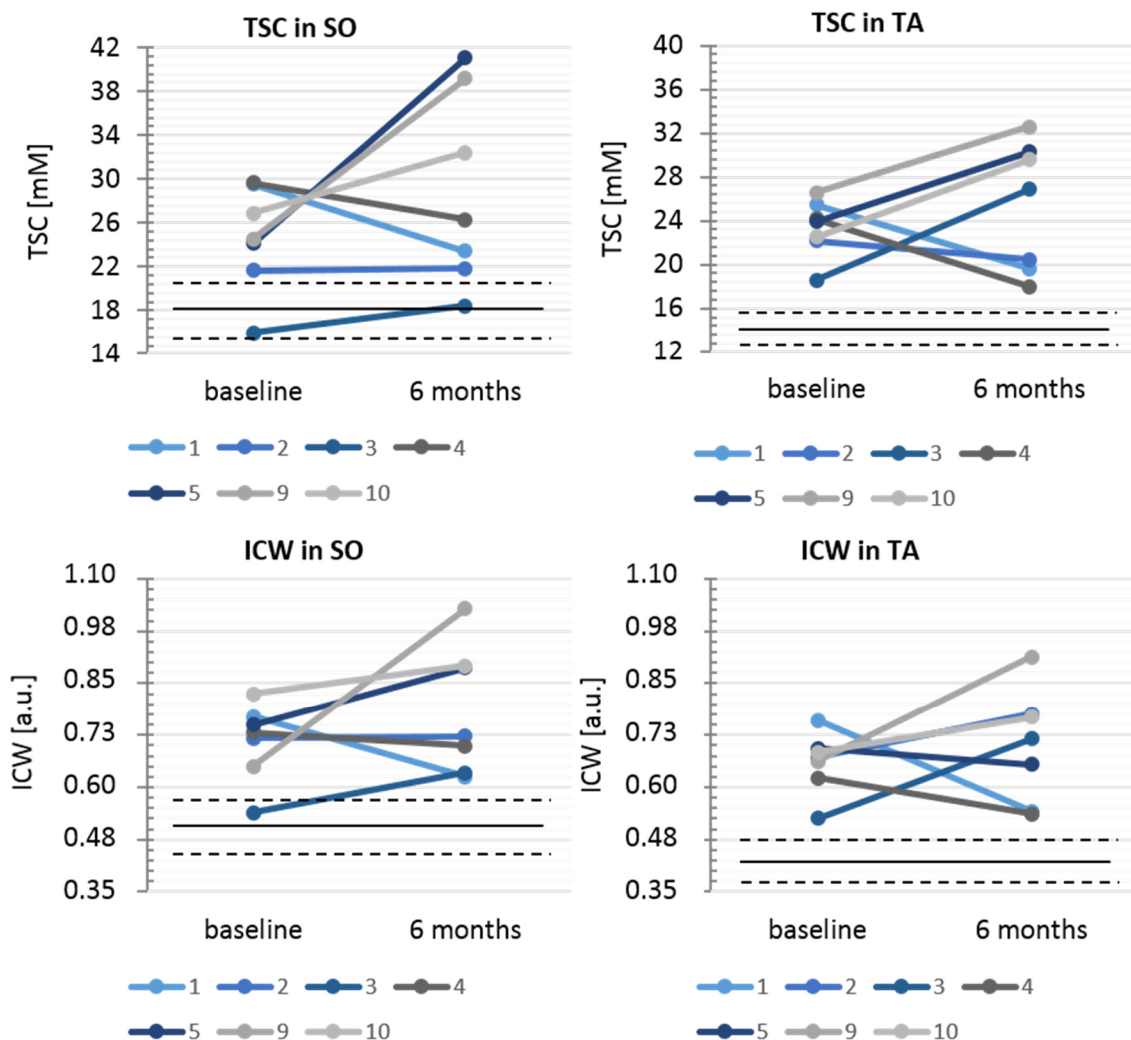


Figure 102: TSC and ICW at baseline and 6 months follow up of the SO and TA muscles for the eight DMD patients (Patient #1, #2, #3, #4, #5, #9, and #10). Black lines represent the mean \pm SD (dashed line) of control cohort.

7.4 Discussion

Here, we applied a multi-parametric NMR protocol comprising standard and emerging techniques to characterize the different pathological processes observed in a small cohort of DMD patients. In line with what has been previously described in a pilot ^{23}Na NMRI study, we reported increased sodium concentrations in the muscle of dystrophic patients [14]. In our work, we demonstrated that DMD patients exhibited elevated TSC and ICW as well as water T_2 in the early disease stage preceding the fatty infiltrations quantified with the Dixon-based fat fraction. The multi-parametric approach allowed comparing the sensitivity of different NMR outcome measures to monitor the pathological processes in the dystrophic muscle tissue.

The FF increases with age, and is currently the most used NMR outcome measure for the assessment of the disease progression in DMD. Natural history studies try to establish cut-off values to predict loss of ambulation [123], but the non-linear progression on an individual basis remains a big hurdle. The disease evolution depends on multiple factors, which are responsible for a high intra- and inter-subject variability. Here, we examined for example three boys of the same age (patient #3, #4, and #5) displaying a range of fatty infiltration as well as the ability to walk. While one was still able to walk without aid, the two others used a wheelchair to cover longer distances. Furthermore, we report a muscle- and subject-depending increase in the FF between the first and the second visit, which was only significant for the TA muscle.

Water T_2 and tissue heterogeneity were elevated in the muscle tissue of DMD patients reflecting the ongoing disease activity in the muscle tissue. However, water T_2 fluctuated with age; while the youngest DMD patients showed increased water T_2 values, some older patients had relatively mildly elevated water T_2 values. Furthermore, no trend was observed between the first and second visit. It has been previously shown that the water T_2 values are reduced by the corticoid treatment [12]. A significant drop in water T_2 can be already observed after three months of corticosteroid therapy. In our study, all but two patients received a corticoid therapy, which could partly explain the drop in water T_2 for some treated patients. An in-depth analysis of the water T_2 relaxation using ISIS-CPMG could provide additional information about changes of the myowater distribution in the different anatomical compartments. While the short T_2 component reflects the relaxation behaviour of the water within the intracellular and interstitial spaces, the long T_2 component is attributed to the water within the vascular space [17]. In the present study, we observed an increase in the short T_2 indicating pathological changes in the extravascular compartment. The elevated short T_2 could for example point to present interstitial oedema a common feature of the dystrophic muscle.

The cell volume is indeed tightly linked to the tissue sodium concentration and the intracellular pH. For DMD patients, we derived from the ^1H NMR spectra increased pH values that are thought to be predominantly if not exclusively of intracellular origin [137]. In line with this study, we also found normal carnosine-based pH values in presence of elevated water T_2 . No significant changes in the pH were observed between the two visits. Furthermore, TSC and ICW values were elevated in DMD patients. The sodium anomalies seemed to be systematically present in patients with DMD compared to controls and precede fatty degenerative changes. In addition, muscles that were relatively spared, such as the TA, showed increased TSC and ICW in all participating DMD patients. TSC and ICW were at baseline and after 6 months increased. The strong correlation between water T_2 and TSC could reflect oedematous changes. On the other hand, the ICW was found to be also elevated in the presence of normal water T_2 . The ICW signal correlated with the intracellular pH, which underlines their tight connection in the cell's homeostasis. Similar to the *mdx* mice (6.5), the TQF/FID was also significantly elevated in DMD patients. Since the TQF increases with increasing correlation times, an elevation can indicate an increased intracellular sodium concentration. Thus, our observations of intracellular sodium accumulation and elevated intracellular pH strengthen the hypothesis of osmotic and intracellular oedema in the muscle of DMD patients [14].

The question remains how the ICW can be elevated at normal water T_2 values since the water distribution is tightly linked to the sodium homeostasis. One hypothesis could include an increased cellular fraction of normal myocytes, which is in contradiction with the known pathological processes in the dystrophic muscle. The second hypothesis includes an increase in ICW, which is associated with cell oedema resulting in a water T_2 increase. However, this increase is counterbalanced by a decrease in extracellular fraction.

Limitations

This study, which is still in progress, has currently its limitation in the small number of subjects. For two out of the twelve participating patients, we had to stop the acquisition after the ^1H part, because the children were not able to remain calm in the scanner. The parent of one of this child declined to come for a second visit. However, the second boy managed to pass the entire protocol during his follow-up examination after six months. Nevertheless, an appropriate choice of the most useful NMR outcome measures is necessary for upcoming studies to reduce acquisition time.

A special case represents the 16-year-old patient, who showed a preserved mobility and relatively mildly altered NMR variables when compared to the younger DMD patients. There was no confirmation of a genetic mutation in the dystrophin gene; however, the patient did exhibit high creatine kinase values. These observations could point towards a mild form of dystrophy, excluding DMD. Yet, we decided to keep the patient in the study cohort, because the main objective of the present study was to test the sensitivity of different NMR outcome measures.

Compared to a previous study that investigated the pH and water T_2 alterations in DMD patients [137], the water T_2 values of our control group were higher. The increased mean water T_2 can be attributed to one healthy volunteer that presented increased water T_2 values in all muscles (defined as mean plus two SD). Furthermore, the water T_2 in the DMD cohort could be influenced by the different pharmaceutical treatments, which was not taken into account due to the limited number of participants. Secondly, to confirm the ^1H -based pH observations in young DMD patients, more data are needed. We thus might pool the data from the Institute of Myology with the current study to confirm the pH alterations depending on age.

Partial volume effects may lower the measured TSC and ICW, in particular in patients with high fat fraction, since fat tissue has lower sodium concentrations than muscle tissue [225]. Thus, the FF was taken into account for the sodium quantification in DMD patients. To prevent T_1 weighting, sodium quantification should have been performed with a longer TR. Here, a T_1 weighting was accepted to reduce the acquisition time of the protocol. The present T_1 weighting of the ^{23}Na images might affect the sodium quantification, in particular if T_1 of muscle tissue deviates from the T_1 values of the reference tubes and subcutaneous fat. Although, the T_1 values of skeletal muscle tissue, subcutaneous fat, and agarose phantoms, which were measured in one healthy adult volunteer (T_1 between 22 and 25 ms), are in the same range, the impact of the dystrophic processes on the T_1 of fat and muscle remains unclear. We assumed no T_1 variances with pathology in the muscle tissue. It is possible that the global ^{23}Na T_1 is decreased in DMD patients, that would be compatible with an increase in the intracellular sodium content. Animal experiments showed that the intracellular T_1 is smaller than the extracellular T_1 [80], however exact values in human muscles are not known. Nagel *et al.* demonstrated on patients with muscular channelopathies, where increased intracellular sodium can be easily provoked, that the IR method could offer a weighting toward intracellular sodium [83]. However, the sufficiency to suppress the extracellular sodium is still not fully elucidated as it depends on the underlying T_1 values. Thus, we cannot exclude possible contributions from extracellular sodium and further investigations are needed. Another limitation is that ^{23}Na NMR signal of subcutaneous fat tissue might deviate from the signal of fat tissue in muscle. The IR

sequence was performed to suppress the ^{23}Na signal from extracellular oedema and vessels. However, using the IR method, the signal of the free sodium (NaCl solution containing phantoms) was not completely suppressed mainly due to B_1 inhomogeneities.

Thus, further steps would include increasing the number of subjects for the DMD and the control cohort. This could allow tackling the question of the benefit of ^{23}Na NMR to the standard ^1H protocol. Although, sodium anomalies were systematically present in the present DMD cohort, it is difficult to conclude that sodium alterations occur before water T_2 increases. Nevertheless, sodium changes can occur while the water T_2 remains normal. Additionally, further protocols could combine ^{23}Na NMR with ^{31}P NMR to study in parallel alterations in the sodium concentration and the PDE levels, which has been proposed as early indicator of membrane functional disturbances in the dystrophic muscle [121], [135].

7.5 Conclusion

Our study shows that ^{23}Na NMR might offer a sensitive outcome measure to monitor alteration of the dystrophic muscle at a very early stage. The observed sodium anomalies in DMD patients preceded clearly the fibro-fatty infiltration of the muscle tissue. Furthermore, we have seen elevated sodium indices even at normal water T_2 and pH values. Based on our results, we are convinced that the role of ^{23}Na NMR in myopathies is worth to be investigated further. Intracellular sodium accumulations are not always paralleled with proton T_2 increases. Continuing the work - even in a combination with other NMR methods - might contribute to the understanding of various (patho-) physiological processes. In summary, the present data supports that ^{23}Na NMR could serve as an early and sensitive biomarker in order to investigate ion channel leakage and membrane integrity.

General discussion, conclusion & perspectives

In this chapter, the contributions of my work are discussed and some directions for future research are outlined. The objective of this thesis was to investigate the sensitivity of new NMR outcome measures to monitor the dystrophic processes in skeletal muscle tissue. NMR allows a non-invasive evaluation of skeletal muscles over time, making it very well suited for longitudinal evaluation of patients during clinical trials. In MD patients, different NMR methods are currently being used to reveal the progressive destruction of muscle tissue that is gradually replaced by adipose tissues. Standard NMR techniques quantitatively estimate the degree of fat infiltration or measure the water T_2 . However, the fat fraction does not seem to be a predicative index of disease evolution due to the diverse phenotypic expression and non-linear progression as previously discussed (3.4.1). On the other hand, water T_2 is a sensitive biomarker of the inflammatory/necrotic/oedematous processes that precede the muscle replacement by fat, but might not detect the beneficial effect of any intervention in steroid-treated patients (3.4.1). Thus, sensitive and early NMR biomarkers that are more predictive of disease evolution are still needed to allow a short-term assessment of the response to treatment, such as perceptible changes in dystrophin expression.

8.1 Methodological contributions of the thesis

I therefore investigated the sensitivity of ^{23}Na NMR to monitor changes in the ionic homeostasis and fluid distribution in healthy and dystrophic muscle. To do so, a non-localized ^{23}Na NMR protocol was proposed to overcome the time constraints imposed in a clinical setting (4.6.1). My first contribution was to evaluate the sensitivity of the proposed protocol to monitor alterations in the vascular compartment fraction of healthy muscles (5.1). Different ^{23}Na indices were tested including FID signal, TQF signal, TQF/FID ratio, the transversal relaxation times and their fractions, and the global longitudinal relaxation time. Among these indices, the TQF/FID ratio was the most sensitive parameter, which increased during vascular draining and decreased during vascular filling. While the decrease in the TQF/FID seemed mainly driven by the expansion of the vascular volume, the observed increase during draining was explained by a more important interaction between the ^{23}Na nuclei and interstitial macromolecules. It has been previously reported that only the vascular and interstitial water fractions changed between the three different vascular filling conditions in this time frame [17]. Therefore, the observed alterations in the TQF signal are not of intracellular but rather of interstitial origin. Thus, this work touched also upon the important question of the origin of

MQF signals, which will be further discussed below. Furthermore, with this human study, we demonstrated the higher sensitivity of ^{23}Na NMR compared to standard ^1H T_2 methods to track changes in the extracellular volume fraction. This comparison was crucial to underline the utility and additional value of ^{23}Na NMR and consequently to support its application in clinical studies. Another interesting contribution of my thesis consisted on studying the subtle effect of ischemia on the ^{23}Na signals in human skeletal muscle. The intracellular sodium concentration in the ischemic heart increased three to four fold within a few minutes [167], [226]. Moreover, the interpretation of the ^{23}Na results of our vascular filling study was challenged by one reviewer when submitting the manuscript of our study for publication and during conference presentations. They expected a more substantial increase in intracellular sodium concentration during an ischemic paradigm that would affect ^{23}Na signals during the 15 minutes of vascular draining. Consequently, the ischemic paradigm was extended to a murine experiment where the impact of a prolonged ischemia was examined (5.3). This murine study confirmed that - in stark contrast to the myocardium - the skeletal muscles seem to possess mechanisms that prevent an intracellular sodium overload over a longer time.

As a next step, the ^{23}Na NMR signal needed to be calibrated to obtain a reliable and reproducible outcome measure for longitudinal and interventional studies. I demonstrated the feasibility of signal calibration using an external reference phantom taking into account the leg volume and coil sensitivity (5.2). Since the FID and TQF signals were not dependent on the volume after the correction, we considered our non-localized ^{23}Na protocol with this calibration approach to be suitable to examine the pathological changes associated to dystrophic muscles.

Another contribution was the investigation of the higher-order energy-transitions by ^{23}Na NMR (5.4). The majority of ^{23}Na studies rely on the quantification of total sodium signal and - but to a lesser extent - on intracellular weighted signal based on IR methods. However, the analysis of the molecular environment of sodium ions is also of interest, as we would expect distinctive relaxation characteristics in muscular pathologies. MQFs provide direct information about the molecular environment based on quadrupolar interactions. Here, we reported a low DQF-MA/TQF ratio indicating that only a very small fraction of slowly tumbling sodium ions are bound to ordered structures in skeletal muscle tissue. We further reported for the first time *in vivo* short and long T_2 values of the TQF in skeletal muscle. Thus, this preliminary study on a healthy cohort provides a basis for further relaxation-based ^{23}Na NMR studies on muscular dystrophies.

In chapter 6, I first used standard NMR methods to characterize a new dysferlin-deficient murine model. My work delivered a detailed NMR characterization of the MMex38 model and compared it to BLAJ model, whose histological and functional features are well-described. To the

best of my knowledge, this study was the first comprehensive description of a murine dysferlin-deficient model by different NMR modalities to concurrently measure FF, water T_2 characteristics, ^{31}P metabolites, and ^{23}Na signals. Oil Red O staining and electron microscopy have already revealed before significant lipid accumulations within the myofibres of dysferlin-deficient mice [50]. This important fat infiltration, which is more pronounced in the proximal muscles than in the distal, was confirmed by increased NMR-based fat ratios. Our model description thus confirms the suitability of the *MMex38* model to mimic the disease activity and progression of human LGMD 2B. This is in contrast to other murine dystrophic models like the *mdx* that fail to replicate the important progressive muscle-wasting present in human patients. An appealing next step in dysferlin-deficient muscle research would be thus to set up an exercise study to study the impairments in the membrane repair mechanisms. A multi-modality NMR protocol including ^1H T_2 relaxometry, ^{31}P , and ^{23}Na NMR could investigate the impact of eccentric and concentric movement on dysferlin-deficient muscle tissue.

In the second preclinical study, I tested the sensitivity of the proposed NMR parameters on different murine models of MD (*mdx* and *MMex38* versus WT). This was the first ^{23}Na NMR study on murine dystrophic muscle. The ^{23}Na NMR indices were sensitive to distinguish the dystrophic from healthy skeletal muscle tissue. During the course of the experiment, I encountered the problem that the SR evaporated progressively from the calibration phantom, which complicated the quantification step. Changing the plastic vial to one made of glass solved this issue. The second parameter for validation was the T_2 spectrum obtain from the ISIS-CPMG sequence. *mdx* mice exhibited higher short T_2 compared to WT, which points together with constant relative fractions to a redistribution of water within the extravascular compartment. The same trend was observed in dystrophic patients (7.3.1), which encourages an extensive correlation with histology on mice to understand the pathophysiology behind these variations (alterations in the membrane permeability, necrosis, inflammation...). Thus, ^1H T_2 spectra and ^{23}Na NMR indices were shown to be sensitive to detect changes in the dystrophic muscle in a small cohort. After further validation on more animals, these methods could be added to preclinical NMR studies as outcome measures for short-term assessment of the response to treatment.

The final chapter on DMD patients constitutes the most important contribution of this thesis. Here, I demonstrated the utility of ^{23}Na NMR in a clinical setting. Weber *et al.* reported that the muscular Na^+ concentration in boys with DMD - as detected by ^{23}Na NMRI - was increased and remained elevated in a re-examination compared to healthy controls [14], [60]. Based on these initial experiments, we further wanted to investigate the potential of ^{23}Na NMR to serve as an early and

sensitive biomarker in MDs. Thanks to the collaboration with the University Hospital Erlangen, a comprehensive ^1H and ^{23}Na NMR study was organized to monitor pathological changes in the dystrophic muscle of DMD boys. In this ongoing work, we have evidence that an overload of Na^+ is already present in muscle tissue of DMD patients before alterations of investigated ^1H NMR-based parameters such as water T_2 , FF, and pH occur. This Na^+ overload might be caused by an increased intracellular Na^+ concentration as indicated by measurements with the inversion recovery ^{23}Na NMRI technique. Our study indicates that ^{23}Na NMR-based outcome measures offer new physiological information about the state of the tissue since we reported cases with normal water T_2 and/or pH but increased TSC or ICW. Muscles that were relatively spared, such as the TA, also showed increased TSC and ICW in DMD patients. While we found a good correlation between water T_2 and TSC, which could reflect oedematous changes, the ICW was found to be also elevated in the presence of normal water T_2 . Thus, ICW is most likely a more sensitive biomarker than TSC to reflect the Na^+ imbalances.

8.2 ^{23}Na NMR in the future: is it worth it?

Today, clinical ^{23}Na NMR remains limited due to the high costs, long acquisition times as well as the complexity. Thus, the question is whether it is worth to lift ^{23}Na NMR beyond the research field to address the need of an early and sensitive biomarker. This would be the case, if ^{23}Na NMR proves to be more sensitive to certain pathological changes than ^1H NMR and ^{31}P NMRS providing additional information, which cannot be retrieved by other methods.

A selection of sensitive ^{23}Na NMR-based biomarkers related to disease activity has been proposed and provide additional information to ^1H NMR-based indices. Several studies quantified the extent of disturbances in metabolism by ^{23}Na NMRI in different tissues including brain, breast, and heart. After myocardial infarct, ^{23}Na signal intensity stayed elevated in non-viable infarction at all time points up to one year. On the contrary, not all signal intensities in $T_2\text{w}$ ^1H images were still elevated at day 90 [227]. During breast tumour screening, TSC were elevated in breast lesions as compared to normal glandular tissue and most likely benign lesions as well [228]. TSC as indicator associated with malignancy might hence improve specificity of lesion detection that commonly relies on gadolinium contrast-enhanced NMRI. In multiple sclerosis patients, increases of TSC were observed in lesions and more importantly in regions of normal-appearing white matter of ^1H $T_2\text{w}$ images [229]. The authors suggested that TSC might represent an earlier marker of tissue injury. In addition to the commonly used TSC quantification, exploring relaxation based ^{23}Na NMRI contrast could have interesting applications since relaxation is influenced by structure and content of molecular environment that change during pathologies. At 7T, ^{23}Na NMRI depicted already variation in T_2^* times and concentrations between white and grey matter as well as between sub-cortical

regions in healthy subjects [230]. These few examples underline the potential role of ^{23}Na NMR to either provide additional information or at least compensate controversial contrast-enhanced techniques.

In this thesis, I showed that TSC and ICW are elevated in DMD, while the latter seems to be even more sensitive for the underlying pathological changes since it was elevated even when water T_2 and pH was normal. Although, the number of participants is still limited, these observations can give already a strong indication in favour of the additional benefit of ^{23}Na NMR in the MD field. It would be further interesting to study also the less severe BMD by ^{23}Na NMR since these patients exhibit almost normal ^1H T_2 values, while metabolic changes occur early prior to fat infiltration [53], [133]. In FSHD, which is characterized by asymmetric dysfunction of muscular tissue, metabolic changes were observed only in fat infiltrated muscles [141]. Conversely, increased ^1H T_2 signal consistent with oedema were present in fat infiltrated and spared muscles [231]. Thus, we plan to explore further the pathological process of these MDs by ^{23}Na NMR.

All the aforementioned considerations make ^{23}Na NMR an appealing method for non-invasive, early, and longitudinal monitoring of dystrophic diseases. However, the signal origin should be investigated before the technique can be used at larger scale. Since the ^{23}Na NMR signal originates from both intra- and extracellular compartments, the exact pathophysiological mechanisms behind the variations of ^{23}Na signals in dystrophies is not perfectly understood. In the following, several experiments are proposed to expand current limited knowledge about the origin of signal in order to optimize and validate the most sensitive/specific ^{23}Na indices for MD trials.

The microscopic environment of Na^+ ions in muscle tissue can be analysed with MQF sequences including TQF and DQF-MA since they are sensitive to the mobility of Na^+ ions. The molecular correlation times can be additionally determined by measuring the ^{23}Na longitudinal and transverse relaxation times at two different magnetic field strengths (e.g. 3T and 7T). A combination of the different parameters might then help to understand the origin of NMR signal alterations that are present in dystrophic muscle tissues, and to evaluate the specificity of ^{23}Na NMR biomarkers. Moreover, application of SR in mice clearly separates the intra- from extracellular ^{23}Na signal. First, relaxation times and derived correlation times for intra- and extracellular space can be determined based on SR experiments. Second, administering SR in *mdx* mice enables to study the potential leakage of the cell membrane by separating between intra- and extracellular sodium. Third, it permits to measure the fraction of signal arising from the different compartments for both MQF and IR methods. This would finally evaluate the most efficient sequence to separate the two compartments and propose a method based on ^{23}Na NMR that could be applicable in MD patients.

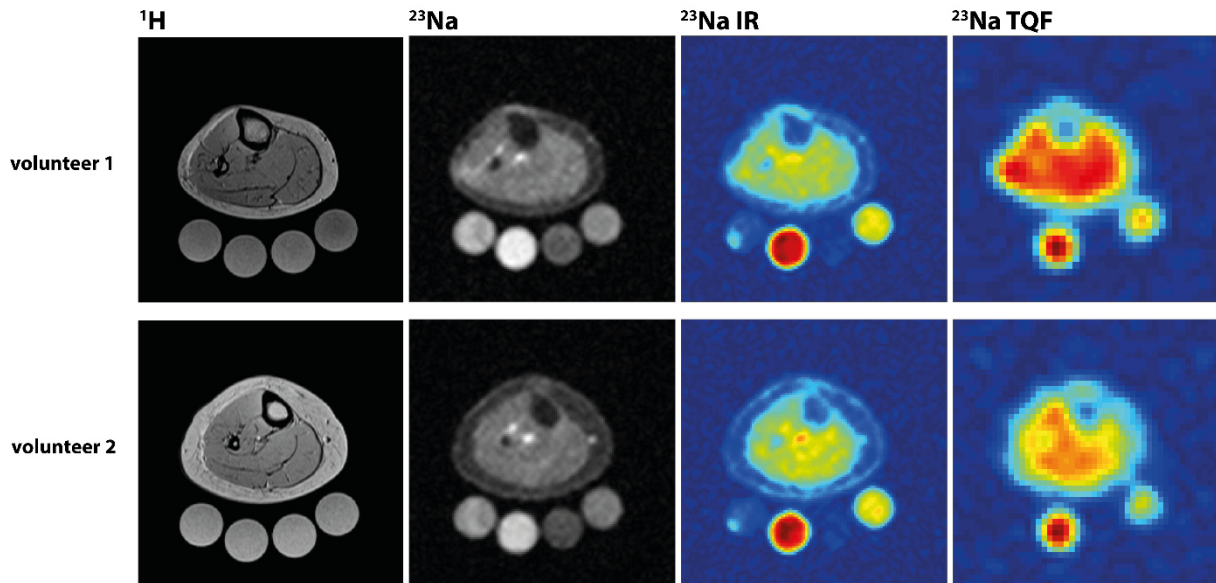


Figure 103: Conventional ^1H and ^{23}Na lower leg images of two healthy volunteers are compared to ^{23}Na IR and TQF images (Reference tubes from left to right: 40 mM NaCl, 40 mM NaCl + 4 % agarose, 20 mM NaCl, 20 mM NaCl + 4 % agarose). Although the TQF images suffer from a lower SNR, the IR images showed remaining signal in agarose-free reference phantom. Furthermore, some ^{23}Na IR images showed remaining signal originating from blood vessels (volunteer 2), which was not seen in TQF images.

Figure 103 depicts IR and TQF ^{23}Na images of the leg of two healthy women in comparison to ^1H and conventional ^{23}Na images. Both sequences had an acquisition time of 10 minutes. The IR method is prone to B_1 inhomogeneities, which can be appreciated by the remaining signal in the periphery of agarose-free reference phantoms. Moreover, the ^{23}Na IR image from volunteer 2 showed remaining signal originating from blood vessels. Relaxation times need to be known exactly and residual signal contribution from extracellular compartment remains unclear. On the other hand, the TQF images suffer from a lower SNR compared to IR images. However, we achieved a good suppression of the mono-exponential relaxing sodium signal. Even if the MQF ^{23}Na signal is only weighted towards intracellular compartment, it is a tool to obtain ratios of restricted ^{23}Na vs hydrated ^{23}Na . Nevertheless, off-resonances can result in signal loss due to destructive interference during phase cycling.

One direction of new research is to optimize ^{23}Na techniques for better suppression characteristics. This could be achieved for example by B_0 and B_1 correction or improving the phase cycling [105]. Phase sensitive B_1 mapping has been shown to correct the transmit/receive profile of the RF coil and hence improve the accuracy of ^{23}Na measurements [232]. However, this will add additional scan time to the protocol as two acquisitions with opposite phase offsets are required. Compressed sensing could be therefore a solution to accelerate image acquisition.

One important obstacle and limitation in this work was the absolute calibration of the ²³Na NMRS signals. I validated the non-localized protocol in Paris on a healthy population at different vascular filling conditions. However, I was not able to calibrate the ²³Na NMR signals in the same way in Erlangen and to render the ²³Na signal independent of the leg volume. One cause could be the coils used. Although, the same manufacturer has built both ²³Na coils, they have different SNR and B₁ homogeneity properties. We could therefore speculate that while the coil in Paris is independent of the charge it is not the case for Erlangen. Further experiments need to confirm this assumption. Thus, our idea to set up a non-localized protocol to reduce the acquisition time was not successful in Erlangen. Nevertheless, since a ²³Na signal calibration was possible in Paris, we extended a current natural history protocol on DMD patients with the proposed protocol. This study is still ongoing and we will know more about the sensitivity of the ²³Na spectroscopic indices in the near future.

In a final step, the sensitivity of ²³Na parameters to intervention has to be investigated so that ²³Na NMR-based biomarkers are established for larger scale clinical trials. Different therapeutic approaches for the disease treatment have been tested giving hope for finding an effective drug in the future [1]. These therapeutic strategies include pharmacological, gene-based, and cell-based approaches. Pharmacological strategies promote the regeneration of the affected muscle and do not deliver the missing or repaired gene or protein. Thus, they treat the pathological consequences of the related mutation and not the cause per se. The used drugs try to improve the phenotype by counteracting the inflammation (e.g. corticosteroids), improving the calcium/sodium homeostasis (calcium/sodium channel blockers), increasing muscle strength (e.g. anabolic steroids, growth hormones), or increase the expression level of compensatory proteins (e.g. utrophin for dystrophin) [233], [234]. On the contrary, gene- and cell-based therapies target directly the mutation causing the disease and are especially promising when initiated at the early phase of the disease course. New genome editing tools such as TALEN and CRISPR Cas9 enable a precise editing of the DNA correcting for the genetic mutations targeting the stem cell population in the muscle tissue. For example, mutations in exons can be restored by changing the reading frame of transcripts via exon skipping, exon deletion, frame shifting, or exon knock-in [235], [236]. One prominent example of an exon-skipping based medication is eteplirsen, which was conditionally approved recently by the U.S. Food and Drug Administration for the treatment of DMD patients with a premature stop codon in exon 51 (<https://www.fda.gov/NewsEvents/Newsroom/PressAnnouncements/ucm521263.htm>).

Whichever is the chosen treatment, NMR protocol should monitor the short-term treatment response in future clinical studies related to muscular dystrophies. So far, only a small number of clinical studies included NMR as outcome measure to test the sensitivity of the therapeutic strategies. DMD patients on corticosteroid treatment demonstrated a decrease in muscle water T₂

and a slower fatty infiltration progression than steroid-naïve DMD boys [12]. In one pilot study, DMD boys were treated over a period of 16 weeks with L-arginine and metformin to increase nitric oxide levels to stimulate mitochondrial function and reduce oxidative stress in skeletal muscle tissue [237]. They stated a disease-slowng effect of the treatment since they have seen no significant increase in the Dixon-based fat fraction in line with improved muscle function. They expanded this study with a randomised placebo-controlled trial with functional test as primary endpoint and quantitative muscle NMR including Dixon and water T₂ as secondary endpoint. NMR has also been suggested to be a useful outcome measure in DMD trials that aim to restore truncated dystrophin protein. Internal data has shown that exon-skipping based treatment improves to a small but significant extent ¹H NMR-based outcome measures (delta FF). However, exploitation of ²³Na NMR-based outcome measures in preclinical or clinical trials has not been yet described. Only one case report demonstrated that the diuretic agent eplerenone reduced the Na⁺ overload in one DMD patient [145]. Thus, the performance of ²³Na NMR-based outcome measures in monitoring treatment response detection must be still precisely determined and compared to other advanced NMR biomarkers. Preclinical studies in dystrophic animal models can evaluate the short-term sensitivity of ²³Na NMR methods to a pharmaceutical intervention. Finally, the resulting selection of outcome measures could be transferred to clinical setting with a larger cohort using the current standard of care including corticosteroids or citrulline-metformin as well as new therapeutic strategies such as ion channel blockers, eplerenone, and eteplirsen.

To sum up, ²³Na NMR suffers from a low SNR and longer acquisition times when compared to ¹H NMR. It nevertheless provides additional physiological information about the state of tissue. Although only a small cohort of DMD patients have been so far scanned within the framework of this thesis, the application of ²³Na NMR methods in dystrophic patients and animal models deserves further investigation, particularly in relation with their capacity to evaluate the disease evolution and treatment response.

List of abbreviations and symbols

Symbols

^1H	proton
^{23}Na	sodium
^{31}P	phosphorus
B_0	external static magnetic field (e.g. 3 Tesla)
B_1	radio frequency field
$d_{p',p}^l$	Wigner rotation matrix element (used to describe MQF)
E	magnetic energy
eQ	electric quadrupole moment of the nucleus
$f_{p',p}^l(t)$	time-dependent relaxation function (used to describe MQF)
\hbar	Dirac's constant equals to $h/2\pi$ (1.055×10^{-34} J s)
h	Planck's constant (6.626×10^{-34} J s)
I	spin quantum number (e.g. for ^1H $I = 1/2$ and ^{23}Na $I = 3/2$)
k	Boltzmann constant (1.381×10^{-23} J K $^{-1}$)
l	rank of tensor T_{1p}
m	spin state (azimuthal quantum number, direction of rotation)
M_0	longitudinal magnetization
M_x and M_y	transverse magnetizations
M_z	longitudinal magnetization
n	total number of nuclear spins in the macroscopic sample
p	order (or coherence) of the tensor T_{1p} with $\text{abs}(p) \leq l$
r	radius
T	absolute temperature in units of Kelvin
t	acquisition time (in MQF sequence)
T_1	longitudinal relaxation time constant
T_2	transverse relaxation time constant
T_2^*	fictitious transverse magnetization time constant due to the presence of inhomogeneity (shorter than T_2)
T_{2l} and T_{2l}	short and long transverse relaxation time constant
T_{2w}	T_2 weighted (NMR contrast)
T_{1p}	irreducible spherical tensor operator (describes process during MQF sequences)
γ	gyromagnetic ratio (e.g. ^1H 267.5×10^6 rad s $^{-1}$ T $^{-1}$ and ^{23}Na 70.8×10^6 rad s $^{-1}$ T $^{-1}$)
δ	chemical shift
η	viscosity coefficient
$\theta_1, \theta_2, \theta_3$	flip angle of the three RF pulses (in MQF experiment)
μ	nuclear magnetic moment
σ	shielding constant

τ_1	preparation time (in MQF sequence)
τ_2	evolution time (in MQF sequence)
τ_c	rotational correlation time
ϕ_1, ϕ_2, ϕ_3	RF pulse phases (in MQF experiment)
Ψ	receiver phase
ω_L	Larmor frequency
ω_Q	quadrupolar interaction frequency
$\overline{\omega_Q}$	averaged quadrupolar interaction frequency

Abbreviations

ADP	adenosine diphosphate
AMP	adenosine monophosphate
ATP	adenosine triphosphate
BMD	Becker muscular dystrophy
BW	bandwidth
CPMG	Carr-Purcell-Meiboom-Gill (method to measure T_2)
CSA	cross sectional area
CT	computed tomography
CV	coefficient of variation
DA-3DPR	density-adapted 3D radial projection pulse sequence
DGC	dystrophin-glycoprotein complex
DMD	Duchenne muscular dystrophy
DQC	double quantum coherences
DQF	double quantum filter
DQF-MA	DQF with magic angle excitation (flip angle of 54.7°)
DYSF	dysferlin gene (mutations associated to LGMDs)
ECM	extracellular matrix
ED	extensor digitorum muscle
EFG	electric field gradients
EMF	electromotive force
EPG	extended phase graph (fitting approach)
ES	echo spacing
FA	flip angle
FF	fat fraction
FID	free induction decay
FLASH	fast low angle shot magnetic resonance imaging
FSHD	Facioscapulohumeral muscular dystrophy
GL	gastrocnemius lateral muscle
GM	gastrocnemius medial muscle
GRE	gradient-echo imaging
ICW	intracellular weighted ^{23}Na signal
IR	inversion recovery method (technique for T_1 measurements)
ISIS	image selected in vivo spectroscopy (localization method for spectroscopy)
LGMD	limb-girdle muscular dystrophy

LL-IR	Look-Locker inversion recovery
MD	muscular dystrophy
MQC	multiple quantum coherences
MQF	multiple quantum filters
MSME	multi-slice multi-echo sequence
MyHC	myosin heavy chain
Na-K ATPase	sodium-potassium pump
Nav 1.4/1.5	sodium channels (two isoforms found in skeletal muscle)
NCX	sodium-calcium exchanger (membrane transporter)
NEX	number of experiments
NHE	sodium-proton exchanger (membrane transporter)
NMR	nuclear magnetic resonance
NMRI	nuclear magnetic resonance imaging
NMRS	nuclear magnetic resonance spectroscopy
PCr	phosphocreatine
PDE	phosphodiester
Pi	inorganic phosphorus
PL	peroneus longus muscle
PME	phosphomonoesters
PRESS	point resolved spectroscopy (localization method for spectroscopy)
RARE	Rapid Acquisition with Relaxation Enhancement
RF	radio frequency pulse
ROI	region of interest
RQI	residual quadrupolar interaction
SC	satellite cells
SD	standard deviation
SNR	signal to noise ratio
SO	soleus muscle
SQC	single quantum coherences
SR	shift reagent
TA	tibialis anterior muscle
T _{acq}	acquisition time
TE	echo time
TI	inversion time
TP	tibialis posterior muscle
TQC	triple quantum coherences
TQF	triple quantum filter
TR	repetition time
TSC	total sodium content
UTE	ultra-short echo time technique
VAPOR	variable power and optimized relaxation delays (water suppression technique in NMR)
WT	wild-type (control in murine studies)

List of figures

Figure 1: Scheme of skeletal muscle and associated structures [21].....	9
Figure 2: Distinctive banding pattern of muscle myofibrils originating from the arrangement of actin and myosin filaments. Zoom-in from [20].....	10
Figure 3: Muscle metabolism systems supplying energy for muscle contraction. Adapted from [20].	12
Figure 4: Schematic diagram of main Na ⁺ fluxes across the membrane. The following transmembrane proteins are involved: Na channel, Na-H exchanger, Na-Ca exchanger, and the Na-K ATPase.....	14
Figure 5: Scheme of skeletal muscle regeneration represented by the four interrelated and time-dependent phases: necrosis, inflammation, regeneration, and remodelling and maturation of the injured myofibre. Time line based on murine experiments. Adapted from [34]. h hours, d days, SC satellite cells.	16
Figure 6: Inflammatory infiltration in acute and chronic muscle repair. Acute injury of skeletal muscle leads to a rapid and controlled inflammation. Transient inflammatory infiltration occurs to remove damaged myofibres and promote regeneration and remodelling of the muscle. During chronic injury on the contrary, a persistent inflammatory infiltration leads to an excessive accumulation of extracellular matrix components. This deposition inhibits the myofibres repair and muscle replacement by fibrotic tissue occurs [37]. Bars = 50 μm.....	17
Figure 7: Dysferlin plays a key role in the Ca ²⁺ -dependent membrane repair. The dysferlin protein is located in the cell membrane and cytoplasmic vesicles. After a local injury, the Ca ⁺ influx activates local calpains that cleave dysferlin protein. Dysferlin-containing cytoplasmic vesicles are recruited to the site of membrane injury. These vesicles fuse with one another and with the sarcolemma thus resealing the disrupted area. Adapted from [35].	19
Figure 8: The dystrophin-glycoprotein complex (DGC) connects actin filaments through the cell membrane to the surrounding ECM [54].....	20
Figure 9: Zeeman splitting of energy levels of a nucleus with spin I = 1/2. The degeneracy of the m sublevels is broken in the presence of an external magnetic field causing an energy separation between the m sublevels.	24
Figure 10: Zeeman diagrams from spin I= 1/2 (¹ H and ³¹ P) and spin I= 3/2 (²³ Na) in an external magnetic field B ₀ = 3T.	24

Figure 11: Population of spins in the presence of an external magnetic field B_0 . While the lower energy level corresponds to the magnetic moments parallel with B_0 , the spins in the higher energy level are aligned anti-parallel with B_0 .	25
Figure 12: Magnetic moment μ precessing in an external magnetic field B_0 .	26
Figure 13: Excitation of magnetization in the rotating frequency frame. A) At thermal equilibrium, a net magnetization vector along +z without a net magnetization in the transverse plane. B) The net magnetization rotates towards the +y-axis during the application of B_1 . C) If the RF pulse is calibrated for a complete excitation, a net magnetization vector along +y-axis is created and no magnetization remains along z-axis.	27
Figure 14: Spin-lattice (T_1) relaxation. A) The longitudinal magnetization relaxes back to thermal equilibrium value with a T_1 relaxation time constant. B) After a 90° RF pulse no net macroscopic magnetization M_z remains. Given time, the longitudinal magnetization returns in an exponential manner.	29
Figure 15: Spin-spin (T_2) relaxation. A) The transverse magnetization decays with a T_2 relaxation time constant in a perfect homogeneous magnetic field and with a T_2^* relaxation time constant at presence of magnetic field inhomogeneity. B) After a 90° RF pulse excitation, the net magnetization is rotated towards +y'-axis and phase coherence is generated (transverse magnetization along the +y'-axis). During the relaxation, the phase coherence decreases in the transverse plane and the resulting transverse magnetization disappears with time.	30
Figure 16: T_1 and T_2 relaxation times as a function of the correlation rate. The minimum of T_1 and the "dip" of the T_2 are at Larmor frequency f_0 .	31
Figure 17: The free induction decay following an excitation pulse in the time-domain. The corresponding frequency-domain spectrum is obtained by computing the Fourier transform of the FID.	33
Figure 18: Electric charge distribution of 1/2 and 3/2 nuclei. A spin 1/2 is spherical exhibiting no electric interaction between the nucleus and the electric field. On the other hand, a spin of 3/2 has a quadrupolar electric charge distribution that interacts with the electric field gradient.	35
Figure 19: Time dependence of quadrupolar interactions in the laboratory frame. The quadrupolar interaction frequency ω_Q is modulated in time due to thermal motion within the lattice. In liquid, the quadrupolar interactions are averaged to zero in a relatively short time. In biological tissue, the quadrupolar interaction frequency is slower resulting in non-zero averaged ω_Q . Adapted from [69].	35

Figure 20: **A)** In vivo ^{23}Na spectrum from human calf: the three single quantum coherences give rise to one broad peak. **B)** Energy levels of sodium nucleus in an external magnetic field. The spin 3/2 nuclei can undergo single ($-3/2 \leftrightarrow -1/2$, $-1/2 \leftrightarrow +1/2$, $+1/2 \leftrightarrow +3/2$), double ($-3/2 \leftrightarrow +1/2$, $-1/2 \leftrightarrow +3/2$), and triple ($-3/2 \leftrightarrow +3/2$) quantum coherences/transitions. 36

Figure 21: Schema of multiple quantum filter RF diagram with corresponding coherence order transfers and tensors $T_{l,p}$. A typical MQF sequence consists of three RF pulse of angle Θ and phase Φ . By proper phase cycling, DQC and TQC are selected and detected at the end of the third RF pulse. . 39

Figure 22: Dependency of the transfer functions of second rank tensor T_{2-1} for DQF and of third rank tensor T_{3-1} for DQF and TQF on the flip angle in MQF experiments. At the magic angle (54.7°) only the contribution of T_{2-1} is detected by the DQF..... 43

Figure 23: Dixon-based fat fraction plotted against the age at baseline and one-year follow up. The FF in the upper limb correlated with age. Ambulatory patients are represented in blue, non-ambulant in red. Adapted from [125]. 46

Figure 24: ^1H NMRS based water T_2 values for the soleus and vastus lateralis muscles were lower in CS boys compared to CS-naïve boys. CS corticosteroid treatment. Adapted from [12]...... 47

Figure 25: PDE/ATP ratios are increased in leg muscles in BMD patients with non-increased fat levels (NIFL) and increased fat levels (IFL) compared to healthy controls. * significantly higher PDE/ATP in BMD NIFL compared to controls. ■ significantly higher PDE/ATP in BMD IFL compared to controls. GCL gastrocnemius lateralis, GCM, gastrocnemius medialis, PER, peroneus, SOL soleus, and TA tibialis anterior [53]. 48

Figure 26: Correlations between the water T_2 and ^1H -based pH (**A**) or the ^{31}P -based pH (**B**). A group of DMD patients had normal ^1H -measured pH values but elevated ^{31}P -based pH and increased water T_2 cut-off value: mean value plus two standard deviation in young healthy group [137]. 49

Figure 27: ^1H (left) and ^{23}Na NMR (right) image of a patient with myotonic dystrophy. Significant elevations in normalized ^{23}Na signal intensities were measured in the patient (up to 70 % compared to not affected side). Adapted from [143]. 50

Figure 28: Temporal changes of TSC in DMD patients before and after start of treatment. While the first patient (on the left) underwent eplerenone treatment, the second patient (on the right) was under glucocorticoid treatment. Both DMD patients were seven years old. ^{23}Na signals were normalized using one phantom filled with 51.3 mM NaCl in 5 % agarose [145]. 51

Figure 29: Typical localized in vivo ^1H NMR spectra from a murine skeletal muscle (acquired at 7T) with water suppression showing the different resonances originating from lipids. 56

Figure 30: The fat fraction map (FFmap) are generated by computing pixel wise the ratio between the fat map (Fmap) and the sum of water map (Wmap) and fat map (Fmap) based on the 3-point Dixon approach.....	58
Figure 31: General diagram of the RARE sequence showing the RF-pulse sequence and sampling scheme of the k-space. The individual echoes are used to fill the lines of the k-space of a single image.....	59
Figure 32: The spin echo pulse sequence consists of an initial 90° RF pulse followed by train of 180° RF pulses and results in multiple spin echo formations.....	60
Figure 33: Plot of ¹ H T ₂ -decay curve of muscle tissue obtained for a healthy subject. Examples of images acquired at different echo times are assigned to the relaxation curve. The green line fitting the blue points corresponds to the tri-component exponential fit without the two first points. T ₂ values are calculated pixel wise to compute the corresponding T ₂ map.....	60
Figure 34: General diagram of the ISIS-CPMG method showing the RF-pulse sequence and slice-selecting gradient. Signal localization is achieved by the ISIS method using inversion pulses that are selectively turned on following an eight-step combination (Acqu 1 to 8). A fat-suppression module is launched just after the ISIS module to suppress the unwanted signal from intramuscular lipids. Then, the signal of the CPMG echo train is acquired.	62
Figure 35: Plot of ¹ H T ₂ -decay curve obtained from the gastrocnemius medialis muscle of a healthy, male subject. The green line fitting the blue points corresponds to the fitted curve resulting from the regularized inversion solution using a nonnegative least-square method. The corresponding T ₂ spectrum shows two distinct T ₂ components characterized by their relative fraction and T ₂ value. Typical values in accordance with literature were observed: T _{2,s} = 31.5 ms with relative fraction of 0.93 and T _{2,l} = 100.7 ms with relative fraction of 0.07.	63
Figure 36: Typical in vivo ³¹ P NMR spectrum from a murine skeletal leg (non-localized acquisition at 7T) showing relevant ³¹ P containing metabolites such as adenosine triphosphate (ATP), phosphocreatine (PCr), and inorganic phosphate (Pi). By measuring the chemical shift difference between the Pi and PCr resonances, the pH can be determined.	64
Figure 37: Typical localized in vivo ¹ H NMR spectra from a voxel within the gastrocnemius muscle of a healthy human subject (acquired at 3T) A) with imperfect water suppression. B) In ¹ H NMR, intracellular pH measurement is based on the shift between the carnosine peaks at around 8 and 7 ppm and the water peak (zoom of A).	65

Figure 38: Voltage calibration for the ^{23}Na NMR protocol: the RF voltage to produce a 90° FA was determined by increasing stepwise the emitter voltage. The voltage resulting in the highest signal intensity was used for the ^{23}Na protocol acquisition..... 66

Figure 39: RF sequence diagram for ^{23}Na spectroscopy protocol that includes non- localized **A)** FID, **B)** TQF and **C)** IR-LL sequences. Next to the sequence diagram, corresponding human in vivo spectra are plotted for the FID and TQF sequence (acquired at 3T). Note the difference in the signal intensities between the FID and TQF signal. The IR-LL data was fit with a mono-exponential model to obtain a global T_1 of the leg. TE echo time, TR repetition time, ϕ_1 , ϕ_2 , ϕ_3 phase of pulses, TI inversion time, ES echo spacing..... 67

Figure 40: Plot of ^{23}Na T_2^* -decay curve obtained for a healthy subject. The violet line fitting the blue points corresponds to the fitted curve resulting from the regularized inversion solution using a nonnegative least-square method. The corresponding T_2^* spectra shows two distinct T_2^* components characterized by their relative fraction and T_2^* value. Typical values in accordance with literature were observed: $T_{2,s}^* = 0.9$ ms with relative fraction of 0.38 and $T_{2,l}^* = 13.4$ ms with relative fraction of 0.62..... 68

Figure 41: Correlation of FID signal with different concentrations of NaCl and correlations of FID signal, TQF signal, and T_1 value with different concentrations of agarose. 69

Figure 42: RF sequence diagram for ^{23}Na DQF-MA spectroscopic sequence. Next to the sequence diagram, corresponding human in vivo spectrum is plotted (acquired at 3T). TR repetition time, ϕ_1 , ϕ_2 , ϕ_3 phase of pulses. 70

Figure 43: **A)** RF pulse and gradient diagram of the 3D radial sequence with i) a conventional gradient readout and ii) a density-adapted gradient readout. The conventional gradient readout uses a constant gradient strength after the gradient ramp, while the density-adapted readout gradient consists of three parts: (1) the gradient ramp, (2) a trapezoidal part with gradient strength G_0 , and (3) a density-adapted part that starts after t_0 allowing in the following constant sampling density in the outer part of the k-space. **B)** Radial sampling scheme of the k-space: without density-adapted sampling, the centre of k-space is more densely sampled than the outer part. By manipulating the readout gradient, the sampling velocity is slowed down in the outer part of k-space leading to a more homogenous sampling scheme..... 71

Figure 44: Images of two healthy female volunteers. **A)** T_1 weighted ^1H image of right leg with corresponding **B)** DA-3DPR ^{23}Na image and **C)** DA-3DPR ^{23}Na image with IR pulse (TI 34 ms). Four calibration standards are shown at the bottom of the leg with sodium concentration of 20 mM (3)

and 40 mM (1) and with 4 % agarose and 20 mM (4) and 40 mM (2) mimicking Na ⁺ with restricted mobility.....	74
Figure 45: ²³ Na signal calibration using two reference phantoms with 20 mM and 40 mM NaCl in 4 % agarose and the background noise. Based on the calibration curve, TSC and ICW maps are calculated pixel-wise.....	75
Figure 46: ²³ Na signal calibration of the leg. A) ROIs are drawn manually on the ¹ H image in TA (green), SO (yellow), GM (orange), subcutaneous fat (blue), in the calibration standards, and in the background (red). B) TSC map and C) ICW map were calculated based on the calibration curve using the agarose phantoms (2 and 4) and the background noise.	75
Figure 47: Timeline of the ischemia protocol (protocol 1): (i) After 30 min supine rest, (ii) the medical cuff placed above the knee was rapidly inflated and the acquisition of the sodium spectra started. .	78
Figure 48: Timeline of the vascular filling conditions (protocol 2): (i) vascular draining was first applied with the calf positioned in the coil followed by the NMR acquisition (non-localized ²³ Na spectroscopic and ¹ H imaging acquisition or by ¹ H MSME acquisition). (ii) After vascular filling during a 5-minute interval initiated by a reduced cuff pressure, another NMR acquisition was launched. (iii) Normal condition: the pressure of the cuff was completely released and after a 5-minute break, the final sodium NMR and proton imaging were performed.....	79
Figure 49: Standard ¹ H T ₂ imaging: A) a cross-sectional T ₂ w image (TE = 34 ms); B) The ROIs used for analysis were traced within the muscles (TA orange; ED brown; TP pink; PL green; SO yellow; GL red; GM beige; Background noise grey).	80
Figure 50: The effect of short-term ischemia in vivo in skeletal muscle measured by ²³ Na NMR.....	81
Figure 51: The sodium FID, TQF, and T ₁ recovery signals measured in a healthy young 22-year-old female volunteer under different vascular filling conditions. A) The FID signal in the time domain is Fourier transformed to obtain the FID spectrum, which gives then the T ₂ * spectrum by a T ₂ * deconvolution of the FID signal decay. The T ₂ * spectrum is plotted with logarithmically scaled abscise. The plots show the characteristic course of the vascular draining (red), vascular filling (blue), and control (black) conditions. B) The drawn ROI on the FLASH image of the right calf of the volunteer were used for the volume calculations.	82
Figure 52: Evolution of different ²³ Na parameters (FID signal, TQF/FID ratio, TQF signal, T ₁ value, long T ₂ * signal, short T ₂ * fraction, and short T ₂ * signal) and leg volume under three different vascular filling conditions (vascular draining: drain, vascular filling: fill, and control condition: ctrl). The boxes	

have lines at the lower quartile, median (red), and upper quartile with the length of the whiskers specified as 1.5 times the interquartile range. The red crosses mark outliers of the datasets. 83

Figure 53: The percentages of change of the ^{23}Na parameters under vascular filling and vascular draining conditions compared with the control condition (\S : $p < 0.05$). 84

Figure 54: Correlation between FID signal and volume and between TQF/FID ratio and T_1 value. Additionally, highly significant correlations between TQF/FID ration and short T_2^* fraction and short T_2^* values were detected. Data acquired under vascular draining and vascular filling are depicted as red and blue circles, respectively. Black circles represent the data points collected during the control condition..... 85

Figure 55: The percentages of change of the mean T_2w signal intensities and the mean T_2 for all muscles under the vascular filling and vascular draining conditions compared with the control condition..... 86

Figure 56: Calibration of the in vivo ^{23}Na signal: **A)** Costume-made linear volume ^{23}Na leg coil with the leg holder and shift reagent phantom used as external reference. **B)** Dixon image ($TE = 2.75$ ms) of the leg and SR phantom. The ROI used for volume analysis was traced over all muscles (in violet) excluding bone, skin, and subcutaneous fat. 91

Figure 57: Sensitivity profile of the ^{23}Na coil along the length measured on a 140 mM NaCl containing bottle with a diameter of 9 cm..... 92

Figure 58: The sodium FID and TQF signals measured in a healthy young 23-year-old female volunteer at control condition. Notice the presence at around 0.7 kHz of the SR in the FID spectrum and its absence in the TQF spectre. 93

Figure 59: Evolution of ^{23}Na FID signal and TQF signal before volume correction under three different vascular filling conditions (vascular draining: drain, vascular filling: fill, and control condition: ctrl). Based on the ^{23}Na signals, TSC and ICW values were calculated for the three different vascular filling conditions taking the muscle volume and coil sensitivity into account. The boxes have lines at the lower quartile, median (red), and upper quartile with the length of the whiskers specified as 1.5 times the interquartile range. The red crosses mark outliers of the datasets..... 93

Figure 60: Important correlations of ^{23}Na FID and TQF signal with muscle volume were detected. After correction, TSC and ICW showed no correlation with the muscle volume. Data acquired under vascular draining and vascular filling are depicted as red and blue circles, respectively. Black circles represent the data points collected during the control condition..... 94

Figure 61: The effect of prolonged ischemia in vivo in skeletal muscle measured by ^{23}Na NMR. Evolution of the A) ^{23}Na FID signal, B) ^{23}Na TQF signal, and C) TQF/FID ratio during a 40-minute ischemia in skeletal muscle tissue (normalized with first time point, presented as mean with SD bars, $n = 4$).....	98
Figure 62: The effect of prolonged ischemia in vivo in skeletal muscle measured by ^1H NMR. Evolution of A) the mean T_2 of the leg muscles measured by a MSME sequence during ischemia and of B) the short and C) long T_2 with D) the relative short T_2 amplitude obtained by a biexponential fit of the ISIS-CPMG signal decay during ischemia (presented as mean with SD bars, $n = 4$).....	99
Figure 63: Examples of A) FID signal, B) TQF signal, and C) DQF-MA signal acquired on one volunteer showing the important differences in signal intensity between the three techniques.....	103
Figure 64: Example of A) normalized FID and B) normalized TQF signal decays acquired on one volunteer. The resulting fit curves are shown in red.	103
Figure 65: Histology of the quadriceps muscle of MMex38 mice at A) 12 weeks, B) 20 weeks, and C) 60 weeks of age. The dystrophic phenotype worsens with age. Stained with Gomori's trichrome. Provided by V. Schöwel.....	108
Figure 66: A) Representative T_1 -weighted image of the thigh of a MMex38 mouse. CSA of the quadriceps were drawn on the contractile tissue avoiding the complete fat-replaced parts of the muscle (ROI_2). B) Representative axial MSME image (at TE 4 ms) of the left leg and thigh of a WT mouse. The overlay represents the manually traced ROIs in the different muscle compartments. Leg: Ant. (red) = TA/EDL, med. (green) = TP, and pos. (yellow, blue and turquois) = gastrocnemius, plantaris muscles; Thigh: ant. (red) = quadriceps, med. and pos. (yellow and blue) = biceps femoris and gluteus maximus.....	111
Figure 67: ^1H NMR spectra with water suppression in the calf of a MMex38 and a WT mouse. Lipid 1 was assigned to methylene protons at $\Delta\text{ppm} = 0.8 - 1.8$, Lipid 2 to α - or β -methylene protons at $\Delta\text{ppm} = 2 - 2.8$, and Lipid 3 to olefinic protons at $\Delta\text{ppm} = 5.3 - 5.7$. Note the residual peak of water at 4.7 ppm.....	112
Figure 68: T_1 -weighted images of the thigh and leg of WT, MMex38, and BLAJ mice. The images showed highly fat infiltrated muscles in the thighs of both dysferlin-deficient mouse models. Parts of the quadriceps of MMex38 were systematically replaced by fatty tissue.....	114
Figure 69: T_1 values of WT and dysferlin-deficient MMex38 and BLAJ mice: No significant differences were seen in the leg between the strains. In the thigh, the dysferlin-deficient mice showed decreased	

T₁ values in the medial posterior compartment compared to WT (MMex38 n = 10, BLAJ n = 4, and WT n = 10; \$: p < 0.05)..... 115

Figure 70: Fat fraction and water T₂ values measured in the leg of WT and dysferlin-deficient MMex38 and BLAJ mice: No significant differences were seen in the FF between the strains. Dysferlin-deficient mice showed increased water T₂ values in the anterior and posterior compartment compared to the (MMex38 n = 10, BLAJ n = 4, and WT n = 10; \$: p < 0.05)..... 115

Figure 71: Fat fraction and water T₂ values measured in the thigh of WT and dysferlin-deficient MMex38 and BLAJ mice: Dysferlin-deficient mice showed systematically increased FF and water T₂ values compared to WT (MMex38 n = 10, BLAJ n = 4, and WT n = 10; \$: p < 0.05)..... 116

Figure 72: Elevated water T₂ and water T₂ CV measured in the leg of WT and dysferlin-deficient MMex38 and BLAJ mice: Dysferlin-deficient mice showed a higher percentage of elevated water T₂ values as well as higher CV in the anterior and posterior compartment compared to WT (MMex38 n = 10, BLAJ n = 4, and WT n = 10; \$: p < 0.05). 116

Figure 73: Elevated water T₂ and water T₂ CV measured in the thigh of WT and dysferlin-deficient MMex38 and BLAJ mice: Dysferlin-deficient mice showed higher percentage of elevated water T₂ values as well as higher CV compared to WT (MMex38 n = 10, BLAJ n = 4, and WT n = 10; \$: p < 0.05). 117

Figure 74: Fat ratios measured by ¹H spectroscopy in the leg of WT and dysferlin-deficient MMex38 and BLAJ mice: Dysferlin-deficient mice showed higher fat ratios especially in the thigh muscles compared to WT (MMex38 n = 10, BLAJ n = 4, and WT n = 10; \$: p < 0.05)..... 117

Figure 75: Resting ³¹P spectra (TR 2.5 s) acquired of the right leg are shown for MMex38 and WT. Peaks were assigned to PME (around 6 ppm), Pi (4.95 ppm), PCr (0 ppm), and the γ- (-2.4 ppm), α- (-7.5 ppm), and β-phosphate (-16 ppm) of ATP. Each spectra represents an average of 720 FIDs over 30 minutes..... 118

Figure 76: T₁-weighted imaging showed slightly fat infiltrated muscles in the thigh of mdx compared to WT. 119

Figure 77: T₁ values of the WT and mdx mice: Significant differences were seen in the leg between the strains (\$: p < 0.05)..... 119

Figure 78: Water T₂ values measured in the leg and thigh of the WT and mdx mice: Mdx mice showed increased water T₂ values in several muscle compartments compared to WT (\$: p < 0.05)..... 120

Figure 79: Elevated water T ₂ and water T ₂ CV measured in the leg of WT and mdx mice: mdx showed a higher percentage of elevated water T ₂ values as well as higher CV in the anterior and posterior compartment compared to WT (\$: p < 0.05).	121
Figure 80: Elevated water T ₂ and water T ₂ CV measured in the leg of WT and mdx mice: mdx showed a higher percentage of elevated water T ₂ values as well as higher CV in the anterior and posterior compartment compared to WT (\$: p < 0.05).	121
Figure 81: Resting ³¹ P spectra (TR 2.5 s) acquired on the right leg are shown for mdx and WT mice. Peaks were assigned to PME (around 6 ppm), Pi (4.95 ppm), PCr (at 0 ppm), and γ- (-2.4 ppm), α- (-7.5 ppm), and β- (-16 ppm) ATP. Each spectrum represents an average of 720 FIDs over 30 minutes.	122
Figure 82: Results obtained from the bi-exponential fit for the relative short fraction and short and long T ₂ values in WT and mdx (n = 6 mice per group). Short T ₂ s were increased in the thigh and anterior compartment of the leg compared to the WT (\$: p < 0.05).....	123
Figure 83: Correlation between the TQF/FID ratio and ²³ Na T ₁ values and PCr/ATP ratio (including MMex38, mdx, and WT mice).	124
Figure 84: Visualisation of myofibre damage and mononuclear cell infiltration in the quadriceps of MMex38. H&E staining of the quadriceps muscle cross sections reveals the dysferlin-deficient pathological process. The images show centrally nucleated fibres indicating ongoing necrosis and recuperation and fatty tissue replacement. Several accumulations of mononuclear cells were observed in dysferlin-deficient muscle tissue (right).	125
Figure 85: Visualisation of myofibre degenerating and regenerating fibres in the leg of MMex38. H&E staining of the tibialis anterior muscle cross sections reveals centrally nucleated fibres, some atrophic fibres and lipid droplets. Few areas are infiltrated by mononuclear cells.....	125
Figure 86: Visualisation of healthy myofibres in the quadriceps of WT. The images show neither centrally nucleated fibres nor lipid droplets in the muscle tissue.	126
Figure 87: Visualisation of myofibre damage and mononuclear cell infiltration in the tibialis anterior (left) and quadriceps muscles (right) of mdx. The images show centrally nucleated fibres indicating ongoing necrosis and recuperation. In the quadriceps of mdx mice, several accumulations of mononuclear cells and few lipid droplets were observed.	126
Figure 88: Similarities and discrepancies of different NMR parameters between murine models and corresponding human myopathy.....	132

Figure 89: Schema of supposed underlying pathological processes in dystrophin-deficient muscle. While sodium and pH impairments occur at an early stage, the fibro-fatty infiltration presents the end stage of the disease leading to immobility at the beginning of the second decade of life. Different NMR methods are used to track the disease-related alterations including ^{23}Na NMR, ^1H T_2 mapping, ^1H spectroscopy, and Dixon techniques. Figure based on [59], [61], [63], [145], [223]. 135

Figure 90: ROIs were traced manually on the leg muscles: Orange tibialis anterior (TA), bordeaux extensor digitorum (ED), green peroneus longus (PL), pink tibialis posterior (TP), yellow soleus (SO), red gastrocnemius medialis (GM), and salmon pink gastrocnemius lateralis (GL). 139

Figure 91: Examples of **A)** fat image **B)** water image, and **C)** fat fraction map in the leg of six- (Patient #1) and eleven-year-old (Patient #3) DMD patient derived from the Dixon method. 140

Figure 92: Examples of **A)** MSME images (at TE 9.5ms) and corresponding **B)** water T_2 maps in the leg of six- (Patient #1) and eleven-year-old (Patient #3) DMD patient as well as seven-year-old control. 142

Figure 93: FF and water T_2 alterations for selected muscles of DMD patients plotted against the age. Dashed grey lines represent the mean \pm SD of control cohort. 142

Figure 94: pH alterations for the GM muscle of DMD patients plotted against the age. Grey lines represent the mean \pm SD (dashed line) of control cohort. 143

Figure 95: Examples of **A)** anatomical ^1H images and corresponding **B)** TSC and **C)** ICW maps in the leg of five- (Patient #12) and eleven-year-old (Patient #3) DMD patient as well as eight-year-old control. 144

Figure 96: TSC and ICW alterations for different muscles of DMD patients plotted against the age. Grey lines represent the mean \pm SD (dashed line) of control cohort. 145

Figure 97: Examples of **A)** anatomical ^1H images and corresponding **B)** TSC and **C)** ICW maps of two DMD patients (#2 and #10). While the proton T_2 and ^{23}Na TSC maps present muscles with values in a normal range, the ICW signals are elevated. 146

Figure 98: TQF/FID alterations in the leg of DMD patients plotted against the age. Grey lines represent the mean \pm SD (dashed line) of control cohort. 147

Figure 99: Correlations of the TSC and ICW sodium signal with water T_2 : significant correlations between water T_2 and TSC as well as ICW. Ctr control. 147

Figure 100: Correlations of water T_2 , TSC, and ICW with pH. Ctr control. 148

Figure 101: FF and water T_2 at baseline and 6 months follow up of the SO and TA muscles for the eight DMD patients (Patient #1, #2, #3, #4, #5, #8, #9, and #10). Black lines represent the mean \pm SD (dashed line) of control cohort.....	149
Figure 102: TSC and ICW at baseline and 6 months follow up of the SO and TA muscles for the eight DMD patients (Patient #1, #2, #3, #4, #5, #9, and #10). Black lines represent the mean \pm SD (dashed line) of control cohort.	150
Figure 103: Conventional ^1H and ^{23}Na lower leg images of two healthy volunteers are compared to ^{23}Na IR and TQF images (Reference tubes from left to right: 40 mM NaCl, 40 mM NaCl + 4 % agarose, 20 mM NaCl, 20 mM NaCl + 4 % agarose). Although the TQF images suffer from a lower SNR, the IR images showed remaining signal in agarose-free reference phantom. Furthermore, some ^{23}Na IR images showed remaining signal originating from blood vessels (volunteer 2), which was not seen in TQF images.	160

List of tables

Table 1: The four major classes of fibre and their phenotypes identified in mammalian muscle based on the MyHC composition. Note that IIB fibres are usually not found in human. MyHC, myosin heavy chain. Data extracted from [23].	11
Table 2: Ion concentrations of intracellular and extracellular compartment of a mammalian cell. Values taken from [26].	13
Table 3: Selection of muscular dystrophies that are relevant to the current work. Note that all these diseases are inherited.	18
Table 4: NMR properties of commonly used nuclei. Values extracted from [64].	32
Table 5: List of main biological and physical differences between ^1H and ^{23}Na NMR.	34
Table 6: Irreducible spherical tensor operators for spin $I = 3/2$. Values taken from [70].	39
Table 7: Composition of calibration phantoms used for ^{23}Na imaging.	73
Table 8: Signal intensities of calibration phantoms (1, 2, 3, and 4), muscle, blood, and subcutaneous fat in DA-3DPR ^{23}Na images and DA-3DPR ^{23}Na images with IR preparation pulse ($n = 6$).	73
Table 9: Measured TSC and ICW of healthy volunteers ($n = 6$) of the TA, SO, and GM muscle as well as the subcutaneous fat. Values presented as mean and SD (standard deviation).	76
Table 10: Mean values \pm SD for the different phosphate metabolites in WT and MMex38 (MMex38 $n = 6$ and WT $n = 5$). Only the pH was significantly increased ($\$: p < 0.05$).	118
Table 11: Mean values \pm SD for the different phosphate metabolites in WT and mdx ($n = 5$ mice per group). No significant alterations were observed.	122
Table 12: Mean values \pm SD of the ^{23}Na TQF/FID ratio and the ^{23}Na T_1 in WT and MMex38 (MMex38 $n = 6$, WT $n = 5$). Significant alterations were observed in the TQF signal and the T_1 values ($\$: p < 0.05$).	123
Table 13: Mean values \pm SD of the sodium indices measured in WT and mdx: FID signal, TQF signal, TQF/FID ratio, and the T_1 (mdx $n = 6$, WT $n = 5$). Significant alterations were observed in the TQF/FID ratio ($\$: p < 0.05$).	124
Table 14: List of participating DMD patients with age, diagnosis and therapy.	137

Table 15: ^1H imaging results. FF, water T_2 , percentage of voxels with elevated T_2 , and coefficient of variation of T_2 for DMD (n = 12) and control (n = 12) group per muscle and as mean over all muscles. \$: significant difference between DMD and control group ($p < 0.05$). 141

Table 16: ISIS-CPMG results. Relative fraction of short T_2 , short T_2 and long T_2 values for the GM muscle of DMD (n = 10) and control group (n = 11). \$: significant difference between DMD and control group ($p < 0.05$). 143

Table 17: ^{23}Na imaging results. TSC, ICW, and their ratio for DMD (n = 10) and control group (n = 12) per muscle and as mean over all muscles. \$: significant difference between DMD and control group ($p < 0.05$). 145

Table 18: ^{23}Na spectroscopy results. Non-localized TQF/FID ratio and global T_1 value of DMD (n = 9) and control group (n = 10). \$: significant difference between DMD and control group ($p < 0.05$). ... 147

Table 19: FF, water T_2 , TSC, and ICW across time in DMD patients for GM, SL, TA, and TP muscle (n = 8 for FF and T_2 , n = 7 for TSC and ICW). \$: significant difference between 1st and 2nd visit ($p < 0.05$). ... 149

Bibliography

- [1] A. E. H. Emery, "The muscular dystrophies.," *Lancet*, vol. 359, no. 9307, pp. 687–95, Feb. 2002.
- [2] Y. Blat and S. Blat, "Drug Discovery of Therapies for Duchenne Muscular Dystrophy," *J. Biomol. Screen.*, vol. 20, no. 10, pp. 1189–1203, Dec. 2015.
- [3] T. Aslesh, R. Maruyama, and T. Yokota, "Skipping Multiple Exons to Treat DMD—Promises and Challenges," *Biomedicines*, vol. 6, no. 1, p. 1, 2018.
- [4] J. Heckmatt, V. Dubowitz, and S. Leeman, "Detection of Pathological Change in Dystrophic Muscle with B-Scan Ultrasound Imaging," *Lancet*, vol. 315, no. 8183, pp. 1389–1390, Jun. 1980.
- [5] M. Swash, M. M. Brown, and C. Thakkar, "CT muscle imaging and the clinical assessment of neuromuscular disease," *Muscle Nerve*, vol. 18, no. 7, pp. 708–714, Jul. 1995.
- [6] G.-H. Jahng, K.-L. Li, L. Ostergaard, and F. Calamante, "Perfusion magnetic resonance imaging: a comprehensive update on principles and techniques.," *Korean J. Radiol.*, vol. 15, no. 5, pp. 554–77, 2014.
- [7] T. Bezabeh, O. B. Ijare, A. E. Nikulin, R. L. Somorjai, and I. C. Smith, "MRS-based Metabolomics in Cancer Research.," *Magn. Reson. Insights*, vol. 7, pp. 1–14, Jan. 2014.
- [8] E. Moser, F. Stahlberg, M. E. Ladd, and S. Trattnig, "7-T MR--from research to clinical applications?," *NMR Biomed.*, vol. 25, no. 5, pp. 695–716, May 2012.
- [9] P. G. Carrier, B. Marty, O. Scheidegger, P. Loureiro de Sousa, P.-Y. Baudin, E. Snezhko, and D. Vlodayets, "Skeletal Muscle Quantitative Nuclear Magnetic Resonance Imaging and Spectroscopy as an Outcome Measure for Clinical Trials," *J. Neuromuscul. Dis.*, vol. 3, no. 1, pp. 1–28, Mar. 2016.
- [10] C. Tonon, L. L. Gramegna, and R. Lodi, "Magnetic resonance imaging and spectroscopy in the evaluation of neuromuscular disorders and fatigue," *Neuromuscul. Disord.*, vol. 22, pp. S187–S191, 2012.
- [11] U. Bonati, P. Hafner, S. Schädelin, M. Schmid, A. Naduvilekoot Devasia, J. Schroeder, S. Zuesli, U. Pohlman, C. Neuhaus, A. Klein, M. Sinnreich, T. Haas, M. Gloor, O. Bieri, A. Fischmann, and D. Fischer, "Quantitative muscle MRI: A powerful surrogate outcome measure in Duchenne muscular dystrophy," *Neuromuscul. Disord.*, vol. 25, no. 9, pp. 679–685, Sep. 2015.
- [12] I. Arpan, R. J. Willcocks, S. C. Forbes, R. S. Finkel, D. J. Lott, W. D. Rooney, W. T. Triplett, C. R. Senesac, M. J. Daniels, B. J. Byrne, E. L. Finanger, B. S. Russman, D.-J. Wang, G. I. Tennekoon, G. A. Walter, H. L. Sweeney, and K. Vandenborne, "Examination of effects of corticosteroids on skeletal muscles of boys with DMD using MRI and MRS," *Neurology*, vol. 83, no. 11, pp. 974–980, Sep. 2014.
- [13] A. M. Nagel, M.-A. Weber, A. Borthakur, and R. Reddy, "Skeletal Muscle MR Imaging Beyond Protons: With a Focus on Sodium MRI in Musculoskeletal Applications," in *Magnetic*

- Resonance Imaging of the Skeletal Musculature*, M.-A. Weber, Ed. Springer Berlin Heidelberg, 2013, pp. 115–133.
- [14] M.-A. Weber, A. M. Nagel, K. Jurkat-Rott, and F. Lehmann-Horn, "Sodium (^{23}Na) MRI detects elevated muscular sodium concentration in Duchenne muscular dystrophy," *Neurology*, vol. 77, no. 23, pp. 2017–2024, Dec. 2011.
- [15] B. Marty, P.-Y. Baudin, H. Reyngoudt, N. Azzabou, E. C. A. Araujo, P. G. Carlier, and P. L. de Sousa, "Simultaneous muscle water T2 and fat fraction mapping using transverse relaxometry with stimulated echo compensation," *NMR Biomed.*, vol. 29, no. 4, pp. 431–443, Apr. 2016.
- [16] N. Azzabou, P. Loureiro de Sousa, E. Caldas, and P. G. Carlier, "Validation of a generic approach to muscle water T2 determination at 3T in fat-infiltrated skeletal muscle," *J. Magn. Reson. Imaging*, vol. 41, no. 3, pp. 645–653, Mar. 2015.
- [17] E. C. A. Araujo, Y. Fromes, and P. G. Carlier, "New Insights on Human Skeletal Muscle Tissue Compartments Revealed by In Vivo T2 NMR Relaxometry," *Biophys. J.*, vol. 106, no. 10, pp. 2267–2274, May 2014.
- [18] A. M. Nagel, F. B. Laun, M. A. Weber, C. Matthies, W. Semmler, and L. R. Schad, "Sodium MRI using a density-adapted 3D radial acquisition technique," *Magn. Reson. Med.*, vol. 62, pp. 1565–1573, 2009.
- [19] T. Gerhalter, P. G. Carlier, and B. Marty, "Acute changes in extracellular volume fraction in skeletal muscle monitored by ^{23}Na NMR spectroscopy," *Physiol. Rep.*, vol. 5, no. 16, p. e13380, Aug. 2017.
- [20] A. C. Guyton and J. E. Hall, *Textbook of Medical Physiology*, 11th ed. Philadelphia: Elsevier Inc., 2006.
- [21] S. Tajbakhsh, "Skeletal muscle stem cells in developmental versus regenerative myogenesis.," *J. Intern. Med.*, vol. 266, no. 4, pp. 372–89, Oct. 2009.
- [22] E. Negroni, T. Gidaro, a Bigot, G. Butler-Browne, V. Mouly, and C. Trollet, "Stem cells and muscle diseases: advances in cell therapy strategies.," *Neuropathol. Appl. Neurobiol.*, vol. 33, no. 0, Nov. 2014.
- [23] K. Gundersen, "Excitation-transcription coupling in skeletal muscle: the molecular pathways of exercise.," *Biol. Rev. Camb. Philos. Soc.*, vol. 86, no. 3, pp. 564–600, Aug. 2011.
- [24] S. Schiaffino and C. Reggiani, "Fiber types in mammalian skeletal muscles.," *Physiol. Rev.*, vol. 91, no. 4, pp. 1447–531, Oct. 2011.
- [25] M. Floeter, "Structure and Function of Muscle Fibers and Motor Units," *Disord. Volunt. Muscle*, pp. 1–10, 2010.
- [26] B. Alberts, A. Johnson, J. Lewis, M. Raff, K. Roberts, and P. Walter, "Membrane Transport of small molecules and the electrical properties of membranes," in *Molecular Biology of the Cell*, 4th ed., New York: Garland Science, 2002, pp. 615–658.
- [27] Y. Vilin and P. Ruben, "Slow inactivation in voltage-gated sodium channels," *Cell Biochem. Biophys.*, vol. 35, pp. 171–190, Dec. 2001.
- [28] D. Baycin-Hizal, A. Gottschalk, E. Jacobson, S. Mai, D. Wolozny, H. Zhang, S. S. Krag, and M. J. Betenbaugh, "Physiologic and pathophysiologic consequences of altered sialylation and

-
- glycosylation on ion channel function.," *Biochem. Biophys. Res. Commun.*, vol. 453, no. 2, pp. 243–253, Oct. 2014.
- [29] F. Bezanilla, "How membrane proteins sense voltage.," *Nat. Rev. Mol. Cell Biol.*, vol. 9, no. 4, pp. 323–332, Apr. 2008.
- [30] E. Murphy and D. A. Eisner, "Regulation of Intracellular and Mitochondrial Sodium in Health and Disease," *Circ. Res.*, vol. 104, no. 3, pp. 292–303, Feb. 2009.
- [31] T. Clausen, "Quantification of Na⁺,K⁺ pumps and their transport rate in skeletal muscle: functional significance.," *J. Gen. Physiol.*, vol. 142, pp. 327–45, 2013.
- [32] G. Bhave and E. G. Neilson, "Body Fluid Dynamics: Back to the Future," *J. Am. Soc. Nephrol.*, vol. 22, pp. 2166–2181, Dec. 2011.
- [33] R. H. Sterns, "Disorders of Plasma Sodium — Causes, Consequences, and Correction," *N. Engl. J. Med.*, vol. 372, no. 1, pp. 55–65, 2015.
- [34] L. Barberi, B. M. Scicchitano, M. De Rossi, A. Bigot, S. Duguez, A. Wielgosik, C. Stewart, J. McPhee, M. Conte, M. Narici, C. Franceschi, V. Mouly, G. Butler-Browne, and A. Musarò, "Age-dependent alteration in muscle regeneration: The critical role of tissue niche," *Biogerontology*, vol. 14, pp. 273–292, 2013.
- [35] S. T. Cooper and P. L. McNeil, "Membrane Repair: Mechanisms and Pathophysiology," *Physiol. Rev.*, vol. 95, no. 4, pp. 1205–1240, Oct. 2015.
- [36] I. Desguerre, M. Mayer, F. Leturcq, J.-P. Barbet, R. K. Gherardi, and C. Christov, "Endomysial fibrosis in Duchenne muscular dystrophy: a marker of poor outcome associated with macrophage alternative activation.," *J. Neuropathol. Exp. Neurol.*, vol. 68, no. 7, pp. 762–773, 2009.
- [37] C. J. Mann, E. Perdiguero, Y. Kharraz, S. Aguilar, P. Pessina, A. L. Serrano, and P. Muñoz-Cánoves, "Aberrant repair and fibrosis development in skeletal muscle.," *Skelet. Muscle*, vol. 1, no. 1, p. 21, Jan. 2011.
- [38] F. Lehmann-horn and K. Jurkat-rott, "Voltage-Gated Ion Channels and Hereditary Disease," *Physiol. Rev.*, vol. 79, no. 4, pp. 1317–1373, 1999.
- [39] R. Mantegazza and P. Bernasconi, "Inflammatory Myopathies: Dermatomyositis, Polymyositis and Inclusion Body Myositis," in *Madame Curie Bioscience Database*, Austin: Landes Bioscience, 2000.
- [40] I. Dalkilic and L. M. Kunkel, "Muscular dystrophies: genes to pathogenesis," *Curr. Opin. Genet. Dev.*, vol. 13, no. 3, pp. 231–238, Jun. 2003.
- [41] W. Klingler, K. Jurkat-rott, F. Lehmann-horn, and R. Schleip, "The role of fibrosis in Duchenne muscular dystrophy," *Acta Myol.*, vol. 31, pp. 184–195, 2012.
- [42] J. Liu, M. Aoki, I. Illa, C. Wu, M. Fardeau, C. Angelini, C. Serrano, J. A. Urtizberea, F. Hentati, M. Ben Hamida, S. Bohlega, E. J. Culper, A. A. Amato, K. Bossie, J. Oeltjen, K. Bejaoui, D. McKenna-Yasek, B. A. Hosler, E. Schurr, K. Arahata, P. J. de Jong, and R. H. Brown, "Dysferlin, a novel skeletal muscle gene, is mutated in Miyoshi myopathy and limb girdle muscular dystrophy," *Nat. Genet.*, vol. 20, no. 1, pp. 31–36, Sep. 1998.
- [43] R. Bashir, S. Britton, T. Strachan, S. Keers, E. Vafiadaki, M. Lako, I. Richard, S. Marchand, N.

- Bourg, Z. Argov, M. Sadeh, I. Mahjneh, G. Marconi, M. R. Passos-Bueno, E. de S. Moreira, M. Zatz, J. S. Beckmann, and K. Bushby, "A gene related to *Caenorhabditis elegans* spermatogenesis factor *fer-1* is mutated in limb-girdle muscular dystrophy type 2B," *Nat. Genet.*, vol. 20, no. 1, pp. 37–42, Sep. 1998.
- [44] M. Fanin and C. Angelini, "Progress and challenges in diagnosis of dysferlinopathy," *Muscle Nerve*, vol. 54, no. 5, pp. 821–835, Nov. 2016.
- [45] A. M. Cárdenas, A. M. González-Jamett, L. A. Cea, J. A. Bevilacqua, and P. Caviedes, "Dysferlin function in skeletal muscle: Possible pathological mechanisms and therapeutical targets in dysferlinopathies," *Exp. Neurol.*, vol. 283, pp. 246–254, Sep. 2016.
- [46] S. T. Cooper and S. I. Head, "Membrane Injury and Repair in the Muscular Dystrophies," *Neurosci.*, pp. 1–16, 2014.
- [47] D. Bansal, K. Miyake, S. S. Vogel, S. Groh, C.-C. Chen, R. Williamson, P. L. McNeil, and K. P. Campbell, "Defective membrane repair in dysferlin-deficient muscular dystrophy.," *Nature*, vol. 423, no. 6936, pp. 168–72, May 2003.
- [48] J. P. Kerr, A. P. Ziman, A. L. Mueller, J. M. Muriel, E. Kleinhans-Welte, J. D. Gumerson, S. S. Vogel, C. W. Ward, J. a Roche, and R. J. Bloch, "Dysferlin stabilizes stress-induced Ca²⁺ signaling in the transverse tubule membrane," *Proc. Natl. Acad. Sci. U. S. A.*, vol. 110, no. 51, pp. 20831–20836, 2013.
- [49] R. Han and K. P. Campbell, "Dysferlin and muscle membrane repair," *Curr. Opin. Cell Biol.*, vol. 19, no. 4, pp. 409–416, 2007.
- [50] M. D. Grounds, J. R. Terrill, H. G. Radley-Crabb, T. Robertson, J. Papadimitriou, S. Spuler, and T. Shavlakadze, "Lipid accumulation in dysferlin-deficient muscles," *Am. J. Pathol.*, vol. 184, no. 6, pp. 1668–1676, 2014.
- [51] A. Kumar, N. Khandelwal, R. Malya, M. B. Reid, and A. M. Boriek, "Loss of dystrophin causes aberrant mechanotransduction in skeletal muscle fibers.," *FASEB J.*, vol. 18, pp. 102–113, 2004.
- [52] M. M. Ghahramani Seno, C. Trollet, T. Athanasopoulos, I. R. Graham, P. Hu, and G. Dickson, "Transcriptomic analysis of dystrophin RNAi knockdown reveals a central role for dystrophin in muscle differentiation and contractile apparatus organization.," *BMC Genomics*, vol. 11, p. 345, 2010.
- [53] B. H. Wokke, M. T. Hooijmans, J. C. van den Bergen, a G. Webb, J. J. Verschuuren, and H. E. Kan, "Muscle MRS detects elevated PDE/ATP ratios prior to fatty infiltration in Becker muscular dystrophy," *NMR Biomed.*, vol. 27, no. 11, pp. 1371–1377, Nov. 2014.
- [54] R. J. Fairclough, M. J. Wood, and K. E. Davies, "Therapy for Duchenne muscular dystrophy: renewed optimism from genetic approaches," *Nat. Rev. Genet.*, vol. 14, no. 6, pp. 373–378, Jun. 2013.
- [55] A. R. Burr, D. P. Millay, S. A. Goonasekera, K. H. Park, M. A. Sargent, J. Collins, F. Altamirano, K. D. Philipson, P. D. Allen, J. Ma, J. R. Lopez, and J. D. Molkenin, "Na⁺ Dysregulation Coupled with Ca²⁺ Entry through NCX1 Promotes Muscular Dystrophy in Mice," *Mol. Cell. Biol.*, vol. 34, no. 11, pp. 1991–2002, Jun. 2014.

-
- [56] D. G. Allen and N. P. Whitehead, "Duchenne muscular dystrophy – What causes the increased membrane permeability in skeletal muscle?," *Int. J. Biochem. Cell Biol.*, vol. 43, no. 3, pp. 290–294, Mar. 2011.
- [57] A. Vontzalidis, G. Terzis, and P. Manta, "Increased dysferlin expression in Duchenne muscular dystrophy," *Anal. Quant. Cytopathol. Histopathol.*, vol. 36, no. 1, pp. 15–22, Feb. 2014.
- [58] P. R. Turner, T. Westwood, C. M. Regen, and R. A. Steinhardt, "Increased protein degradation results from elevated free calcium levels found in muscle from mdx mice," *Nature*, vol. 335, no. 6192, pp. 735–8, 1988.
- [59] J. F. Dunn, K. a Burton, and M. J. Dauncey, "Ouabain sensitive Na⁺/K⁽⁺⁾-ATPase content is elevated in mdx mice: implications for the regulation of ions in dystrophic muscle.," *J. Neurol. Sci.*, vol. 133, pp. 11–15, 1995.
- [60] M.-A. Weber, A. M. Nagel, M. B. Wolf, K. Jurkat-Rott, H.-U. Kauczor, W. Semmler, and F. Lehmann-Horn, "Permanent muscular sodium overload and persistent muscle edema in Duchenne muscular dystrophy: a possible contributor of progressive muscle degeneration," *J. Neurol.*, vol. 259, no. 11, pp. 2385–2392, Nov. 2012.
- [61] C. Hirn, G. Shapovalov, O. Petermann, E. Roulet, and U. T. Rugg, "Nav1.4 deregulation in dystrophic skeletal muscle leads to Na⁺ overload and enhanced cell death.," *J. Gen. Physiol.*, vol. 132, pp. 199–208, 2008.
- [62] E. Deval, D. O. Levitsky, E. Marchand, A. Cantereau, G. Raymond, and C. Cognard, "Na⁺/Ca²⁺ exchange in human myotubes: Intracellular calcium rises in response to external sodium depletion are enhanced in DMD," *Neuromuscul. Disord.*, vol. 12, pp. 665–673, 2002.
- [63] Y. Iwata, Y. Katanosaka, T. Hisamitsu, and S. Wakabayashi, "Enhanced Na⁺/H⁺ exchange activity contributes to the pathogenesis of muscular dystrophy via involvement of P2 receptors.," *Am. J. Pathol.*, vol. 171, no. 5, pp. 1576–1587, 2007.
- [64] R. A. De Graaf, *In Vivo NMR Spectroscopy*, 2nd ed. West Sussex: John Wiley & Sons, Ltd., 2007.
- [65] M. H. Levitt, *Spin Dynamics: Basics of Nuclear Magnetic Resonance*, 2nd ed. West Sussex: John Wiley & Sons, Ltd., 2008.
- [66] P. A. Bottomley, "Selective volume method for performing localized NMR spectroscopy," *US Pat.*, vol. US 4480228, 1984.
- [67] R. . Ordidge, A. Connelly, and J. A. . Lohman, "Image-selected in Vivo spectroscopy (ISIS). A new technique for spatially selective nmr spectroscopy," *J. Magn. Reson.*, vol. 66, no. 2, pp. 283–294, Feb. 1986.
- [68] W. D. Rooney and C. S. Springer, "The molecular environment of intracellular sodium: ²³Na NMR relaxation.," *NMR Biomed.*, vol. 4, pp. 227–245, 1991.
- [69] W. D. Rooney and C. S. Springer Jr, "A Comprehensive Approach to the Analysis and Interpretation of the Resonances of Spins 3 / 2 from-Living Systems," *NMR Biomed.*, vol. 4, no. March, pp. 209–226, 1991.
- [70] G. Madelin, J.-S. Lee, R. R. Regatte, and A. Jerschow, "Sodium MRI: Methods and applications," *Prog. Nucl. Magn. Reson. Spectrosc.*, vol. 79, pp. 14–47, May 2014.

- [71] J. S. Tauskela, J. M. Dizon, J. Whang, and J. Katz, "Evaluation of multiple-quantum-filtered ^{23}Na NMR in monitoring intracellular Na content in the isolated perfused rat heart in the absence of a chemical-shift reagent.," *J. Magn. Reson.*, vol. 127, pp. 115–127, 1997.
- [72] N. Bansal, L. Szczepaniak, D. Ternullo, J. L. Fleckenstein, and C. R. Malloy, "Effect of exercise on (^{23}Na) MRI and relaxation characteristics of the human calf muscle.," *J. Magn. Reson. Imaging*, vol. 11, no. 5, pp. 532–538, May 2000.
- [73] F. E. Boada, J. D. Christensen, F. R. Huang-Hellinger, T. G. Reese, and K. R. Thulborn, "Quantitative in vivo tissue sodium concentration maps: The effects of biexponential relaxation," *Magn. Reson. Med.*, vol. 32, pp. 219–223, 1994.
- [74] M. M. Pike, S. R. Simon, J. a Balschi, and C. S. Springer, "High-resolution NMR studies of transmembrane cation transport: use of an aqueous shift reagent for ^{23}Na ," *Proc. Natl. Acad. Sci.*, vol. 79, no. 3, pp. 810–814, Feb. 1982.
- [75] R. K. Gupta, P. Gupte, and R. D. Moore, "NMR Studies of Intracellular Metal Ions in Intact Cells and Tissues," *Ann. Revi. Biophys. Bioeng.*, vol. 13, pp. 221–246, 1984.
- [76] M. M. Pike, J. C. Frazer, D. F. Dedrick, J. S. Ingwall, P. D. Allen, C. S. Springer, and T. W. Smith, " ^{23}Na and ^{39}K nuclear magnetic resonance studies of perfused rat hearts. Discrimination of intra- and extracellular ions using a shift reagent," *Biophys. J.*, vol. 48, no. 1, pp. 159–173, Jul. 1985.
- [77] H. Naritomi, M. Kanashiro, M. Sasaki, Y. Kuribayashi, and T. Sawada, "In vivo measurements of intra- and extracellular Na^+ and water in the brain and muscle by nuclear magnetic resonance spectroscopy with shift reagent.," *Biophys. J.*, vol. 52, no. 4, pp. 611–616, 1987.
- [78] H. Blum, M. D. Schnall, B. Chance, and G. P. Buzby, "Intracellular sodium flux and high-energy phosphorus metabolites in ischemic skeletal muscle.," *Am. J. Physiol.*, vol. 255, no. 3 Pt 1, pp. C377–84, Sep. 1988.
- [79] J. D. Makos, C. R. Malloy, and A. D. Sherry, "Distribution of TmDOTP5- in rat tissues: TmDOTP5- vs. CoEDTA- as markers of extracellular tissue space.," *J. Appl. Physiol.*, vol. 85, no. 5, pp. 1800–1805, Nov. 1998.
- [80] P. M. Winter, V. Seshan, J. D. Makos, a D. Sherry, C. R. Malloy, and N. Bansal, "Quantitation of intracellular $[\text{Na}^+]$ in vivo by using TmDOTP5- as an NMR shift reagent and extracellular marker.," *J. Appl. Physiol.*, vol. 85, no. 5, pp. 1806–1812, 1998.
- [81] P. M. Winter and N. Bansal, "TmDOTP(5-) as a (^{23}Na) shift reagent for the subcutaneously implanted 9L gliosarcoma in rats.," *Magn. Reson. Med.*, vol. 45, no. 3, pp. 436–442, 2001.
- [82] N. Bansal, M. J. Germann, I. Lazar, C. R. Malloy, and a D. Sherry, "In vivo Na- 23 MR imaging and spectroscopy of rat brain during TmDOTP5- infusion.," *J. Magn. Reson. Imaging*, vol. 2, pp. 385–391, 1992.
- [83] A. M. Nagel, E. Amarteifio, F. Lehmann-horn, and K. Jurkat-rott, "3 Tesla Sodium Inversion Recovery Magnetic Resonance Imaging Allows for Improved Visualization of Intracellular Sodium Content Changes in Muscular Channelopathies," *Invest. Radiol.*, vol. 46, no. 12, pp. 759–766, 2011.
- [84] G. Jaccard, S. Wimperis, and G. Bodenhausen, "Multiple-quantum NMR spectroscopy of $S=3/2$

-
- spins in isotropic phase: A new probe for multiexponential relaxation," *J. Chem. Phys.*, vol. 85, no. 11, p. 6282, 1986.
- [85] J. Pekar and J. S. Leigh, "Detection of biexponential relaxation in sodium-23 facilitated by double-quantum filtering," *J. Magn. Reson.*, vol. 69, no. 3, pp. 582–584, Oct. 1986.
- [86] G. Navon, "Complete elimination of the extracellular ^{23}Na NMR signal in triple quantum filtered spectra of rat hearts in the presence of shift reagents," *Magn. Reson. Med.*, vol. 30, pp. 503–506, 1993.
- [87] C. Tanase and F. E. Boada, "Triple-quantum-filtered imaging of sodium in presence of B(0) inhomogeneities," *J. Magn. Reson.*, vol. 174, no. 2, pp. 270–8, Jun. 2005.
- [88] G. Navon, H. Shinar, U. Eliav, and Y. Seo, "Multiquantum filters and order in tissues," *NMR Biomed.*, vol. 14, no. 2, pp. 112–132, Apr. 2001.
- [89] R. Reddy, M. Shinnar, Z. Wang, and J. S. Leigh, "Multiple-quantum filters of spin-3/2 with pulses of arbitrary flip angle," *J. Magn. Reson. B*, vol. 104, no. 2, pp. 148–52, Jun. 1994.
- [90] N. Müller, G. Bodenhausen, and R. R. Ernst, "Relaxation-induced violations of coherence transfer selection rules in nuclear magnetic resonance," *J. Magn. Reson.*, vol. 75, no. 2, pp. 297–334, 1987.
- [91] R. Reddy, L. Bolinger, M. Shinnar, E. Noyszewski, and J. S. Leigh, "Detection of Residual Quadrupolar Interaction in Human Skeletal Muscle and Brain in vivo via Multiple Quantum Filtered Sodium NMR Spectra," *Magn. Reson. Med.*, vol. 33, no. 1, pp. 134–139, Jan. 1995.
- [92] J. R. C. van der Maarel, "Thermal relaxation and coherence dynamics of spin 3/2. I. Static and fluctuating quadrupolar interactions in the multipole basis," *Concepts Magn. Reson.*, vol. 19A, no. 2, pp. 97–116, 2003.
- [93] S. Wimperis, P. Cole, and P. Styles, "Triple-quantum-filtration NMR imaging of 200 mM sodium at 1.9 Tesla," *J. Magn. Reson.*, vol. 98, no. 3, pp. 628–636, Jul. 1992.
- [94] G. Bodenhausen, H. Kogler, and R. R. Ernst, "Selection of coherence transfer pathways in NMR experiments," *J. Magn. Reson.*, vol. 58, pp. 370–388, 1984.
- [95] U. Eliav, H. Shinar, and G. Navon, "The formation of a second-rank tensor in ^{23}Na double-quantum-filtered NMR as an indicator for order in a biological tissue," *J. Magn. Reson.*, vol. 98, no. 1, pp. 223–229, Jun. 1992.
- [96] R. Stobbe and C. Beaulieu, "In vivo sodium magnetic resonance imaging of the human brain using soft inversion recovery fluid attenuation," *Magn. Reson. Med.*, vol. 54, pp. 1305–1310, 2005.
- [97] R. Griffey, B. Griffey, and N. Matwiyoff, "Triple-Quantum-Coherence-Filtered Imaging of Sodium Ions in Vivo at 4.7 Tesla," *Magn. Reson. Med.*, vol. 13, pp. 305–313, 1990.
- [98] Y. Gao, J. James, and N. Bansal, "Noninvasive Monitoring of CCl₄ Induced Acute and Chronic Liver Damage in Rat by SQ and TQF ^{23}Na MRI," in *ISMRM*, 2009, vol. 17, p. 614.
- [99] K. J. Ooms, M. Cannella, A. J. Vega, M. Marcolongo, and T. Polenova, " ^{23}Na TQF NMR imaging for the study of spinal disc tissue," *J. Magn. Reson.*, vol. 195, no. 1, pp. 112–5, Nov. 2008.
- [100] A. M. Babsky, S. Ju, S. Bennett, B. George, G. McLennan, and N. Bansal, "Effect of

- implantation site and growth of hepatocellular carcinoma on apparent diffusion coefficient of water and sodium MRI.," *NMR Biomed.*, vol. 25, no. 2, pp. 312–21, Feb. 2012.
- [101] A. Borthakur, E. Mellon, S. Niyogi, W. Witschey, J. B. Kneeland, and R. Reddy, "Sodium and T1rho MRI for molecular and diagnostic imaging of articular cartilage.," *NMR Biomed.*, vol. 19, no. 7, pp. 781–821, Nov. 2006.
- [102] C. Tanase and F. E. Boada, "Algebraic description of spin 3/2 dynamics in NMR experiments.," *J. Magn. Reson.*, vol. 173, no. 2, pp. 236–53, Apr. 2005.
- [103] A. Tsang, R. W. Stobbe, and C. Beaulieu, "Evaluation of B0-inhomogeneity correction for triple-quantum-filtered sodium MRI of the human brain at 4.7 T.," *J. Magn. Reson.*, vol. 230, pp. 134–44, May 2013.
- [104] N. Benkhedah, P. Bachert, W. Semmler, and A. M. Nagel, "Three-dimensional biexponential weighted 23 Na imaging of the human brain with higher SNR and shorter acquisition time," *Magn. Reson. Med.*, vol. 70, no. 3, pp. 754–765, Sep. 2013.
- [105] L. Fleysler, N. Oesingmann, and M. Inglese, "B0 inhomogeneity-insensitive triple-quantum-filtered sodium imaging using a 12-step phase-cycling scheme.," *NMR Biomed.*, vol. 23, no. 10, pp. 1191–1198, Dec. 2010.
- [106] N. Benkhedah, P. Bachert, and A. M. Nagel, "Two-pulse biexponential-weighted 23Na imaging.," *J. Magn. Reson.*, vol. 240, pp. 67–76, Mar. 2014.
- [107] D. P. Fiege, S. Romanzetti, C. C. Mirkes, D. Brenner, and N. J. Shah, "Simultaneous single-quantum and triple-quantum-filtered MRI of 23Na (SISTINA).," *Magn. Reson. Med.*, vol. 69, no. 6, pp. 1691–6, Jun. 2013.
- [108] V. Seshan, A. D. Sherry, and N. Bansal, "Evaluation of triple quantum-filtered 23Na NMR spectroscopy in the in situ rat liver," *Magn. Reson. Med.*, vol. 38, no. 5, pp. 821–827, Nov. 1997.
- [109] V. D. Schepkin, I. O. Choy, T. F. Budinger, D. Y. Obayashi, S. E. Taylor, W. M. DeCampi, S. C. Amatur, and J. N. Young, "Sodium TQF NMR and intracellular sodium in isolated crystalloid perfused rat heart.," *Magn. Reson. Med.*, vol. 39, no. 4, pp. 557–563, Apr. 1998.
- [110] T. R. Eykyn, D. Aksentijević, K. L. Aughton, R. Southworth, W. Fuller, and M. J. Shattock, "Multiple quantum filtered 23Na NMR in the Langendorff perfused mouse heart: Ratio of triple/double quantum filtered signals correlates with [Na]i," *J. Mol. Cell. Cardiol.*, vol. 86, pp. 95–101, Sep. 2015.
- [111] L. A. Jelicks and R. K. Gupta, "On the extracellular contribution to multiple quantum filtered 23Na NMR of perfused rat heart.," *Magn. Reson. Med.*, vol. 29, no. 1, pp. 130–3, Jan. 1993.
- [112] L. A. Jelicks and R. K. Gupta, "Double-quantum NMR of sodium ions in cells and tissues. Paramagnetic quenching of extracellular coherence," *J. Magn. Reson.*, vol. 81, no. 3, pp. 586–592, Feb. 1989.
- [113] W. a Murphy, W. G. Totty, and J. E. Carroll, "MRI of normal and pathological skeletal muscle," *Am. J. Radiol.*, vol. 146, pp. 565–574, 1986.
- [114] V. Ricotti, M. R. B. Evans, C. D. J. Sinclair, J. W. Butler, D. A. Ridout, J.-Y. Hogrel, A. Emira, J. M. Morrow, M. M. Reilly, M. G. Hanna, R. L. Janiczek, P. M. Matthews, T. A. Yousry, F.

-
- Muntoni, and J. S. Thornton, "Upper Limb Evaluation in Duchenne Muscular Dystrophy: Fat-Water Quantification by MRI, Muscle Force and Function Define Endpoints for Clinical Trials," *PLoS One*, vol. 11, no. 9, p. e0162542, Sep. 2016.
- [115] S. C. Forbes, R. J. Willcocks, W. T. Triplett, W. D. Rooney, D. J. Lott, D.-J. Wang, J. Pollaro, C. R. Senesac, M. J. Daniels, R. S. Finkel, B. S. Russman, B. J. Byrne, E. L. Finanger, G. I. Tennekoon, G. a. Walter, H. L. Sweeney, and K. Vandenborne, "Magnetic Resonance Imaging and Spectroscopy Assessment of Lower Extremity Skeletal Muscles in Boys with Duchenne Muscular Dystrophy: A Multicenter Cross Sectional Study," *PLoS One*, vol. 9, no. 9, p. e106435, 2014.
- [116] D. J. Lott, S. C. Forbes, S. Mathur, S. A. Germain, C. R. Senesac, H. Lee Sweeney, G. A. Walter, and K. Vandenborne, "Assessment of intramuscular lipid and metabolites of the lower leg using magnetic resonance spectroscopy in boys with Duchenne muscular dystrophy," *Neuromuscul. Disord.*, vol. 24, pp. 574–582, 2014.
- [117] W. T. Triplett, C. Baligand, S. C. Forbes, R. J. Willcocks, D. J. Lott, S. DeVos, J. Pollaro, W. D. Rooney, H. L. Sweeney, C. G. Bönnemann, D.-J. Wang, K. Vandenborne, and G. A. Walter, "Chemical shift-based MRI to measure fat fractions in dystrophic skeletal muscle," *Magn. Reson. Med.*, vol. 72, no. 1, pp. 8–19, Jul. 2014.
- [118] A. Mankodi, C. A. Bishop, S. Auh, R. D. Newbould, K. H. Fischbeck, and R. L. Janiczek, "Quantifying disease activity in fatty-infiltrated skeletal muscle by IDEAL-CPMG in Duchenne muscular dystrophy," *Neuromuscul. Disord.*, vol. 26, no. 10, pp. 650–658, Oct. 2016.
- [119] J. Burakiewicz, C. D. J. Sinclair, D. Fischer, G. A. Walter, H. E. Kan, and K. G. Hollingsworth, "Quantifying fat replacement of muscle by quantitative MRI in muscular dystrophy," *J. Neurol.*, vol. 264, no. 10, pp. 2053–2067, Oct. 2017.
- [120] B. H. Wokke, C. Bos, M. Reijnierse, C. S. van Rijswijk, H. Eggers, A. Webb, J. J. Verschuuren, and H. E. Kan, "Comparison of dixon and T1-weighted MR methods to assess the degree of fat infiltration in duchenne muscular dystrophy patients," *J. Magn. Reson. Imaging*, vol. 38, no. 3, pp. 619–624, Sep. 2013.
- [121] C. Wary, N. Azzabou, C. Giraudeau, J. Le Louër, M. Montus, T. Voit, L. Servais, and P. Carlier, "Quantitative NMRI and NMRS identify augmented disease progression after loss of ambulation in forearms of boys with Duchenne muscular dystrophy," *NMR Biomed.*, vol. 28, no. 9, 2015.
- [122] J.-Y. Hogrel, Y. Barnouin, N. Azzabou, G. Butler-Browne, T. Voit, A. Moraux, G. Leroux, A. Behin, J. S. McPhee, and P. G. Carlier, "NMR imaging estimates of muscle volume and intramuscular fat infiltration in the thigh: variations with muscle, gender, and age," *Age (Omaha)*, vol. 37, no. 60, pp. 1–11, Jun. 2015.
- [123] A. Fischmann, P. Hafner, M. Gloor, M. Schmid, A. Klein, U. Pohlman, T. Waltz, R. Gonzalez, T. Haas, O. Bieri, and D. Fischer, "Quantitative MRI and loss of free ambulation in Duchenne muscular dystrophy.," *J. Neurol.*, vol. 260, no. 4, pp. 969–74, Apr. 2013.
- [124] M. Torriani, E. Townsend, B. J. Thomas, M. A. Bredella, R. H. Ghomi, and B. S. Tseng, "Lower leg muscle involvement in Duchenne muscular dystrophy: an MR imaging and spectroscopy

- study," *Skeletal Radiol.*, vol. 41, no. 4, pp. 437–445, Apr. 2012.
- [125] J.-Y. Hogrel, C. Wary, A. Moraux, N. Azzabou, V. Decostre, G. Ollivier, A. Canal, C. Lilien, I. Ledoux, M. Annoussamy, N. Reguiba, T. Gidaro, A. G. Le Moing, R. Cardas, T. Voit, P. G. Carlier, and L. Servais, "Longitudinal functional and NMR assessment of upper limbs in Duchenne muscular dystrophy," *Neurology*, vol. 86, pp. 1022–1030, Mar. 2016.
- [126] R. J. Willcocks, W. D. Rooney, W. T. Triplett, S. C. Forbes, D. J. Lott, C. R. Senesac, M. J. Daniels, D.-J. Wang, A. T. Harrington, G. I. Tennekoon, B. S. Russman, E. L. Finanger, B. J. Byrne, R. S. Finkel, G. A. Walter, H. L. Sweeney, and K. Vandeborne, "Multicenter prospective longitudinal study of magnetic resonance biomarkers in a large duchenne muscular dystrophy cohort," *Ann. Neurol.*, vol. 79, no. 4, pp. 535–547, Apr. 2016.
- [127] I. Arpan, S. C. Forbes, D. J. Lott, C. R. Senesac, M. J. Daniels, W. T. Triplett, J. K. Deol, H. L. Sweeney, G. A. Walter, and K. Vandeborne, "T2 mapping provides multiple approaches for the characterization of muscle involvement in neuromuscular diseases: a cross-sectional study of lower leg muscles in 5-15-year-old boys with Duchenne muscular dystrophy," *NMR Biomed.*, vol. 26, no. 3, pp. 320–328, Mar. 2013.
- [128] Y. Huang, S. Majumdar, H. K. Genant, W. P. Chan, K. R. Sharma, P. Yu, M. Mynhier, and R. G. Miller, "Quantitative MR relaxometry study of muscle composition and function in duchenne muscular dystrophy," *J. Magn. Reson. Imaging*, vol. 4, no. 1, pp. 59–64, Jan. 1994.
- [129] H. K. Kim, T. Laor, P. S. Horn, J. M. Racadio, B. Wong, and B. J. Dardzinski, "T2 Mapping in Duchenne Muscular Dystrophy: Distribution of Disease Activity and Correlation with Clinical Assessments," *Radiology*, vol. 255, no. 3, pp. 899–908, Jun. 2010.
- [130] R. J. Willcocks, W. T. Triplett, S. C. Forbes, H. Arora, C. R. Senesac, D. J. Lott, T. R. Nicholson, W. D. Rooney, G. A. Walter, and K. Vandeborne, "Magnetic resonance imaging of the proximal upper extremity musculature in boys with Duchenne muscular dystrophy," *J. Neurol.*, vol. 264, no. 1, pp. 64–71, Jan. 2017.
- [131] P. G. Carlier, "Global T2 versus water T2 in NMR imaging of fatty infiltrated muscles: Different methodology, different information and different implications," *Neuromuscul. Disord.*, vol. 24, no. 5, pp. 390–392, May 2014.
- [132] R. M. Lebel and A. H. Wilman, "Transverse relaxometry with stimulated echo compensation.," *Magn. Reson. Med.*, vol. 64, no. 4, pp. 1005–14, Oct. 2010.
- [133] B. H. Wokke, J. C. Van Den Bergen, M. T. Hooijmans, J. J. Verschuuren, E. H. Niks, and H. E. Kan, "T2 relaxation times are increased in Skeletal muscle of DMD but not BMD patients," *Muscle Nerve*, vol. 53, no. 1, pp. 38–43, Jan. 2016.
- [134] T.-J. Hsieh, T.-S. Jaw, H.-Y. Chuang, Y.-J. Jong, G.-C. Liu, and C.-W. Li, "Muscle Metabolism in Duchenne Muscular Dystrophy Assessed by In Vivo Proton Magnetic Resonance Spectroscopy," *J. Comput. Assist. Tomogr.*, vol. 33, no. 1, pp. 150–154, Jan. 2009.
- [135] M. T. Hooijmans, E. H. Niks, J. Burakiewicz, J. J. G. M. Verschuuren, A. G. Webb, and H. E. Kan, "Elevated phosphodiester and T2 levels can be measured in the absence of fat infiltration in Duchenne muscular dystrophy patients," *NMR Biomed.*, vol. 30, no. 1, p. e3667, Jan. 2017.
- [136] B. Barbiroli, R. Funicello, A. Ferlini, P. Montagna, and P. Zaniol, "Muscle energy metabolism in

-
- female DMD/BMD carriers: A31P-MR spectroscopy study," *Muscle Nerve*, vol. 15, no. 3, pp. 344–348, Mar. 1992.
- [137] H. Reyngoudt, S. Turk, and P. G. Carlier, "1 H NMRS of carnosine combined with 31 P NMRS to better characterize skeletal muscle pH dysregulation in Duchenne muscular dystrophy," *NMR Biomed.*, vol. 31, no. 1, p. e3839, Jan. 2018.
- [138] T. a. Willis, K. G. Hollingsworth, A. Coombs, M.-L. Sveen, S. Andersen, T. Stojkovic, M. Eagle, A. Mayhew, P. L. de Sousa, L. Dewar, J. M. Morrow, C. D. J. Sinclair, J. S. Thornton, K. Bushby, H. Lochmüller, M. G. Hanna, J.-Y. Hogrel, P. G. Carlier, J. Vissing, and V. Straub, "Quantitative muscle MRI as an assessment tool for monitoring disease progression in LGMD2I: a multicentre longitudinal study," *PLoS One*, vol. 8, no. 8, p. e70993, 2013.
- [139] T. a Willis, K. G. Hollingsworth, A. Coombs, M.-L. Sveen, S. Andersen, T. Stojkovic, M. Eagle, A. Mayhew, P. L. de Sousa, L. Dewar, J. M. Morrow, C. D. J. Sinclair, J. S. Thornton, K. Bushby, H. Lochmüller, M. G. Hanna, J.-Y. Hogrel, P. G. Carlier, J. Vissing, and V. Straub, "Quantitative Magnetic Resonance Imaging in Limb-Girdle Muscular Dystrophy 2I: A Multinational Cross-Sectional Study," *PLoS One*, vol. 9, no. 2, p. e90377, Feb. 2014.
- [140] B. Janssen, N. Voet, A. Geurts, B. van Engelen, and A. Heerschap, "Quantitative MRI reveals decelerated fatty infiltration in muscles of active FSHD patients," *Neurology*, vol. 86, no. 18, pp. 1700–1707, May 2016.
- [141] H. E. Kan, D. W. J. Klomp, M. Wohlgemuth, I. van Loosbroek-Wagemans, B. G. M. van Engelen, G. W. Padberg, and A. Heerschap, "Only fat infiltrated muscles in resting lower leg of FSHD patients show disturbed energy metabolism.," *NMR Biomed.*, vol. 23, no. 6, pp. 563–8, Jul. 2010.
- [142] S. Gerevini, M. Scarlato, L. Maggi, M. Cava, G. Caliendo, B. Pasanisi, A. Falini, S. C. Previtali, and L. Morandi, "Muscle MRI findings in facioscapulohumeral muscular dystrophy," *Eur. Radiol.*, vol. 26, no. 3, pp. 693–705, Mar. 2016.
- [143] C. D. Constantinides, J. S. Gillen, F. E. Boada, M. G. Pomper, and P. A. Bottomley, "Human skeletal muscle: sodium MR imaging and quantification-potential applications in exercise and disease.," *Radiology*, vol. 216, no. 2, pp. 559–68, Aug. 2000.
- [144] T. Kushnir, T. Knubovets, Y. Itzchak, U. Eliav, M. Sadeh, L. Rapoport, E. Kott, and G. Navon, "In Vivo ²³Na NMR Studies of Myotonic Dystrophy," *Magn. Reson. Med.*, vol. 37, pp. 192–196, 1997.
- [145] P. A. Glemser, H. Jaeger, A. M. Nagel, A. E. Ziegler, D. Simons, H. Schlemmer, F. Lehmann-Horn, K. Jurkat-Rott, and M. Weber, "²³Na MRI and myometry to compare eplerenone vs. glucocorticoid treatment in Duchenne dystrophy.," *Acta Myol.*, vol. 36, no. 1, pp. 2–13, 2017.
- [146] F. Lehmann-Horn, M.-A. Weber, A. M. Nagel, H.-M. Meinck, S. Breitenbach, J. Scharrer, and K. Jurkat-Rott, "Rationale for treating oedema in Duchenne muscular dystrophy with eplerenone.," *Acta Myol.*, vol. 31, no. 1, pp. 31–9, May 2012.
- [147] G. Chang, L. Wang, M. E. Schweitzer, and R. R. Regatte, "3D ²³Na MRI of human skeletal muscle at 7 Tesla: initial experience.," *Eur. Radiol.*, vol. 20, no. 8, pp. 2039–46, Aug. 2010.
- [148] P. W. de Bruin, P. Koken, M. J. Versluis, S. A. Aussenhofer, I. Meulenbelt, P. Börnert, and A.

- G. Webb, "Time-efficient interleaved human ^{23}Na and ^1H data acquisition at 7 T," *NMR Biomed.*, vol. 28, no. 10, pp. 1228–1235, Oct. 2015.
- [149] W. T. Dixon, "Simple proton spectroscopic imaging.," *Radiology*, vol. 153, no. 1, pp. 189–194, Oct. 1984.
- [150] F. Schick, B. Eismann, W.-I. Jung, H. Bongers, M. Bunse, and O. Lutz, "Comparison of localized proton NMR signals of skeletal muscle and fat tissue in vivo: Two lipid compartments in muscle tissue," *Magn. Reson. Med.*, vol. 29, no. 2, pp. 158–167, Feb. 1993.
- [151] G. H. Glover and E. Schneider, "Three-point Dixon technique for true water/fat decomposition with B_0 inhomogeneity correction.," *Magn. Reson. Med.*, vol. 18, no. 2, pp. 371–83, 1991.
- [152] D. C. Look and D. R. Locker, "Time saving in measurement of NMR and EPR relaxation times," *Rev. Sci. Instrum.*, vol. 41, no. 1970, pp. 250–251, 1970.
- [153] G. Saab, R. T. Thompson, and G. D. Marsh, "Multicomponent T_2 Relaxation of In Vivo Skeletal Muscle," *Magn. Reson. Med.*, vol. 157, no. 1999, pp. 150–157, 2000.
- [154] G. Saab, R. T. Thompson, and G. D. Marsh, "Effects of exercise on muscle transverse relaxation determined by MR imaging and in vivo relaxometry," *J Appl Physiol*, vol. 88, no. 1, pp. 226–233, 2000.
- [155] E. A. Louie, D. F. Gochberg, M. D. Does, and B. M. Damon, "Transverse relaxation and magnetization transfer in skeletal muscle: Effect of pH," *Magn. Reson. Med.*, vol. 61, no. 3, pp. 560–569, Mar. 2009.
- [156] C. F. Hazlewood, D. C. Chang, B. L. Nichols, and D. E. Woessner, "Nuclear Magnetic Resonance Transverse Relaxation Times of Water Protons in Skeletal Muscle," *Biophys. J.*, vol. 14, no. 3, pp. 583–606, 1974.
- [157] P. S. Belton, R. R. Jackson, and K. J. Packer, "Pulsed NMR Studies in striated muscle. Transverse nuclear spin relaxation times and freezing effects," *Biochim. Biophys. Acta (BBA)-General Subj.*, vol. 286, pp. 16–25, 1972.
- [158] B. M. Fung and P. S. Puon, "Nuclear magnetic resonance transverse relaxation in muscle water.," *Biophys. J.*, vol. 33, no. January, pp. 27–37, 1981.
- [159] R. B. Moon and J. H. Richards, "Determination of intracellular pH by ^{31}P magnetic resonance.," *J. Biol. Chem.*, vol. 248, no. 20, pp. 7276–8, Oct. 1973.
- [160] C. Wary, T. Naulet, J.-L. Thibaud, A. Monnet, S. Blot, and P. G. Carlier, "Splitting of P_i and other ^{31}P NMR anomalies of skeletal muscle metabolites in canine muscular dystrophy," *NMR Biomed.*, vol. 25, no. 10, pp. 1160–1169, Oct. 2012.
- [161] J. Pan, J. Hamm, D. Rothman, and R. Shulman, "Intracellular pH in human skeletal muscle by ^1H NMR.," *Proc. Natl. Acad. Sci. USA*, vol. 85, no. 21, pp. 7836–7839, 1988.
- [162] G. S. Payne and P. Styles, "Multiple-quantum-filtered ^{23}Na NMR spectroscopy in model systems," *J. Magn. Reson.*, vol. 95, pp. 253–266, 1991.
- [163] J.-R. Liao, J. M. Pauly, T. J. Brosnan, and N. J. Pelc, "Reduction of motion artifacts in cine MRI using variable-density spiral trajectories," *Magn. Reson. Med.*, vol. 37, no. 4, pp. 569–575, Apr. 1997.
- [164] D. Stefan, F. Di Cesare, A. Andrasescu, E. Popa, A. Lazariev, E. Vescovo, O. Strbak, S.

-
- Williams, Z. Starcuk, M. Cabanas, D. van Ormondt, and D. Graveron-Demilly, "Quantitation of magnetic resonance spectroscopy signals: the jMRUI software package," *Meas. Sci. Technol.*, vol. 20, no. 10, p. 104035, Oct. 2009.
- [165] P. a. Yushkevich, J. Piven, H. C. Hazlett, R. G. Smith, S. Ho, J. C. Gee, and G. Gerig, "User-guided 3D active contour segmentation of anatomical structures: Significantly improved efficiency and reliability," *Neuroimage*, vol. 31, no. 3, pp. 1116–1128, 2006.
- [166] W. S. Rasband, "ImageJ," *U. S. National Institutes of Health, Bethesda, Maryland, USA*. U.S. National Institutes of Health, Bethesda, Maryland, p. <http://imagej.nih.gov/ij/>, 2017.
- [167] M. M. Pike, M. Kitakaze, and E. Marban, "23Na-NMR measurements of intracellular sodium in intact perfused ferret hearts during ischemia and reperfusion," *Am. J. Physiol. Heart Circ. Physiol.*, vol. 259, no. 6, pp. H1767-1773, 1990.
- [168] C. Brillault-Salvat, E. Giacomini, L. Jouvensal, C. Wary, G. Bloch, and P. G. Carlier, "Simultaneous determination of muscle perfusion and oxygenation by interleaved NMR plethysmography and deoxyhemoglobin spectroscopy," *NMR Biomed.*, vol. 10, no. 7, pp. 315–323, 1997.
- [169] J. M. Dizon, J. S. Tauskela, D. Wise, D. Burkhoff, P. J. Cannon, and J. Katz, "Evaluation of triple-quantum-filtered 23Na NMR in monitoring of Intracellular Na content in the perfused rat heart: comparison of intra- and extracellular transverse relaxation and spectral amplitudes," *Magn. Reson. Med.*, vol. 35, no. 3, pp. 336–45, Mar. 1996.
- [170] T. Binzoni, V. Quresima, G. Barattelli, E. Hiltbrand, L. Gürke, F. Terrier, P. Cerretelli, and M. Ferrari, "Energy metabolism and interstitial fluid displacement in human gastrocnemius during short ischemic cycles.," *J. Appl. Physiol.*, vol. 85, no. 4, pp. 1244–1251, 1998.
- [171] G. Navon, H. Shinar, U. Eliav, and Y. Seo, "Multiquantum filters and order in tissues.," *NMR Biomed.*, vol. 14, no. 2, pp. 112–132, Apr. 2001.
- [172] P. M. Winter and N. Bansal, "Triple-Quantum-Filtered 23Na NMR Spectroscopy of Subcutaneously Implanted 9L Gliosarcoma in the Rat in the Presence of TmDOTP5-," *J. Magn. Reson.*, vol. 152, no. 1, pp. 70–78, Sep. 2001.
- [173] L. L. Ploutz-Snyder, S. Nyren, T. G. Cooper, E. J. Potchen, and R. a Meyer, "Different effects of exercise and edema on T2 relaxation in skeletal muscle.," *Magn. Reson. Med.*, vol. 37, no. 5, pp. 676–82, May 1997.
- [174] G. Madelin and R. R. Regatte, "Biomedical applications of sodium MRI in vivo.," *J. Magn. Reson. Imaging*, vol. 38, no. 3, pp. 511–529, Sep. 2013.
- [175] R. W. Stobbe and C. Beaulieu, "Residual quadrupole interaction in brain and its effect on quantitative sodium imaging," *NMR Biomed.*, vol. 29, no. 2, pp. 119–128, Feb. 2016.
- [176] L. Fleysher, N. Oesingmann, R. Brown, D. K. Sodickson, G. C. Wiggins, and M. Inglese, "Noninvasive quantification of intracellular sodium in human brain using ultrahigh-field MRI," *NMR Biomed.*, vol. 26, no. January, pp. 9–19, 2013.
- [177] S. Nilles-Vallespin, M.-A. Weber, M. Bock, A. Bongers, P. Speier, S. E. Combs, J. Wöhrle, F. Lehmann-Horn, M. Essig, and L. R. Schad, "3D radial projection technique with ultrashort echo times for sodium MRI: clinical applications in human brain and skeletal muscle.," *Magn. Reson.*

- Med.*, vol. 57, no. 1, pp. 74–81, Jan. 2007.
- [178] P. A. Bottomley, "Spatial localization in NMR spectroscopy in vivo," *Ann. N. Y. Acad. Sci.*, vol. 508, pp. 333–548, Jan. 1987.
- [179] A. M. Babsky, S. Topper, H. Zhang, Y. Gao, J. R. James, S. K. Hekmatyar, and N. Bansal, "Evaluation of extra- and intracellular apparent diffusion coefficient of sodium in rat skeletal muscle: Effects of prolonged ischemia," *Magn. Reson. Med.*, vol. 59, no. 3, pp. 485–491, Mar. 2008.
- [180] M. I. Lindinger and G. J. Heigenhauser, "Intracellular ion content of skeletal muscle measured by instrumental neutron activation analysis," *J. Appl. Physiol.*, vol. 63, no. 1, pp. 426–33, Jul. 1987.
- [181] J. A. Balschi, J. A. Bittl, C. S. Springer, and J. S. Ingwall, "³¹P and ²³Na NMR spectroscopy of normal and ischemic rat skeletal muscle. Use of a shift reagent in vivo," *NMR Biomed.*, vol. 3, no. 2, pp. 47–58, Apr. 1990.
- [182] P. M. Walker, "Ischemia/Reperfusion Injury in Skeletal Muscle," *Ann. Vasc. Surg.*, vol. 5, no. 4, pp. 399–402, Jul. 1991.
- [183] B. Matot, G. Jouvion, A. B. Martins-Bach, C. Wary, and P. G. Carlier, "Metabolic and hemodynamic alterations in the mdx skeletal muscle revisited using multi-parametric functional NMR," in *WMS*, 2012.
- [184] S. Loerakker, C. W. J. Oomens, E. Manders, T. Schakel, D. L. Bader, F. P. T. Baaijens, K. Nicolay, and G. J. Strijkers, "Ischemia-reperfusion injury in rat skeletal muscle assessed with T2-weighted and dynamic contrast-enhanced MRI," *Magn. Reson. Med.*, vol. 66, no. 2, pp. 528–537, Aug. 2011.
- [185] M. Petracca, R. O. Vancea, L. Fleysheer, L. E. Jonkman, N. Oesingmann, and M. Inglese, "Brain intra- and extracellular sodium concentration in multiple sclerosis: a 7 T MRI study," *Brain*, vol. 139, no. 3, pp. 795–806, Mar. 2016.
- [186] L. V. Gast, M. Uder, and A. M. Nagel, "In Vivo Double Quantum Filtered ²³Na Imaging of Human Skeletal Muscle," in *ISMRM*, 2017, p. 2959.
- [187] I. Hancu, J. R. C. van der Maarel, and F. E. Boada, "A Model for the Dynamics of Spins 3/2 in Biological Media: Signal Loss during Radiofrequency Excitation in Triple-Quantum-Filtered Sodium MRI," *J. Magn. Reson.*, vol. 147, no. 2, pp. 179–191, Dec. 2000.
- [188] A. Tsang, R. W. Stobbe, and C. Beaulieu, "In vivo double quantum filtered sodium magnetic resonance imaging of human brain," *Magn. Reson. Med.*, vol. 73, no. 2, pp. 497–504, Feb. 2015.
- [189] J. S. Tauskela, J. M. Dizon, P. J. Cannon, and J. Katz, "Detection of an Extracellular Contribution from a Second-Rank Tensor to the Double-Quantum-Filtered ²³Na NMR Spectrum in the Isolated Perfused Rat Heart," *J. Magn. Reson.*, vol. 108, pp. 165–169, 1995.
- [190] E. N. Marieb and K. Hoehn, *Human Anatomy & Physiology*, 7th ed. San Francisco, CA: Pearson Benjamin Cummings, 2007.
- [191] S. M. Eleff, M. D. Schnall, L. Ligetti, M. Osbakken, V. H. Subramanian, B. Chance, and J. S. Leigh, "Concurrent measurements of cerebral blood flow, sodium, lactate, and high-energy

-
- phosphate metabolism using ^{19}F , ^{23}Na , ^1H , and ^{31}P nuclear magnetic resonance spectroscopy,” *Magn. Reson. Med.*, vol. 7, no. 4, pp. 412–24, Aug. 1988.
- [192] P. Linz, D. Santoro, W. Renz, J. Rieger, A. Ruehle, J. Ruff, M. Deimling, N. Rakova, D. N. Muller, F. C. Luft, J. Titze, and T. Niendorf, “Skin sodium measured with ^{23}Na MRI at 7.0 T.,” *NMR Biomed.*, vol. 28, no. 1, pp. 54–62, Jan. 2015.
- [193] G. Madelin, R. Kline, R. Walvick, and R. R. Regatte, “A method for estimating intracellular sodium concentration and extracellular volume fraction in brain in vivo using sodium magnetic resonance imaging,” *Sci. Rep.*, vol. 4, pp. 1–7, Apr. 2014.
- [194] W. Lostal, M. Bartoli, N. Bourg, C. Roudaut, A. Bentaib, K. Miyake, N. Guerchet, F. Fougereousse, P. McNeil, and I. Richard, “Efficient recovery of dysferlin deficiency by dual adeno-associated vector-mediated gene transfer,” *Hum. Mol. Genet.*, vol. 19, no. 10, pp. 1897–1907, May 2010.
- [195] J. N. Robinson-Hamm and C. A. Gersbach, “Gene therapies that restore dystrophin expression for the treatment of Duchenne muscular dystrophy,” *Hum. Genet.*, vol. 135, no. 9, pp. 1029–1040, Sep. 2016.
- [196] S. Perrin, “Preclinical research: Make mouse studies work,” *Nature*, vol. 507, no. 7493, pp. 423–425, Mar. 2014.
- [197] T. A. Partridge, “The mdx mouse model as a surrogate for Duchenne muscular dystrophy,” *FEBS J.*, vol. 280, no. 17, pp. 4177–4186, Sep. 2013.
- [198] G. Bulfield, W. G. Siller, P. A. Wight, and K. J. Moore, “X chromosome-linked muscular dystrophy (mdx) in the mouse,” *Proc. Natl. Acad. Sci. U. S. A.*, vol. 81, no. 4, pp. 1189–92, 1984.
- [199] H. H. Stedman, H. L. Sweeney, J. B. Shrager, H. C. Maguire, R. a Panettieri, B. Petrof, M. Narusawa, J. M. Leferovich, J. T. Sladky, and a M. Kelly, “The mdx mouse diaphragm reproduces the degenerative changes of Duchenne muscular dystrophy,” *Nature*, vol. 352, no. 6335, pp. 536–539, Aug. 1991.
- [200] G. B. Banks and J. S. Chamberlain, “Chapter 9 The Value of Mammalian Models for Duchenne Muscular Dystrophy in Developing Therapeutic Strategies,” in *Current Topics in Developmental Biology*, 1st ed., vol. 84, no. 8, Elsevier Inc., 2008, pp. 431–453.
- [201] M. a. Hornsey, S. H. Laval, R. Barresi, H. Lochmüller, and K. Bushby, “Muscular dystrophy in dysferlin-deficient mouse models,” *Neuromuscul. Disord.*, vol. 23, pp. 377–387, 2013.
- [202] O. Biondi, M. Villemeur, A. Marchand, F. Chretien, N. Bourg, R. K. Gherardi, I. Richard, and F.-J. Authier, “Dual Effects of Exercise in Dysferlinopathy,” *Am. J. Pathol.*, vol. 182, no. 6, pp. 2298–2309, Jun. 2013.
- [203] L. Heidt, M. Bader, S. Spuler, and V. Schoewel, “A novel mutation in DNAJB6 causes a more severe phenotype and greater loss of anti-aggregation function,” *Neuromuscul. Disord.*, vol. 24, no. 9–10, pp. 902–903, Oct. 2014.
- [204] K. Wenzel, M. Carl, A. Perrot, J. Zabojszcza, M. Assadi, M. Ebeling, C. Geier, P. N. Robinson, W. Kress, K.-J. Osterziel, and S. Spuler, “Novel sequence variants in dysferlin-deficient muscular dystrophy leading to mRNA decay and possible C2-domain misfolding,” *Hum.*

- Mutat.*, vol. 27, no. 6, pp. 599–600, Jun. 2006.
- [205] H. Gudbjartsson and S. Patz, “The rician distribution of noisy mri data,” *Magn. Reson. Med.*, vol. 34, no. 6, pp. 910–914, Dec. 1995.
- [206] D. M. Bates and D. G. Watts, Eds., *Nonlinear Regression Analysis and Its Applications*. Hoboken, NJ, USA: John Wiley & Sons, Inc., 1988.
- [207] N. Nagy, R. J. Nonneman, T. Llanga, C. F. Dial, N. V. Riddick, T. Hampton, S. S. Moy, K. K. Lehtimäki, T. Ahtoniemi, J. Puoliväli, H. Windish, D. Albrecht, I. Richard, and M. L. Hirsch, “Hip region muscular dystrophy and emergence of motor deficits in dysferlin-deficient Bla/J mice,” *Physiol. Rep.*, vol. 5, no. 6, p. e13173, Mar. 2017.
- [208] J. L. Thibaud, A. Monnet, D. Bertoldi, I. Barthélémy, S. Blot, and P. G. Carlier, “Characterization of dystrophic muscle in golden retriever muscular dystrophy dogs by nuclear magnetic resonance imaging,” *Neuromuscul. Disord.*, vol. 17, no. 7, pp. 575–584, 2007.
- [209] N. Azzabou, H. Reyngoudt, F. E. Smith, H. Hilsden, A. Blamire, P. G. Carlier, and J. F. Consortium, “NMR imaging and 31P-NMRS of the skeletal muscle in a multi-center dysferlinopathy study: One-year follow-up,” in *ESMRMB*, 2016, p. 428.
- [210] J. A. Roche, M. E. Tulapurkar, A. L. Mueller, N. van Rooijen, J. D. Hasday, R. M. Lovering, and R. J. Bloch, “Myofiber Damage Precedes Macrophage Infiltration after in Vivo Injury in Dysferlin-Deficient A/J Mouse Skeletal Muscle,” *Am. J. Pathol.*, vol. 185, no. 6, pp. 1686–1698, Jun. 2015.
- [211] J.-L. Thibaud, N. Azzabou, I. Barthelemy, S. Fleury, L. Cabrol, S. Blot, and P. G. Carlier, “Comprehensive longitudinal characterization of canine muscular dystrophy by serial NMR imaging of GRMD dogs,” *Neuromuscul. Disord.*, vol. 22, pp. S85–S99, Oct. 2012.
- [212] S. J. Pratt, S. Xu, R. J. Mullins, and R. M. Lovering, “Temporal changes in magnetic resonance imaging in the mdx mouse,” *BMC Res. Notes*, vol. 6, no. 1, p. 262, 2013.
- [213] R. S. Vohra, S. Mathur, N. D. Bryant, S. C. Forbes, K. Vandenborne, and G. A. Walter, “Age-related T2 changes in hindlimb muscles of mdx mice,” *Muscle Nerve*, vol. 53, no. 1, pp. 84–90, Jan. 2016.
- [214] S. Mathur, R. S. Vohra, S. A. Germain, S. Forbes, N. D. Bryant, K. Vandenborne, and G. A. Walter, “Changes in muscle T2 and tissue damage after downhill running in mdx Mice,” *Muscle Nerve*, vol. 43, no. 6, pp. 878–886, Jun. 2011.
- [215] G. Walter, L. Cordier, D. Bloy, and H. L. Sweeney, “Noninvasive monitoring of gene correction in dystrophic muscle,” *Magn. Reson. Med.*, vol. 54, no. 6, pp. 1369–1376, 2005.
- [216] G. J. Kemp, D. J. Taylor, J. F. Dunn, S. P. Frostick, and G. K. Radda, “Cellular energetics of dystrophic muscle,” *J. Neurol. Sci.*, vol. 116, no. 2, pp. 201–206, Jun. 1993.
- [217] J. F. Dunn, S. Frostick, G. Brown, and G. K. Radda, “Energy status of cells lacking dystrophin: an in vivo/in vitro study of mdx mouse skeletal muscle,” *Biochim. Biophys. Acta - Mol. Basis Dis.*, vol. 1096, no. 2, pp. 115–120, Feb. 1991.
- [218] C. R. Heier, A. D. Guerron, A. Korotcov, S. Lin, H. Gordish-Dressman, S. Fricke, R. W. Sze, E. P. Hoffman, P. Wang, and K. Nagaraju, “Non-Invasive MRI and Spectroscopy of mdx Mice Reveal Temporal Changes in Dystrophic Muscle Imaging and in Energy Deficits,” *PLoS One*,

-
- vol. 9, no. 11, p. e112477, Nov. 2014.
- [219] L. S. Prince, S. K. Miller, G. M. Pohost, and G. A. Elgavish, "The longitudinal relaxation time (T₁) of the intracellular ²³Na NMR signal in the isolated perfused rat heart during hypoxia and reoxygenation.," *Magn. Reson. Med.*, vol. 23, no. 2, pp. 376–82, Feb. 1992.
- [220] V. D. Schepkin, U. Gawlick, B. D. Ross, and T. L. Chenevert, "Detection of triple quantum Na NMR in normal and tumored mouse brain.," in *ISMRM*, 2003, vol. 11, p. 39.
- [221] J. F. Dunn, N. Bannister, G. J. Kemp, and S. J. Publicover, "Sodium is elevated in mdx muscles: Ionic interactions in dystrophic cells," *J. Neurol. Sci.*, vol. 114, no. 1, pp. 76–80, Jan. 1993.
- [222] C. A. Pacak, G. A. Walter, G. Gaidosh, N. Bryant, M. A. Lewis, S. Germain, C. S. Mah, K. P. Campbell, and B. J. Byrne, "Long-term skeletal muscle protection after gene transfer in a mouse model of LGMD-2D," *Mol. Ther.*, vol. 15, no. 10, pp. 1775–1781, 2007.
- [223] A. R. Burr and J. D. Molkenkin, "Genetic evidence in the mouse solidifies the calcium hypothesis of myofiber death in muscular dystrophy," *Cell Death Differ.*, vol. 22, no. 9, pp. 1402–1412, Sep. 2015.
- [224] M. A. Griswold, P. M. Jakob, R. M. Heidemann, M. Nittka, V. Jellus, J. Wang, B. Kiefer, and A. Haase, "Generalized autocalibrating partially parallel acquisitions (GRAPPA)," *Magn. Reson. Med.*, vol. 47, no. 6, pp. 1202–1210, Jun. 2002.
- [225] R. Umathum, M. B. Rösler, and A. M. Nagel, "In Vivo 39K MR Imaging of Human Muscle and Brain.," *Radiology*, vol. 269, no. 2, pp. 569–76, 2013.
- [226] S. E. Anderson, C. Z. Dickinson, H. Liu, and P. M. Cala, "Effects of Na-K-2Cl cotransport inhibition on myocardial Na and Ca during ischemia and reperfusion," *Am J Physiol Cell Physiol*, vol. 270, no. 2, pp. C608-618, Feb. 1996.
- [227] J. J. W. Sandstede, H. Hillenbrand, M. Beer, T. Pabst, F. Butter, W. Machann, W. Bauer, D. Hahn, and S. Neubauer, "Time course of ²³Na signal intensity after myocardial infarction in humans," *Magn. Reson. Med.*, vol. 52, no. 3, pp. 545–51, 2004.
- [228] R. Ouwkerk, M. a. Jacobs, K. J. MacUra, A. C. Wolff, V. Stearns, S. D. Mezban, N. F. Khouri, D. a. Bluemke, and P. a. Bottomley, "Elevated tissue sodium concentration in malignant breast lesions detected with non-invasive ²³Na MRI," *Breast Cancer Res. Treat.*, vol. 106, pp. 151–160, 2007.
- [229] M. Inglese, G. Madelin, N. Oesingmann, J. S. Babb, W. Wu, B. Stoeckel, J. Herbert, and G. Johnson, "Brain tissue sodium concentration in multiple sclerosis: a sodium imaging study at 3 tesla.," *Brain*, vol. 133, no. Pt 3, pp. 847–57, Mar. 2010.
- [230] B. Ridley, A. M. Nagel, M. Bydder, A. Maarouf, J.-P. Stellmann, S. Gherib, J. Verneuil, P. Viout, M. Guye, J.-P. Ranjeva, and W. Zaaraoui, "Distribution of brain sodium long and short relaxation times and concentrations: a multi-echo ultra-high field ²³Na MRI study," *Sci. Rep.*, vol. 8, no. 1, p. 4357, Dec. 2018.
- [231] S. D. Friedman, S. L. Poliachik, G. T. Carter, C. B. Budech, T. D. Bird, and D. W. W. Shaw, "The magnetic resonance imaging spectrum of facioscapulohumeral muscular dystrophy," *Muscle Nerve*, vol. 45, no. 4, pp. 500–506, 2012.

- [232] J. Lommen, S. Konstandin, P. Krämer, and L. R. Schad, "Enhancing the quantification of tissue sodium content by MRI: time-efficient sodium B 1 mapping at clinical field strengths," *NMR Biomed.*, vol. 29, no. 2, pp. 129–136, Feb. 2016.
- [233] C. Mozzetta, G. Minetti, and P. L. Puri, "Regenerative pharmacology in the treatment of genetic diseases: The paradigm of muscular dystrophy," *Int. J. Biochem. Cell Biol.*, vol. 41, no. 4, pp. 701–710, Apr. 2009.
- [234] T. S. Khurana and K. E. Davies, "Pharmacological strategies for muscular dystrophy," *Nat. Rev. Drug Discov.*, vol. 2, no. 5, pp. 379–390, May 2003.
- [235] V. Pini, J. E. Morgan, F. Muntoni, and H. C. O'Neill, "Genome Editing and Muscle Stem Cells as a Therapeutic Tool for Muscular Dystrophies," *Curr. Stem Cell Reports*, vol. 3, no. 2, pp. 137–148, Jun. 2017.
- [236] P. Gee, H. Xu, and A. Hotta, "Cellular Reprogramming, Genome Editing, and Alternative CRISPR Cas9 Technologies for Precise Gene Therapy of Duchenne Muscular Dystrophy," *Stem Cells Int.*, vol. 2017, no. DMD, pp. 1–11, 2017.
- [237] P. Hafner, U. Bonati, B. Erne, M. Schmid, D. Rubino, U. Pohlman, T. Peters, E. Rutz, S. Frank, C. Neuhaus, S. Deuster, M. Gloor, O. Bieri, A. Fischmann, M. Sinnreich, N. Gueven, and D. Fischer, "Improved Muscle Function in Duchenne Muscular Dystrophy through L-Arginine and Metformin: An Investigator-Initiated, Open-Label, Single-Center, Proof-Of-Concept-Study," *PLoS One*, vol. 11, no. 1, p. e0147634, Jan. 2016.

Titre : Caractérisation du muscle dystrophique par RMN du ^{23}Na et spectre RMN T_2 du ^1H

Mots clés : muscle squelettique, dystrophie musculaire, résonance magnétique nucléaire du sodium, T_2 du proton

Résumé : Le but de la thèse était d'étudier la sensibilité de nouveaux biomarqueurs RMN visant à quantifier les changements pathologiques dans le muscle dystrophique. La dystrophie musculaire (DM) désigne un groupe hétérogène de maladies avec une atrophie musculaire progressive associée à un état de faiblesse. Elle est caractérisée par des degrés variables de nécrose, de régénération, de troubles de l'homéostasie ionique, d'inflammation chronique et finalement par le remplacement des muscles par du tissu fibro-gras.

Mon objectif était d'évaluer la RMN du ^{23}Na et les techniques avancées de mesure du temps de relaxation transversal ^1H (T_2) en tant que des biomarqueurs sensibles et précoces. La RMN du ^{23}Na mesure les concentrations de sodium étroitement contrôlées et donne sa distribution dans le tissu. Cette information peut être utilisée

pour évaluer l'homéostasie ionique et l'intégrité cellulaire. Cependant, la concentration *in vivo* en ^{23}Na est faible, la RMN du ^{23}Na souffre donc d'une faible sensibilité par rapport à ^1H . L'altération du T_2 ^1H du muscle, communément interprétée comme un indicateur de l'activité de la maladie, est liée à une variété d'événements non-spécifiques tels que l'œdème, l'inflammation ou la nécrose, qui précèdent le remplacement musculaire par la graisse.

Des protocoles comprenant diverses méthodes de RMN du ^{23}Na et de ^1H T_2 ont été mis en œuvre pour évaluer les tissus musculaires squelettiques sains et dystrophiques sur des modèles animaux et sur patients. Ce travail fournit des preuves que la RMN du ^{23}Na pourrait offrir un biomarqueur sensible capable de surveiller l'altération spécifique du muscle dystrophique à un stade très précoce.

Title: Characterization of the dystrophic muscle by ^{23}Na NMR and ^1H NMR T_2 spectrum

Keywords: skeletal muscle, muscle dystrophy, sodium nuclear magnetic resonance, proton T_2

Abstract: The aim of the thesis is to investigate the sensitivity of novel NMR outcome measures (OM) aiming to quantify pathological changes in the dystrophic muscle. Muscular dystrophy (MD) refers to a heterogeneous group of diseases with progressive muscle wasting and associated weakness characterized by variable degrees of necrosis, regeneration, ionic homeostasis disturbances, chronic inflammation, and, ultimately, resulting in the replacement of muscles by fibro-fatty tissue.

My focus was on the evaluation of ^{23}Na NMR and advanced ^1H transverse relaxation time (T_2) techniques as early, sensitive OM. ^{23}Na NMR measures the tightly controlled sodium concentrations and distribution in skeletal muscle tissue. This biophysical information can

be used to assess ion homeostasis and cell integrity. However, ^{23}Na NMR suffers from a low sensitivity and *in vivo* concentration compared to ^1H . Alterations in the muscle ^1H T_2 , commonly interpreted as an indicator of disease activity, are linked to a variety of non-specific events like oedema, inflammation, or necrosis that precede the actual muscle replacement by fat.

Protocols including different ^{23}Na NMR and ^1H T_2 methods were implemented to evaluate healthy and dystrophic skeletal muscle tissues of animal models and patients. This work provides evidence that ^{23}Na NMR could offer a sensitive outcome measure able to monitor specific alteration of the dystrophic muscle at a very early stage.